

UNIVERSITY OF CALIFORNIA
SANTA CRUZ

**EVOLUTION OF GALAXY STRUCTURE USING VISUAL
MORPHOLOGIES IN CANDELS AND HYDRO-ART
SIMULATIONS**

A dissertation submitted in partial satisfaction of the
requirements for the degree of

DOCTOR OF PHILOSOPHY

in

ASTRONOMY & ASTROPHYSICS

by

Mark W. Mozena

December 2013

The Dissertation of Mark W. Mozena
is approved:

Professor Sandra Faber, Chair

Professor David Koo

Professor Joel Primack

Tyrus Miller
Vice Provost and Dean of Graduate Studies

Copyright © by

Mark W. Mozena

2013

Table of Contents

List of Figures	v
List of Tables	viii
Abstract	x
Dedication	xii
Acknowledgments	xiii
1 CANDELS GOODS-South Observations	1
1.1 Introduction	1
1.2 Data	5
1.2.1 CANDELS Observations	5
1.2.2 SEXTRACTOR	9
1.2.3 Photometry and SED Fitting	10
1.2.4 GALFIT Parameters	13
1.2.5 Visual Classifications	15
1.2.6 Sample Selection	22
1.3 MWGunified Populations	28
1.3.1 Spheroidicity (\mathcal{S})	37
1.3.2 Clumpy Galaxies, Chains, and Tadpoles	56
1.3.3 Asymmetric, Irregular, & Merger/Interacting Galaxies	69
1.4 Quiescent $z\sim 2$ populations	77
1.5 Axial Ratio Distribution at $z\sim 2$	86
1.6 Summary	96
2 Comparison of Hydro-ART Simulated Galaxies with Observations	100
2.1 Introduction	100
2.2 Data	105
2.2.1 Hydro ART Simulations	105
2.2.2 Simulation Processing	107

2.2.3	CANDELS Observations	111
2.2.4	Data Processing	113
2.3	Morphology Classifications	117
2.3.1	Sample Selection	125
2.3.2	Hydro-ART Simulation Caveats	128
2.4	Global Parameters	131
2.5	Visual Classifications and Sérsic	143
2.6	Clumpiness	147
2.7	Conclusions	160
A	MWGunified Visual Classification System Examples	164
B	GOODS-South Galaxy Fractions Evolution Tables - ‘Bin Fraction’	169
C	Morphology Evolution of Individual $z \sim 2$ Hydro-ART Simulations	179

List of Figures

1.1	GOODS-South Field	8
1.2	GOODS-South F160W Sample Selection	26
1.3	GOODS-South Galaxy Fractions in Mass and Redshift Bins	27
1.4	Galaxy Population Fractions	38
1.5	Disk Galaxy Fractions in Mass and Redshift Bins	41
1.6	Intermediate/Transitional Galaxy Fractions in Mass and Redshift Bins	42
1.7	Spheroid Galaxy Fractions in Mass and Redshift Bins	42
1.8	Global Properties of $z \sim 2$ GOODS-South Sample by Sérsic Indices	49
1.9	Global Properties of $z \sim 2$ GOODS-South Sample by Visual Classifications	50
1.10	Global Properties of Edge-on $z \sim 2$ GOODS-South Sample	54
1.11	Global Properties of Face-on $z \sim 2$ GOODS-South Sample	55
1.12	Clumpy Galaxy Fractions in Mass and Redshift Bins	63
1.13	Chain Galaxy Fractions in Mass and Redshift Bins	63
1.14	Tadpole Galaxy Fractions in Mass and Redshift Bins	67
1.15	Global Properties of $z \sim 2$ Clumpy, Tadpole & Chain Galaxies in GOODS-South and Elmegreen UDF Samples.	68
1.16	Asymmetric Galaxy Fractions in Mass and Redshift Bins	72
1.17	Merger/Interaction Galaxy Fractions in Mass and Redshift Bins	75
1.18	Global Properties of $z \sim 2$ Asymmetric, Irregular, and Interacting Galaxies in GOODS-South	76
1.19	Global Properties of UVJ Selected Quiescent $z \sim 2$ Galaxies in GOODS-South	78
1.20	Global Properties of sSFR Selected Quiescent $z \sim 2$ Galaxies in GOODS-South	81
1.21	Global Properties of $M_{\text{stellar}}\text{-}R_{\text{eff}}$ Selected Quiescent $z \sim 2$ Galaxies in GOODS-South	83
1.22	Axis Ratio- R_{eff} Relation in Different Mass Bins with Sérsic for $z \sim 2$ GOODS-South Galaxies	88
1.23	Axis Ratio- R_{eff} Relation in Different Mass Bins with Spheroidicity for $z \sim 2$ GOODS-South Galaxies	89

1.24	Axis Ratio- R_{eff} Relation in Different Mass Bins with UVJ Populations for $z\sim 2$ Galaxies in GOODS-South Galaxies	92
1.25	Axis Ratio- R_{eff} Relation in Different Mass Bins with sSFR Populations for $z\sim 2$ Galaxies in GOODS-South Galaxies	93
1.26	Axis Ratio- R_{eff} Relation in Different Mass Bins with Sérsic for the ‘Clean’ Star-Forming $z\sim 2$ GOODS-South Galaxies	95
2.1	Sample Selection	127
2.2	Stellar to Halo Mass Fraction of Simulations	130
2.3	Global Properties of Full ‘clean’ $z\sim 2$ GOODS-South Sample by Visual Classifications	132
2.4	Global Properties of Full ‘clean’ $z\sim 2$ GOODS-South Sample by Sérsic Indices	133
2.5	Global Properties of Full ‘clean’ $z\sim 2$ Star-Forming Only GOODS-South Sample by Visual Classification	137
2.6	Global Properties of Full ‘clean’ $z\sim 2$ Star-Forming Only GOODS-South Sample by Sérsic Index	138
2.7	Global Properties of the Hydro-ART $z\sim 2$ Simulations by Visual Classification	141
2.8	Global Properties of the Hydro-ART $z\sim 2$ Simulations by Sérsic Index	142
2.9	Sérsic - R_{eff} of Various Visual Classifications for the ‘clean’ Star-Forming GOODS-South Galaxies	145
2.10	Sérsic - R_{eff} of Various Visual Classifications for the Hydro-ART Simulations	146
2.11	Clumpy Star-Forming GOODS-South Galaxies	151
2.12	Clumpy Hydro-ART Simulations	152
2.13	Clumpy Star-Forming GOODS-South Low Mass Galaxies	154
2.14	Clumpy Star-Forming GOODS-South Moderate Mass Galaxies	155
2.15	Clumpy Star-Forming GOODS-South High Mass Galaxies	156
2.16	Clumpy Hydro-ART Low Mass Simulations	157
2.17	Clumpy Hydro-ART Intermediate Mass Simulations	158
2.18	Clumpy Hydro-ART High Mass Simulations	159
A.1	Global Morphology Classes	165
A.2	Interaction Classes	166
A.3	Structural Flags - Part 1	167
A.4	Structural Flags - Part 2	168
A.5	Clumpiness-Patchiness Classification Matrix	168
C.1	Sérsic - R_{eff} Evolution of $z\sim 2$ Hydro-ART Simulations: 1	181
C.2	Sérsic - R_{eff} Evolution of $z\sim 2$ Hydro-ART Simulations: 2	182
C.3	Axis Ratio - R_{eff} Evolution of $z\sim 2$ Hydro-ART Simulations: 1	183
C.4	Axis Ratio - R_{eff} Evolution of $z\sim 2$ Hydro-ART Simulations: 2	184
C.5	Axis Ratio - Sérsic Evolution of $z\sim 2$ Hydro-ART Simulations: 1	185

C.6 Axis Ratio - Sérsic Evolution of $z \sim 2$ Hydro-ART Simulations: 2 186

List of Tables

1.1	Clumpiness Matrix (\mathcal{C})	22
1.2	GOODS-South Galaxy Fractions Evolution with Redshift in Mass and sSFR Bins	33
1.3	GOODS-South Galaxy Fractions Evolution with Redshift in Mass and R_{eff} Bins	33
1.4	Elmegreen UDF Visual Classifications vs MWGunified Visual Classifications	36
1.5	Disk Galaxy Fractions Evolution with Redshift in Mass and sSFR Bins	44
1.6	Disk Galaxy Fractions Evolution with Redshift in Mass and R_{eff} Bins .	44
1.7	Intermediate Galaxy Fractions Evolution with Redshift in Mass and sSFR Bins	45
1.8	Intermediate Galaxy Fractions Evolution with Redshift in Mass and R_{eff} Bins	45
1.9	Spheroid Galaxy Fractions Evolution with Redshift in Mass and sSFR Bins	46
1.10	Spheroid Galaxy Fractions Evolution with Redshift in Mass and R_{eff} Bins	46
1.11	Clumpy Galaxy Fractions Evolution with Redshift in Mass and sSFR Bins	64
1.12	Clumpy Galaxy Fractions Evolution with Redshift in Mass and R_{eff} Bins	64
1.13	Chain Galaxy Fractions Evolution with Redshift in Mass and sSFR Bins	65
1.14	Chain Galaxy Fractions Evolution with Redshift in Mass and R_{eff} Bins	65
1.15	Tadpole Galaxy Fractions Evolution with Redshift in Mass and sSFR Bins	66
1.16	Tadpole Galaxy Fractions Evolution with Redshift in Mass and R_{eff} Bins	66
1.17	Asymmetric Galaxy Fractions Evolution with Redshift in Mass and sSFR Bins	73
1.18	Asymmetric Galaxy Fractions Evolution with Redshift in Mass and R_{eff} Bins	73
1.19	Merger Galaxy Fractions Evolution with Redshift in Mass and sSFR Bins	74
1.20	Merger Galaxy Fractions Evolution with Redshift in Mass and R_{eff} Bins	74
2.1	Clumpiness Matrix (\mathcal{C})	125
2.2	Simulation Classification Dependence on Viewing Angle	149

B.1	Disk Galaxy Evolution Fractions with Redshift in Mass and sSFR Bins - 'Bin Fraction'	171
B.2	Disk Galaxy Fractions Evolution with Redshift in Mass and R_{eff} Bins - 'Bin Fraction'	171
B.3	Intermediate Galaxy Fractions Evolution with Redshift in Mass and sSFR Bins - 'Bin Fraction'	172
B.4	Intermediate Galaxy Fractions Evolution with Redshift in Mass and R_{eff} Bins - 'Bin Fraction'	172
B.5	Spheroid Galaxy Fractions Evolution with Redshift in Mass and sSFR Bins - 'Bin Fraction'	173
B.6	Spheroid Galaxy Fractions Evolution with Redshift in Mass and R_{eff} Bins - 'Bin Fraction'	173
B.7	Clumpy Galaxy Fractions Evolution with Redshift in Mass and sSFR Bins - 'Bin Fraction'	174
B.8	Clumpy Galaxy Fractions Evolution with Redshift in Mass and R_{eff} Bins - 'Bin Fraction'	174
B.9	Chain Galaxy Fractions Evolution with Redshift in Mass and sSFR Bins - 'Bin Fraction'	175
B.10	Chain Galaxy Fractions Evolution with Redshift in Mass and R_{eff} Bins - 'Bin Fraction'	175
B.11	Tadpole Galaxy Fractions Evolution with Redshift in Mass and sSFR Bins - 'Bin Fraction'	176
B.12	Tadpole Galaxy Fractions Evolution with Redshift in Mass and R_{eff} Bins - 'Bin Fraction'	176
B.13	Asymmetric Galaxy Fractions Evolution with Redshift in Mass and sSFR Bins - 'Bin Fraction'	177
B.14	Asymmetric Galaxy Fractions Evolution with Redshift in Mass and R_{eff} Bins - 'Bin Fraction'	177
B.15	Merger Galaxy Fractions Evolution with Redshift in Mass and sSFR Bins - 'Bin Fraction'	178
B.16	Merger Galaxy Fractions Evolution with Redshift in Mass and R_{eff} Bins - 'Bin Fraction'	178

Abstract

Evolution of Galaxy Structure using Visual Morphologies in CANDELS and
Hydro-ART Simulations

by

Mark W. Mozena

The general properties, morphologies, and classes of galaxies in the local Universe are well studied. Most local galaxies are morphologically members of the Hubble sequence and can be crudely separated into elliptical red quiescent galaxies or disk blue star-forming galaxies. This Hubble sequence of relaxed structures has been shown to dominate galaxy populations out to a redshift of $z \sim 1$. The description of galaxies at earlier times is not well known nor is it understood how and at what epoch the Hubble sequence formed. Of particular interest is the structure of galaxies at $z \sim 2$. This epoch was an active time for galaxy growth and was the peak epoch for star formation rate, active galactic nuclei activity, and mergers between galaxies.

With the installation of the near-infrared Wide Field Camera 3 (WFC3) on the Hubble Space Telescope in 2009, large area photometric surveys of galaxies were able to be performed for the first time at moderate redshifts ($z \sim 2$) in wavebands that effectively trace the older stellar populations and stellar mass of the galaxies rather than the clumpy star-forming regions. Using WFC3 HST images, an in-depth morphology classification system was developed to probe the galaxy populations at higher redshifts (focusing on $z \sim 2$). These visual classifications were used with other galaxy parameters

(stellar mass, color, star formation rate, radius, Sérsic profiles, etc) to identify and quantify the moderate redshift galaxy populations and study how these populations changed with time to form the relaxed Hubble sequence Universe we observe today.

Additionally, these same tools that were used to probe galaxy populations at $z \sim 2$ in the observed Universe were also used on simulated galaxy images produced from state-of-the-art cosmological simulations. These Hydro-ART simulations build artificial galaxies that are compared to observations so as to shed light on the relevant mechanisms in galaxy evolution. By classifying and comparing the populations present in the simulations with our observations, we are able to probe the model's ability to create realistic galaxy populations.

The first chapter of this thesis focuses on visually classifying and studying galaxy populations at $z \sim 2$ and how they change with redshift for a given mass. The second chapter focuses on applying our techniques to Hydro-ART simulations at $z \sim 2$ and comparing these mock 'observed' simulations with our real WFC3 HST observations. Both of these chapters closely resemble manuscripts in the process of being submitted for independent publication.

For my part,
I know nothing with any certainty,
but the sight of the stars
makes me dream

-Vincent Van Gogh

Acknowledgments

Thank you to my family, friends, and colleagues all of whom have encouraged and supported me through the wandering roads that led to this PhD. It has been quite the adventure and I am grateful to have shared it with each of you.

Thank you to my wonderful advisors (especially Sandra Faber, David Koo, and Joel Primack) who have shared their exceptional scientific insights and leadership. Their support and guidance was invaluable as I pursued not only my research priorities but also my various nonacademic interests in science communication, outreach, and government. I consider myself extremely lucky to have worked with such exceptional scientific leaders who helped me find my path.

I thank my extended research family - the CANDELS, DEEP, AEGIS and CATS collaborations. Working as a member of the CANDELS team, in particular, helped to shape me as a researcher and scientist.

Thank you to my parents, sister and Tyler who have provided endless support and encouragement throughout this process. I am blessed to have such a wonderful family who doesn't tease me too often about being in 23rd grade...

Lastly, thank you to all of my friends in Santa Cruz. We have lived in a beautiful place and I am grateful to have explored it with you over these last six years. Quite the adventure indeed!

Thank you Santa Cruz!

Chapter 1

CANDELS GOODS-South Observations

1.1 Introduction

Massive galaxies in the local Universe are seen to be well described morphologically by the Hubble sequence (Hubble, 1926). A galaxy's global properties (radii, stellar light profile, color, star formation rates, rotation, dominance of central bulge) tend to correspond with its place on the Hubble sequence (spiral, elliptical, etc). The large sample of local galaxies observed in the Sloan Digital Sky Survey (SDSS) helped establish this general connection for massive galaxies between their morphological shapes and their global properties. The state of this correlation and the evolution of galaxies on the Hubble sequence at higher redshifts is far less understood. Determining the global properties of massive galaxies at earlier redshifts will help identify when the morphological Hubble sequence formed and how the general correlation between morphology and global properties came about.

In the local Universe, most galaxies can be classified into a morphological and color bimodality in which the elliptical galaxies have higher optical light Sérsic (Sersic, 1968) profiles, have lower star formation rates, and are red in color. The disk systems have exponential light profiles, have higher star formation rates, and are bluer in color (Sandage (1986), Strateva et al. (2001), Kauffmann et al. (2003), Conselice (2006), Nair & Abraham (2010), Conselice (2003), Conselice et al. (2005), Scarlata et al. (2007)). Studies have shown that these relations are similar out to a redshift $z \sim 1$ (Brinchmann et al. (1998), Abraham et al. (1996), van den Bergh et al. (2000), Ilbert et al. (2006), Oesch et al. (2010), and Buitrago et al. (2013)). These studies have found that the galaxy populations up to a red shift of $z=1$ are dominated by the Hubble sequence and that the irregular galaxies are similar to the local population. Many of the local relations between the morphology and global properties of galaxies are present back to a redshift of $z=1$ including the relation between visual morphology and a galaxy's color and SFR (Bell et al., 2004). There is strong evidence to support a hierarchical merger history of massive galaxies that simultaneously shuts down star formation and changes the morphology from disk dominated to bulge dominated elliptical systems (Driver et al. (2006), Baldry et al. (2004), and Drory & Fisher (2007)). The exact mechanism and path local massive galaxies take along the Hubble sequence is not fully understood though leading theories favor quenching by major mergers. The existence of blue star-forming spheroids and red quenched disks is not fully understood and seems inconsistent with this hierarchical model driven by major mergers (Bamford et al. (2009) and Masters et al. (2010)).

Our understanding of galaxy morphology at redshifts beyond $z=1$ is less clear. Some studies (Papovich et al. (2005), Cameron et al. (2011), Dickinson (2000)) suggest that Hubble type galaxies were not present at redshifts beyond $z=2$ and the Universe was filled with irregular structures. This would require a significant amount of galaxy evolution to transform these irregular structures at $z\sim 2$ to a more settled Hubble sequence population by $z\sim 1$ (Kriek et al., 2009). Other studies (Driver et al. (1998), Conselice et al. (2005), Szomoru et al. (2011), Conselice et al. (2011a), and Buitrago et al. (2013)) have found that a Hubble sequence population does exist at $z\sim 2$ but that the dominant population of galaxies are irregular. The discrepancies between these studies could be due to sample selection, completeness issues, or poor image quality preventing reliable visual classifications. Until recently, morphological studies at redshifts above 1 were based either on observed optical filters or low spatial resolution near-infrared (NIR) observations. High spatial resolution optical surveys performed using instruments such as WFPC2 and ACS on the Hubble Space Telescope (HST) have allowed morphological studies of nearby galaxies but are limited beyond a redshift of 1. At higher redshifts, these optical filters are measuring rest-frame wavelengths shorter than 4000\AA and are thus probing ultraviolet (UV) light which is sensitive to star-forming regions and does not accurately trace the underlying stellar population distribution. To properly compare the morphologies of galaxies beyond a redshift of 1 to local galaxy samples, it is necessary to use NIR filters to observe the rest-frame optical light distribution which more reliably traces the older stellar populations and gives a better representation of the underlying stellar mass distribution of the galaxies. Previous NIR photometric surveys

used either ground based wide-field cameras with poor spatial resolution (limiting the reliability of morphology measurements) or used the high spatial resolution but small field of view ground based adaptive optics cameras or NICMOS (Kriek et al. (2009) and Conselice et al. (2011b)) on HST (limiting the galaxy sample size). The installation of near-infrared Wide Field Camera 3 (WFC3) on HST in 2009 allowed high spatial resolution rest-frame optical light observations of a large sample of $z>1$ galaxies. Using observations in GOODS-South as part of the Cosmic Assembly Near-infrared Deep Extragalactic Legacy Survey (CANDELS)(Grogin et al. (2011) and Koekemoer et al. (2011)), this work studies the morphology and global galaxy properties of the $z>1$ universe in a way that is comparable (similar rest wavelengths) to the observations that have been made in the local universe. We are especially interested in galaxies at $z=1-3$. This $z\sim 2$ epoch is a particularly critical time for galaxy evolution as it is the peak of the star formation rate, a time of increased merger rates, and increased active galactic nuclei (AGN) activity.

To study this active epoch, we develop a detailed visual classification system to classify all bright ($H<24.5AB$) galaxies in the observed NIR F160W (rest-frame optical at $z>1$) wavelengths. We combine these visual classifications with color, size, star formation rate (SFR), and Sérsic profiles from the light distribution to probe the galaxy populations in this exciting epoch. This is the first study that uses a statistically significant sample of high spatial resolution images in rest-frame optical wavelengths to compare the visual morphology and global parameters of $z>1$ galaxies. Several papers from the CANDELS team are published that use a subsample of these visual

classifications to study particular high redshift populations including AGN (Kocevski et al., 2012), bulge evolution (Bruce et al., 2012), and Ultraluminous infrared galaxies (Kartaltepe et al., 2012). We present the GOODS-South sample in full and analyze the entire galaxy population rather than a subset. In addition, this study uses the full depth of the visual classification scheme rather than just the general (elliptical, disk, irregular) classifications used in all other CANDELS studies.

This chapter is organized into seven Sections. Section 2 describes the observations and data used as well provides a description of our visual classification system, the processing of various global parameters used, and the selection of our sample. Section 3 discusses the general galaxy populations and analyzes the characteristics of interesting subclasses - particularly clumpy, irregular, and interacting galaxies. Section 4 focuses on the properties of the quiescent sample of $z \sim 2$ galaxies. Section 5 analyzes the axis ratio relation to galaxy mass and radii at $z \sim 2$. We summarize the findings in Section 6. Throughout this chapter we state all magnitudes as AB magnitudes and we assume a standard Λ CDM cosmology with $H_0 = 71 \frac{km}{s \cdot Mpc}$, $\Omega_\Lambda = 0.73$, and $\Omega_m = 0.27$.

1.2 Data

1.2.1 CANDELS Observations

The galaxy sample for this study comes entirely from observations made as part of The Great Observatories Origins Deep Survey (GOODS) (Giavalisco et al., 2004) and the Cosmic Assembly Near-infrared Deep Extragalactic Legacy Survey (CAN-

DELS)(Grogin et al. (2011) and Koekemoer et al. (2011)) in the GOODS-South field. The CANDELS survey is a Hubble Space Telescope (HST) Multi-Cycle Treasury Program (PIs: S. Faber and H.Ferguson, PID: GO-12060) that provides Wide Field Camera 3 (WFC3) and parallel Advance Camera for Surveys (ACS) imaging in five legacy fields (GOODS-S, GOODS-N, COSMOS, UDS, and EGS). The three year, 902 orbit survey will cover a total area of ~ 800 arcmin² over the five fields. For this paper, we will focus only on the GOODS-South region. The GOODS-South portion of the CANDELS has a two tiered approach to partially cover the field of the original GOODS-South survey. A 7' x 10' 'deep' area consists of 13 orbits per WFC3 tile divided over the F105W (Y), F125W (J), and F160W (H) filters. A 4' x 10' 'wide' area consists of 2-3 orbits per WFC3 tile divided over the F125W and F160W filters. The 5σ point source magnitude limit in the F160W filter is ~ 28 AB in the 'deep' region and is ~ 27 AB in the 'wide' region. All of the infrared WFC3 exposures were accompanied by parallel visible light observations with ACS that were offset to lie in other parts of the WFC3 region so as to create a ACS region that nearly completely overlaps with the CANDELS WFC3 region. Please see Koekemoer et al. (2011) and Grogin et al. (2011) for further details on the GOODS-South observations.

WFC3 data from two previously completed surveys conducted in GOODS-South was combined with the CANDELS WFC3 observations. The Ultra Deep Field (UDF) is located within the CANDELS 'deep' region and was observed for ~ 28 orbits in F160W and ~ 15 orbits in both F105Y and F125W over a single WFC3 pointing (see Bouwens et al. (2010) for further details). The Early Release Science program (ERS)

is located just north of the CANDELS GOODS-South region and was observed for ~ 2 orbits in F098M, F125W, and F160W each over a $4' \times 9'$ area (see Windhorst et al. (2011) for further details). The WFC3 observations from these three surveys (CANDELS, ERS, and UDF) were combined to cover a large portion of the original GOODS-South survey field at varying filter depths. Figure 1.1 shows the complete CANDELS GOODS-South field with the ‘Deep’, ‘Wide’, ERS, and UDF regions superimposed. For this study we used the deepest available combined WFC3 observations. By drizzling individual WFC3 exposures together using the Multidrizzle pipeline and techniques described in Koekemoer et al. (2011), final mosaics of the observations and accompanying weight maps were created at a resampled pixel scale of 60 milliarcseconds ($0.06''$). These WFC3 mosaics were combined with mosaics of deep ACS observations taken in 2004 (Giavalisco et al., 2004) in the F435W (B), F606W(V), F775W (i), and F850LP (z) filters. These bands were similarly drizzled together into mosaics of 30 milliarcsec ($0.03''$) pixel scale with a 5σ point source magnitude limit of ~ 28.2 in the F850LP filter. These ACS and WFC3 mosaics form the fundamental dataset used in this study.

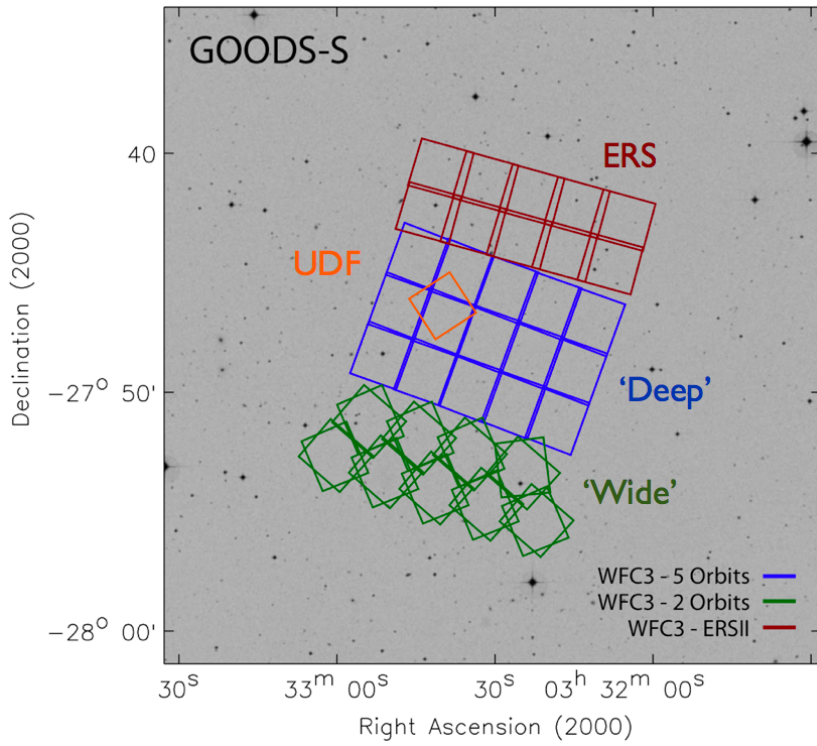


Figure 1.1: GOODS-South Field

An image of the CANDELS WFC3 GOODS-South region showing the tile pointings for the 'Deep' and 'Wide' epochs as well as for the overlapping ERS and UDF fields.

1.2.2 SEXTRACTOR

As described in Guo et al. (2013), a modified SEXTRACTOR v2.5 (Bertin & Arnouts, 1996) was used on the WFC3 CANDELS mosaics to detect objects in F160W. In order to detect large, bright objects as well as small, dim objects, the SEXTRACTOR routine is run with both ‘hot’ and ‘cold’ mode parameters and then the two catalogs are combined into a single detection catalog as implemented by the GALAPAGOS routine and described in Barden et al. (2012). The ‘cold’ mode parameters are optimized to detect bright objects without being too aggressive and dividing single systems into multiple objects. The ‘hot’ mode parameters are optimized to detect smaller, dimmer objects at the magnitude limit of the mosaics but in doing so has the unwanted effect of over deblending brighter systems into multiple objects with clumps and patchy regions flagged as independent galaxies. By combining the ‘hot’ catalog with the ‘cold’ catalog, we create a robust catalog that includes dim objects at the magnitude limit of the mosaics and still preserves bright objects being labeled as single systems. In addition to identifying the number of objects in the F160W mosaic, a segmentation map assigning pixels in the mosaic to specific objects as well as a catalog of basic object parameters (magnitude, radii, axis ratio, position angle) are also created by SEXTRACTOR. This segmentation map and global structure catalog are later used in both the visual classification system (see Section 2.5) and as starting points for GALFIT to make single Sérsic fits to the F160W light profiles (see Section 2.4). Full descriptions of running SEXTRACTOR and generating these catalogs can be found in Guo et al. (2013) and

Galamez et al. (2013). In total, 34930 objects are detected in the maximum depth CANDELS GOODS-South field (combines the full depth F160W observations of the CANDELS ‘deep’ and ‘wide’ fields with those of the ERS and UDF fields).

1.2.3 Photometry and SED Fitting

Using public archival data from ground and space-based surveys, reliable multiwavelength photometry was measured from the ultraviolet (UV) to the mid-infrared (mid-IR) for each of the 34930 objects identified by SEXTRACTOR in the F160W mosaic (see Guo et al. (2013) for complete details and descriptions). HST optical and near infrared observations were made as part of the GOODS-South (Giavalisco et al., 2004) and CANDELS (Grogin et al. (2011) and Koekemoer et al. (2011)) surveys. Many ground-based surveys have imaged the GOODS-South field in recent years. In order to perform our photometry and SED fitting, we combined the HST ACS and WFC3 observations with U-band data from the CTIO Blanco telescope, Visible Multi-Object Spectrograph (VIMOS) U-band data from the Very Large Telescope (VLT), Infrared Spectrometer and Array Camera (ISAAC) Ks-band data from the VLT, High Acuity Wide field K-band Imager (HAWK-I) K-band data from the VLT, and 3.5, 4.5, 5.8, and 8.0 μm data from Spitzer. Photometry from the high resolution HST filters (ACS F435W, F606W, F775W, F814W, F850LP and WFC3 F098M, F105W, and F125W) was measured by first rebinning all the mosaics to the F160W 0.06” pixel scale and smoothing the images to the same effective spatial resolution of F160W ($\sim 0.17''$) by matching their point spread function (PSF) to the PSF of the F160W observations.

SEXTRACTOR was then run in dual-image mode with the CANDELS F160W mosaic as the detection image. By removing the effects of the different PSFs in the different wavebands and HST cameras, this method ensures that the segmentation areas (and thus the SEXTRACTOR measured photometry) for each object identified in F160W are identical in all of the HST wavebands. This method can not be used reliably to measure consistent photometry from the ground based or Spitzer observations because their spatial resolutions differ greatly from the WFC3 observations (often by a factor of 10 or more). To account for the possible blending of sources in the lower resolution data, TFIT (Laidler et al., 2006) is used to measure accurate photometry in these wavebands. TFIT generates a high resolution template for each object using the location and morphology information from the F160W catalog. It then smoothes this template to the spatial resolution of the lower resolution image and fits it to the low-resolution object. By fitting multiple templates concurrently, TFIT is able to estimate the flux for multiple objects that are blended together in the low resolution observations. These photometry matching techniques enable us to obtain reliable photometry from the U-band to the NIR for the bright, faint, and crowded sources found in the F160W GOODS-South source catalog. Further details on TFIT can be found in Laidler et al. (2006) and further details on obtaining the photometry and running TFIT in the GOODS-South CANDELS field can be found in Guo et al. (2013).

The EAZY routine (Brammer et al., 2008) was used to determine the photometric redshifts of the 34930 F160W detected objects by fitting combinations of seven different galaxy templates to the object SEDs created by combining the TFIT magni-

tudes from over a dozen wavebands covering the UV to the IR. As demonstrated in Brammer et al. (2008) and Whitaker et al. (2011), linearly combining these templates is sufficient to cover a diverse range of galaxy colors and yet minimize uncertainties and degeneracies in redshift and galaxy color. Comparing the photometric redshifts to available spectroscopic redshifts in the GOODS-South field demonstrates the high degree of accuracy of our method. For $z < 1$, our photometric redshifts have a normalized median absolute deviation (NMAD) (defined as $1.48 \times \text{median}(|\Delta z|/(1+z_{spec}))$) of 2.8% and an outlier fraction ($|\Delta z|/(1+z_{spec}) > 0.15$) of 5.5%. For higher redshift galaxies ($z > 1.5$), these values become 2.3% and 4.0% respectively (Guo et al., 2013). The sample of spectroscopic redshifts was collected from a multitude of past redshift surveys in the GOODS-South field and were combined in the FIREWORKS catalog (Wuyts et al., 2008). The final redshift sample for the F160W GOODS-South sources includes the spectroscopic redshifts with the best fit photometric redshifts from EAZY. To estimate the rest-frame colors, stellar masses and star formation rates (SFR), the FAST routine (Kriek et al., 2009) was used adopting a grid of Bruzual & Charlot (2003) models, a Chabrier (2003) initial mass function (IMF), and a range of star formation histories, galaxy ages, and extinction parameters. The total SFR for each galaxy was estimated using rest-frame UV luminosities and correcting for extinction (A_v) (Bell et al. (2005) and Kennicutt (1998)). Taking the extinction derived from SED fits (Wuyts et al., 2011b) and using the slope of the Calzetti (Calzetti et al., 2000) extinction law, total SFRs are determined using $\text{SFR}_{total} = \text{SFR}_{2800} * 10^{0.4 * 1.8 A_v}$ where A_v and SFR_{2800} come from FAST and the 1.8 factor comes from the slope of the Calzetti extinction

law (Calzetti et al., 2000) to convert A_v into the ultraviolet. More information on the techniques used to implement EAZY and FAST can be found in Wuyts et al. (2011a), Dahlen et al. (2013), and Guo et al. (2013).

1.2.4 GALFIT Parameters

GALFIT (Peng et al., 2002) was used to measure a single component Sérsic fit to the F160W light profiles of each of the 34930 objects identified in the SEXTRACTOR catalog (van der Wel et al., 2012). GALAPAGOS (Barden et al., 2012) was used as a wrapping routine to run GALFIT. GALAPAGOS estimates the sky value for the mosaic, runs SEXTRACTOR, and makes cutouts of the observations and noise images for use by GALFIT. GALAPAGOS uses the magnitudes, radii, axis ratios, and positions estimated by SEXTRACTOR as starting values for the GALFIT fits to reduce processing time and help ensure that GALFIT finds a global χ^2 minimum. The segmentation maps created by SEXTRACTOR are used to identify each object and nearby companion objects. Nearby objects are either fit simultaneously or masked-out during the fitting process (as determined by GALAPAGOS depending on their brightness - see van der Wel et al. (2012) for more details). GALFIT uses a chi-squared minimization algorithm to fit a two-dimensional single Sérsic profile to each object (as defined by the SEXTRACTOR segmentation maps). These best-fit Sérsic profiles provide an estimated F160W magnitude (H_{F160W}), a global Sérsic index (n) describing the light profile slope, an effective radii (R_{eff}), and an axis ratio ($\frac{b}{a}$) (as well as their estimated errors) for each galaxy. The radii presented in this study are the semi-major axis containing

half the F160W light in the ellipse of the best fit single Sérsic model.

The Sérsic index is the exponent in the Sérsic profile (Sersic, 1968) describing how the intensity of light of a galaxy changes as a function of distance from the center. Lower Sérsic values indicate a flatter light profile in the center with a quicker drop off at larger radii. A Sérsic value of 0.5 describes a Gaussian profile. A Sérsic value of 1 is an exponential disk and is a good description of spiral, bulgeless disk galaxies in the local Universe. A Sérsic value of 4 describes the de Vaucouleurs profile and has been used historically in literature as a description of traditional elliptical galaxies in the local Universe.

To help ensure GALFIT provides a reasonable fit to the galaxy profiles, a constraints file is used. Key constraints on the GALFIT Sérsic fits include: a Sérsic index (n) between 0.2 and 8, an effective radius between 0.3 and 400 pixels, an axis ratio between 0.0001 and 1, and a F160W magnitude between 0 and 40 and within ± 3 magnitudes from the SEXTRACTOR estimated magnitude. We ran GALFIT with GALAPAGOS on the full 34930 objects in the hot+cold SEXTRACTOR catalog on the maximum depth images in GOODS-South. Of these 34930 objects, 21072 (60.3%) had GALFIT fits that are considered reliable and are used in this study. An additional 1918 (5.5%) objects had fits that were ‘suspicious’ (flag=1) (magnitudes found by SEXTRACTOR and GALFIT differed by more than 3 magnitudes), 11898 (34%) objects had ‘bad’ fits (flag=2), and 42 (0.1%) objects had failed fits (flag=4) in which GALFIT was unable to converge. Though it is possible to reclaim many of the flag=1 ‘suspicious’ fit objects by visual inspection of the objects, fits, and residuals, for this study we chose

to use only the 21072 galaxies in the reliable GALFIT set. Additional details on this publicly available GALFIT catalog of GOODS-South objects can be found in van der Wel et al. (2012).

1.2.5 Visual Classifications

To classify galaxies in the CANDELS survey, a visual morphology classification system was developed called the ‘Morphology Working Group Unified System’ (MWGUNified). This system was developed for the CANDELS observations and while applied to galaxies at all redshifts, was developed specifically with $z \sim 2$ galaxies in mind. The MWGUNified system ensures that the often clumpy and asymmetric nature as well as the high fraction of interactions and mergers of $z \sim 2$ galaxies is properly recorded in the visual inspections. van der Wel et al. (2012) showed that galaxy size and profile fits from GALFIT are reliable to better than 10% down to a F160W magnitude limit of 24.5 AB. We adopt this $H_{F160W} \leq 24.5$ magnitude cutoff and only galaxies brighter than this limit were visually classified. After applying this H_{F160W} cut, the remaining objects were visually classified by over fifty astronomers and students in the CANDELS team. Each object was independently visually classified by at least five team members. By comparing and combining the various classifiers, we are able to create a final catalog of visual classifications for all objects with $H_{F160W} \leq 24.5$.

The visual classifications of each galaxy were based primarily on cutouts from the F160W 2-orbit mosaic that covers the full CANDELS GOODS-South area including the ERS, and UDF regions. Postage stamps were made in F606W (V-Band), F850L

(z-Band) from archival ACS data (Giavalisco et al., 2004) and in F125W (J-Band) and F160W (H-band) from the CANDELS WFC3 observations. The visual classifications were based primarily on the H-Band cutouts with the other bands being used for supplemental information and to classify clumpy structure. The cutout sizes were scaled to each object using the semi-major axis (r_{sma}), the ellipticity (ε), and the position angle (Θ_{PA}) estimated by the SEXTRACTOR routine (as described in Peng et al. (2002)) with a minimum box size set to three arcseconds (3").

$$\text{POSTAGE STAMP SIZE} \begin{cases} = 2.5r_{sma} * (|\sin(\Theta_{PA})| + (1 - \varepsilon) * |\cos(\Theta_{PA})|) \\ \geq 3'' \end{cases}$$

Using the V, z, J, and H postage stamps along with an image of the object's segmentation map (determined by SEXTRACTOR), each object was visually classified in terms of: basic morphology, interactions, structural and image quality flags, and clumpiness/patchiness. Examples of all the visual morphology classes are provided in the Appendix. The basic morphology section allows classifiers to classify an object's global morphological shape in F160W as a spheroid, disk, irregular/peculiar, compact/unresolved, or unclassifiable or some combination thereof. Visually classified spheroids are defined as objects that are generally round and appear to have a smooth, centrally concentrated light profile. Disks are objects with clear disk structures or profiles that may or may not contain spiral arms and central bulges. Irregular objects are those that are not regular nor easily classified by one of the other core morphology classes. This class includes objects severely affected by mergers and interactions. Compact objects are objects that are either a clear point source (such as a star with airy

rings) or an object that is unresolved in F160W. Unclassifiable objects are problematic objects that can not be classified by any of the other morphological classes such as unreal objects caused by image artifacts and bad pixels or an object on the edge of the mosaic or an object with extremely low surface brightness. Classifiers base their classifications on the dominant object in F160W within the segmentation map and may select as many global morphology classifications as are applicable.

The interaction morphology class allows classifiers to identify objects that are interacting with neighboring objects, undergoing a merger, or have nearby objects without any visible sign of interaction. Classifiers select the degree of interaction (or lack of interaction) based on the F160W cutout stamps. Classifiers were to select one of the following: merger, interaction within the primary object’s segmentation map, interaction beyond the primary object’s segmentation map, non-interacting companion, or none. Mergers are defined as objects that are single objects (including sources with double nuclei) that appear to have undergone a merger by evidence of tidal features/structures such as tails, loops or highly-irregular outer isophotes (note: all mergers are irregular but not all irregular galaxies are mergers). An interacting galaxy is defined as objects that appear to be tidally interacting with a companion galaxy. Interactions have clear signatures of tidal interaction; e.g., tidal arms, bridges, dual asymmetries, off-center isophotes, or otherwise disturbed morphologically. If the 2 interacting objects are located within the same segmentation map then ‘interaction within the primary object’s segmentation map’ is selected. If the two interacting objects have been identified as separate objects in the segmentation map then ‘interaction beyond the primary object’s

segmentation map' is selected. A non-interacting companion is defined as objects that have a close companion (in projection), yet no evidence of tidal interaction or disturbed morphology is apparent. The companion galaxy may be within or beyond the primary galaxy's segmentation map. If each neighboring galaxy resides in its own segmentation map, the companion segmentation map must be separated from the primary galaxy's segmentation map by less than the diameter of whichever galaxy's segmentation map is larger.

Image and quality flags allow the classifier to further comment on the structure and features of the objects as well as flag any potential problems/issues with the images. Quality flags are used to identify cases where the classifier believes their classification to be uncertain/unreliable. These cases include examples of a poorly deblended (both over and under deblended) objects by SEXTRACTOR in the segmentation map, image quality problems where nearby bright objects, an image edge, or other image defects are inhibiting a reliable classification, and uncertain cases where the classifier is uncertain of his/her classification yet no image quality problem exists. K-Correct Flags are for cases where the difference in morphological structure between the F160W cutout and bluer bands is so severe that a classifier would select a different classification for that band. These flags are used to identify objects where galaxies do not appear in certain bands or appear but are drastically different from the F160W image. Structural flags are used to identify common object properties as well as to provide more details about the general morphology classification. The structure flags include: tidal arms, double nuclei (within a single stellar envelope), asymmetric light distribution in F160W, spiral arm/ring, bar,

point source contamination, edge-on disk, face-on disk, tadpole (object with at least a 2:1 axis ratio with a bright core at one end of an elongated structure), chain (elongated object with at least a 3:1 axis ratio and multiple bright clumps embedded in a considerable background envelope with no signs of a tidal interaction), disk-dominated (an object in which multiple morphology classifications were selected and the disk classification is the dominant class in F160W), and bulge-dominated (an object in which multiple morphology classifications were selected and the spheroid classification is the dominant class in F160W).

The clumpiness matrix is a method developed to allow classifiers to characterize the observed presence of clear clumps and/or patchy light distributions in the objects. The clumpiness classification is based largely on the bluer bands (F606W and F850L). Clumps are defined as clear self-contained, centrally concentrated knots of light while patches are defined as spotty, uneven light distributions within the profile. Patchiness can be viewed as obscured/faded clumps. This difference between clumps and patchiness is used to help the classifier but there is no distinction made between clumps and patches when determining an objects degree of clumpiness. The classifier selects the degree of clumpiness (none, a couple clumps, many clumps) as well as the degree of patchiness (none, some, and a lot) as is able to select multiple classes if unsure. The values are then averaged together to produce a single clumpiness/patchiness value for that classifier for each object.

The classifications from the over fifty classifiers were combined to create a single ‘metric’ visual morphology catalog which is publicly available. For all of the combined

classifications provided in the ‘metric’ catalog, three different combined values were given based on the completeness/reliability of the individual classifiers. The ‘reliable’ values use only galaxy classifications in which the galaxy was fully classified (defined as having both a standard morphology classifications and clumpy/patchy classification) and the catalog/classifier is considered reliable ($\geq 85\%$ of galaxies in the catalog by that classifier were fully classified). These galaxy classifications can reliably be used for all parameters and flags. It was determined that if the classifier classifies both the morphology and the clumpiness/patchiness then he/she has gone through all four sections of the MWGUnified system and has thus provided a complete classification. The ‘all fully’ values use all galaxy classifications that are fully classified (defined as having both a standard morphology classifications and clumpy/patchy classification) including those fully classified in catalogs in which the classifier is not considered reliable ($< 85\%$ of the galaxies in the catalog were fully classified). With some care, these galaxy classifications may be used for all parameters and flags though they may contain some unreliable classifications. The ‘all’ values use all galaxy classifications - including incomplete classifications in which clumpy/patchiness, interaction, and flags were not classified. These galaxy classifications have only been classified using standard morphology classifications (disk, spheroid, irregular, compact, and unclassifiable) and should not be considered reliable for other measurements. The ‘metric’ catalog provides all three sets of values for all of the classifications but for this paper only the ‘all fully’ values are used. Mean values as well as the sigma of the distribution of the values between classifiers of the various morphology classes, interaction classes, flags, and clumpiness/patchiness were

determined for each galaxy for all three classes of galaxy classification reliability. The complete ‘metric’ catalog of the MWGUNified visual classification system is released with this publication.

In addition to providing the combined mean values for the MWGUNified visual classification system, the catalog also includes several unique quantities derived from the combined classifications. A new measurement, Spheroidicity (\mathcal{S}), is designed to measure the gradient of object shapes from a pure traditional spheroid to a traditional disk. Bulge dominated and disk dominated flags are used in conjunction with spheroid and disk morphology classifications to assign Spheroidicity values for each classifier which are then combined with other classifiers to determine an object’s mean Spheroidicity. Below is a description for determining Spheroidicity:

$$\text{SPHEROIDICITY}(\mathcal{S}) = \begin{cases} 1.00 \text{ (Spheroid Only)} \\ 0.75 \text{ (Spheroid and Disk [Bulge Dominated])} \\ 0.50 \text{ (Spheroid and Disk [No Domination Flag])} \\ 0.25 \text{ (Spheroid and Disk [Disk Dominated])} \\ 0.00 \text{ (Disk selected only)} \end{cases}$$

In addition to Spheroidicity, several other metrics were derived for the ‘metric’ catalog. Irregularity (ι) quantifies how likely a galaxy was seen to be irregular and has the following values: an object classified as only irregular has $\iota = 1.0$, an object classified as irregular in addition to another global morphology class has $\iota = 0.5$, an object not classified as irregular has $\iota = 0.0$. Interaction Class (\mathcal{I}) measures the degree of interaction an object is experiencing. Mergers have $\mathcal{I}=1.0$, interactions within a common segmentation map have $\mathcal{I}=0.75$, interactions between objects with independent segmentation maps have $\mathcal{I}=0.5$, objects with nearby non-interacting companions have

Table 1.1: Clumpiness Matrix (\mathcal{C})

	No Major Clumps	1-2 Major Clumps	3+ Major Clumps
No Patchiness	0.00	0.25	0.50
Low/Moderate levels of Patchiness	0.25	0.50	0.75
High Levels of Patchiness	0.50	0.75	1.0

$\mathcal{I}=0.25$, and objects classified as ‘None’ in the interaction section of the MWGunified syste have $\mathcal{I}=0.0$. A combined interaction flag was also created to combine the two interaction classes (interactions between 2 objects within a common segmentation map and interactions between objects in two separate segmentation maps). Lastly, a single Clumpiness (\mathcal{C}) quantity was included in the ‘metric’ catalog to combine the clumpiness/patchiness values selected by the classifiers. The clumpiness/patchiness matrix selections made by each classifier were assigned values and averaged together before being combined with the other classifiers to determine a single Clumpiness value for each galaxy. A Clumpiness value of 0 refers to an object with no clumps or areas of patchiness while a Clumpiness value of 1 refers to an object with multiple clumps and a high degree of patchiness. As discussed earlier in this section, Clumpiness is based in large part on the bluer images (F606W and F850L).

1.2.6 Sample Selection

A total of 34930 independent objects were identified by SEXTRACTOR in the F160W GOODS-South CANDELS mosaic (CANDELS ‘wide’ + CANDELS ‘deep’ + ERS + UDF) in GOODS-S. TFIT observed magnitudes were determined for these 34930 objects from the available U to NIR wavebands and were used by EAZY and FAST to determine photometric redshifts, rest colors, star formation rates, and stellar

masses (as described in previous sections). This complete sample was also fit to single Sérsic 2-dimensional profiles in F160W using GALFIT (Section 2.4). For this study we focus on galaxies in this catalog of 34930 objects that had reliable TFIT magnitudes and parameters derived by FAST and EAZY as well as believable GALFIT fits (flag=0) and were visually classified using the MWGunified system. This visual classification system had a $H_{F160W} \leq 24.5$ cutoff which proved to be the primary cut on our sample. There are 7628 galaxies in the full CANDELS GOODS-South field (including the ERS, UDF, and CANDELS ‘wide’ and ‘deep’ regions) with $H_{F160W} \leq 24.5$. Of these 7628 visually classified galaxies, 6095 had F160W fits from GALFIT that were deemed reliable (flag=0). This gives a sample of 6095 galaxies across all redshifts and masses that have been visually classified, have reliable F160W GALFIT fits, rest colors, Star formation rates, photometric redshifts, and stellar masses. In this paper, we are interested in studying galaxy morphologies across redshifts as a function of mass. To this end, we focus on galaxies with redshift=0.5-3.0 (4914 galaxies) and divide this redshift range into six slices of roughly equal comoving volumes ($z = 0.5-1.0, 1.0-1.4, 1.4-1.8, 1.8-2.2, 2.2-2.6, 2.6-3.0$). Our sample has been shown to be $> 90\%$ complete at $z=1.4-3.0$ at stellar masses $> 10^{10}$ (Wuyts et al. (2011a) and Newman et al. (2012)). Figure 2.1 plots the full $z \sim 2$ sample as a function of F160W magnitude and the derived stellar mass. Investigating the galaxies that were visually classified ($H_{160W} < 24.5AB$) we find that our high redshift sample does not start becoming greatly incomplete until stellar masses below $10^{9.4}$. This figure emboldens us to lower our completeness limit from 10^{10} to $10^{9.4}$. Using this mass limit, we divide our sample into three mass bins ($10^{9.4} \leq M_{stellar} < 10^{10}$,

$10^{10} \leq M_{\text{stellar}} < 10^{11}$, and $10^{11} \leq M_{\text{stellar}}$) across our $z=0.5-3.0$ redshift range. This stellar mass cut of $10^{9.4}$ brings our total sample to 2781 objects of which 2727 objects are visually classified as galaxies with enough classifiers to be considered reliable. These 2727 galaxies are the final sample used in this study and is the result of conservative cuts to ensure that the observed TFIT colors, photometric redshifts, stellar masses, rest colors, star formation rates, GALFIT single Sérsic fits, visual classifications, and mass and redshift ranges are reliable and complete. Figure 1.3 shows the distribution of this final 2727 galaxy sample across our stellar mass and redshift bins.

To improve reliability of the visual classifications, we focused on the ‘allfully’ values from the metric catalog (see Section 2.5). By using the ‘allfully’ classifications, we ensure that our classifiers were actively classifying in the Merger/Interaction, Flags, and Clumpy categories as well as the basic visual morphology category. Analysis using the ‘all’ classifications which used every classifier’s values (including classifiers shown to be incomplete/sporadic in their classification) showed that the MWGunified visual classification values were biased low due to null classification values pulling down classification means. Minimal differences were found between using the ‘reliable’ and the ‘allfully’ classification groups - classifiers seem to be attentive when they do remember to classify the four MWGunified sections even if they were inconsistent over the catalog as a whole. By adopting the ‘allfully’ catalog, we are able to increase the number of classifications that go into making the final visual classification metrics and thus improve the statistics involved in the values.

An additional cut can be made to create the ‘clean’ subset in our sample. Using

the visual classifications to remove galaxies affected by mergers, interactions, irregular morphologies, and deblending/image processing errors creates a subset that has more reliable galaxy colors and morphologies. This subset employs harsh cuts using the visual classification flags resulting in a clean sample of 1678 galaxies from the 2727 full catalog of visually classified galaxies. This sample is used to confirm that observed effects in the full sample are not the result of inaccurate colors resulting from complicated interactions and bad image processing. In this study, it is assumed that the full 2727 sample is used unless otherwise stated that the 1678 ‘clean’ sample is used.

This paper’s analysis focuses on general populations and trends observed in the visual morphology catalog as a function of mass and redshift. The large number of reliably visually classified galaxies in this study gives us the unique ability to study how the fraction of the visually identified classes of galaxies changes with redshift. Section 3 focuses on the global visually identified morphological classes and how they evolve over redshift as a function of mass. We present tables of the full visual morphology catalog and demonstrate the wealth of information available in performing in-depth visual classifications along the lines of the MWG unified system. In Section 4, we focus on the properties of quiescent galaxies in the $z \sim 2$ Universe. Section 5, focuses on the axis ratio of galaxies at $z \sim 2$. This $z \sim 2$ Universe represents an epoch of peaking star formation rates, increased mergers/interactions, increasing AGN activity, and is an epoch thought to be undergoing a transition from clumpy, irregular systems to the relaxed Hubble Sequence galaxies observed today.

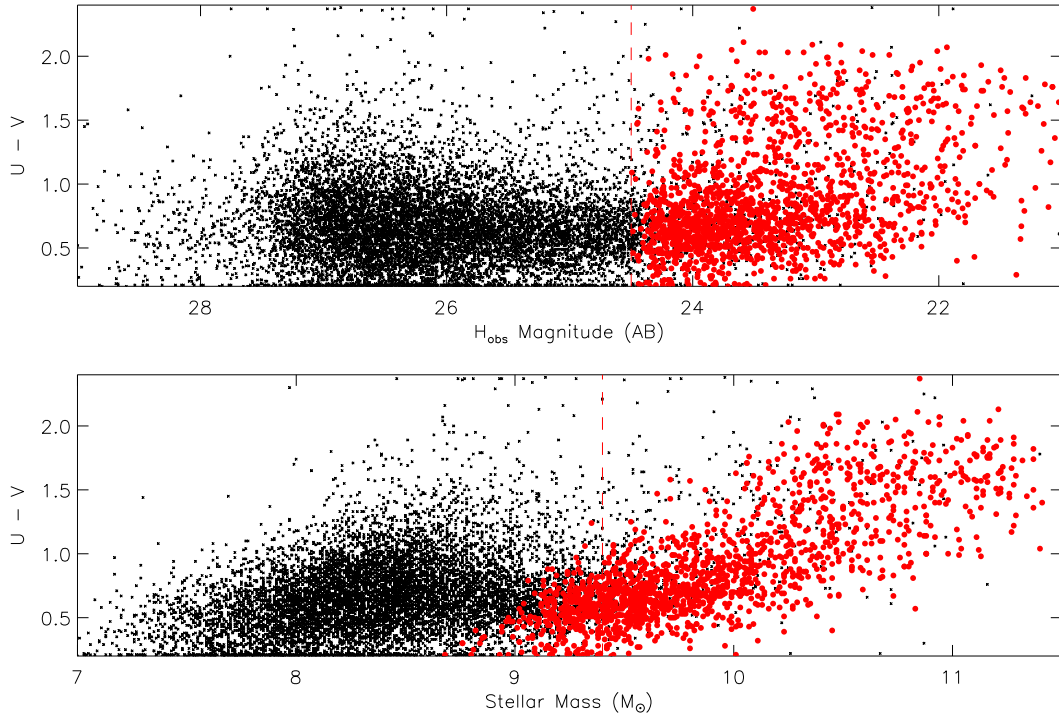


Figure 1.2: GOODS-South F160W Sample Selection. The black points represent the 11706 objects identified in the GOODS-South region using SEXTRACTOR that were fit with EAZY to have photometric redshifts between $z=1.4$ and $z=2.6$. The red points represent the 1695 galaxies in this redshift range that had an observed F160W magnitude ≤ 24.5 AB (imposed cut for visual classifications) and were successfully visually classified. As can be seen from the bottom plot, there does not seem to be a significant population of red galaxies with stellar masses between $10^{9.4}$ and $10^{10.0}$. Thus the adopted F160W magnitude cut of 24.5AB gives a fairly complete visually classified sample down to a stellar mass of $\sim 10^{9.4}$. We are emboldened by this figure at $z\sim 2$ and decided to use $M_{\text{stellar}}=10^{9.4}$ as our lower mass limit for this study.

All Galaxy Classes
2727 (100.0%)

	$\log M_{stellar}$ 9.4-10.0	$\log M_{stellar}$ 10-11	$\log M_{stellar}$ >11
$2.6 \leq z < 3.0$ (237)	136 (57.4%)	93 (39.2%)	8 (3.4%)
$2.2 \leq z < 2.6$ (268)	153 (57.1%)	98 (36.6%)	17 (6.3%)
$1.8 \leq z < 2.2$ (332)	176 (53.0%)	134 (40.4%)	22 (6.6%)
$1.4 \leq z < 1.8$ (531)	317 (59.7%)	184 (34.7%)	30 (5.6%)
$1.0 \leq z < 1.4$ (636)	358 (56.3%)	241 (37.9%)	37 (5.8%)
$0.5 \leq z < 1.0$ (723)	377 (52.1%)	306 (42.3%)	40 (5.5%)
Total: 2727	1517 (55.6%)	1056 (38.7%)	154 (5.6%)

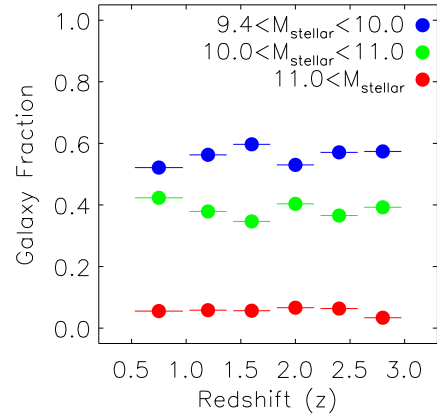


Figure 1.3: GOODS-South Galaxy Fractions in Mass and Redshift Bins. The number and fraction of galaxies in the GOODS-South catalog in $M_{stellar}$ and redshift bins. The percentages given represent the fraction of galaxies at a given redshift bin that are of a certain mass. Across all redshifts, the majority of galaxies are in the $\log M_{stellar}=10^{9.4} - 10^{10}$ and $\log M_{stellar}=10^{10.0} - 10^{11}$ mass bins. The high mass bin contains relatively few galaxies (154 from $z=0.5-3.0$) in the GOODS-South field and thus results and trends in the $\log M_{stellar} \geq 10^{11}$ population should be taken with a grain of salt particularly when the total number of galaxies is further subdivided into classes.

1.3 MWGunified Populations

Using the MWGunified visual classification scheme, analysis was performed to study how different types of visually classified objects changed in redshift as a function of mass. We divided our visually classified GOODS-South sample into six redshift bins from $z=0.5$ to $z=3.0$ selected to contain roughly equal comoving volumes ($z = 0.5-1.0, 1.0-1.4, 1.4-1.8, 1.8-2.2, 2.2-2.6, 2.6-3.0$). Our visual classification metric was used to identify several core populations within our catalog. Our spheroidicity metric was primarily used to determine how the global F160W morphological shapes of our galaxies evolved. We divided our galaxies into three types using spheroidicity. Disk-like objects had spheroidicity values of 0.3 and below. Spheroid-like objects had total spheroidicity values of 0.7 and above and the region between disk-like and spheroid-like with $\mathcal{S}=0.3-0.7$ were called transitional/intermediate objects. Additionally, a subclass of the visually identified spheroidal class was identified as also having a global Sérsic fit in F160W of $n=2.5-5.0$ (a spheroid both visually and by light profile). MWGunified flags were used to identify additional galaxy classes including galaxies that were classified as asymmetric, undergoing a merger or interaction, containing clumpy/patchy substructure, or having a chain or tadpole structure. Tables of these nine visually identified galaxy classes are presented in the following subsections. Two sets of tables are presented with each subclass. Both tables give the number of galaxies of a certain visually identified subclass that were identified at a given redshift and mass bin within a certain specific star formation rate (sSFR) or radius range. The first set of tables then gives the fraction

of these objects in these mass, redshift, and sSFR or radius bins compared to the total number of galaxies of this class at that redshift. These tables show how a given visual classification class is distributed at a given redshift. These are the tables provided in this chapter. The second set of tables (called ‘bin fraction’) are provided in the Appendix. These ‘bin fraction’ tables give the percentage of a given morphology class as a fraction of total number of galaxies in the same redshift, mass, and sSFR/radii bin. These tables demonstrate how galaxies of a certain mass, redshift, and sSFR or radii are distributed among the different morphology classes. Also presented for each class is a basic table and accompanying plot showing how the number and fraction of galaxies in that subclass varies as a function of redshift for a given mass bin. Key observations and trends found in these subclass catalog tables are discussed in the following subsections.

Galaxies were broken into specific star formation rate bins and radii bins. For radii, we define three classes of galaxy sizes. Compact: galaxies with GALFIT $R_{eff} < 1\text{kpc}$. GALFIT was run on our F160W mosaics which have a pixel scale of $0.06''$ and a spatial resolution of $\sim 0.17''$. van der Wel et al. (2012) shows that GALFIT can reliably fit single Sérsic profiles to galaxies with radii at our below the resolution limit as long as the PSF is precisely known allowing for the image to be deconvolved accurately. Our visual classifications, however, do not deconvolve the images and thus are limited by the resolution of the image. At a $z \sim 2$, the $0.06''$ pixel size on our WFC3 images corresponds to $\sim 0.5\text{kpc}$ and a spatial resolution of $0.17''$ is $\sim 1.4\text{kpc}$. We define any object with a GALFIT deconvolved radii below 1kpc as compact. 7% of galaxies in our visually classified sample from $z=0.5-3.0$ with $M_{stellar} \geq 10^{9.4}$ are in this compact

class. A second class of galaxy radii contains all objects with ‘moderate’ radii and is defined as galaxies with GALFIT $1\text{kpc} \leq R_{eff} < 3\text{kpc}$. This ‘moderate’ radii class contains 51% of galaxies in our total sample. The final class of radii is the ‘extended’ class and contains all galaxies with $R_{eff} \geq 3\text{kpc}$. This class contains 42% of our total galaxy sample.

In addition to these radii divisions, we divide our sample into star-forming classes based on each galaxy’s specific star formation rates (sSFR) as determined by FAST using the UV flux and correcting for extinction (See Section 2.3). To divide between systems with low specific star formation rates (quiescent) and star-forming galaxies, we look at the histogram distribution of sSFR at $z \sim 2$ ($1.4 \leq z < 2.6$). Analysis shows a bimodality between high and low star-forming systems with a separation around $\log \text{sSFR} \sim -0.6$ [Gyr^{-1}]. This dividing line is picked somewhat arbitrarily but the exact dividing value is shown not to have a significant effect on our results since the bimodality of star formation rates is clear out to a $z \sim 3$. Our chosen division point between star-forming and quiescent systems is in good agreement with previous work by Barro et al. (2013) (they used $\log \text{sSFR} = -0.5$ [Gyr^{-1}]). We further divide our sample into transitional star-forming galaxies and galaxies with exceptionally high specific star formation rates. Galaxies with transitional sSFR values are defined as the 10% of $z \sim 2$ galaxies with sSFR around the division line of $\log \text{sSFR} \sim -0.6$ [Gyr^{-1}]. We find that the range $-0.9 \leq \log \text{sSFR} < -0.3$ encloses $\sim 10\%$ of our $z \sim 2$ sample. Likewise, we define the high star-forming systems as the 10% of $z \sim 2$ galaxies with the highest specific star formation rates. This cutoff is found to be $\log \text{sSFR} \geq 0.95$ [Gyr^{-1}]. These cuts (based

on our $1.4 \leq z < 2.6$ galaxy sample) are applied to our catalog at all redshifts and create four categories of sSFRs: quiescent $\log \text{sSFR} < -0.9$ [Gyr^{-1}] (containing 16% of our total sample), transitional $-0.9 \leq \log \text{sSFR} < -0.3$ [Gyr^{-1}] (containing 9% of our total sample), star-forming $-0.3 \leq \log \text{sSFR} < 0.95$ [Gyr^{-1}] (containing 68% of our total sample), and high star-forming $\log \text{sSFR} \geq 0.95$ [Gyr^{-1}] (containing 7% of our total sample).

Table 1.2 shows how our galaxies are separated by the chosen sSFR divisions. Similarly, Table 1.3 shows the breakdown of our sample with the chosen R_{eff} divisions. The colors in the tables correspond to different percentages and are provided only to guide the eye. The tables provide a huge wealth of information and can be overwhelming at first. To help guide the reader, we will walk through Table 1.2 and Table 1.3 briefly. Looking at Table 1.2, we see that 121 galaxies at $z=2.6-3.0$ are star-forming ($\text{sSFR}=-0.3-0.95$) in the low mass bin ($\log M_{stellar} = 9.4-10.0$) which is 51.1% of the total population of galaxies at this $z=2.6-3.0$ redshift (237). At lower redshifts ($z=0.5-1.0$), 286 galaxies are star-forming ($\text{sSFR}=-0.3-0.95$) in the low mass bin ($\log M_{stellar} = 9.4-10.0$) which is 39.6% of the total population of galaxies at this $z=0.5-1.0$ redshift (723). Similarly, using Table 1.3, we see that 97 galaxies at $z=2.6-3.0$ have moderate radii ($R_{eff}=1-3\text{kpc}$) in the low mass bin ($\log M_{stellar} = 9.4-10.0$) which is 40.9% of the total population of galaxies at this $z=2.6-3.0$ redshift (237). At lower redshifts ($z=0.5-1.0$), 190 galaxies have moderate radii ($R_{eff}=1-3\text{kpc}$) in the low mass bin ($\log M_{stellar} = 9.4-10.0$) which is 26.3% of the total population of galaxies at this $z=0.5-1.0$ redshift (723). Follow these examples to help you read the tables provided in this chapter for each visually identified subclass. Note that the total number of galaxies at each redshift in these tables are the

total number of galaxies at that redshift with those visual classifications.

A 2005 study by Elmegreen et al. (2005) visually classified and analyzed the morphologies and photometric properties of 884 galaxies in the Hubble Ultra Deep Field (UDF). This study was based on very deep mosaics from the Hubble Space Telescope Advanced Camera for Surveys (HST ACS) in the observed visible light bands. Using a 347110s exposure in F775W (i-band i_{775}), the study identified and visually classified all 884 galaxies with i_{775} ranging from 18.5 to 29 mag (surface brightness = 22.5-27 mag/as²) and i_{775} radii $\geq 0.3''$ into six categories: chain (114, 13%), clump cluster (178, 20%), double (126, 14%), tadpole (97, 11%), spiral (269, 30%), and elliptical (100, 11%). The Elmegreen UDF study used the following visual classification definitions (Elmegreen et al., 2005): *Chain (Linear objects dominated by several giant clumps and having no exponential light profiles or central red bulges.); Clump Cluster (Oval or circular objects resembling chain galaxies in their dominance by several giant clumps and having no exponential profiles or bulges.); Double clump (Systems dominated by two similar clumps with no exponential profile or bulge.); Tadpole (Systems dominated by a single clump that is off center from, or at the end of, a more diffuse linear emission.); Spiral (Galaxies with exponential-like disks, evident spiral structure if they have low inclination, and usually a bulge or a nucleus. Edge-on spirals have relatively at emission from a midplane, and often extended emission perpendicular to the midplane, as well as a bulge.); Elliptical (Centrally concentrated oval galaxies with no obvious spiral structure.)* These definitions are in line with those of previous works namely the chain definition established in Cowie et al. (1995), the tadpole definition by van den Bergh et al. (1996)

Table 1.2: GOODS-South Galaxy Fractions Evolution with Redshift in Mass and sSFR Bins

	sSFR															
	Quiescent sSFR < -0.9				Transitional -0.9 ≤ sSFR < -0.3				Star Forming -0.3 ≤ sSFR < 0.95				High Star Forming 0.95 ≤ sSFR			
	$M_{stellar}$ 9.4-10.0	$M_{stellar}$ 10-11	$M_{stellar}$ >11	$M_{stellar}$ >11	$M_{stellar}$ 9.4-10.0	$M_{stellar}$ 10-11	$M_{stellar}$ >11	$M_{stellar}$ >11	$M_{stellar}$ 9.4-10.0	$M_{stellar}$ 10-11	$M_{stellar}$ >11	$M_{stellar}$ >11	$M_{stellar}$ 9.4-10.0	$M_{stellar}$ 10-11	$M_{stellar}$ >11	
2.6 ≤ z < 3.0 (237)	0 (0.0%)	4 (1.7%)	5 (2.1%)	3 (1.3%)	0 (0.0%)	5 (2.1%)	3 (1.3%)	121 (51.1%)	74 (31.2%)	0 (0.0%)	0 (0.0%)	15 (6.3%)	10 (4.2%)	0 (0.0%)		
2.2 ≤ z < 2.6 (268)	2 (0.7%)	13 (4.9%)	7 (2.6%)	3 (1.1%)	1 (0.4%)	10 (3.7%)	3 (1.1%)	142 (53.0%)	71 (26.5%)	6 (2.2%)	6 (2.2%)	8 (3.0%)	4 (1.5%)	1 (0.4%)		
1.8 ≤ z < 2.2 (332)	1 (0.3%)	13 (3.9%)	12 (3.6%)	4 (1.2%)	1 (0.3%)	9 (2.7%)	4 (1.2%)	162 (48.8%)	99 (29.8%)	6 (1.8%)	6 (1.8%)	12 (3.6%)	13 (3.9%)	0 (0.0%)		
1.4 ≤ z < 1.8 (531)	0 (0.0%)	42 (7.9%)	21 (4.0%)	8 (1.5%)	9 (1.7%)	29 (5.5%)	8 (1.5%)	278 (52.4%)	94 (17.7%)	1 (0.2%)	1 (0.2%)	30 (5.6%)	19 (3.6%)	0 (0.0%)		
1.0 ≤ z < 1.4 (636)	14 (2.2%)	79 (12.4%)	24 (3.8%)	12 (1.9%)	15 (2.4%)	46 (7.2%)	12 (1.9%)	298 (46.9%)	105 (16.5%)	1 (0.2%)	1 (0.2%)	31 (4.9%)	11 (1.7%)	0 (0.0%)		
0.5 ≤ z < 1.0 (723)	31 (4.3%)	128 (17.7%)	29 (4.0%)	5 (0.7%)	24 (3.3%)	59 (8.2%)	5 (0.7%)	286 (39.6%)	107 (14.8%)	6 (0.8%)	6 (0.8%)	36 (5.0%)	12 (1.7%)	0 (0.0%)		
Total: 2727	48	279	98	35	50	158	35	1287	550	20	20	132	69	1		

 Table 1.3: GOODS-South Galaxy Fractions Evolution with Redshift in Mass and R_{eff} Bins

	R_{eff} (F160W)													
	Compact $R_{eff} < 1kpc$				Moderate $1kpc \leq R_{eff} < 3kpc$				Extended $3kpc \leq R_{eff}$					
	$M_{stellar}$ 9.4-10.0	$M_{stellar}$ 10-11	$M_{stellar}$ >11	$M_{stellar}$ >11	$M_{stellar}$ 9.4-10.0	$M_{stellar}$ 10-11	$M_{stellar}$ >11	$M_{stellar}$ >11	$M_{stellar}$ 9.4-10.0	$M_{stellar}$ 10-11	$M_{stellar}$ >11	$M_{stellar}$ >11	$M_{stellar}$ 9.4-10.0	$M_{stellar}$ 10-11
2.6 ≤ z < 3.0 (237)	8 (3.4%)	10 (4.2%)	1 (0.4%)	4 (1.7%)	97 (40.9%)	45 (19.0%)	4 (1.7%)	31 (13.1%)	38 (16.0%)	3 (1.3%)	3 (1.3%)	3 (1.3%)	3 (1.3%)	3 (1.3%)
2.2 ≤ z < 2.6 (268)	13 (4.9%)	25 (9.3%)	1 (0.4%)	8 (3.0%)	106 (39.6%)	38 (14.2%)	8 (3.0%)	34 (12.7%)	35 (13.1%)	8 (3.0%)	8 (3.0%)	8 (3.0%)	8 (3.0%)	8 (3.0%)
1.8 ≤ z < 2.2 (332)	11 (3.3%)	10 (3.0%)	1 (0.3%)	7 (2.1%)	125 (37.7%)	50 (15.1%)	7 (2.1%)	40 (12.0%)	74 (22.3%)	14 (4.2%)	14 (4.2%)	14 (4.2%)	14 (4.2%)	14 (4.2%)
1.4 ≤ z < 1.8 (531)	19 (3.6%)	23 (4.3%)	0 (0.0%)	19 (3.6%)	174 (32.8%)	80 (15.1%)	19 (3.6%)	124 (23.4%)	81 (15.3%)	11 (2.1%)	11 (2.1%)	11 (2.1%)	11 (2.1%)	11 (2.1%)
1.0 ≤ z < 1.4 (636)	17 (2.7%)	21 (3.3%)	0 (0.0%)	10 (1.6%)	173 (27.2%)	112 (17.6%)	10 (1.6%)	168 (26.4%)	108 (17.0%)	27 (4.2%)	27 (4.2%)	27 (4.2%)	27 (4.2%)	27 (4.2%)
0.5 ≤ z < 1.0 (723)	21 (2.9%)	20 (2.8%)	0 (0.0%)	6 (0.8%)	190 (26.3%)	150 (20.7%)	6 (0.8%)	166 (23.0%)	136 (18.8%)	34 (4.7%)	34 (4.7%)	34 (4.7%)	34 (4.7%)	34 (4.7%)
Total: 2727	89	109	3	54	865	475	54	563	472	97	97	97	97	97

and Straughn et al. (2006), the clump cluster-type objects as ‘protospirals’ from van den Bergh et al. (1996) or a subsample of the ? identified clump-dominated young disk galaxies, and the ‘double’ binary objects from van den Bergh (2002). This UDF Elmegreen sample is contained within the CANDELS GOODS-South field and thus the morphology classifications from the Elmegreen visible light selected sample can be compared to our F160W infrared light selected sample and MWGunified classification system. Of the 884 Elmegreen galaxies, 334 are in our final GOODS-South catalog (the majority of objects that are not in our catalog are due to their F160W magnitudes being below our magnitude cut of 24.5AB and consequently most are also low mass and below our $M_{stellar} > 10^{9.4}$). The original Elmegreen sample is shown to be dominated by low magnitude objects as well as galaxies with redshifts below 1.0 and thus the full Elmegreen sample can not be compared to our sample. Table 1.4 shows how the 334 Elmegreen galaxies in the CANDELS GOODS-South catalog were classified using both the Elmegreen F775W classifications and the MWGunified F160W classifications. Note that while the majority of our MWGunified classifications (including basic morphology type/spheroidicity) is based on the longer wavelength F160W mosaics, certain flags (like chain and tadpole) and the clumpy/patchiness measurements were based on the bluer ACS mosaics and are thus very comparable to the Elmegreen mosaics used. There is general agreement between the Elmegreen classifications and the MWGunified classifications of these 334 galaxies. Despite Elmegreen’s classifications being based on F775W, 80% of the Elmegreen spiral galaxies were also identified as disks and 87% of the Elmegreen elliptical galaxies were also identified as spheroidal or intermediate

classes using the F160W based MWGunified system. This general agreement between classifications using visible and NIR wavebands suggests that basic global galaxy structure does not differ much between rest UV and rest optical wavelengths. We expect the agreement between the Elmegreen and MWGunified systems to be high for clumpiness and other flags using observed optical data since both systems are using similar wavebands. Indeed this is found to be true with 86% of the Elmegreen clump clusters found to be clumpy using MWGunified and 65% of the Elmegreen chains and tadpoles found to be chains or tadpoles in the MWGunified system. Overall there is good agreement between our MWGunified the visual classifications performed by Elmegreen. A side study of reclassifying the full 884 Elmegreen sample using the Elmegreen visual classification definitions on the CANDELS data confirms that the agreement between the two systems is on the 80-85% level. Our MWGunified sample is much larger and has an order of magnitude more objects in the $z=0.5-3.0$ and $M_{stellar} \geq 10^{9.4}$ redshift and mass ranges than the Elmegreen UDF sample. This allows us to study trends in galaxy morphologies as a function of mass over a wide redshift range. In the following sections will analyze these morphological trends from $z=0.5-3.0$ with special emphasis on $z \sim 2$ galaxies.

Table 1.4: Elmegreen UDF Visual Classifications vs MWGunified Visual Classifications

	Disk ($S < 0.3$)	Intermediate ($0.3 \leq S < 0.7$)	Spheroid ($0.7 \leq S$)	Spheroid w/Sérsic ($0.7 \leq S$ & $n > 2.5$)	Clumpy	Chain	Tadpole	Asymmetric	Merger / Interaction
Elliptical (68)	9 (13.2%)	20 (29.4%)	39 (57.4%)	14 (20.6%)	8 (11.8%)	0 (0.0%)	1 (1.5%)	16 (23.5%)	8 (11.8%)
Spiral (136)	109 (80.1%)	23 (16.9%)	4 (2.9%)	2 (1.5%)	84 (61.8%)	2 (1.5%)	6 (4.4%)	59 (43.4%)	27 (19.9%)
CC (79)	60 (75.9%)	14 (17.7%)	3 (3.8%)	1 (1.3%)	68 (86.1%)	4 (5.1%)	11 (13.9%)	68 (86.1%)	32 (40.5%)
Chain (18)	15 (83.3%)	3 (16.7%)	0 (0.0%)	0 (0.0%)	16 (88.9%)	9 (50.0%)	6 (33.3%)	14 (77.8%)	5 (27.8%)
Tadpole (16)	9 (56.2%)	5 (31.2%)	2 (12.5%)	0 (0.0%)	10 (62.5%)	2 (12.5%)	5 (31.2%)	12 (75.0%)	5 (31.2%)
Double (21)	14 (66.7%)	4 (19.0%)	3 (14.3%)	0 (0.0%)	16 (76.2%)	1 (4.8%)	6 (28.6%)	15 (71.4%)	9 (42.9%)

The table shows how Elmegreen’s UDF galaxy sample (Elmegreen et al., 2005) are classified in our MWGunified visual classification system. Elmegreen’s visible light (F775W) classification classes are the rows and the MWGunified near-infrared (F160W) classifications are the columns. The galaxies are across our full redshift coverage ($z=0.5-3.0$). There is general agreement between the two classification systems - 80% of the Elmegreen spiral galaxies were also identified as disks and 87% of the Elmegreen elliptical galaxies were also identified as spheroidal or intermediate classes using the F160W based MWGunified system. 86% of the Elmegreen clump clusters are found to be clumpy using MWGunified and 65% of the Elmegreen chains and tadpoles are found to be chains or tadpoles in the MWGunified system.

1.3.1 Spheroidicity (\mathcal{S})

Global morphological classifications from the MWGunified system were collapsed into a new ‘Spheroidicity’ parameter (\mathcal{S}) that places each galaxy on a scale from 0 (completely disk-like) to 1 (completely spheroidal-like). The data section of this paper describes the production of this metric in more detail. From this Spheroidicity parameter, the GOODS-South catalog is divided into three subsections: disk-like ($\mathcal{S} < 0.3$), intermediate/transitional ($0.3 \leq \mathcal{S} < 0.7$), and Spheroid-like ($0.7 \leq \mathcal{S}$).

Figures 1.5, 1.6, and 1.7 give the number of galaxies visually classified as disks, intermediate, and spheroids (respectively) as a function of galaxy mass and redshift. The percentages and fractions presented in these tables and accompanying plots are calculated from the total number of galaxies in a given mass and redshift bin. For example, in Figure 1.5 we see that at $z=1.4-1.8$ there are 8 galaxies visually classified as disks that have high masses ($\log M_{\text{stellar}} > 11$). These 8 galaxies represent 26.7% of the total galaxy population at this mass and redshift range. Similarly, there are 140 galaxies classified as disks at $z=2.6-3.0$ across all mass bins. These 140 galaxies are 59.1% of the total galaxy population in this redshift range. The accompanying diagrams show how the fraction of galaxies classified as a certain morphology in a mass bin changes with redshift. The blue points are for the low mass bin ($\log M_{\text{stellar}}=9.4-10.0$), the green points are for the intermediate mass bin ($\log M_{\text{stellar}}=10.0-11.0$), the red points are for the high mass bin ($\log M_{\text{stellar}} > 11.0$), and the black points represent the total galaxy sample across all three mass bins. Figure 1.4 replots these visual morphology class fractions along

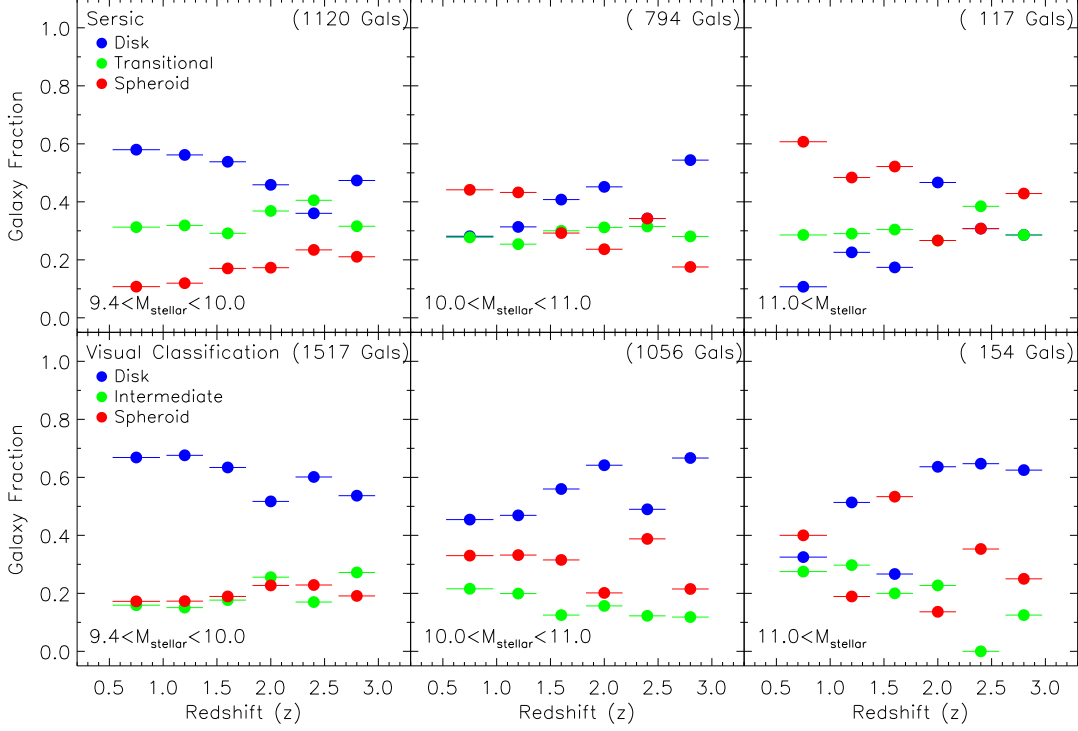


Figure 1.4: Galaxy Population Fractions. The fraction of galaxies classified by Sérsic (top row) and by MWGunified Spheroidicity (bottom row) as a disk, intermediate/transitional, and spheroid. For the Sérsic plots in the top row, disks are defined as having Sérsic indices (n) $0.8 \leq n < 1.5$, transitional objects have $1.5 \leq n < 2.5$, and spheroidal galaxies have $2.5 \leq n < 5.0$. For the Spheroidicity plots in the bottom row, disks are $\mathcal{S} < 0.3$, intermediate/transitional objects are $0.3 \leq \mathcal{S} < 0.7$, and spheroids are $0.7 \leq \mathcal{S}$. The three columns are the three mass bins used in this study ($10^{9.4} \leq M_{\text{stellar}} < 10^{10.0}$, $10^{10.0} \leq M_{\text{stellar}} < 10^{11.0}$, and $M_{\text{stellar}} \geq 10^{11.0}$). Disks are the dominant population in the low mass bin and increase slightly at lower redshifts. In the middle and upper mass bins the spheroidal population increases at lower redshifts while the disk population decreases.

with the Sérsic fractions (Disk: $n=0.8-1.5$; Transitional: $n=1.5-2.5$; Spheroid: $n=2.5-5.0$) as a function of redshift for our three mass bins. Similar trends with redshift are observed in both the Sérsic identified morphologies and MWGunified visually identified morphologies. In both cases, the lower mass bin ($10^{9.4} \leq M_{stellar} < 10^{10.0}$) is dominated by disk galaxies. Across the full redshift range from 0.5 to 3.0, disks are the dominant low mass classification accounting for $\sim 50\%$ of galaxies at $z \sim 3$ and gradually increasing to $\sim 60\%$ by $z \sim 0.5$. As the disk population increases, the spheroidal population is seen to decrease while the transitional/intermediate population remains roughly flat across the redshift range. The opposite trend is seen in the $10^{10.0} \leq M_{stellar} < 10^{11.0}$ mass bin where the fraction of disk galaxies decreases from $z \sim 3$ to $z \sim 0.5$. This is most pronounced when the Sérsic index is used to identify disks which identifies $\sim 55\%$ of galaxies as disks at $z \sim 3$ and drops steadily to $\sim 30\%$ by $z \sim 0.5$. The Sérsic index identified spheroidal population increases from $\sim 18\%$ to $\sim 45\%$ over this redshift while the transitional class remains fairly flat. These same trends can be seen in this mass bin when using the MWGunified visual classifications but the trends are less smooth and less pronounced. In our high mass bin ($M_{stellar} \geq 10^{11.0}$), this increase in the number of spheroids at lower redshift is even more pronounced with high mass spheroids reaching $\sim 60\%$ of the total population at $z \sim 0.5$ when Sérsic is used. Previous studies (Patel et al. (2013) and Brammer et al. (2011)) have shown that the fraction of high mass systems that are quiescent spheroidal galaxies dramatical increases from $\sim 23\%$ at $z \sim 2.8$ to $\sim 89\%$ at $z \sim 0.4$ and that at $z \sim 3$ nearly all high mass galaxies are star-forming. Using Table 1.2, we see that our population of high mass ($M_{stellar} \geq 10^{11.0}$) galaxies is

overwhelmingly quiescent at all redshifts. We do not see a large high mass star-forming population that these earlier studies found. At $z=2.2-2.6$ and $z=1.8-2.2$, our fraction of high mass star-forming galaxies peaks at 35% (7/17) and 27% (6/22), respectively. This is far from the ‘nearly all’ claim of previous works. One possible difference is the Patel et al. (2013) work used a model determined mass range that extends to lower stellar masses ($10^{10.6}$) which would pick up dozens more star-forming objects in our sample. Lowering our mass threshold for high mass systems to match theirs, we do indeed find that a vast majority of these high redshift galaxies are star-forming and a high mass quiescent population quickly builds towards lower redshifts. It is reassuring that our visual classifications are able to reproduce these global trends in all the mass bins. It should be noted that the number of galaxies in our upper mass bin ($M_{stellar} \geq 10^{11.0}$) across all redshifts is less than a couple hundred and we do not have the numbers to make definitive statements about galaxy evolution in this high mass bin.

Tables 1.5 - 1.10 give full number break downs for the visually classified Disk, Intermediate, and Spheroidal populations as functions of galaxy sSFR and radii for given mass and redshift bins. One interesting observation from these tables is the bimodality of the spheroid population. Tables 1.9 and 1.10 show the fractional breakdown of the spheroidal population. These tables show strong fractional numbers of spheroids in a moderate mass ($10^{10.0} \leq M_{stellar} < 10^{11.0}$) population with low (quiescent) sSFR and a population of lower mass ($10^{9.4} \leq M_{stellar} < 10^{10.0}$) spheroids with high sSFR. This points to a bimodality between traditional quiescent spheroids and so-called ‘blue spheroids’ (Barro et al., 2013). To probe the population of these spheroids further, we focus on

Disk Galaxies
1572 (57.6%)

	$\log M_{\text{stellar}}$ 9.4-10.0	$\log M_{\text{stellar}}$ 10-11	$\log M_{\text{stellar}}$ >11
$2.6 \leq z < 3.0$ (140) (59.1%)	73 (53.7%)	62 (66.7%)	5 (62.5%)
$2.2 \leq z < 2.6$ (151) (56.3%)	92 (60.1%)	48 (49.0%)	11 (64.7%)
$1.8 \leq z < 2.2$ (191) (57.5%)	91 (51.7%)	86 (64.2%)	14 (63.6%)
$1.4 \leq z < 1.8$ (312) (58.8%)	201 (63.4%)	103 (56.0%)	8 (26.7%)
$1.0 \leq z < 1.4$ (374) (58.8%)	242 (67.6%)	113 (46.9%)	19 (51.4%)
$0.5 \leq z < 1.0$ (404) (55.9%)	252 (66.8%)	139 (45.4%)	13 (32.5%)
Total: 1572 (57.6%)	951 (62.7%)	551 (52.2%)	70 (45.5%)

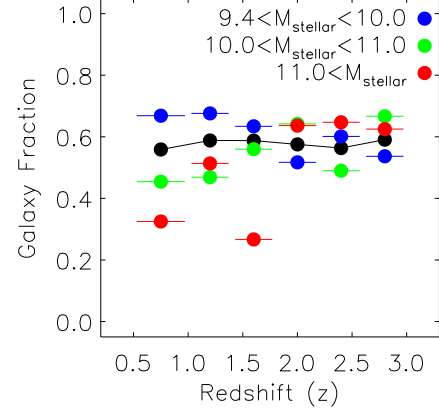


Figure 1.5: Disk Galaxy Fractions in Mass and Redshift Bins. The number of galaxies visually classified as disks ($\mathcal{S} < 0.3$) in a given mass and redshift bin. The percentages given are the fraction of disks from the total number of galaxies in that mass and redshift bin. Across almost all masses and redshifts, disks are the dominant classification in GOODS-South.

galaxies at $z=1.4-2.6$. Looking at the tables we see that for $z=1.4-2.6$ there 283 galaxies visually classified as a spheroid. Of these 283 galaxies, 70 (25%) have sSFR below our -0.9 cut and are considered quiescent and 169 (60%) have sSFR between -0.3 and 0.95 and are considered star-forming. Identifying galaxy classes by Sérsic index rather than visual classification yields similar results with 192 objects at $z=1.4-2.6$ being identified as spheroids ($2.5 \leq n < 5.0$) of which 44 (23%) have quiescent sSFR values and 114 (59%) are star-forming. Using either visual classifications or Sérsic indices, $\sim 2/3$ of our GOODS-South $z \sim 2$ spheroids are blue and star-forming rather than traditional red and quiescent systems.

Intermediate Galaxies
493 (18.1%)

	$\log M_{\text{stellar}}$ 9.4-10.0	$\log M_{\text{stellar}}$ 10-11	$\log M_{\text{stellar}}$ >11
$2.6 \leq z < 3.0$ (49) (20.7%)	37 (27.2%)	11 (11.8%)	1 (12.5%)
$2.2 \leq z < 2.6$ (38) (14.2%)	26 (17.0%)	12 (12.2%)	0 (0.0%)
$1.8 \leq z < 2.2$ (71) (21.4%)	45 (25.6%)	21 (15.7%)	5 (22.7%)
$1.4 \leq z < 1.8$ (85) (16.0%)	56 (17.7%)	23 (12.5%)	6 (20.0%)
$1.0 \leq z < 1.4$ (113) (17.8%)	54 (15.1%)	48 (19.9%)	11 (29.7%)
$0.5 \leq z < 1.0$ (137) (18.9%)	60 (15.9%)	66 (21.6%)	11 (27.5%)
Total: 493 (18.1%)	278 (18.3%)	181 (17.1%)	34 (22.1%)

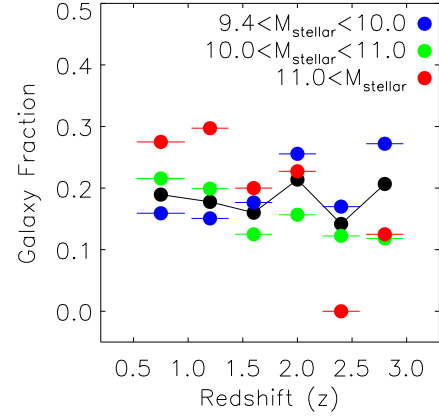


Figure 1.6: Intermediate/Transitional Galaxy Fractions in Mass and Redshift Bins. The number of galaxies visually classified as intermediate ($0.3 \leq \mathcal{S} < 0.7$) in a given mass and redshift bin. The percentages given are the fraction of intermediate galaxies from the total number of galaxies in that mass and redshift bin.

Spheroid Galaxies
662 (24.3%)

	$\log M_{\text{stellar}}$ 9.4-10.0	$\log M_{\text{stellar}}$ 10-11	$\log M_{\text{stellar}}$ >11
$2.6 \leq z < 3.0$ (48) (20.3%)	26 (19.1%)	20 (21.5%)	2 (25.0%)
$2.2 \leq z < 2.6$ (79) (29.5%)	35 (22.9%)	38 (38.8%)	6 (35.3%)
$1.8 \leq z < 2.2$ (70) (21.1%)	40 (22.7%)	27 (20.1%)	3 (13.6%)
$1.4 \leq z < 1.8$ (134) (25.2%)	60 (18.9%)	58 (31.5%)	16 (53.3%)
$1.0 \leq z < 1.4$ (149) (23.4%)	62 (17.3%)	80 (33.2%)	7 (18.9%)
$0.5 \leq z < 1.0$ (182) (25.2%)	65 (17.2%)	101 (33.0%)	16 (40.0%)
Total: 662 (24.3%)	288 (19.0%)	324 (30.7%)	50 (32.5%)

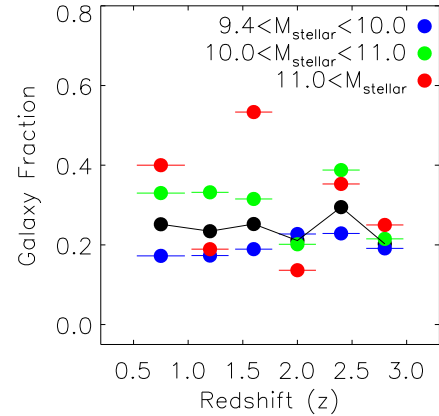


Figure 1.7: Spheroid Galaxy Fractions in Mass and Redshift Bins. The number of galaxies visually classified as intermediate ($0.7 \leq \mathcal{S}$) in a given mass and redshift bin. The percentages given are the fraction of spheroids from the total number of galaxies in that mass and redshift bin.

To further probe this bimodal spheroidal population and other populations at $z \sim 2$, we will introduce a five-plot figure. Figures 1.8 and 1.9, as well as figures used in following sections, plot our $z=1.4-2.6$ GOODS-South sample in five separate diagrams: Color-Mass, Color-Color, sSFR-Mass, R_{eff} -Mass, and R_{eff} -sSFR. These plots were selected as useful tools in previous works to display various populations of galaxies. Plotting these five diagrams together allows us to study how the various $z \sim 2$ galaxy populations appear in this five parameter space. It has been shown that galaxies can be classified and separated into two categories based on their star-forming activities out to $z \sim 3$ and beyond (Whitaker et al., 2011) and these figures will help demonstrate the difference in properties of these two populations at $z \sim 2$. We plot a color-mass diagram using rest frame U-V (3730Å- 6030Å) and stellar mass. This U-V - $M_{stellar}$ diagram shows how galaxies are increasingly red at higher masses but is unable to separate between galaxies that are red because they are quiescent and those that are dust reddened blue star-forming systems. To make this distinction we include a U-V vs V-J color-color diagram. This diagram has been used in previous works (Labbé et al. (2006), Wuyts et al. (2007), Williams et al. (2009), Patel et al. (2011), and Patel et al. (2012)) to separate between a quiescent population in the upper region and an extended sequence of star-forming galaxies from the blue systems to the dusty reddened systems located below the quiescent sample. Following Patel et al. (2013), we isolate our quiescent population using the UVJ selection criteria determined by Williams et al.

Table 1.5: Disk Galaxy Fractions Evolution with Redshift in Mass and sSFR Bins

	sSFR											
	Quiescent sSFR < -0.9			Transitional -0.9 ≤ sSFR < -0.3			Star Forming -0.3 ≤ sSFR < 0.95			High Star Forming 0.95 ≤ sSFR		
	$M_{9.4-10.0}^{stellar}$	$M_{10-11}^{stellar}$	$M_{>11}^{stellar}$	$M_{9.4-10.0}^{stellar}$	$M_{10-11}^{stellar}$	$M_{>11}^{stellar}$	$M_{9.4-10.0}^{stellar}$	$M_{10-11}^{stellar}$	$M_{>11}^{stellar}$	$M_{9.4-10.0}^{stellar}$	$M_{10-11}^{stellar}$	$M_{>11}^{stellar}$
2.6 ≤ z < 3.0 (140)	0 (0.0%)	0 (0.0%)	4 (2.9%)	0 (0.0%)	3 (2.1%)	1 (0.7%)	68 (48.6%)	52 (37.1%)	0 (0.0%)	5 (3.6%)	7 (5.0%)	0 (0.0%)
2.2 ≤ z < 2.6 (151)	2 (1.3%)	1 (0.7%)	4 (2.6%)	1 (0.7%)	2 (1.3%)	3 (2.0%)	83 (55.0%)	44 (29.1%)	3 (2.0%)	6 (4.0%)	1 (0.7%)	1 (0.7%)
1.8 ≤ z < 2.2 (191)	0	4 (2.1%)	6 (3.1%)	0 (0.0%)	4 (2.1%)	4 (2.1%)	82 (42.9%)	69 (36.1%)	4 (2.1%)	9 (4.7%)	9 (4.7%)	0 (0.0%)
1.4 ≤ z < 1.8 (312)	0	6 (1.9%)	2 (0.6%)	5 (1.6%)	9 (2.9%)	5 (1.6%)	175 (56.1%)	73 (23.4%)	1 (0.3%)	21 (6.7%)	15 (4.8%)	0 (0.0%)
1.0 ≤ z < 1.4 (374)	2 (0.5%)	12 (3.2%)	10 (2.7%)	7 (1.9%)	22 (5.9%)	8 (2.1%)	205 (54.8%)	73 (19.5%)	1 (0.3%)	28 (7.5%)	6 (1.6%)	0 (0.0%)
0.5 ≤ z < 1.0 (404)	7 (1.7%)	13 (3.2%)	3 (0.7%)	10 (2.5%)	33 (8.2%)	5 (1.2%)	215 (53.2%)	84 (20.8%)	5 (1.2%)	20 (5.0%)	9 (2.2%)	0 (0.0%)
Total: 1572	11	36	29	23	73	26	828	395	14	89	47	1

 Table 1.6: Disk Galaxy Fractions Evolution with Redshift in Mass and R_{eff} Bins

	R_{eff} (F160W)											
	Compact $R_{eff} < 1\text{kpc}$			Moderate $1\text{kpc} \leq R_{eff} < 3\text{kpc}$			Extended $3\text{kpc} \leq R_{eff}$					
	$M_{9.4-10.0}^{stellar}$	$M_{10-11}^{stellar}$	$M_{>11}^{stellar}$	$M_{9.4-10.0}^{stellar}$	$M_{10-11}^{stellar}$	$M_{>11}^{stellar}$	$M_{9.4-10.0}^{stellar}$	$M_{10-11}^{stellar}$	$M_{>11}^{stellar}$	$M_{9.4-10.0}^{stellar}$	$M_{10-11}^{stellar}$	$M_{>11}^{stellar}$
2.6 ≤ z < 3.0 (140)	0 (0.0%)	0 (0.0%)	0 (0.0%)	47 (33.6%)	29 (20.7%)	2 (1.4%)	26 (18.6%)	33 (23.6%)	3 (2.1%)	0	0	0
2.2 ≤ z < 2.6 (151)	0 (0.0%)	0 (0.0%)	0 (0.0%)	63 (41.7%)	18 (11.9%)	4 (2.6%)	29 (19.2%)	30 (19.9%)	7 (4.6%)	0	0	0
1.8 ≤ z < 2.2 (191)	0 (0.0%)	0 (0.0%)	0 (0.0%)	53 (27.7%)	18 (9.4%)	2 (1.0%)	38 (19.9%)	68 (35.6%)	12 (6.3%)	0	0	0
1.4 ≤ z < 1.8 (312)	0 (0.0%)	0 (0.0%)	0 (0.0%)	87 (27.9%)	27 (8.7%)	1 (0.3%)	114 (36.5%)	76 (24.4%)	7 (2.2%)	0	0	0
1.0 ≤ z < 1.4 (374)	0 (0.0%)	0 (0.0%)	0 (0.0%)	83 (22.2%)	25 (6.7%)	2 (0.5%)	159 (42.5%)	88 (23.5%)	17 (4.5%)	0	0	0
0.5 ≤ z < 1.0 (404)	0 (0.0%)	1 (0.2%)	0 (0.0%)	94 (23.3%)	31 (7.7%)	1 (0.2%)	158 (39.1%)	107 (26.5%)	12 (3.0%)	0	0	0
Total: 1572	0	1	0	427	148	12	524	402	58	0	0	0

Table 1.7: Intermediate Galaxy Fractions Evolution with Redshift in Mass and sSFR Bins

	Quiescent sSFR < -0.9		Transitional -0.9 ≤ sSFR < -0.3		Star Forming -0.3 ≤ sSFR < 0.95		High Star Forming 0.95 ≤ sSFR	
	$M_{9.4-10.0}^{stellar}$	$M_{10-11}^{stellar}$	$M_{9.4-10.0}^{stellar}$	$M_{10-11}^{stellar}$	$M_{9.4-10.0}^{stellar}$	$M_{10-11}^{stellar}$	$M_{9.4-10.0}^{stellar}$	$M_{10-11}^{stellar}$
2.6 ≤ z < 3.0 (49)	0 (0.0%)	0 (0.0%)	0 (0.0%)	0 (0.0%)	32 (65.3%)	10 (20.4%)	5 (10.2%)	0 (0.0%)
2.2 ≤ z < 2.6 (38)	0 (0.0%)	0 (0.0%)	0 (0.0%)	2 (5.3%)	25 (65.8%)	10 (26.3%)	1 (2.6%)	0 (0.0%)
1.8 ≤ z < 2.2 (71)	0 (0.0%)	4 (5.6%)	0 (0.0%)	1 (1.4%)	42 (59.2%)	16 (22.5%)	3 (4.2%)	0 (0.0%)
1.4 ≤ z < 1.8 (85)	0 (0.0%)	5 (5.9%)	5 (5.9%)	4 (4.7%)	49 (57.6%)	13 (15.3%)	5 (5.9%)	0 (0.0%)
1.0 ≤ z < 1.4 (113)	2 (1.8%)	19 (16.8%)	7 (6.2%)	7 (6.2%)	47 (41.6%)	19 (16.8%)	0 (0.0%)	3 (2.7%)
0.5 ≤ z < 1.0 (137)	5 (3.6%)	35 (25.5%)	11 (8.0%)	13 (9.5%)	41 (29.9%)	16 (11.7%)	6 (4.4%)	2 (1.5%)
Total: 493	7	61	15	27	236	84	20	9

 Table 1.8: Intermediate Galaxy Fractions Evolution with Redshift in Mass and R_{eff} Bins

	Compact R _{eff} < 1kpc		Moderate 1kpc ≤ R _{eff} < 3kpc		Extended 3kpc ≤ R _{eff}	
	$M_{9.4-10.0}^{stellar}$	$M_{10-11}^{stellar}$	$M_{9.4-10.0}^{stellar}$	$M_{10-11}^{stellar}$	$M_{9.4-10.0}^{stellar}$	$M_{10-11}^{stellar}$
2.6 ≤ z < 3.0 (49)	0 (0.0%)	0 (0.0%)	34 (69.4%)	8 (16.3%)	3 (6.1%)	3 (6.1%)
2.2 ≤ z < 2.6 (38)	1 (2.6%)	0 (0.0%)	21 (55.3%)	8 (21.1%)	4 (10.5%)	4 (10.5%)
1.8 ≤ z < 2.2 (71)	2 (2.8%)	0 (0.0%)	42 (59.2%)	17 (23.9%)	1 (1.4%)	4 (5.6%)
1.4 ≤ z < 1.8 (85)	2 (2.4%)	0 (0.0%)	47 (55.3%)	22 (25.9%)	7 (8.2%)	1 (1.2%)
1.0 ≤ z < 1.4 (113)	1 (0.9%)	2 (1.8%)	45 (39.8%)	31 (27.4%)	8 (7.1%)	15 (13.3%)
0.5 ≤ z < 1.0 (137)	0 (0.0%)	0 (0.0%)	53 (38.7%)	49 (35.8%)	7 (5.1%)	17 (12.4%)
Total: 493	6	2	242	135	30	44

Table 1.9: Spheroidal Galaxy Fractions Evolution with Redshift in Mass and sSFR Bins

	Quiescent sSFR < -0.9			Transitional -0.9 ≤ sSFR < -0.3			Star Forming -0.3 ≤ sSFR < 0.95			High Star Forming 0.95 ≤ sSFR		
	$M_{stellar}^{9.4-10.0}$	$M_{stellar}^{10-11}$	$M_{stellar}^{>11}$	$M_{stellar}^{9.4-10.0}$	$M_{stellar}^{10-11}$	$M_{stellar}^{>11}$	$M_{stellar}^{9.4-10.0}$	$M_{stellar}^{10-11}$	$M_{stellar}^{>11}$	$M_{stellar}^{9.4-10.0}$	$M_{stellar}^{10-11}$	$M_{stellar}^{>11}$
2.6 ≤ z < 3.0 (48)	0 (0.0%)	4 (8.3%)	1 (2.1%)	0 (0.0%)	2 (4.2%)	1 (2.1%)	21 (43.8%)	12 (25.0%)	0 (0.0%)	5 (10.4%)	2 (4.2%)	0 (0.0%)
2.2 ≤ z < 2.6 (79)	0 (0.0%)	12 (15.2%)	3 (3.8%)	0 (0.0%)	6 (7.6%)	0 (0.0%)	34 (43.0%)	17 (21.5%)	3 (3.8%)	1 (1.3%)	3 (3.8%)	0 (0.0%)
1.8 ≤ z < 2.2 (70)	1 (1.4%)	7 (10.0%)	2 (2.9%)	1 (1.4%)	4 (5.7%)	0 (0.0%)	38 (54.3%)	14 (20.0%)	1 (1.4%)	0 (0.0%)	2 (2.9%)	0 (0.0%)
1.4 ≤ z < 1.8 (134)	0 (0.0%)	31 (23.1%)	14 (10.4%)	2 (1.5%)	16 (11.9%)	2 (1.5%)	54 (40.3%)	8 (6.0%)	0 (0.0%)	4 (3.0%)	3 (2.2%)	0 (0.0%)
1.0 ≤ z < 1.4 (149)	10 (6.7%)	48 (32.2%)	7 (4.7%)	3 (2.0%)	17 (11.4%)	0 (0.0%)	46 (30.9%)	13 (8.7%)	0 (0.0%)	3 (2.0%)	2 (1.3%)	0 (0.0%)
0.5 ≤ z < 1.0 (182)	19 (10.4%)	80 (44.0%)	15 (8.2%)	6 (3.3%)	13 (7.1%)	0 (0.0%)	30 (16.5%)	7 (3.8%)	1 (0.5%)	10 (5.5%)	1 (0.5%)	0 (0.0%)
Total: 662	30	182	42	12	58	3	223	71	5	23	13	0

Table 1.10: Spheroidal Galaxy Fractions Evolution with Redshift in Mass and R_{eff} Bins

	Compact $R_{eff} < 1kpc$			Moderate $1kpc \leq R_{eff} < 3kpc$			Extended $3kpc \leq R_{eff}$		
	$M_{stellar}^{9.4-10.0}$	$M_{stellar}^{10-11}$	$M_{stellar}^{>11}$	$M_{stellar}^{9.4-10.0}$	$M_{stellar}^{10-11}$	$M_{stellar}^{>11}$	$M_{stellar}^{9.4-10.0}$	$M_{stellar}^{10-11}$	$M_{stellar}^{>11}$
2.6 ≤ z < 3.0 (48)	8 (16.7%)	10 (20.8%)	1 (2.1%)	16 (33.3%)	8 (16.7%)	1 (2.1%)	2 (4.2%)	2 (4.2%)	0 (0.0%)
2.2 ≤ z < 2.6 (79)	12 (15.2%)	25 (31.6%)	1 (1.3%)	22 (27.8%)	12 (15.2%)	4 (5.1%)	1 (1.3%)	1 (1.3%)	1 (1.3%)
1.8 ≤ z < 2.2 (70)	9 (12.9%)	10 (14.3%)	1 (1.4%)	30 (42.9%)	15 (21.4%)	1 (1.4%)	1 (1.4%)	2 (2.9%)	1 (1.4%)
1.4 ≤ z < 1.8 (134)	17 (12.7%)	23 (17.2%)	0 (0.0%)	40 (29.9%)	31 (23.1%)	15 (11.2%)	3 (2.2%)	4 (3.0%)	1 (0.7%)
1.0 ≤ z < 1.4 (149)	16 (10.7%)	19 (12.8%)	0 (0.0%)	45 (30.2%)	56 (37.6%)	5 (3.4%)	1 (0.7%)	5 (3.4%)	2 (1.3%)
0.5 ≤ z < 1.0 (182)	21 (11.5%)	19 (10.4%)	0 (0.0%)	43 (23.6%)	70 (38.5%)	3 (1.6%)	1 (0.5%)	12 (6.6%)	13 (7.1%)
Total: 662	83	106	3	196	192	29	9	26	18

(2009) for galaxies $1.0 \leq z < 2.0$ ($(U-V) > 0.88(V-J) + 0.49$, with $U-V \geq 1.3$ and $V-J \leq 1.6$). We extend this selection for our full $z \sim 2$ sample out to $z = 2.6$ (slight modifications to this selection criteria at higher redshifts did not make a significant difference in the sample selection). This region selecting quiescent galaxies in UVJ space is over-plotted on the diagram. As discussed in Section 3, specific star formation rates (sSFR) can also be used to identify quiescent and star-forming populations. In the figure, we include a sSFR vs $M_{stellar}$ diagram as well as a sSFR vs R_{eff} diagram to use as an alternative selection method between star-forming and quiescent systems. The divisions shown on these plots represent the quiescent ($\log \text{sSFR} < -0.9$ [Gyr^{-1}]), transitional ($-0.9 \leq \log \text{sSFR} < -0.3$ [Gyr^{-1}]), star-forming ($-0.3 \leq \log \text{sSFR} < 0.95$ [Gyr^{-1}]), and high star-forming ($\log \text{sSFR} \geq 0.95$ [Gyr^{-1}]) divisions discussed earlier. Lastly, a R_{eff} vs $M_{stellar}$ diagram is included in the figure. Recent studies (Williams et al. (2010), Wuyts et al. (2011a), and Barro et al. (2013)) have shown that separate size-mass relations are followed by star-forming and quiescent galaxies at the local and $z \sim 2$ Universe. Our results are inline with these findings and a clear separation exists between the star-forming sequence at lower masses and larger radii and the quiescent galaxies in the lower right at higher masses and smaller radii. The gap between the star-forming and quiescent populations in size-mass is fairly wide at $z \sim 2$ and thus the exact line used to make the division between quiescent and star-forming does not significantly change the findings. We adopt a dividing line from Barro et al. (2013) of $\log M_{stellar}/R_{eff}^{1.5} = 10.3 \text{ M}_{\odot} \text{kpc}^{-1.5}$ which is inline with previous dividing criteria found using $M_{stellar}/R_{eff}$ and $M_{stellar}/R_{eff}^2$ (Franx et al. (2008) and Newman et al. (2012)). In all of the diagrams in these figures, a stellar mass

lower limit of $M_{stellar} \geq 10^{9.4}$ is applied as discussed previously. The diagrams shown are for the full $z \sim 2$ population.

Figure 1.8 displays our $z \sim 2$ population color coded by Sérsic index and Figure 1.9 uses the spheroidicity parameter from our visual classifications to color our galaxy sample. These figures clearly show the bimodality of our spheroidal population found earlier in Tables 1.9 and 1.10. There exists a population of spheroids (both in terms of Sérsic and spheroidicity) that are in the quiescent region of both the UVJ color-color diagram and the sSFR diagram. In addition, there is also a large population of spheroids concentrated at the lower left of the UVJ diagram (grouped with the star-forming primarily disk objects), and the lower mass ($< 10^{10}$) and star-forming region of the sSFR diagrams. These compact star-forming ‘blue nuggets’ are the dominant form of spheroidal galaxies accounting for nearly 2/3 of all spheroids at $z \sim 2$ in our sample. This population is inline with findings from Wuyts et al. (2011a) where they discussed a population of compact, high Sérsic index, galaxies with enhanced star formation rates at $z \sim 2$. Note that this population is independent of whether we use visual classifications or Sérsic indices to identify the spheroids. The lower left panel in Figure 1.9 shows a possible R_{eff} bias in our visual classifications with almost all compact objects ($R_{eff} < 1 \text{ kpc}$) being classified as spheroidal. We find that $> 80\%$ of all compact galaxies ($R_{eff} < 1 \text{ kpc}$) in all mass and redshift bins are visually classified as spheroidal. This result is not unexpected since compact objects are defined to be below the resolution limit ($0.17''$) of F160W. This radii bias could lead to a misclassification of star-forming, low mass, small radii disks as spheroids and could therefore artificially

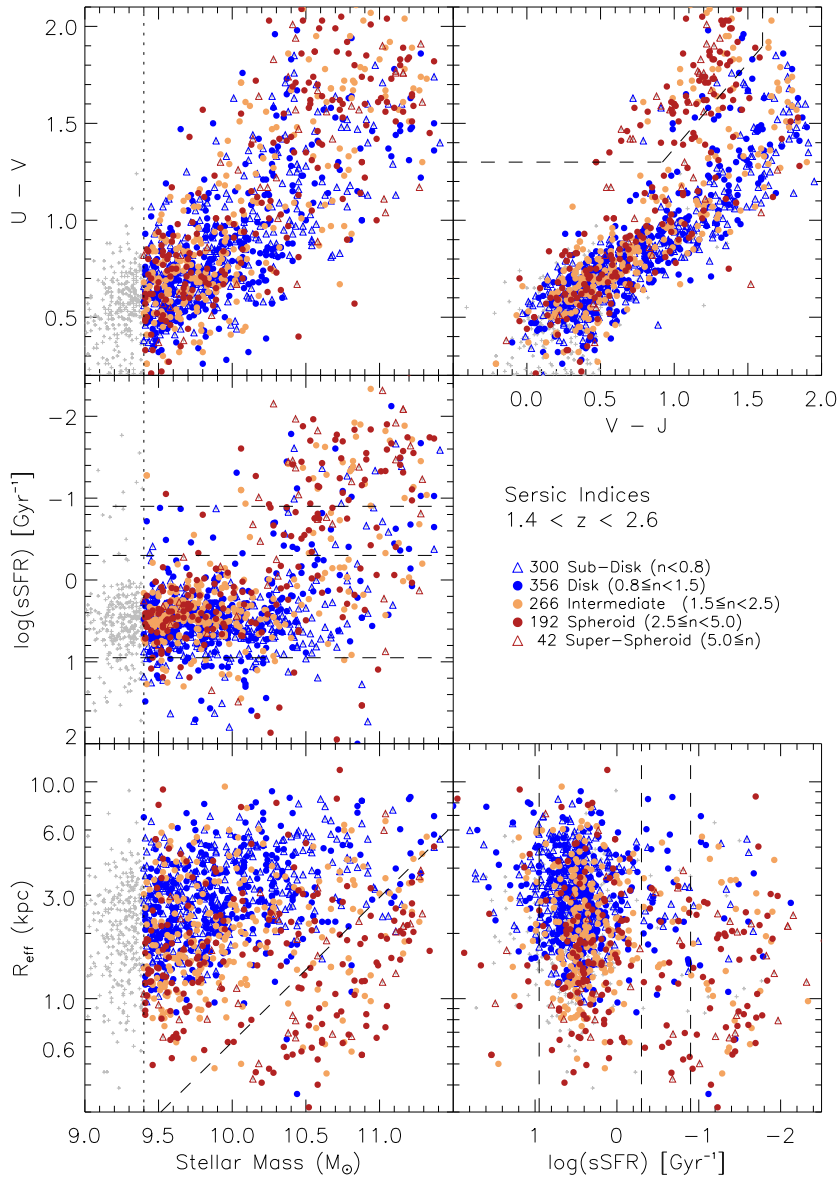


Figure 1.8: Global Properties of $z \sim 2$ GOODS-South Sample by Sérsic Indices. The colors correspond to the Sérsic index of each GOODS-South galaxy. Like Figure 1.9, the divisions in UVJ, sSFR, and $M_{\text{stellar}}-R_{\text{eff}}$ nicely divide our $z \sim 2$ populations. The Sérsic indices do not as cleanly separate the quiescent regions and many galaxies that were visually identified as spheroidal are classified as intermediate in Sérsic. The visual classification bias for spheroids at low radii is not present for Sérsic.

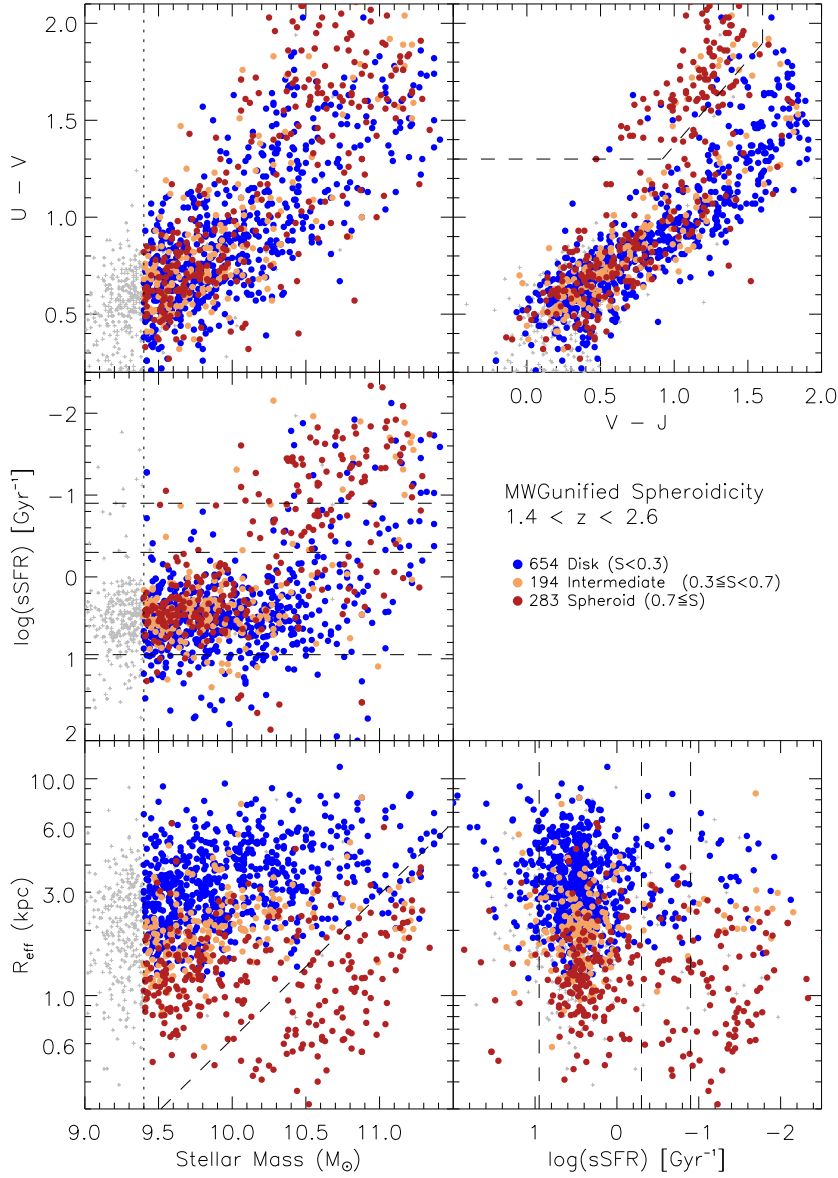


Figure 1.9: Global Properties of $z \sim 2$ GOODS-South Sample by Visual Classifications. The galaxies are colored by their visual classifications. A quiescent spheroidal population can be isolated using UVJ color-color cuts, sSFR cuts, or an $M_{\text{stellar}}\text{-}R_{\text{eff}}$ surface density cut. The visual classifications also highlight an additional spheroidal population located within the star-forming sequence in addition to the quiescent spheroids. There is an apparent radius bias towards identifying all small galaxies as spheroidal. Grey points are below the mass threshold of $9.4 M_{\odot}$.

create a blue spheroid population. This population, however, is also seen when using Sérsic indices to identify spheroids. Unlike the visual classifications, GALFIT is able to fit objects below the resolution limit of the F160W mosaics assuming the PSF is well known (van der Wel et al., 2012). Internal tests show that the Sérsic and radii measured from GALFIT do differ when the PSF is blurred but the results do not change significantly enough under realistic PSFs to affect the observed trends and bimodality of spheroids. We acknowledge the limitation of the visual classification system for accurately classifying unresolved systems and use Sérsic as a check for all compact objects with high spheroidicity.

In addition to compact objects being visually classified as spheroidal, the MW-Gunified system has a radii dependence on all morphological classes. The lower two diagrams in Figure 1.9 illustrate a progression observed in the visual classifications at all masses from being spheroid dominated at small radii to intermediate dominated at larger radii to disk dominated at the largest radii. This clear radii dependence in our visual classifications is not observed in Figure 1.8 where Sérsic indices are used. Though systems with smaller R_{eff} do tend to have Sérsic values that are intermediate or spheroidal, the classes are mixed across the various radii and no clear transitions are present like in the visual classification case. This radii bias is clearly a limitation for reliably classifying galaxies at any radii using a visual classification method.

As shown in earlier studies (Patel et al., 2012), the UVJ diagram separates galaxies into a star-forming main sequence and a quiescent region. The V-J color separates between red galaxies in U-V colors that are red due to being quiescent and those

that are reddened by the effects of dust. Figures 1.8 and 1.9 show that $z\sim 2$ galaxy morphology also divide between these regions. The spheroidicity metric places a nearly uniform sample of spheroidal galaxies in the quiescent region of the UVJ diagram. The lower left portion of the star-forming continuum in the UVJ diagram contains large numbers of disks, intermediate, and spheroids (blue nuggets). The upper right portion of the UVJ diagram has been shown (Brammer et al., 2011) to consist of star-forming galaxies that are being reddened by dust. We find that this ‘dusty’ region of the UVJ diagram contains galaxies mostly visually classified as disks with 10-20% classified as intermediate with the spheroidal population along the border with the quiescent region. Similarly, in Sérsic index, this dusty region is composed mostly of objects with disk and intermediate Sérsic indices. These findings are reassuring and support the UVJ color-color plot’s ability to separate the quiescent spheroidal galaxies from the dusty star-forming disks. One might expect there to be a high number of edge-on galaxies in this dusty region but this is not what we observe. Figures 1.10 and 1.11 show the edge-on and face-on population (determined by visual classification and by axis ratio) of galaxies at $z\sim 2$ respectively. In both cases, the population of visually identified face-on and edge on disks is plotted along with the population with high (face-on) and low (edge-on) axis ratios. Edge-on galaxies (as identified in the MWGunified classifications) are found throughout the star-forming sequence but show no increase in number density in the dusty portion of the UVJ diagram. Similarly, galaxies with low axis ratios ($q<0.3$) are found throughout the star-forming sample (primarily at lower masses) and do exist in the dusty region but do not dominate the population. Likewise, the face-on

population of visually identified disks shows no preferred location in the star-forming sequence of the UVJ diagram though they more evenly cover the mass distribution of the star-forming sequence than the edge-on population. Galaxies with high axis ratios populate the full star-forming sequence similar to the visually identified face-on population. Note that the high axis ratio population includes round spheroids and thus a large number exist in the quiescent spheroidal areas of the figures. The population of UVJ quiescent galaxies matches well with the sSFR identified quiescent population as well as with the ‘red triangle’ of galaxies in the R_{eff} - $M_{stellar}$ diagram. These three regions and the population of galaxies they define together will be discussed in more detail in Section 4.

There are several other trends observed in the $z \sim 2$ figures and general population tables that are worth noting. The disk classification is the dominant classification across all masses and redshifts - nearly 60% of our full sample are visually classified as disks. Nearly all extended objects are visually classified as disks across all masses and redshifts and disks dominate the star-forming and high star-forming classes at all masses and redshifts. The radii of disk galaxies increases at lower redshift. Using Table 1.6, we see that within the galaxies classified as disks, there is an increase among galaxies with extended radii in both the low mass and moderate mass bins as redshift decreases. Galaxies visually classified as intermediate make up a fairly flat fraction ($\sim 18\%$) of the total population of galaxies across all mass and redshifts. Using Tables 1.7 and 1.7, we see that intermediate galaxies are predominantly star-forming lower mass systems with moderate radii. They behave much like the disk population of galaxies but with

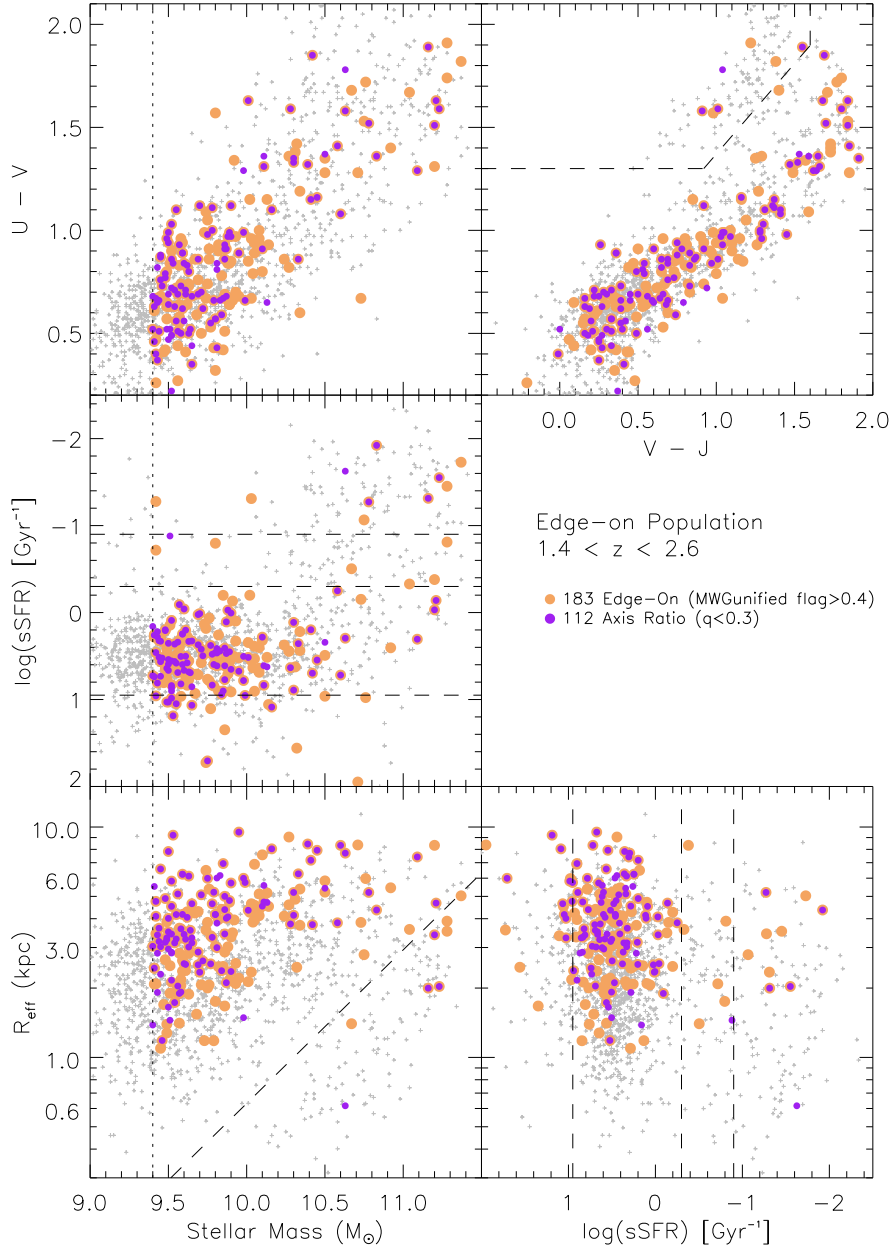


Figure 1.10: Global Properties of Edge-on $z \sim 2$ GOODS-South Sample. The edge-on galaxies are highlighted in gold if they were visually classified as edge-on and purple if they have low axis ratios ($q < 0.3$). Edge-on galaxies are found throughout the star-forming sequence but show no increase in number density in the dusty portion of the UVJ diagram.

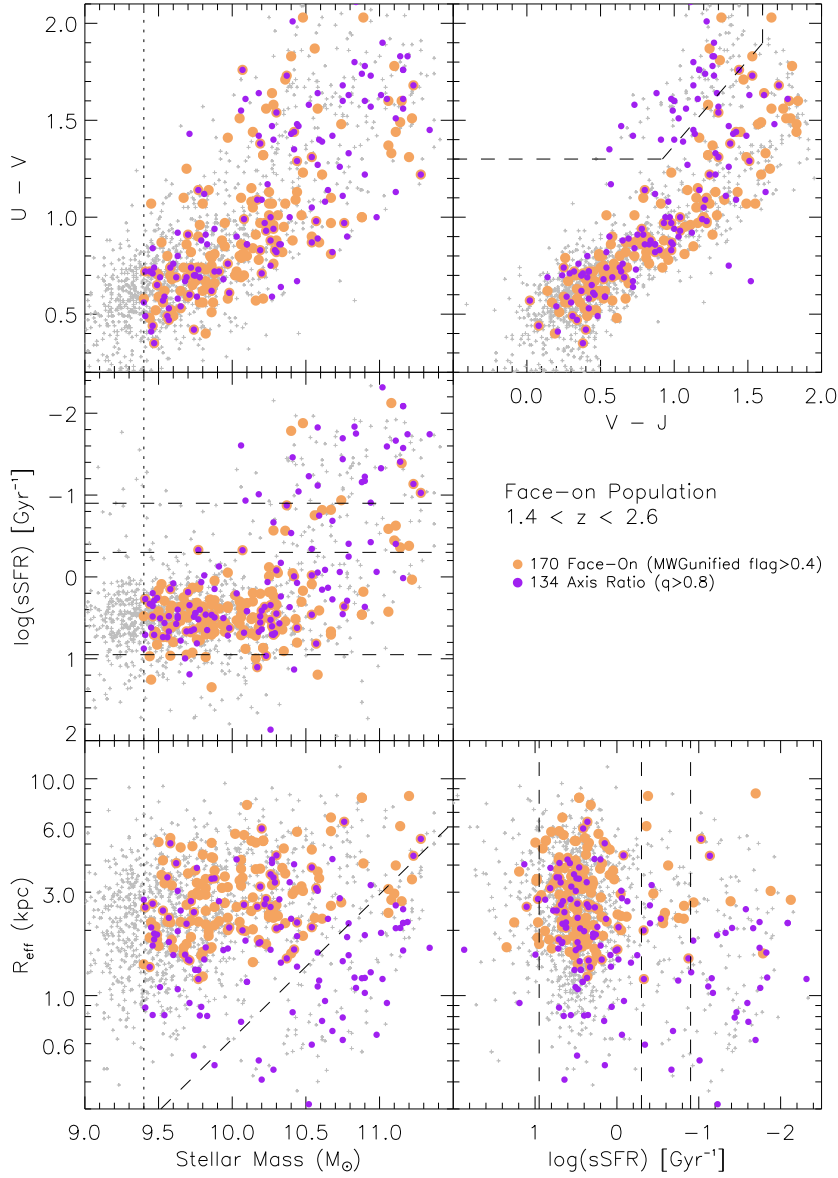


Figure 1.11: Global Properties of Face-on $z \sim 2$ GOODS-South Sample. The face-on galaxies are highlighted in gold if they were visually classified as face-on and purple if they have high axis ratios ($q > 0.8$). The face-on population of visually identified disks shows no preferred location in the star-forming sequence of the UVJ diagram. Galaxies with high axis ratios populate the full star-forming sequence similar to the visually identified face-on population. Note that the high axis ratio population includes round spheroids and thus a large number exist in the quiescent spheroidal areas of the figures.

lower radii. This disk-like behavior is confirmed in the $z\sim 2$ figures where we see this intermediate population cluster with the disk population in the star-forming regions and inhabit the lower R_{eff} of the star-forming group. Additionally, it should be noted in Table 1.2 that there is no population of low mass quiescent galaxies at high redshift. A property confirmed at $z\sim 2$ in the sSFR-Mass diagrams of Figures 1.8 and 1.9. Within the spheroid population, Table 1.9 shows that the fraction of quiescent spheroids increases towards lower redshifts. The ‘blue nugget’ class of low mass star-forming spheroidal galaxies that is $\sim 2/3$ the total spheroidal population at $z\sim 2$ drops significantly and by $z=0.5$ the majority of spheroidal galaxies are quiescent, have moderate masses ($10^{10.0} \leq M_{stellar} < 10^{11.0}$), and have larger (moderate 1-3kpc) radii. The large number of ‘blue nuggets’ at high z that drops off dramatically at later redshifts while the population of compact quiescent galaxies grows is in line with the galaxy evolution model of compact star-forming galaxies as the progenitors of compact quiescent galaxies observed at later redshifts - the so-called ‘fast-track’ evolution presented in Barro et al. (2013) in which AGN and star formation feedback quench these $z\sim 2$ compact star formers to form the compact quiescent galaxies by $z\sim 1$.

1.3.2 Clumpy Galaxies, Chains, and Tadpoles

Our large visually classified sample is ideal to probe the clumpy nature of galaxies as a function of mass over a range of redshifts. Previous studies have shown that galaxies at high redshifts tend to be clumpy, asymmetric disturbed systems that do not exhibit the relaxed mature structures of the local Universe (Papovich et al. (2005),

Conselice et al. (2008), and Elmegreen et al. (2005)). The F160W NIR filter is ideal for classifying global structure out to $z \sim 2$ since this filter corresponds to rest-frame optical light at $z \sim 2$ which is a better tracer of old stellar populations and overall stellar mass. Regions of recent star formations, however, would not stand out in the rest-frame optical images unless there is an underlying older stellar population. To ensure that we do not ignore the young star-forming regions, the MWGunified system uses the observed optical light from the ACS filters (rest frame near ultraviolet at $z \sim 2$) to identify clumpiness and flag clumpy structures like chains and tadpoles. Dickinson (2000) found that UV radiation predominantly traces emission from the star-forming regions and many studies have since used UV light as a star formation tracer to find clumps (Elmegreen et al., 2005).

To identify clumpy galaxies in the MWGunified system, the clumpiness metric (\mathcal{C}) (described in the data section) was used. Internal tests and visual confirmation of a subsample of the GOODS-South objects showed that $\mathcal{C} > 0.2$ acted as a good lower limit to identify clumpy galaxies but not include spurious galaxies misidentified by individual classifiers. Similarly, to identify subclasses of clumpy galaxies (namely chain and tadpole systems), the individual visual classification flags for the systems were used with minimum cutoffs set to 0.1. The lower minimum value for these subclasses was found to be necessary due to the classifiers unreliability at checking morphology flags.

Figures 1.12, 1.13, and 1.14 show the percentage of galaxies in different mass and redshift bins in GOODS-South that are visually classified as clumpy, chain, and tadpoles, respectively. These tables and figures show that clumpy galaxies are primarily

in low and moderate mass ($10^{9.4} \leq M_{stellar} < 10^{10.0}$ and $10^{10.0} \leq M_{stellar} < 10^{11.0}$) systems across all redshifts. We found that the fraction of clumpy systems in these mass bins does not have a strong redshift dependence across $z=0.5-3.0$ and is fairly flat at $\sim 50\%$. The high mass systems ($M_{stellar} \geq 10^{11.0}$), on the other hand, do show a redshift dependence. High mass $z \sim 3$ systems exhibit little sign of being clumpy but at lower redshifts this grows to $\sim 1/3$ of high mass systems at $z \sim 0.5$ exhibiting clumpy structures. These results are not in line with claims of previous studies that $z > 2$ galaxies are dominated by clumpy, unrelaxed systems. We find that clumpy galaxies (particularly in lower masses) exist at all red shifts. Galaxy stellar mass (not redshift) is found to be a better indicator of clumpiness. Clumpy galaxies do not seem to preferentially exist at higher redshifts so they do not seem to trace the peaking merger rates of $z \sim 2$. If galaxy clumpiness was primarily a result of mergers and interactions, one would expect more clumpy systems at $z \sim 2$ since this epoch has a significantly higher merger rate than at $z=0.1-1.0$. Chains and tadpoles, on the other hand, do show a redshift dependence in their fractions. Both chains and tadpoles are predominantly in low and moderate mass systems and are more common at higher redshifts. In the lower mass bin ($10^{9.4} \leq M_{stellar} < 10^{10.0}$), tadpoles and chains are 14 and 7% (respectively) of the total galaxy population at $z \sim 3$. This fraction drops to 4% for both chains and tadpoles by $z \sim 0.5$. Neither the chain nor the tadpole populations are common in the higher mass systems. Tables 1.11 to 1.16 show where the clumpy, chain, and tadpole populations lie in terms of sSFR and radii at given redshifts and stellar mass bins. We confirm that all three classes are predominantly in the lower mass bin ($10^{9.4} \leq M_{stellar} < 10^{10.0}$) and are almost exclusively found in star-

forming systems - an expected result since these NUV clumps are thought to be regions of ongoing star formation. These three classes are predominantly in large radii systems and Table 1.12 shows that >70% of all extended objects in the low and moderate mass bins ($10^{9.4} \leq M_{stellar} < 10^{10.0}$ and $10^{10.0} \leq M_{stellar} < 10^{11.0}$) are clumpy systems across the full redshift range. Since the radii is measured by fitting Sérsic profiles to the F160W light, this means that systems that are clumpy and have extended knots of light beyond the core also have extended old stellar populations and stellar mass. This paints a picture of clumps forming on the outer parts of extended galaxies and not star-forming knots merging with compact galaxies. Clumps are found in lower mass systems that are assembling. This is inline with in-situ disk formation of clumps rather than the clumps being minor mergers of ex-situ formed UV regions (Dekel et al., 2013). Dekel et al. (2013) and Dekel et al. (2009) have shown in Hydro-ART simulations that clumps form in outer parts of disks by gravitational instability and migrate relatively quickly to the center of the galaxy building the bulge. In support of this theoretical work, Guo et al. (2012) has shown that clumps in observations have an age gradient with older clumps residing closer to the centers of galaxies than younger clumps. Chains and tadpoles are seen to be more prominent at higher redshifts than at lower redshifts. The fraction of clumpy galaxies, on the other hand, appears to be fairly flat across all redshifts in the same mass bins. We can not therefore adopt a definition that all chains and tadpoles are clumpy galaxies viewed edge-on or from a particular position angle. Chains and tadpoles must be a sub-population of clumpy galaxies that are more common at high redshift. Suggesting that not all galaxies that are classified as clumpy would be classified as chains

or tadpoles if they were viewed from a different angle. The galaxies classified as clumpy at low redshifts are dominated by relaxed disk systems with star-forming knots but when viewed edge-on are not classified as chains or tadpoles (evidenced by the low fraction of chains/tadpoles at $z \sim 0.5$). This points to a need for a different population (rather than flat disks with star-forming knots) that comprises the chain/tadpole population observed at $z \sim 2$. In the next subsection we will look at asymmetry and see a sharp rise in the number of asymmetric systems above $z \sim 2$. These asymmetric extended systems may be the population from which the chains and tadpoles arise and not relaxed flat disks.

As was previously discussed in this section, there is wide spread agreement in galaxy morphology classifications between the Elmegreen system (Elmegreen et al., 2005) and the MWGunified system. For the 334 galaxies in Elmegreen's UDF sample that are also visually classified by the MWGunified system, the visual classification basic morphologies agree over 80% of the time despite the Elmegreen system using only ACS F775W visible light filters for the classifications while the MWGunified system used F160W near infrared filters for general morphology classifications. Table 1.4 highlights the widespread agreement for both general morphologies and for identifying clumpy, chain, and tadpole systems between our classifications and the Elmegreen classifications. Focusing on the $z \sim 2$ range of galaxies, Figure 1.15 plots the galaxies visually identified as clumpy, tadpoles and chains in the MWGunified and Elmegreen visual classification systems. In the $z = 1.4 - 2.6$ redshift range, the total number of galaxies in Elmegreen's UDF sample is only 59 galaxies. 27 of these 59 galaxies are classified as clump clusters

and 13 are classified as a chain or tadpole system (6 and 7, respectively). The Elmegreen $z\sim 2$ sample is significantly smaller than our GOODS-South sample and is limited to lower masses with the majority of the $z\sim 2$ galaxies having stellar masses below $10^{10.5}$. Comparing the Elmegreen $z\sim 2$ sample to our GOODS-South sample, we find that of the 31 low mass ($10^{9.4} \leq M_{\text{stellar}} < 10^{10.0}$) galaxies classified by both Elmegreen and MWGunified, 14 are classified by Elmegreen as clump clusters, 5 as tadpoles, and 2 as chains. This puts the fraction of clumpy galaxies in the Elmegreen-MWGunified matched sample at 68% and the fraction of chains/tadpoles at 23%. In this same mass and redshift range, there are 646 galaxies in the full GOODS-South MWGunified catalog, 44% of which are clumpy and 15% are classified as chains or tadpoles. The clumpy fractions for our sample is $\sim 2/3$ that of the Elmegreen sample. This can be understood as a selection effect in the Elmegreen sample. Because the Elmegreen sample is a visible light F775W selected sample, it preferentially selects galaxies that are bright in the rest frame NUV at $z\sim 2$. UV light is a good tracer of emissions from star-forming regions (Dickinson, 2000) which tend to be clumpy/patchy regions. Thus the Elmegreen sample is selecting galaxies that will have active star-forming regions and thus are more likely to appear clumpy. The MWGunified sample on the other hand is a NIR selected sample which is tracing visible light at $z\sim 2$, an indicator of older stellar populations and a better proxy for mass. The MWGunified system is not preferentially finding the high star-forming systems and thus includes many quiescent and lower star-forming systems which causes the fraction of clumpy galaxies to be lower than in Elmegreen's sample.

In Figure 1.15 we see that clumpy, tadpole and chain systems are predomi-

nantly low mass systems that lie along the star-forming sequence. Asymmetric galaxies, are shown in the following section to extend up the full star-forming sequence in the UVJ color-color diagram as well as cover the full range of masses including a handful of galaxies with stellar masses $>10^{11.0}$. The chains and tadpoles, however, are a subsample of the clumpy population and are almost exclusively low mass systems with very few/none high mass ($>10^{10.5}$) systems. This low mass preference for chains and tadpoles is also seen in the Elmegreen sample. All of the clumpy classes are preferentially in the lower left star-forming region of the UVJ diagram, but there is a population of clumpy galaxies that extend into the dusty region and even a few in the quiescent region. As expected, no clumpy structures are observed with radii below 1kpc and are mostly in large R_{eff} systems. At $z\sim 2$, 1kpc is roughly the resolution limit of our observations and thus classifiers are unable to visually distinguish clumps and substructures below this size. As pointed out earlier, the systems with the largest radii are almost exclusively clumpy systems meaning that the underlying rest frame optical light (F160W) is extended in these sources with clumpy star-forming regions in rest frame NUV light (F775W).

Clumpy Galaxies
1278 (46.9%)

	$\log M_{\text{stellar}}$ 9.4-10.0	$\log M_{\text{stellar}}$ 10-11	$\log M_{\text{stellar}}$ >11
$2.6 \leq z < 3.0$ (126) (53.2%)	70 (51.5%)	55 (59.1%)	1 (12.5%)
$2.2 \leq z < 2.6$ (115) (42.9%)	68 (44.4%)	43 (43.9%)	4 (23.5%)
$1.8 \leq z < 2.2$ (139) (41.9%)	68 (38.6%)	65 (48.5%)	6 (27.3%)
$1.4 \leq z < 1.8$ (233) (43.9%)	151 (47.6%)	75 (40.8%)	7 (23.3%)
$1.0 \leq z < 1.4$ (325) (51.1%)	190 (53.1%)	116 (48.1%)	19 (51.4%)
$0.5 \leq z < 1.0$ (340) (47.0%)	206 (54.6%)	121 (39.5%)	13 (32.5%)
Total: 1278 (46.9%)	753 (49.6%)	475 (45.0%)	50 (32.5%)

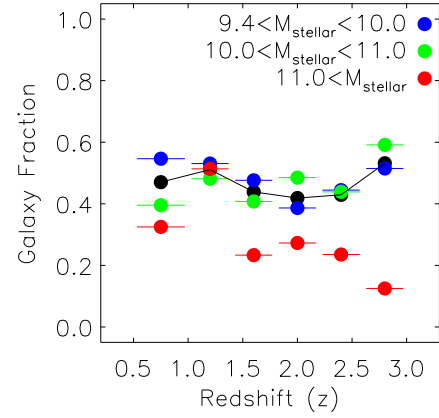


Figure 1.12: Clumpy Galaxy Fractions in Mass and Redshift Bins. The number of galaxies visually classified as clumpy in a given mass and redshift bin. The percentages given are the fraction of clumpy galaxies from the total number of galaxies in that mass and redshift bin. Roughly half of lower mass galaxies are clumpy across all redshifts. Higher mass galaxies are not clumpy at high redshift but the clumpy fraction increases to nearly 40% at $z=0.5$.

Chain Galaxies
100 (3.7%)

	$\log M_{\text{stellar}}$ 9.4-10.0	$\log M_{\text{stellar}}$ 10-11	$\log M_{\text{stellar}}$ >11
$2.6 \leq z < 3.0$ (16) (6.8%)	10 (7.4%)	5 (5.4%)	1 (12.5%)
$2.2 \leq z < 2.6$ (11) (4.1%)	8 (5.2%)	3 (3.1%)	0 (0.0%)
$1.8 \leq z < 2.2$ (13) (3.9%)	11 (6.2%)	2 (1.5%)	0 (0.0%)
$1.4 \leq z < 1.8$ (24) (4.5%)	18 (5.7%)	5 (2.7%)	1 (3.3%)
$1.0 \leq z < 1.4$ (18) (2.8%)	18 (5.0%)	0 (0.0%)	0 (0.0%)
$0.5 \leq z < 1.0$ (18) (2.5%)	15 (4.0%)	3 (1.0%)	0 (0.0%)
Total: 100 (3.7%)	80 (5.3%)	18 (1.7%)	2 (1.3%)

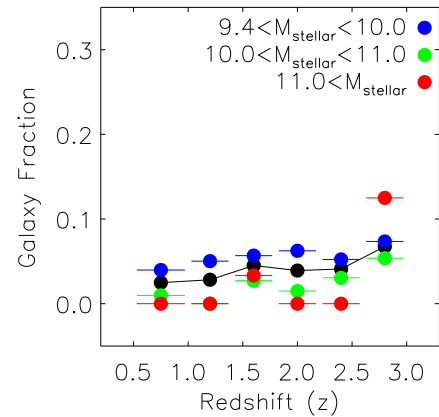


Figure 1.13: Chain Galaxy Fractions in Mass and Redshift Bins. The number of galaxies visually classified as chains in a given mass and redshift bin. The percentages given are the fraction of chain galaxies from the total number of galaxies in that mass and redshift bin. Chains are a small population but are predominantly low and moderate mass systems and are slightly more common at higher redshifts.

Table 1.11: Clumpy Galaxy Fractions Evolution with Redshift in Mass and sSFR Bins

	Quiescent sSFR < -0.9			Transitional -0.9 ≤ sSFR < -0.3			Star Forming -0.3 ≤ sSFR < 0.95			High Star Forming 0.95 ≤ sSFR		
	$M_{9.4-10.0}^{stellar}$	$M_{10-11}^{stellar}$	$M_{>11}^{stellar}$	$M_{9.4-10.0}^{stellar}$	$M_{10-11}^{stellar}$	$M_{>11}^{stellar}$	$M_{9.4-10.0}^{stellar}$	$M_{10-11}^{stellar}$	$M_{>11}^{stellar}$	$M_{9.4-10.0}^{stellar}$	$M_{10-11}^{stellar}$	$M_{>11}^{stellar}$
2.6 ≤ z < 3.0 (126)	0 (0.0%)	0 (0.0%)	0 (0.0%)	0 (0.0%)	2 (1.6%)	1 (0.8%)	62 (49.2%)	49 (38.9%)	0 (0.0%)	8 (6.3%)	4 (3.2%)	0 (0.0%)
2.2 ≤ z < 2.6 (115)	0 (0.0%)	1 (0.9%)	0 (0.0%)	2 (1.7%)	2 (1.7%)	2 (1.7%)	59 (51.3%)	40 (34.8%)	2 (1.7%)	7 (6.1%)	0 (0.0%)	0 (0.0%)
1.8 ≤ z < 2.2 (139)	0 (0.0%)	1 (0.7%)	2 (1.4%)	0 (0.0%)	1 (0.7%)	3 (2.2%)	58 (41.7%)	58 (41.7%)	1 (0.7%)	10 (7.2%)	5 (3.6%)	0 (0.0%)
1.4 ≤ z < 1.8 (233)	0 (0.0%)	1 (0.4%)	2 (0.9%)	2 (0.9%)	2 (0.9%)	4 (1.7%)	136 (58.4%)	62 (26.6%)	1 (0.4%)	13 (5.6%)	10 (4.3%)	0 (0.0%)
1.0 ≤ z < 1.4 (325)	0 (0.0%)	6 (1.8%)	8 (2.5%)	2 (0.6%)	19 (5.8%)	11 (3.4%)	168 (51.7%)	85 (26.2%)	0 (0.0%)	20 (6.2%)	6 (1.8%)	0 (0.0%)
0.5 ≤ z < 1.0 (340)	3 (0.9%)	10 (2.9%)	5 (1.5%)	2 (0.6%)	18 (5.3%)	3 (0.9%)	177 (52.1%)	84 (24.7%)	5 (1.5%)	24 (7.1%)	9 (2.6%)	0 (0.0%)
Total: 1278	3	19	17	8	44	24	660	378	9	82	34	0

Table 1.12: Clumpy Galaxy Fractions Evolution with Redshift in Mass and R_{eff} Bins

	Compact $R_{eff} < 1\text{kpc}$			Moderate $1\text{kpc} \leq R_{eff} < 3\text{kpc}$			Extended $3\text{kpc} \leq R_{eff}$		
	$M_{9.4-10.0}^{stellar}$	$M_{10-11}^{stellar}$	$M_{>11}^{stellar}$	$M_{9.4-10.0}^{stellar}$	$M_{10-11}^{stellar}$	$M_{>11}^{stellar}$	$M_{9.4-10.0}^{stellar}$	$M_{10-11}^{stellar}$	$M_{>11}^{stellar}$
2.6 ≤ z < 3.0 (126)	0 (0.0%)	0 (0.0%)	0 (0.0%)	44 (34.9%)	24 (19.0%)	0 (0.0%)	26 (20.6%)	31 (24.6%)	1 (0.8%)
2.2 ≤ z < 2.6 (115)	0 (0.0%)	0 (0.0%)	0 (0.0%)	38 (33.0%)	16 (13.9%)	1 (0.9%)	30 (26.1%)	27 (23.5%)	3 (2.6%)
1.8 ≤ z < 2.2 (139)	0 (0.0%)	0 (0.0%)	0 (0.0%)	36 (25.9%)	13 (9.4%)	2 (1.4%)	32 (23.0%)	52 (37.4%)	4 (2.9%)
1.4 ≤ z < 1.8 (233)	0 (0.0%)	0 (0.0%)	0 (0.0%)	57 (24.5%)	22 (9.4%)	2 (0.9%)	94 (40.3%)	53 (22.7%)	5 (2.1%)
1.0 ≤ z < 1.4 (325)	0 (0.0%)	0 (0.0%)	0 (0.0%)	61 (18.8%)	33 (10.2%)	0 (0.0%)	129 (39.7%)	83 (25.5%)	19 (5.8%)
0.5 ≤ z < 1.0 (340)	1 (0.3%)	0 (0.0%)	0 (0.0%)	66 (19.4%)	28 (8.2%)	0 (0.0%)	139 (40.9%)	93 (27.4%)	13 (3.8%)
Total: 1278	1	0	0	302	136	5	450	339	45

Table 1.13: Chain Galaxy Fractions Evolution with Redshift in Mass and sSFR Bins

	Quiescent sSFR < -0.9				Transitional -0.9 ≤ sSFR < -0.3				Star Forming -0.3 ≤ sSFR < 0.95				High Star Forming 0.95 ≤ sSFR			
	$M_{9.4-10.0}^{stellar}$	$M_{10-11}^{stellar}$	$M_{>11}^{stellar}$		$M_{9.4-10.0}^{stellar}$	$M_{10-11}^{stellar}$	$M_{>11}^{stellar}$		$M_{9.4-10.0}^{stellar}$	$M_{10-11}^{stellar}$	$M_{>11}^{stellar}$		$M_{9.4-10.0}^{stellar}$	$M_{10-11}^{stellar}$	$M_{>11}^{stellar}$	
2.6 ≤ z < 3.0 (16)	0 (0.0%)	0 (0.0%)	0 (0.0%)	0 (6.2%)	0 (0.0%)	0 (0.0%)	1 (6.2%)	9 (56.2%)	5 (31.2%)	0 (0.0%)	0 (0.0%)	1 (6.2%)	0 (0.0%)	0 (0.0%)	0 (0.0%)	
2.2 ≤ z < 2.6 (11)	0 (0.0%)	0 (0.0%)	0 (0.0%)	0 (0.0%)	0 (0.0%)	0 (0.0%)	0 (0.0%)	7 (63.6%)	3 (27.3%)	0 (0.0%)	0 (0.0%)	1 (9.1%)	0 (0.0%)	0 (0.0%)	0 (0.0%)	
1.8 ≤ z < 2.2 (13)	0 (0.0%)	0 (0.0%)	0 (0.0%)	0 (0.0%)	0 (0.0%)	0 (0.0%)	0 (0.0%)	11 (84.6%)	2 (15.4%)	0 (0.0%)	0 (0.0%)	0 (0.0%)	0 (0.0%)	0 (0.0%)	0 (0.0%)	
1.4 ≤ z < 1.8 (24)	0 (0.0%)	0 (0.0%)	0 (0.0%)	1 (4.2%)	0 (0.0%)	0 (0.0%)	1 (4.2%)	16 (66.7%)	4 (16.7%)	0 (0.0%)	0 (0.0%)	2 (8.3%)	1 (4.2%)	0 (0.0%)	0 (0.0%)	
1.0 ≤ z < 1.4 (18)	0 (0.0%)	0 (0.0%)	0 (0.0%)	0 (0.0%)	0 (0.0%)	0 (0.0%)	0 (0.0%)	15 (83.3%)	0 (0.0%)	0 (0.0%)	0 (0.0%)	3 (16.7%)	0 (0.0%)	0 (0.0%)	0 (0.0%)	
0.5 ≤ z < 1.0 (18)	0 (0.0%)	0 (0.0%)	0 (0.0%)	0 (0.0%)	0 (0.0%)	0 (0.0%)	0 (0.0%)	12 (66.7%)	3 (16.7%)	0 (0.0%)	0 (0.0%)	3 (16.7%)	0 (0.0%)	0 (0.0%)	0 (0.0%)	
Total: 100	0	0	0	2	0	0	2	70	17	0	0	10	1	0	0	

Table 1.14: Chain Galaxy Fractions Evolution with Redshift in Mass and R_{eff} Bins

	Compact $R_{eff} < 1\text{kpc}$			Moderate $1\text{kpc} \leq R_{eff} < 3\text{kpc}$			Extended $3\text{kpc} \leq R_{eff}$		
	$M_{9.4-10.0}^{stellar}$	$M_{10-11}^{stellar}$	$M_{>11}^{stellar}$	$M_{9.4-10.0}^{stellar}$	$M_{10-11}^{stellar}$	$M_{>11}^{stellar}$	$M_{9.4-10.0}^{stellar}$	$M_{10-11}^{stellar}$	$M_{>11}^{stellar}$
2.6 ≤ z < 3.0 (16)	0 (0.0%)	0 (0.0%)	0 (0.0%)	3 (18.8%)	0 (0.0%)	0 (0.0%)	7 (43.8%)	5 (31.2%)	1 (6.2%)
2.2 ≤ z < 2.6 (11)	0 (0.0%)	0 (0.0%)	0 (0.0%)	4 (36.4%)	0 (0.0%)	0 (0.0%)	4 (36.4%)	3 (27.3%)	0 (0.0%)
1.8 ≤ z < 2.2 (13)	0 (0.0%)	0 (0.0%)	0 (0.0%)	1 (7.7%)	0 (0.0%)	0 (0.0%)	10 (76.9%)	2 (15.4%)	0 (0.0%)
1.4 ≤ z < 1.8 (24)	0 (0.0%)	0 (0.0%)	0 (0.0%)	6 (25.0%)	0 (0.0%)	0 (0.0%)	12 (50.0%)	5 (20.8%)	1 (4.2%)
1.0 ≤ z < 1.4 (18)	0 (0.0%)	0 (0.0%)	0 (0.0%)	4 (22.2%)	0 (0.0%)	0 (0.0%)	14 (77.8%)	0 (0.0%)	0 (0.0%)
0.5 ≤ z < 1.0 (18)	0 (0.0%)	0 (0.0%)	0 (0.0%)	7 (38.9%)	0 (0.0%)	0 (0.0%)	8 (44.4%)	3 (16.7%)	0 (0.0%)
Total: 100	0	0	0	25	0	0	55	18	2

Table 1.15: Tadpole Galaxy Fractions Evolution with Redshift in Mass and sSFR Bins

	sSFR											
	Quiescent sSFR < -0.9			Transitional -0.9 ≤ sSFR < -0.3			Star Forming -0.3 ≤ sSFR < 0.95			High Star Forming 0.95 ≤ sSFR		
	$M_{stellar}$ 9.4-10.0	$M_{stellar}$ 10-11	$M_{stellar}$ >11	$M_{stellar}$ 9.4-10.0	$M_{stellar}$ 10-11	$M_{stellar}$ >11	$M_{stellar}$ 9.4-10.0	$M_{stellar}$ 10-11	$M_{stellar}$ >11	$M_{stellar}$ 9.4-10.0	$M_{stellar}$ 10-11	$M_{stellar}$ >11
2.6 ≤ z < 3.0 (27)	0 (0.0%)	0 (0.0%)	0 (0.0%)	0 (0.0%)	0 (0.0%)	0 (0.0%)	16 (59.3%)	7 (25.9%)	0 (0.0%)	3 (11.1%)	1 (3.7%)	0 (0.0%)
2.2 ≤ z < 2.6 (21)	0 (0.0%)	0 (0.0%)	1 (4.8%)	0 (0.0%)	0 (0.0%)	0 (0.0%)	14 (66.7%)	4 (19.0%)	1 (4.8%)	1 (4.8%)	0 (0.0%)	0 (0.0%)
1.8 ≤ z < 2.2 (22)	1 (4.5%)	0 (0.0%)	1 (4.5%)	0 (0.0%)	1 (4.5%)	0 (0.0%)	9 (40.9%)	7 (31.8%)	1 (4.5%)	2 (9.1%)	0 (0.0%)	0 (0.0%)
1.4 ≤ z < 1.8 (39)	0 (0.0%)	0 (0.0%)	0 (0.0%)	2 (5.1%)	0 (0.0%)	0 (0.0%)	27 (69.2%)	6 (15.4%)	0 (0.0%)	3 (7.7%)	1 (2.6%)	0 (0.0%)
1.0 ≤ z < 1.4 (38)	0 (0.0%)	0 (0.0%)	0 (0.0%)	2 (5.3%)	0 (0.0%)	0 (0.0%)	26 (68.4%)	4 (10.5%)	0 (0.0%)	4 (10.5%)	2 (5.3%)	0 (0.0%)
0.5 ≤ z < 1.0 (22)	1 (4.5%)	0 (0.0%)	1 (4.5%)	2 (9.1%)	0 (0.0%)	0 (0.0%)	12 (54.5%)	3 (13.6%)	0 (0.0%)	3 (13.6%)	0 (0.0%)	0 (0.0%)
Total: 169	2	0	3	6	1	104	31	2	16	4	0	0

Table 1.16: Tadpole Galaxy Fractions Evolution with Redshift in Mass and R_{eff} Bins

	R_{eff} (F160W)											
	Compact $R_{eff} < 1\text{kpc}$			Moderate $1\text{kpc} \leq R_{eff} < 3\text{kpc}$			Extended $3\text{kpc} \leq R_{eff}$					
	$M_{stellar}$ 9.4-10.0	$M_{stellar}$ 10-11	$M_{stellar}$ >11	$M_{stellar}$ 9.4-10.0	$M_{stellar}$ 10-11	$M_{stellar}$ >11	$M_{stellar}$ 9.4-10.0	$M_{stellar}$ 10-11	$M_{stellar}$ >11	$M_{stellar}$ 9.4-10.0	$M_{stellar}$ 10-11	$M_{stellar}$ >11
2.6 ≤ z < 3.0 (27)	1 (3.7%)	0 (0.0%)	0 (0.0%)	9 (33.3%)	4 (14.8%)	0 (0.0%)	9 (33.3%)	4 (14.8%)	0 (0.0%)	0 (0.0%)	0 (0.0%)	0 (0.0%)
2.2 ≤ z < 2.6 (21)	0 (0.0%)	0 (0.0%)	13 (61.9%)	13 (61.9%)	1 (4.8%)	0 (0.0%)	3 (14.3%)	3 (14.3%)	1 (4.8%)	1 (4.8%)	0 (0.0%)	0 (0.0%)
1.8 ≤ z < 2.2 (22)	0 (0.0%)	0 (0.0%)	9 (40.9%)	9 (40.9%)	2 (9.1%)	0 (0.0%)	4 (18.2%)	5 (22.7%)	0 (0.0%)	2 (9.1%)	0 (0.0%)	0 (0.0%)
1.4 ≤ z < 1.8 (39)	0 (0.0%)	0 (0.0%)	18 (46.2%)	18 (46.2%)	4 (10.3%)	0 (0.0%)	12 (30.8%)	5 (12.8%)	0 (0.0%)	0 (0.0%)	0 (0.0%)	0 (0.0%)
1.0 ≤ z < 1.4 (38)	0 (0.0%)	0 (0.0%)	13 (34.2%)	13 (34.2%)	4 (10.5%)	0 (0.0%)	17 (44.7%)	4 (10.5%)	0 (0.0%)	0 (0.0%)	0 (0.0%)	0 (0.0%)
0.5 ≤ z < 1.0 (22)	0 (0.0%)	0 (0.0%)	10 (45.5%)	10 (45.5%)	1 (4.5%)	0 (0.0%)	7 (31.8%)	4 (18.2%)	0 (0.0%)	0 (0.0%)	0 (0.0%)	0 (0.0%)
Total: 169	1	0	72	16	0	52	25	3	16	4	0	0

Tadpole Galaxies

	169 (6.2%)		
	$\log M_{\text{stellar}}$ 9.4-10.0	$\log M_{\text{stellar}}$ 10-11	$\log M_{\text{stellar}}$ >11
$2.6 \leq z < 3.0$ (27) (11.4%)	19 (14.0%)	8 (8.6%)	0 (0.0%)
$2.2 \leq z < 2.6$ (21) (7.8%)	16 (10.5%)	4 (4.1%)	1 (5.9%)
$1.8 \leq z < 2.2$ (22) (6.6%)	13 (7.4%)	7 (5.2%)	2 (9.1%)
$1.4 \leq z < 1.8$ (39) (7.3%)	30 (9.5%)	9 (4.9%)	0 (0.0%)
$1.0 \leq z < 1.4$ (38) (6.0%)	30 (8.4%)	8 (3.3%)	0 (0.0%)
$0.5 \leq z < 1.0$ (22) (3.0%)	17 (4.5%)	5 (1.6%)	0 (0.0%)
Total: 169 (6.2%)	125 (8.2%)	41 (3.9%)	3 (1.9%)

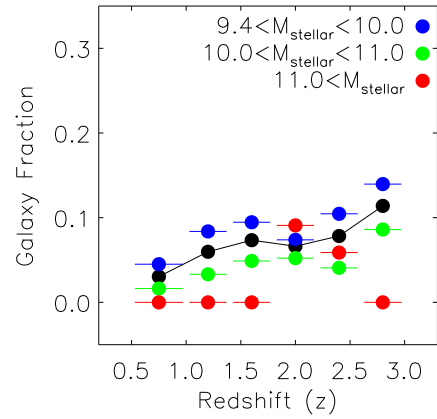


Figure 1.14: Tadpole Galaxy Fractions in Mass and Redshift Bins. The number of galaxies visually classified as tadpoles in a given mass and redshift bin. The percentages given are the fraction of tadpole galaxies from the total number of galaxies in that mass and redshift bin. Tadpoles are predominantly low and moderate mass systems and are more common at higher redshifts.

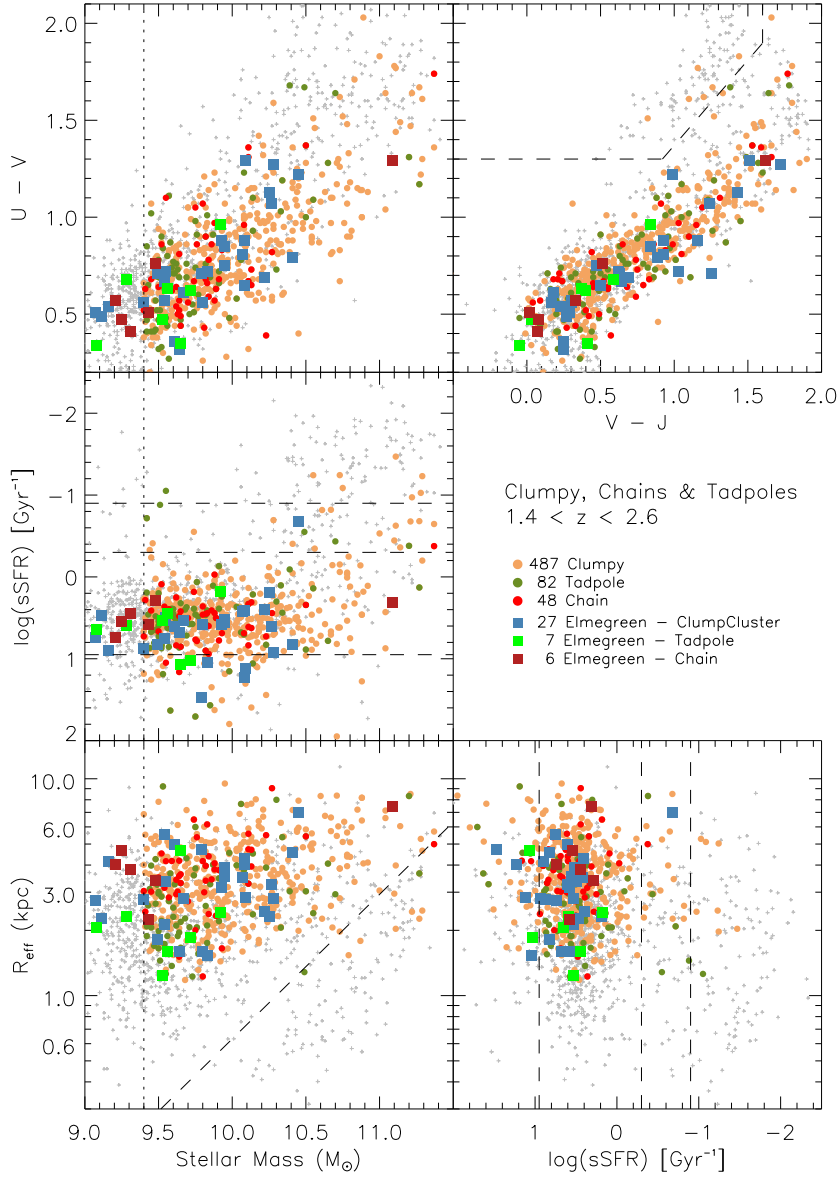


Figure 1.15: Global Properties of $z \sim 2$ Clumpy, Tadpole & Chain Galaxies in GOODS-South and Elmegreen UDF Samples. Galaxies visually identified as clumpy, tadpoles, or chains in our $z \sim 2$ GOODS-South catalog are colored as are the galaxies classified by Elmegreen in his UDF subsample. Clumpy, tadpole and chain galaxies are predominantly low mass systems that lie along the star-forming sequence. There is also a population of clumpy galaxies that exist at higher mass and are predominantly in the dusty star-forming region.

1.3.3 Asymmetric, Irregular, & Merger/Interacting Galaxies

The MWGunified visual classification system includes flags for irregular morphologies, asymmetric light distributions in F160W as well as a section to classify mergers, interactions, and nearby companions. These classifications and flags allow us to study the distribution of these interacting and dynamically unsettled systems. Using the combined metric indices we introduce a 50% cutoff in selecting galaxies as asymmetric, merger/interacting, and irregular. An object is considered asymmetric if 50% or more of the classifiers (in the ‘all fully’ catalog) flag the object as such. We combine the mergers and interacting flags into a single metric and define objects as undergoing an interaction/merger if 50% of the classifiers flag it as either a merger or interacting (either within or beyond the object’s segmentation map). Lastly, irregular galaxies are identified using the irregularity metric defined in Section 2.5 with a 50% cutoff.

Figures 1.16 and 1.17 show the distribution of asymmetric and merging/interacting galaxies (respectively) across our redshift range in different mass bins. Figure 1.16 shows the dramatic drop in the fraction of low and moderate mass galaxies that are classified as asymmetric from 60-70% at $z > 2.5$ to 20-30% by $z = 0.5$. This is inline with previous studies (Mortlock et al. (2013), Conselice et al. (2005), Papovich et al. (2005), Cameron et al. (2011), Szomoru et al. (2011)) that found the $z \sim 2$ universe to be dominated by low mass asymmetric unsettled systems (often called peculiar). At higher redshifts, these peculiar asymmetric galaxies represent the large fraction of still forming unsettled systems (Conselice et al., 2008). By lower redshift, systems at these masses have settled

and become more regular as is demonstrated by the dropping asymmetry fraction. It should be noted that the fraction of high mass galaxies ($M_{stellar} \geq 10^{11.0}$) with asymmetric visual classification flags is relative flat at 20% for all but the highest redshift bin. There is a suggestion of increasing asymmetry at higher redshifts but the low number of objects prevents us from making a strong claim of evolving asymmetry in this high mass bin. This low fraction of asymmetric systems at high masses is inline with previous studies that find a significant fraction of massive galaxies at $z > 2$ are morphologically relaxed and resemble Hubble sequence systems (Conselice et al., 2011b). These massive systems are thought to have built up most of their mass by this $z \sim 2$ epoch (Mortlock et al., 2013) and have settled before their low mass counterparts. Our high mass populations at $z \sim 2$ show low amounts of asymmetry, irregularity, and are undergoing fewer mergers/interactions than their low mass counterparts. In addition, our high mass galaxies are dominated by quenched low star-forming systems - in good agreement with Bundy et al. (2006) that showed that massive galaxies finish their high star-forming periods and are quenched at earlier redshift than less massive systems. All of which is inline with models of morphological downsizing where massive galaxies settle morphologically and quench their star formation before their low mass counterparts.

Looking at Tables 1.17 and 1.18 we see that the majority of extended objects at all radii and masses (particularly low and intermediate masses) are asymmetric. Also, asymmetric galaxies seem to preferentially be star-forming systems. These trends are true for all mass bins but in general, the greatest fraction of asymmetric galaxies lies in the low mass bins ($10^{9.4} \leq M_{stellar} < 10^{10.0}$). Tables 1.19 and 1.20 illustrate that merg-

ing/interacting systems seem to occupy similar populations of galaxies as asymmetric galaxies. Merging/interacting systems are predominantly lower and moderate mass systems ($10^{9.4} \leq M_{\text{stellar}} < 10^{10.0}$ and $10^{10.0} \leq M_{\text{stellar}} < 10^{11.0}$). Interacting systems tend to have larger radii on average - an expected result if light from the nearby interacting object is not perfectly masked when GALFIT is run. The fraction of mergers averages $\sim 20\%$ and is lower than that of asymmetric systems. Figure 1.17 illustrates how this fraction varies for the different mass bins. The interactions are primarily in the low and moderate mass systems which increase modestly from $\sim 15\%$ at $z=0.5$ to $\sim 25\%$ at $z=3.0$. Using Table 1.18 to focus on the low and moderate mass mergers with extended radii, we see a stronger evolution in interaction fraction with redshift. Among extended low and moderate mass galaxies, 36 and 38% of galaxies are undergoing mergers at $z=2.6-3.0$ and $2.2-2.6$, respectively. By $z=0.5-1.0$ and $1.0-1.4$ this fraction of extended objects with lower and moderate masses undergoing mergers drops to 24 and 28% respectively. While the merging/interacting systems are predominantly star-forming galaxies, they do not tend to be the highest star-forming systems - a result one would expect if the mergers/interactions were between gas rich systems that would trigger bursting star formation during the interaction process.

Figure 1.18 highlights the $z\sim 2$ population of interacting, irregular, and asymmetric systems and allows us to further probe where these unsettled systems lie in comparison to the full $z\sim 2$ population. As expected, all three populations lie strongly in the star-forming sequence both in the UVJ color-color diagram and in the sSFR diagrams. There are a handful of objects (mostly interactions) that lie in quiescent

Asymmetric Galaxies
1155 (42.4%)

	$\log M_{\text{stellar}}$ 9.4-10.0	$\log M_{\text{stellar}}$ 10-11	$\log M_{\text{stellar}}$ >11
$2.6 \leq z < 3.0$ (149) (62.9%)	82 (60.3%)	62 (66.7%)	5 (62.5%)
$2.2 \leq z < 2.6$ (144) (53.7%)	91 (59.5%)	49 (50.0%)	4 (23.5%)
$1.8 \leq z < 2.2$ (173) (52.1%)	94 (53.4%)	72 (53.7%)	7 (31.8%)
$1.4 \leq z < 1.8$ (235) (44.3%)	158 (49.8%)	71 (38.6%)	6 (20.0%)
$1.0 \leq z < 1.4$ (255) (40.1%)	177 (49.4%)	71 (29.5%)	7 (18.9%)
$0.5 \leq z < 1.0$ (199) (27.5%)	131 (34.7%)	62 (20.3%)	6 (15.0%)
Total: 1155 (42.4%)	733 (48.3%)	387 (36.6%)	35 (22.7%)

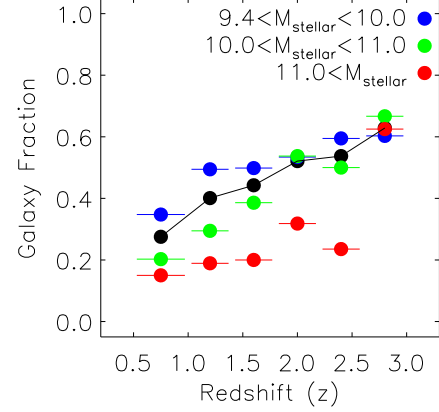


Figure 1.16: Asymmetric Galaxy Fractions in Mass and Redshift Bins. The number of galaxies visually classified as Asymmetric in a given mass and redshift bin. The percentages given are the fraction of asymmetric galaxies from the total number of galaxies in that mass and redshift bin. Asymmetric galaxies are primarily low and mid mass systems and are more common at higher redshifts. The majority of galaxies at $z > 2.5$ are classified as asymmetric.

regions. The asymmetric systems fully populate the star-forming sequence while the irregular and interacting populations are mostly absent from the dusty region of the UVJ diagram. At a given V-J, the interacting systems have slightly higher U-V values within the star-forming sequence. The lack of merging objects in the dusty area of the UVJ diagram is somewhat surprising as it is expected that mergers between gas rich systems at $z \sim 2$ will be dusty systems. Irregular objects are preferential lower mass and larger radii systems within the star-forming sequence.

Table 1.17: Asymmetric Galaxy Fractions Evolution with Redshift in Mass and sSFR Bins

	Quiescent sSFR < -0.9			Transitional -0.9 ≤ sSFR < -0.3			Star Forming -0.3 ≤ sSFR < 0.95			High Star Forming 0.95 ≤ sSFR		
	$M_{stellar}^{9.4-10.0}$	$M_{stellar}^{10-11}$	$M_{stellar}^{>11}$	$M_{stellar}^{9.4-10.0}$	$M_{stellar}^{10-11}$	$M_{stellar}^{>11}$	$M_{stellar}^{9.4-10.0}$	$M_{stellar}^{10-11}$	$M_{stellar}^{>11}$	$M_{stellar}^{9.4-10.0}$	$M_{stellar}^{10-11}$	$M_{stellar}^{>11}$
2.6 ≤ z < 3.0 (149)	0 (0.0%)	0 (0.0%)	4 (2.7%)	0 (0.0%)	2 (1.3%)	1 (0.7%)	70 (47.0%)	53 (35.6%)	0 (0.0%)	12 (8.1%)	7 (4.7%)	0 (0.0%)
2.2 ≤ z < 2.6 (144)	2 (1.4%)	0 (0.0%)	2 (1.4%)	2 (1.4%)	2 (1.4%)	0 (0.0%)	77 (53.5%)	46 (31.9%)	2 (1.4%)	10 (6.9%)	1 (0.7%)	0 (0.0%)
1.8 ≤ z < 2.2 (173)	1 (0.6%)	5 (2.9%)	1 (0.6%)	1 (0.6%)	3 (1.7%)	3 (1.7%)	84 (48.6%)	56 (32.4%)	3 (1.7%)	8 (4.6%)	8 (4.6%)	0 (0.0%)
1.4 ≤ z < 1.8 (235)	0 (0.0%)	3 (1.3%)	1 (0.4%)	4 (1.7%)	7 (3.0%)	4 (1.7%)	138 (58.7%)	49 (20.9%)	1 (0.4%)	16 (6.8%)	12 (5.1%)	0 (0.0%)
1.0 ≤ z < 1.4 (255)	0 (0.0%)	6 (2.4%)	4 (1.6%)	2 (0.8%)	5 (2.0%)	3 (1.2%)	154 (60.4%)	54 (21.2%)	0 (0.0%)	21 (8.2%)	6 (2.4%)	0 (0.0%)
0.5 ≤ z < 1.0 (199)	2 (1.0%)	4 (2.0%)	4 (2.0%)	4 (2.0%)	9 (4.5%)	1 (0.5%)	109 (54.8%)	44 (22.1%)	1 (0.5%)	16 (8.0%)	5 (2.5%)	0 (0.0%)
Total: 1155	5	18	16	13	28	12	632	302	7	83	39	0

Table 1.18: Asymmetric Galaxy Fractions Evolution with Redshift in Mass and R_{eff} Bins

	Compact $R_{eff} < 1kpc$			Moderate $1kpc \leq R_{eff} < 3kpc$			Extended $3kpc \leq R_{eff}$		
	$M_{stellar}^{9.4-10.0}$	$M_{stellar}^{10-11}$	$M_{stellar}^{>11}$	$M_{stellar}^{9.4-10.0}$	$M_{stellar}^{10-11}$	$M_{stellar}^{>11}$	$M_{stellar}^{9.4-10.0}$	$M_{stellar}^{10-11}$	$M_{stellar}^{>11}$
2.6 ≤ z < 3.0 (149)	2 (1.3%)	0 (0.0%)	0 (0.0%)	57 (38.3%)	28 (18.8%)	2 (1.3%)	23 (15.4%)	34 (22.8%)	3 (2.0%)
2.2 ≤ z < 2.6 (144)	2 (1.4%)	0 (0.0%)	0 (0.0%)	58 (40.3%)	23 (16.0%)	2 (1.4%)	31 (21.5%)	26 (18.1%)	2 (1.4%)
1.8 ≤ z < 2.2 (173)	0 (0.0%)	1 (0.6%)	0 (0.0%)	64 (37.0%)	17 (9.8%)	1 (0.6%)	30 (17.3%)	54 (31.2%)	6 (3.5%)
1.4 ≤ z < 1.8 (235)	1 (0.4%)	0 (0.0%)	0 (0.0%)	72 (30.6%)	19 (8.1%)	0 (0.0%)	85 (36.2%)	52 (22.1%)	6 (2.6%)
1.0 ≤ z < 1.4 (255)	0 (0.0%)	1 (0.4%)	0 (0.0%)	69 (27.1%)	16 (6.3%)	1 (0.4%)	108 (42.4%)	54 (21.2%)	6 (2.4%)
0.5 ≤ z < 1.0 (199)	0 (0.0%)	0 (0.0%)	0 (0.0%)	45 (22.6%)	11 (5.5%)	0 (0.0%)	86 (43.2%)	51 (25.6%)	6 (3.0%)
Total: 1155	5	2	0	365	114	6	363	271	29

Table 1.19: Merger Galaxy Fractions Evolution with Redshift in Mass and sSFR Bins

	Quiescent sSFR < -0.9				Transitional -0.9 ≤ sSFR < -0.3				Star Forming -0.3 ≤ sSFR < 0.95				High Star Forming 0.95 ≤ sSFR			
	$M_{9.4-10.0}^{stellar}$	$M_{10-11}^{stellar}$	$M_{>11}^{stellar}$		$M_{9.4-10.0}^{stellar}$	$M_{10-11}^{stellar}$	$M_{>11}^{stellar}$		$M_{9.4-10.0}^{stellar}$	$M_{10-11}^{stellar}$	$M_{>11}^{stellar}$		$M_{9.4-10.0}^{stellar}$	$M_{10-11}^{stellar}$	$M_{>11}^{stellar}$	
2.6 ≤ z < 3.0 (55)	0 (0.0%)	0 (0.0%)	0 (0.0%)	0 (0.0%)	0 (0.0%)	2 (3.6%)	1 (1.8%)	22 (40.0%)	0 (0.0%)	0 (0.0%)	0 (0.0%)	5 (9.1%)	3 (5.5%)	0 (0.0%)		
2.2 ≤ z < 2.6 (64)	2 (3.1%)	0 (0.0%)	0 (0.0%)	1 (1.6%)	0 (0.0%)	0 (0.0%)	0 (0.0%)	35 (54.7%)	17 (26.6%)	2 (3.1%)	7 (10.9%)	0 (0.0%)	0 (0.0%)			
1.8 ≤ z < 2.2 (66)	0 (0.0%)	3 (4.5%)	0 (0.0%)	0 (0.0%)	0 (0.0%)	2 (3.0%)	2 (3.0%)	31 (47.0%)	23 (34.8%)	0 (0.0%)	6 (9.1%)	1 (1.5%)	0 (0.0%)			
1.4 ≤ z < 1.8 (100)	0 (0.0%)	5 (5.0%)	3 (3.0%)	3 (3.0%)	5 (5.0%)	0 (0.0%)	0 (0.0%)	56 (56.0%)	20 (20.0%)	0 (0.0%)	3 (3.0%)	5 (5.0%)	0 (0.0%)			
1.0 ≤ z < 1.4 (123)	1 (0.8%)	3 (2.4%)	0 (0.0%)	0 (0.0%)	6 (4.9%)	2 (1.6%)	2 (1.6%)	71 (57.7%)	26 (21.1%)	0 (0.0%)	11 (8.9%)	3 (2.4%)	0 (0.0%)			
0.5 ≤ z < 1.0 (110)	3 (2.7%)	2 (1.8%)	5 (4.5%)	2 (1.8%)	9 (8.2%)	1 (0.9%)	6 (0.9%)	52 (47.3%)	22 (20.0%)	2 (1.8%)	6 (5.5%)	6 (5.5%)	0 (0.0%)			
Total: 518	6	13	8	6	22	6	6	267	130	4	38	18	0			

 Table 1.20: Merger Galaxy Fractions Evolution with Redshift in Mass and R_{eff} Bins

	Compact R _{eff} < 1kpc				Moderate 1kpc ≤ R _{eff} < 3kpc				Extended 3kpc ≤ R _{eff}						
	$M_{9.4-10.0}^{stellar}$	$M_{10-11}^{stellar}$	$M_{>11}^{stellar}$		$M_{9.4-10.0}^{stellar}$	$M_{10-11}^{stellar}$	$M_{>11}^{stellar}$		$M_{9.4-10.0}^{stellar}$	$M_{10-11}^{stellar}$	$M_{>11}^{stellar}$		$M_{9.4-10.0}^{stellar}$	$M_{10-11}^{stellar}$	$M_{>11}^{stellar}$
2.6 ≤ z < 3.0 (55)	0 (0.0%)	0 (0.0%)	0 (0.0%)	0 (0.0%)	18 (32.7%)	11 (20.0%)	1 (1.8%)	9 (16.4%)	16 (29.1%)	0 (0.0%)	0 (0.0%)	0 (0.0%)			
2.2 ≤ z < 2.6 (64)	0 (0.0%)	0 (0.0%)	0 (0.0%)	29 (45.3%)	7 (10.9%)	0 (0.0%)	16 (25.0%)	16 (25.0%)	10 (15.6%)	2 (3.1%)	2 (3.1%)				
1.8 ≤ z < 2.2 (66)	1 (1.5%)	0 (0.0%)	0 (0.0%)	19 (28.8%)	6 (9.1%)	1 (1.5%)	17 (25.8%)	21 (31.8%)	21 (31.8%)	1 (1.5%)	1 (1.5%)				
1.4 ≤ z < 1.8 (100)	1 (1.0%)	1 (1.0%)	0 (0.0%)	23 (23.0%)	12 (12.0%)	3 (3.0%)	38 (38.0%)	22 (22.0%)	22 (22.0%)	0 (0.0%)	0 (0.0%)				
1.0 ≤ z < 1.4 (123)	0 (0.0%)	1 (0.8%)	0 (0.0%)	30 (24.4%)	14 (11.4%)	0 (0.0%)	53 (43.1%)	23 (18.7%)	23 (18.7%)	2 (1.6%)	2 (1.6%)				
0.5 ≤ z < 1.0 (110)	0 (0.0%)	0 (0.0%)	0 (0.0%)	23 (20.9%)	8 (7.3%)	0 (0.0%)	40 (36.4%)	31 (28.2%)	31 (28.2%)	8 (7.3%)	8 (7.3%)				
Total: 518	2	2	0	142	58	5	173	123	13						

Mergers/Interactions
518 (19.0%)

	$\log M_{\text{stellar}}$ 9.4-10.0	$\log M_{\text{stellar}}$ 10-11	$\log M_{\text{stellar}}$ >11
$2.6 \leq z < 3.0$ (55) (23.2%)	27 (19.9%)	27 (29.0%)	1 (12.5%)
$2.2 \leq z < 2.6$ (64) (23.9%)	45 (29.4%)	17 (17.3%)	2 (11.8%)
$1.8 \leq z < 2.2$ (66) (19.9%)	37 (21.0%)	27 (20.1%)	2 (9.1%)
$1.4 \leq z < 1.8$ (100) (18.8%)	62 (19.6%)	35 (19.0%)	3 (10.0%)
$1.0 \leq z < 1.4$ (123) (19.3%)	83 (23.2%)	38 (15.8%)	2 (5.4%)
$0.5 \leq z < 1.0$ (110) (15.2%)	63 (16.7%)	39 (12.7%)	8 (20.0%)
Total: 518 (19.0%)	317 (20.9%)	183 (17.3%)	18 (11.7%)

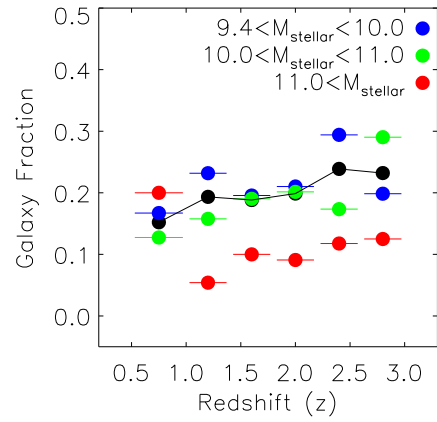


Figure 1.17: Merger/Interaction Galaxy Fractions in Mass and Redshift Bins. The number of galaxies visually classified as being a merger or having an interaction in a given mass and redshift bin. The percentages given are the fraction of interacting galaxies from the total number of galaxies in that mass and redshift bin. Interactions and mergers are more common at higher redshifts and are predominantly seen in low and mid mass systems.

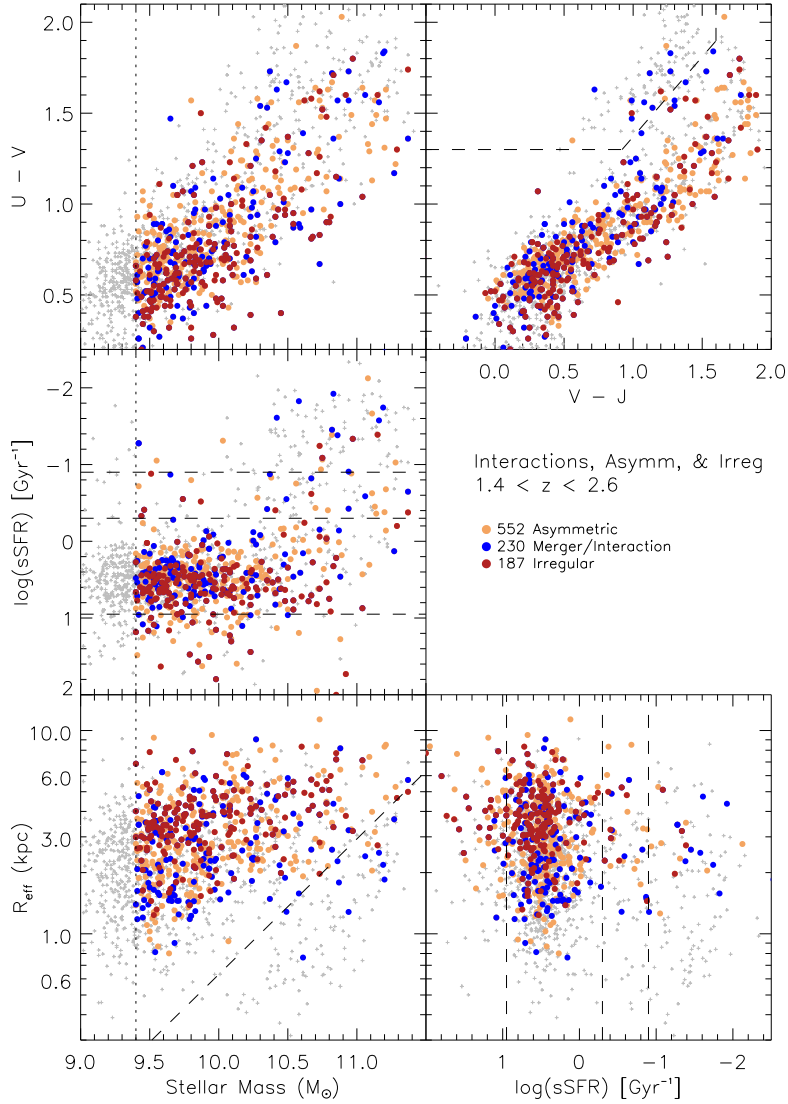


Figure 1.18: Global Properties of $z \sim 2$ Asymmetric, Irregular, and Interacting Galaxies in GOODS-South. Galaxies visually identified as asymmetric, irregular, or undergoing a merger/interaction in our $z \sim 2$ GOODS-South catalog are highlighted. All three populations lie strongly in the star-forming sequence both in the UVJ color-color diagram and in the sSFR diagrams. The asymmetric systems fully populate the star-forming sequence while the irregular and interacting populations are mostly absent from the dusty region of the UVJ diagram. The lack of merging objects in the dusty area of the UVJ diagram is somewhat surprising as it is expected that mergers between gas rich systems at $z \sim 2$ will be dusty systems.

1.4 Quiescent $z\sim 2$ populations

The nature of quiescent galaxies in the $z\sim 2$ Universe is a question of much debate in recent years and our large sample complete down to low masses is an ideal subset to use to probe this population. We identify quiescent systems using three independent methods: UVJ color-color cuts, sSFR cuts, and a $R_{eff}-M_{stellar}$ gap. The UVJ color-color diagram has been shown to effectively separate galaxies with red optical colors (U-V) that are truly quiescent from those that are star-forming systems reddened by dust. We adopt the divisions determined by Williams et al. (2009) for $z\sim 1$ systems. Figure 1.19 show this population of quiescent galaxies for the full $z\sim 2$ sample. Specific star formation rates (sSFR) can also be used to identify quiescent systems. We divide our sample into four regions as described in Section 3: a quiescent region, a star-forming region, a transitional region between them and a high star-forming region for the highest 10% of star-forming galaxies. Our dividing lines are in line with previous works and are illustrated in Figure 1.20. Lastly, we have identified galaxies from the $R_{eff}-M_{stellar}$ that lie in the compact, high mass region - an area we call the ‘red triangle’. Figure 1.21 shows the division made to isolate the ‘red triangle’.

Using sSFR to identify classes of $z\sim 2$ galaxies, Figure 1.20 shows that there is strong agreement between galaxies identified with sSFR in the star-forming region and those that lie on the star-forming sequence in the UVJ diagram. The galaxies with transitional sSFR all have red optical colors (U-V >1.0) and are distributed between the dusty region of the star-forming sequence and the quiescent region. Transitional

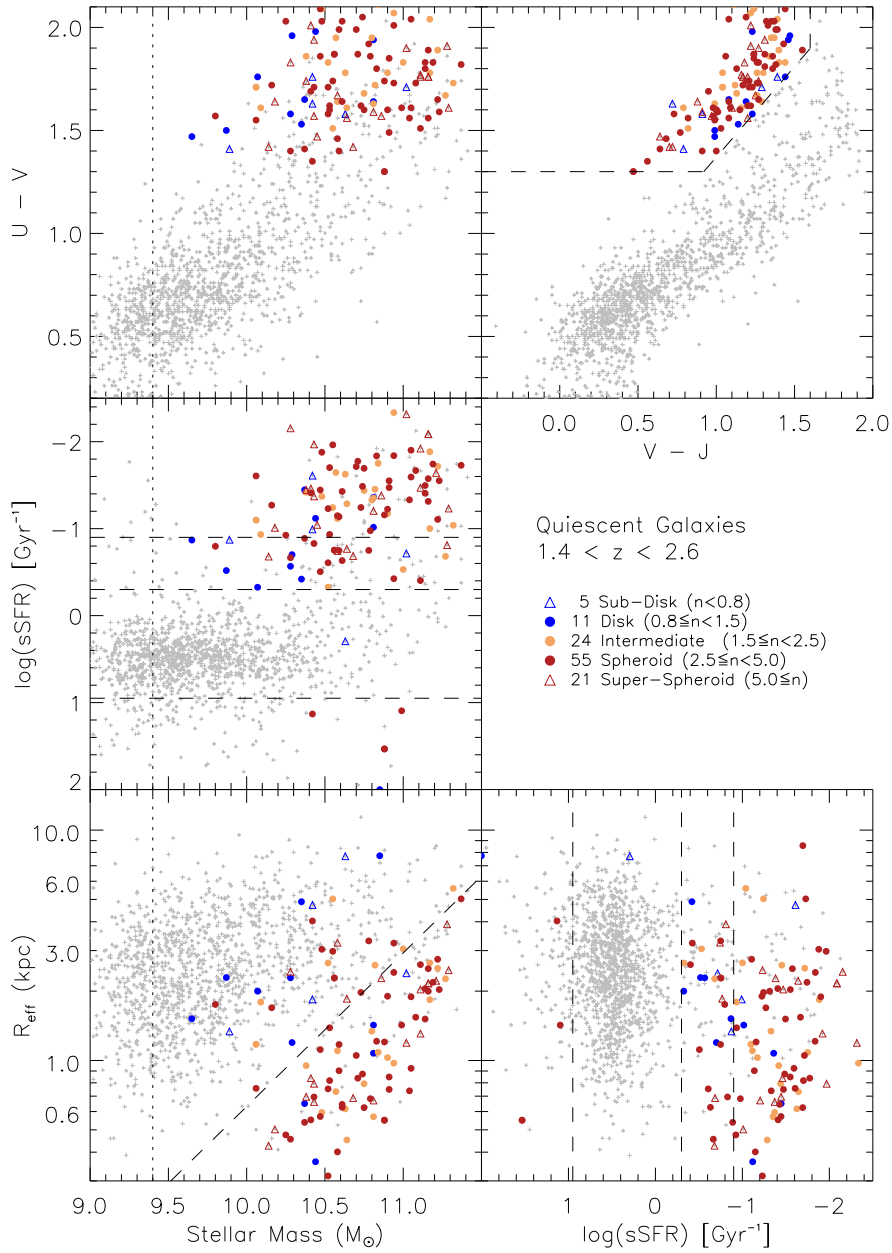


Figure 1.19: Global Properties of UVJ Selected Quiescent $z \sim 2$ Galaxies in GOODS-South. Galaxies are colored by their Sérsic indices. These UVJ selected quiescent galaxies correspond reasonably well with their galaxy morphologies with 66% of the quiescent systems having a Sérsic index > 2.5 and 87% have $n > 1.5$.

objects stretch the full mass range though they are predominantly high mass systems like the quiescent systems. Additionally these transitional galaxies lie in the boundary region of the size-mass relation. Galaxies identified as having transitional sSFR truly seem to be intermediate objects between star-forming blue systems and quiescent red systems. Galaxies with the highest specific star-forming rates tend to be at lower masses ($M_{stellar} < 10^{10.5}$) and for a given optical-NIR color (V-J) tend to have lower optical colors (U-V) causing them to lie at the bottom edge of the UVJ diagram. Indeed the UVJ diagram is striped along the star-forming sequence by sSFR with systems with the highest sSFR residing at the bottom of the sequence and low sSFR systems predominantly to the top of the sequence. The systems with high sSFR have extended radii (as measured in rest optical light from F160W) indicating that galaxies that are forming a lot of stars are imbedded in galaxies with extended mass profiles and not simply star-forming knots located at extended radii. Galaxies with quiescent sSFR lie almost exclusively in the UVJ quiescent region with only a handful of galaxies in the dusty region. 70% of galaxies identified as quiescent in sSFR also lie in the quiescent region of UVJ. This number increases to >95% if you include the transitional region of sSFR. We see this high level of agreement illustrated in Figure 1.19 with only a handful of the UVJ identified quiescent systems having sSFR below the transitional region in the sSFR diagram. The quiescent region of the UVJ diagram correlates reasonably well with galaxy morphology (as defined by Sérsic indices) with 66% of the quiescent systems having elliptical/bulge-dominated Sérsic indices ($n \geq 2.5$) and an additional 21% having transitional Sérsic indices ($1.5 < n \leq 2.5$). The low Sérsic systems ($n \leq 1.5$) in the quiescent

region tend to be at lower masses ($M_{stellar} < 10^{10.3}$) and we shall address this population shortly. In agreement with works performed at $z \sim 1$ (Kauffmann et al. (2003) and Bell et al. (2007)), quiescent galaxies are overwhelmingly systems with $M_{stellar} > 10^{10.3}$. Galaxies below this mass at $z \sim 2$ may be unable to quench themselves or otherwise truncate their star formation. star-forming galaxies exist at all masses but their numbers drop off considerably above this $10^{10.3}$ stellar mass limit, presumably due to their transitioning into quiescent systems as suggested by Lee et al. (2013), Bruce et al. (2012), and Barro et al. (2013).

There has been recent discussion on the existence of disk galaxies that appear to be quiescent. The implication of having quiescent disk populations is that these systems did not undergo a major merger or some other large scale process that turned off the galaxy's star formation rate and also changed its morphology from disk to elliptical. These quiescent disks exhausted their star formation / were quenched without modifying their global structure. Figure 1.19 shows the UVJ selected quiescent population at $z \sim 2$ colored coded by their single Sérsic values. We can see that while high Sérsic dominate the region, there is a significant population of galaxies (14%) with low ($n < 1.5$) Sérsic values as well as a large population of galaxies (21%) with intermediate Sérsic indices ($1.5 \leq n < 2.5$). These intermediate Sérsic systems can be interpreted as systems with a strong disk component in addition to a bulge component. Recent studies have found that many quiescent systems at $z < 1.2$ (Bundy et al., 2010) have strong disk components in addition to bulge components. At higher redshifts ($n \sim 1.5$), recent works (Stockton et al. (2004), McGrath et al. (2008), van Dokkum et al. (2008), and van der Wel et al.

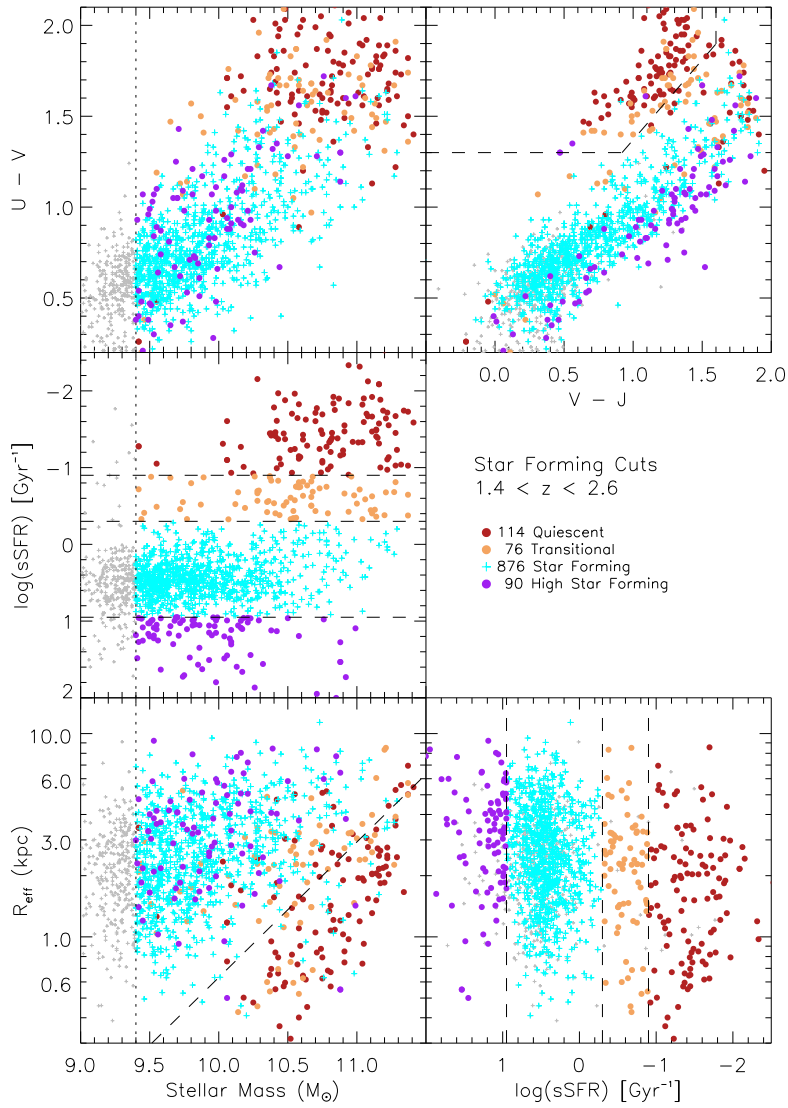


Figure 1.20: Global Properties of sSFR Selected Quiescent $z \sim 2$ Galaxies in GOODS-South. Galaxies are colored by their measured sSFR and are separated into quiescent, transitional, star-forming, and high star-forming populations. There is a high level of correlation between the sSFR populations and a galaxy’s location in the UVJ color-color plot. 95% of galaxies with quiescent or transitional sSFR are also in the quiescent region of the UVJ color-color plot. The galaxies with the lowest sSFR are in the quiescent region while the highest sSFR have the lowest U-V values for a given V-J. Galaxies with the highest sSFR tend to be low mass systems with extended R_{eff} .

(2011)) have continued this analysis among high mass ($M_{stellar} > 10^{11}$) quiescent systems and similarly saw disk components in the galaxies. Our high fraction of moderate Sérsic quiescent systems is in line with and extends their findings out to $z \sim 2$ (in agreement with work by Bell et al. (2012)). Perhaps more interesting is the relative high fraction of seemingly disk only systems at this redshift (Bruce et al., 2012). 14% of our UVJ selected quiescent sample have Sérsic values below 1.5 which is indicative of an exponential profile disk system. These low Sérsic quiescent systems tend to have lower masses ($M_{stellar} < 10.5$) and tend to be in the border region of the UVJ diagram between the quiescent and dust reddened systems. Additionally, these low Sérsic UVJ selected quiescent systems tend to have transitional sSFR perhaps an indication that these disk-like UVJ quiescent systems are star-forming dusty systems and not truly quiescent. Note that this analysis was also conducted on the ‘clean’ sample of galaxies to remove the effects of mergers, interactions, and questionable colors on the results. This ‘clean’ sample removes half of the disk systems in the quiescent region but does not affect the systems with intermediate Sérsic values (now nearly 25% of the total ‘clean’ quiescent sample). Perhaps this gives further weight to the intermediate Sérsic systems (those with prominent disks as well as bulges) being a genuine class of quiescent systems while the pure disk systems that are removed in the ‘clean’ sample are actually the result of photometry errors and poor fits.

Previous studies at $z \sim 2$ have focused on the sizes of high mass ($\log M_{stellar} > 11$) galaxies. These studies have remarked on the high fraction of quiescent galaxies at high masses (Daddi et al. (2005), Kriek et al. (2006), and Newman (2008)) and have also

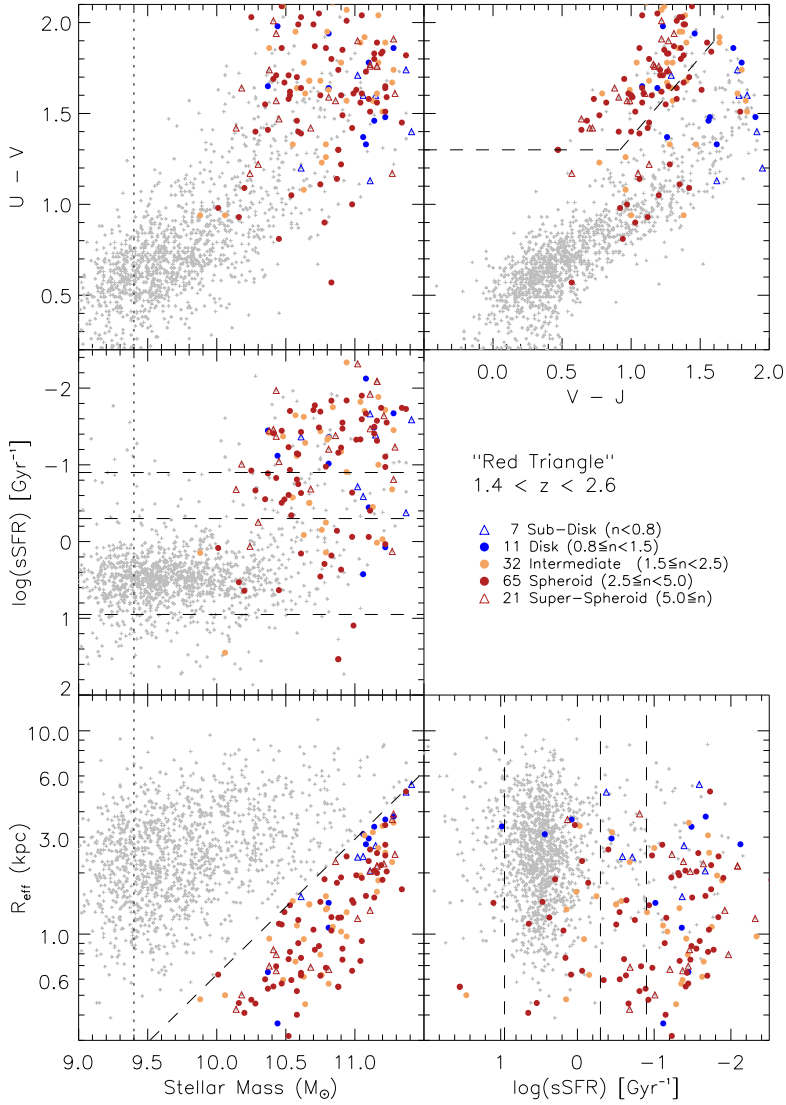


Figure 1.21: Global Properties of $M_{\text{stellar}}\text{-}R_{\text{eff}}$ Selected Quiescent $z\sim 2$ Galaxies in GOODS-South. Galaxies are colored by their Sérsic indices. There is a drop in the density of galaxies in the region between the ‘Red Triangle’ and the ‘Star-Forming Main Sequence’. If galaxies evolve from the star-forming sample to the higher mass ‘red triangle’ then this transition must be a fast process to explain the dearth of points in the transitional region. At a given mass, the R_{eff} of galaxies in the star-forming sample are a factor of 2-5 times larger than the galaxies in the ‘red triangle’. A mechanism is therefore needed to quickly change the radii of galaxies as they evolve into this ‘red triangle’. This mechanism will also need to change the morphologies of the galaxies to higher Sérsic, more spheroidal systems during this quick transition.

focused on the relative compact nature of many of these high mass quiescent systems (Daddi et al. (2005) and Trujillo et al. (2006)). Szomoru et al. (2012) noted the wide range in diversity of sizes among the high mass ($\log M_{stellar} > 10.7$) $z \sim 2$ galaxies. He found that the median effective radius of quiescent $z \sim 2$ galaxies is small ($\sim 1.1 \text{ kpc}$) - a factor of ~ 4 smaller than $z \sim 0$ galaxies. Szomoru also noted that some of the high mass galaxies had radii comparable to galaxies today with similar masses. This paper found that the scatter of galaxy radii for these massive galaxies is 1.5 times as large as the scatter at $z \sim 0$. This suggests that there is great diversity among massive galaxies at $z \sim 2$ and can not be characterized as a single compact quiescent population. Newman et al. (2012) used similar HST ACS and WFC3 data to study the size-mass relation of high mass ($\log M_{stellar} > 10.7$) quiescent and star-forming galaxies. This paper found that at a given mass, there is a significant size dependence on star formation rate with the quiescent low star-forming systems being more compact. Newman's Figure 3 also hints at an increasing size separation between the quiescent and star-forming high mass systems as you go to higher redshifts. We show that this separation/valley between the 'Red Triangle' and the 'Star-Forming Main Sequence' is more pronounced in our larger and higher redshift sample. Our study continues the Newman analysis at higher redshifts ($z \sim 2$) and includes lower mass systems.

Our figures have shown that at lower masses, $z \sim 2$ galaxies populate a large range of effective radii with no strong indication of a color dependence with on radius. For higher mass galaxies ($\log M_{stellar} > 10.0$), galaxies with smaller radii to have redder visible light colors, suggesting a size-color relation at high masses. Figure 1.21 highlights

a gap between the number of high mass compact galaxies (small effective radii) and high mass extended galaxies (large effective radii). The boundary drawn between the star-forming galaxy population and the ‘red triangle’ of higher massed more compact systems is set to a constant surface density of $10.3 \text{ (M/R}^{1.5})$ as is discussed in Barro et al. (2013). There is a drop in the density of galaxies in the region between the ‘Red Triangle’ and the ‘Star-Forming Main Sequence’. If galaxies evolve from the star-forming sample to the higher mass ‘red triangle’ then this transition must be a fast process to explain the dearth of points in the transitional region. At a given mass, the R_{eff} of galaxies in the star-forming sample are a factor of 2-5 times larger than the galaxies in the ‘red triangle’. A mechanism is therefore needed to quickly change the radii of galaxies as they evolve into this ‘red triangle’. This mechanism will also need to change the morphologies of the galaxies to higher Sérsic, more spheroidal systems during this quick transition. This is inline with discussion in Barro et al. (2013).

Galaxies in the ‘red triangle’ (especially those below $R_{eff}=2\text{kpc}$) are dominated by galaxies with spheroidal (and a few intermediate) Sérsic indices. Above $R_{eff}=2\text{kpc}$, there is a small population of disk systems that also lie in the dusty region of the UVJ diagram. 64% of the ‘red triangle’ has spheroidal Sérsic indices while 24% are intermediate and 13% are disk-like. This is in general agreement with the morphology fractions found in the quiescent UVJ region and the quiescent sSFR region. $\sim 60\%$ of galaxies in the ‘red triangle’ are also in the quiescent sSFR and UVJ regions (78% if you include the transition region of the sSFR diagram). This is a high level of agreement but still leaves a large number of galaxies in this red triangle that are not

considered quiescent in sSFR nor in color-color diagrams. Figure 1.21 shows that 20% of the spheroidal systems (30% if you include systems with intermediate Sérsic indices) in the ‘red triangle’ are star-forming high mass compact systems. This population of ‘blue nuggets’ is in agreement with recent papers (Barro et al., 2013) and represents a new population of objects at $z \sim 2$. An interesting open question is whether these blue compact star-forming systems quench and become red quiescent systems or if they continue to form stars and form large disk systems before having their star formation shut off and quenching into a quiescent system.

1.5 Axial Ratio Distribution at $z \sim 2$

In the following figures, we show the axis ratio (q) distribution for our galaxy classes as function of mass for our $z \sim 2$ ($z=1.4-2.6$) population. Using these distributions we can probe the intrinsic galaxy shapes (triaxial, prolate, oblate, thin disk, etc) of galaxy classes. In each figure, the subclasses identified in the legend are plotted in a scatter plot of axis ratio vs. R_{eff} with a bar graph of the axial ratio distribution for each subsample. The median values for these subsamples are drawn on these bar graphs for all populations with at least 10 members (below this number there are too few galaxies for the median value to be meaningful). Note that in the case of color coding by Sérsic indices, only the disk, intermediate, and spheroidal classes are shown in the axis ratio distribution bar graph. The three rows in these plots are our mass divisions from low mass ($10^{9.4} \leq M_{stellar} < 10^{10.0}$) at the bottom, intermediate mass

($10^{10.0} \leq M_{stellar} < 10^{11.0}$) in the middle and high mass ($M_{stellar} \geq 10^{11.0}$) in the top row.

As expected and in agreement with previous works both at low (Padilla & Strauss, 2008) and high redshifts (Chang et al., 2013), Figures 1.22 and 1.23 show that our intermediate ($10^{10.0} \leq M_{stellar} < 10^{11.0}$) and high mass ($M_{stellar} > 10^{11.0}$) spheroidal galaxies are round systems with high axis ratios (vast majority have $q > 0.4$). This is true both for spheroids identified through Sérsic indices and those visually classified as spheroids. In the case of Sérsic identified spheroids ($2.5 \leq n < 5.0$), the median axial ratio distribution is 0.71 and 0.69 for the intermediate and high mass systems respectively. Similarly, for the visually identified spheroids, the median axial ratio is 0.72 for the intermediate mass galaxies and 0.78 for the high mass galaxies. In both cases, these spheroidal populations are rounder than the average galaxy at the given mass and their distributions are inline with an elliptical triaxial distribution (in agreement with Bruce et al. (2012) and Patel et al. (2012)). The disk-type galaxies at $z \sim 2$ cover a larger range of axis ratios. The axis ratio distributions do not match that of the higher mass spheroidal population and their median axis ratio values are lower than that of the spheroidal classes. There is a mass dependence on the shape of these disk-like galaxies. The axial ratio increases for these systems as their mass increases. The distribution of axis ratios is not flat as one would expect for an optically thick thin-disk population. This is particularly true in the lower mass bin where the axis ratio distributions peak at 0.42 and 0.49 (for visually identified and $0.8 \leq n < 1.5$, respectively) and the shape of the axis ratio distribution resembles a prolate distribution. At higher masses, this distribution shifts to higher axis ratios and is less peaked as for the lower mass galaxies.

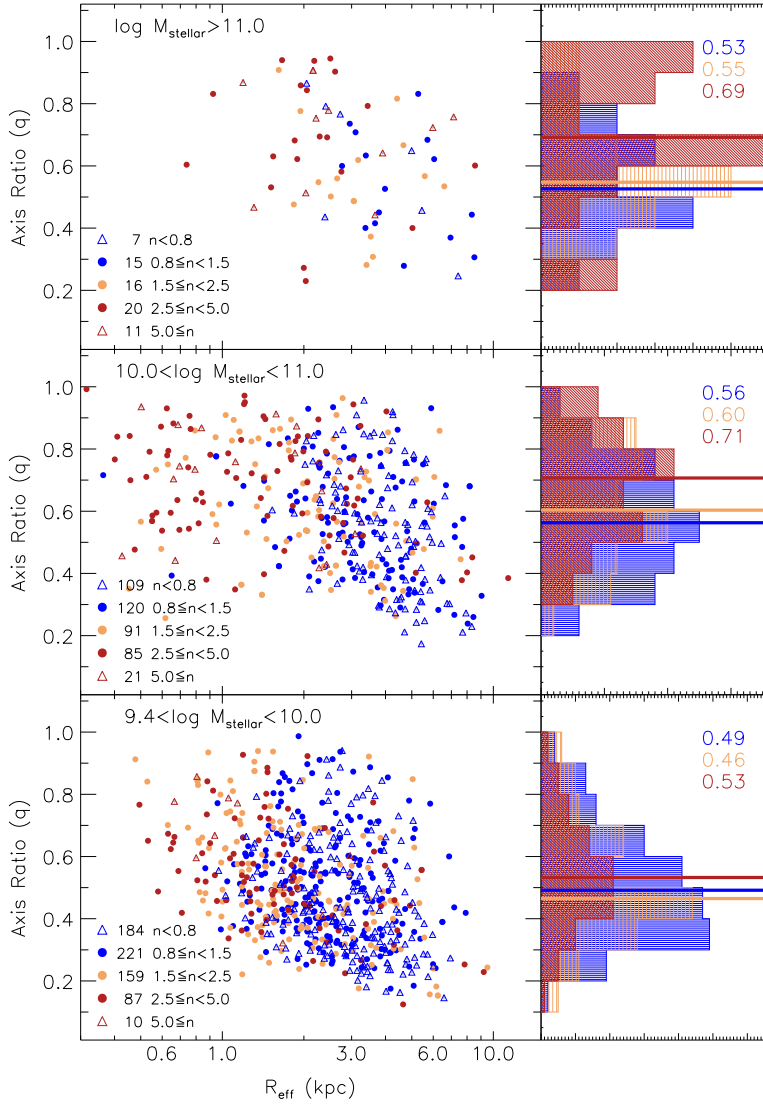


Figure 1.22: Axis Ratio- R_{eff} Relation in Different Mass Bins with Sérsic for $z \sim 2$ GOODS-South Galaxies. High mass galaxies are in the top row with intermediate mass systems in the middle and low mass galaxies are on the bottom. The galaxies are colored by Sérsic index and the accompanying bar graphs show the axis ratio distribution and median value for each subsample. Intermediate and high mass spheroidal galaxies are round systems with have high axis ratios. There is a mass dependence on the shape of these disk-like galaxies. The axial ratio increases for these systems as their mass increases. The distribution of axis ratios is not flat as one would expect for an optically thick thin-disk population.

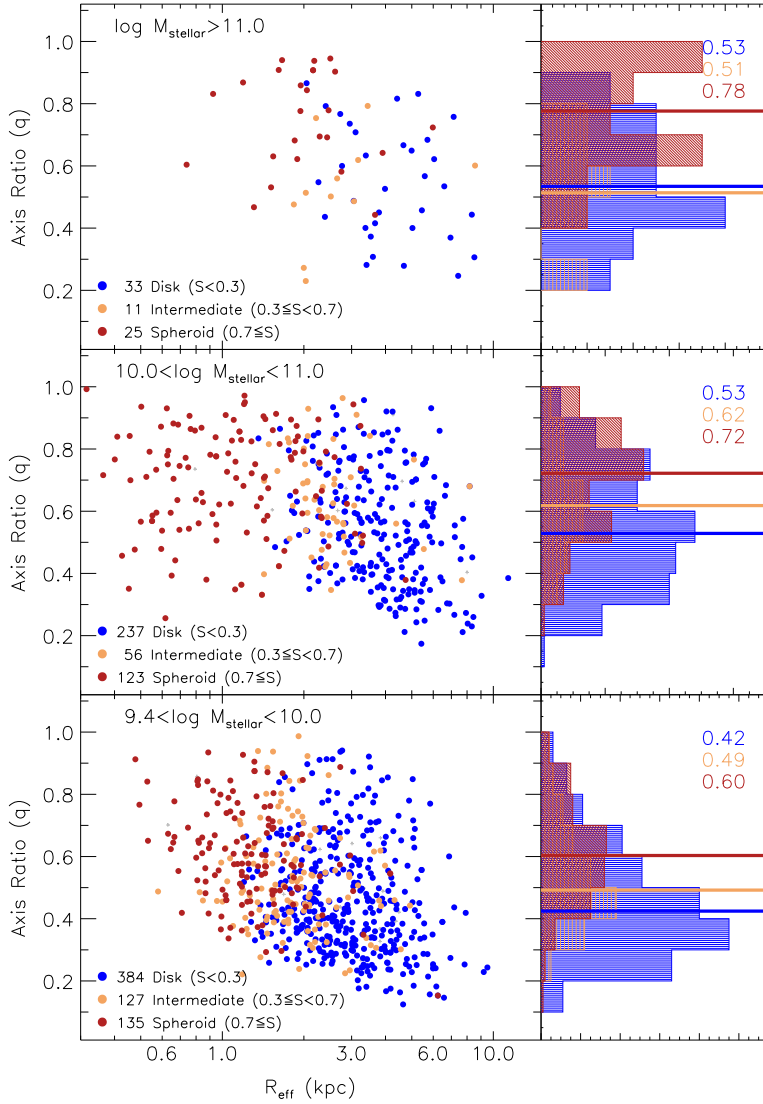


Figure 1.23: Axis Ratio- R_{eff} Relation in Different Mass Bins with Spheroidicity for $z \sim 2$ GOODS-South Galaxies. High mass galaxies are in the top row with intermediate mass systems in the middle and low mass galaxies are on the bottom. The galaxies are colored by their visual classification and the accompanying bar graphs show the axis ratio distribution and median value for each subsample. Intermediate and high mass spheroidal galaxies are round systems with have high axis ratios. There is a mass dependence on the shape of these disk-like galaxies. The axial ratio increases for these systems as their mass increases. The distribution of axis ratios is not flat as one would expect for an optically thick thin-disk population.

It is also worth noting an appearance of a ridge-line in the lower mass bin among the disk-like objects. Galaxies seem to be clustering along a R_{eff} -axis ratio ridge line where flatter galaxies (lower axis ratio) have larger radii. From this ridge line there is a smooth distribution vertically towards higher axis ratio systems. Perhaps there is an underlying flat disk population (with a smooth axis ratio distribution) in addition to a prolate population (forming a R_{eff} -axis ratio ridge-line).

In previous sections we used both specific star formation rate (sSFR) and rest-frame optical and near infrared color-color cuts to identify quiescent and star-forming systems. Figure 1.24 displays the populations identified in the UVJ diagram and Figure 1.25 displays the populations from the sSFR divisions. As was seen earlier, there is excellent agreement between the quiescent samples identified using UVJ and sSFR divisions so we expect the populations to have similar axis ratios distributions. In both the UVJ and sSFR identified samples, the quiescent populations are mostly in the intermediate and high mass bins and exhibit axis ratio distributions peaking at ~ 0.6 - slightly lower than the 0.7 expected for a triaxial elliptical population. Perhaps this is an indication that our quiescent population may include some flattened disks (as suggested by Barro et al. (2013) and van der Wel et al. (2011)) in addition to a traditional quiescent elliptical population. For both the sSFR and UVJ identified star-forming galaxies, we see a ridge-line distribution at lower masses peaking at $q=0.48$ while for the intermediate masses we see a more uniform distribution of axis ratios with a higher median value ($q\sim 0.60$). We interpret the lower mass bin distribution to be indicative of the presence of a prolate system in addition to a population of flatter disks. The intermediate masses

do not exhibit this prolate ridge-line and have a more even distribution in axis ratios. In the sSFR identified samples, the galaxies with transitional sSFR behave very similarly to the quiescent population in their distribution of axis ratios. For the galaxies identified in the ‘dusty’ region of the UVJ diagram, there does not seem to be a preference for edge-on, low axis ratio systems. The axis ratio distribution of this ‘dusty’ sample is fairly uniform perhaps indicative of a disk population but the median and distribution show no bias towards flatter/edge on systems with low axis ratios.

In Figure 1.26 we focus on the distribution of star-forming (as indicated by sSFR) galaxies as a function of their morphology (Sérsic index). To remove any effects of mergers, interactions, asymmetric systems, and other questionable results, we focus on the ‘clean’ sample (described in Section 2.5) to probe the star-forming $z \sim 2$ galaxies. Among these star-forming systems, the lower Sérsic systems have lower axis ratios and peak around $q=0.46$ while the intermediate and spheroidal systems have higher axis ratio distributions and are less skewed. The distribution among these low Sérsic star-forming galaxies does not resemble that of a flat disk population and instead resembles the distribution of a prolate population. There is a trend with mass within the star-forming galaxies where the axis ratio distributions shift higher at higher masses. This is true for all morphology types. The star-forming disk population at intermediate masses ($10^{10.0} \leq M_{stellar} < 10^{11.0}$) is a flat distribution centered around $q=0.56$ - perhaps indicative of a flat-disk population. Our distribution among the lower mass bin of star-forming disks does not agree with the findings of Bruce et al. (2012) or Law et al. (2012) for high mass star-forming galaxies at $z \sim 2$. Their high mass star-forming

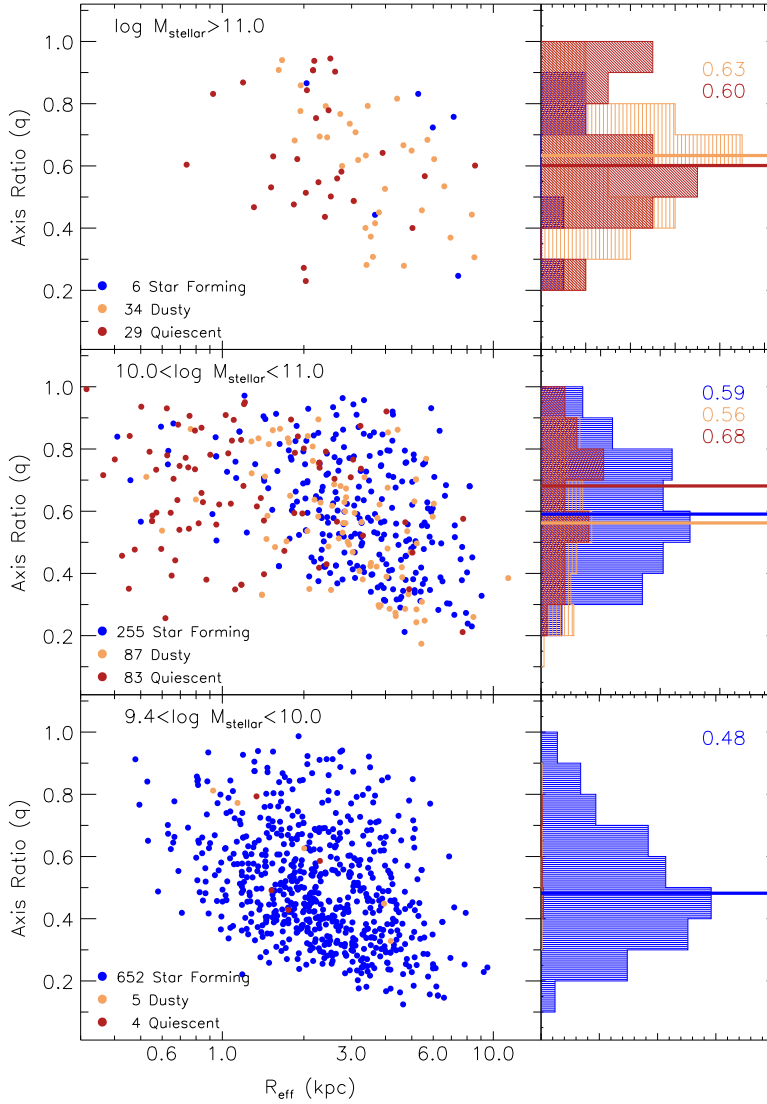


Figure 1.24: Axis Ratio- R_{eff} Relation in Different Mass Bins with UVJ Populations for $z \sim 2$ Galaxies in GOODS-South Galaxies. High mass galaxies are in the top row with intermediate mass systems in the middle and low mass galaxies are on the bottom. The galaxies are colored by where they lie in the UVJ color-color diagram and are separated into quiescent, star-forming, and dusty systems. The quiescent populations are mostly in the intermediate and high mass bins and exhibit axis ratio distributions peaking at ~ 0.6 - slightly lower than the 0.7 expected for a triaxial elliptical population. There is a ridge-line distribution at lower masses peaking at $q=0.48$ perhaps indicating the presence of a prolate system in addition to a population of flatter disks.

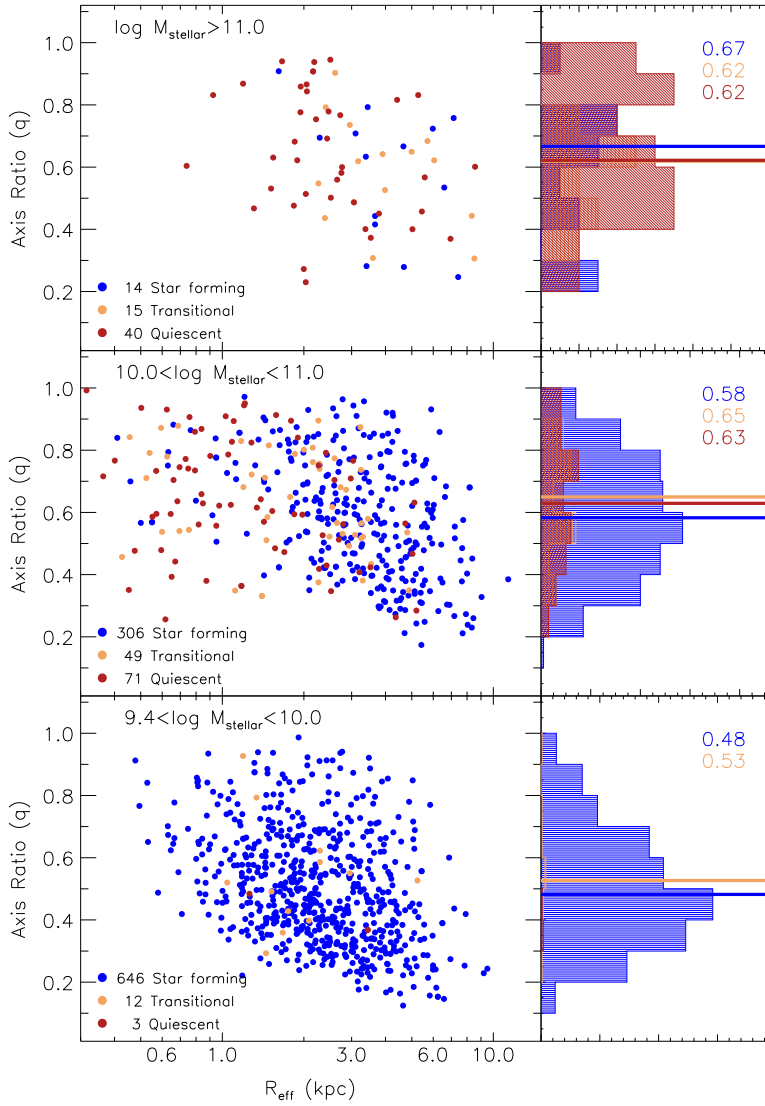


Figure 1.25: Axis Ratio- R_{eff} Relation in Different Mass Bins with sSFR Populations for $z \sim 2$ Galaxies in GOODS-South Galaxies. High mass galaxies are in the top row with intermediate mass systems in the middle and low mass galaxies are on the bottom. The galaxies are colored by their sSFR and are separated into quiescent, star-forming, and transitional systems. The results are very similar to the results of Figure 1.24 that used a UVJ color-color diagram to identify populations.

population peaked at 0.6-0.7 with very few objects with $q \leq 0.3$. We do not have enough high mass star-forming disk galaxies to compare with them but our lower mass star-forming population is completely at odds with their distribution indicating that there is a morphology transition between low mass, low axis ratio prolate systems and the high mass, high axis ratio systems.

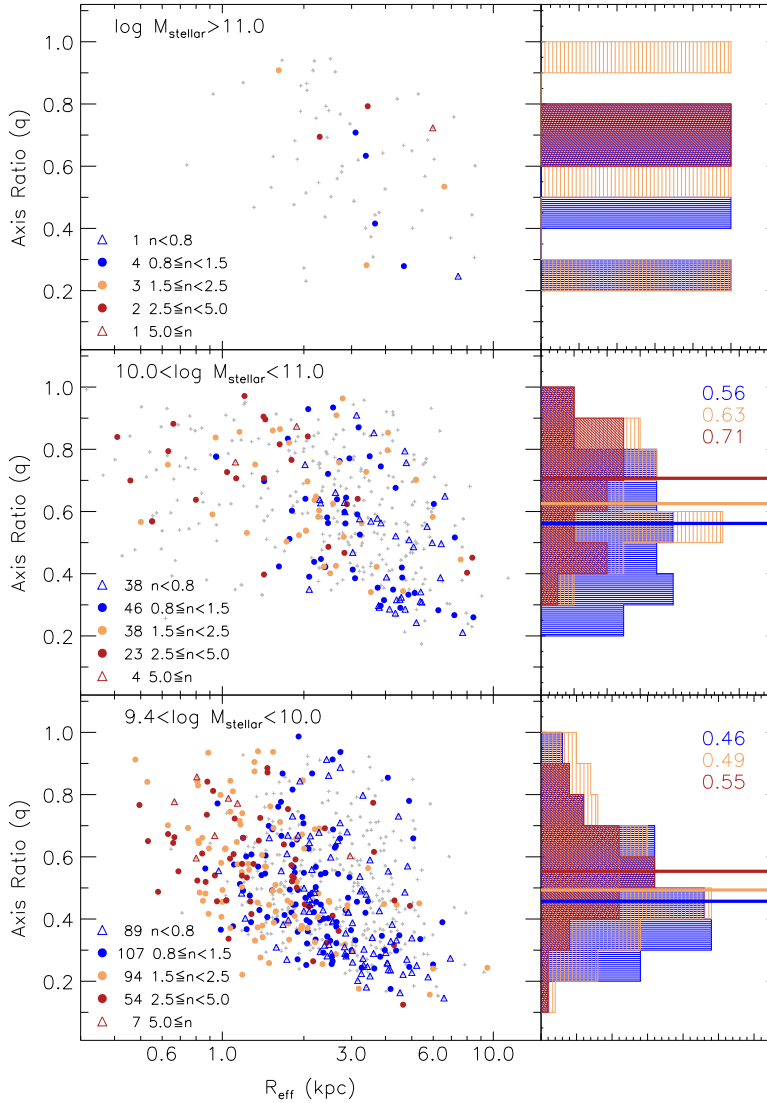


Figure 1.26: Axis Ratio- R_{eff} Relation in Different Mass Bins with Sérsic for the ‘Clean’ Star-Forming $z \sim 2$ GOODS-South Galaxies. High mass galaxies are in the top row with intermediate mass systems in the middle and low mass galaxies are on the bottom. The galaxies are colored by Sérsic index and the accompanying bar graphs show the axis ratio distribution and median value for each subsample. The ‘clean’ sample removes possible contamination from uncertain classifications, photometry, as well as interacting and asymmetric systems. The distribution among low Sérsic star-forming galaxies does not resemble that of a flat disk population and instead resembles the distribution of a prolate population. There is a trend with mass within the star-forming galaxies where the axis ratio distributions shift higher at higher masses.

1.6 Summary

The visual classification system we have developed and implemented on the CANDELS GOODS-South field has produced one of the largest and most detailed visual inspections of high redshift galaxies. This is the largest catalog of its kind that is based primarily on high resolution near-infrared observations allowing classifications beyond a $z \sim 2$ to be based on rest-frame visible wavelengths probing old stellar populations which better trace stellar mass than the rest-UV based surveys from the past. The spheroidicity and basic morphologies from the visual classification system couple well with Sérsic index. The structural flags and clumpiness matrix from the visual classifications have proved to be unique values and have allowed us to probe a wide variety of galaxy populations across a range of masses and redshifts. This study has produced several key results:

- GALFIT Sérsic indices and our visual classification system correspond well with each other at $z \sim 2$. Systems visually identified as disks tend to have lower Sérsic indices and systems visually identified as spheroids have higher Sérsic indices.
- A comparison with Elmegreen’s UDF population yielded agreement on the classification of 80-85% of the shared galaxies. This was better agreement than expected given that Elmegreen’s classifications were based on observed-frame visible wavebands (rest-frame UV beyond $z \sim 2$) while our classifications were based on observed-frame NIR wavebands (rest-frame optical beyond $z \sim 2$).
- The visual classification system is unable to distinguish between disks and spheroids

below the spatial resolution of the image ($0.17''$). 80% of all compact galaxies ($R_{eff} < 0.17''$) are identified visually as spheroids. GALFIT (with a well known PSF) is able to fit diverse Sérsic models to these compact systems and is not biased towards spheroids at small radii.

- Disks are the dominant population among low mass ($9.4 < \log M_{stellar} < 10.0$) systems across all redshift bins ($z=0.5-3.0$). The higher mass bins have an increasing fraction of spheroids at lower redshifts coupled with a decreasing fraction of disks.
- There are two spheroidal populations. In addition to the traditional quiescent red spheroidal population, there is a low mass, blue, and star-forming spheroidal population. At $z \sim 2$, 2/3 of all spheroids are these blue star-forming systems. This bimodality of spheroids is independent of using visual classifications or Sérsic index to identify spheroids.
- There is a high level of correlation between sSFR and a galaxy's location in the UVJ color-color plot. 95% of galaxies with quiescent or transitional sSFR are also in the quiescent region of the UVJ color-color plot. The galaxies with the lowest sSFR are in the quiescent region while the galaxies with the highest sSFR have the lowest U-V values for a given V-J. Galaxies with the highest sSFR tend to be low mass systems with large R_{eff} .
- Local Universe morphology correlations with sSFR and locations on UVJ color-color diagrams exist in the $z \sim 2$ Universe. The color-color diagram cleanly separates between red dusty star-forming disk-like objects and truly red quiescent

spheroidal galaxies.

- The dusty region of the UVJ diagram is not overly populated with edge-on galaxies. Edge-on galaxies are found throughout the star-forming sequence but show no increase in number density in the dusty portion of the UVJ diagram. A surprising result since light from edge-on galaxies would be more likely to be affected by their dust and thus more likely to be reddened. This result is true for both visually identified edge-on systems and systems with low axis ratios.
- Clumps are predominantly in systems with large radii and low to intermediate masses. Half of all low and intermediate mass systems are clumpy regardless of redshift.
- Chains and tadpoles are low mass extended systems and are more common at higher redshifts. Not observing a large number at low redshifts makes it unlikely that chains and tadpoles are clumpy flat disks viewed edge-on.
- Asymmetric galaxies increase dramatically in number fraction at higher redshifts. Asymmetric galaxies are primarily low and intermediate mass systems and are more common at higher redshifts. The majority of galaxies at $z > 2.5$ are classified as asymmetric.
- Mergers and interacting systems at $z \sim 2$ are not common in the dusty region of the UVJ diagram. This is surprising since it is expected that mergers between gas rich galaxies would be dusty systems.

- There is a drop in the density of galaxies in the region between the ‘Red Triangle’ and the ‘Star Forming Main Sequence’ in the $z\sim 2$ R_{eff} - $M_{stellar}$ diagram. If galaxies evolve from the star forming sample to the higher mass quiescent ‘red triangle’ then this transition must be a fast process to explain the dearth of points in the transitional region. At a given mass, the R_{eff} of galaxies in the star forming sample are a factor of 2-5 times larger than the galaxies in the ‘red triangle’. A mechanism is therefore needed to quickly change the radii of galaxies as they evolve into this ‘red triangle’. This mechanism will also need to change the morphologies of the galaxies to higher Sérsic, more spheroidal systems during this quick transition.
- The axis ratio distribution at $z\sim 2$ among low Sérsic star-forming galaxies with $9.4 < \log M_{stellar} < 10.0$ does not resemble that of a flat disk population and instead resembles the distribution of a prolate population. Higher massed star-forming systems have distributions resembling those of flattened disks. This suggests that our star forming population at $z\sim 2$ consists of prolate low mass asymmetric galaxies while the higher mass systems have relaxed into a more disk-like population.

As is apparent in the figures and tables provided in this chapter and appendix, there is an enormous wealth of information about galaxy morphology and structure that is provided by our visual classifications.

Chapter 2

Comparison of Hydro-ART Simulated Galaxies with Observations

2.1 Introduction

Massive galaxies in the local Universe are seen to be well described morphologically by the Hubble sequence (Hubble, 1926). A galaxy's global properties (radii, stellar light profile, color, star formation rates, rotation, dominance of central bulge) tend to correspond with its place on the Hubble sequence (spiral, elliptical, etc). The state of this correlation and the evolution of galaxies on the Hubble sequence at higher redshifts is less understood.

In the local Universe, most galaxies can be classified into a morphological and color bimodality in which the elliptical galaxies have higher optical light Sérsic (Sersic, 1968) profiles, have lower star formation rates, and are red in color. The disk systems

have exponential light profiles ($n \sim 1$), have higher star formation rates, and are bluer in color (Sandage (1986), Strateva et al. (2001), Kauffmann et al. (2003), Conselice (2006), Nair & Abraham (2010), Conselice (2003), Scarlata et al. (2007)). Studies have shown that these relations are similar out to a redshift $z \sim 1$ (Brinchmann et al. (1998), Abraham et al. (1996), van den Bergh et al. (2000), Ilbert et al. (2006), Oesch et al. (2010) and Buitrago et al. (2013)). These studies have found that the galaxy populations up to a redshift of $z = 1$ are dominated by the Hubble sequence and that the $z=1$ irregular galaxies are similar to the irregular galaxies in the local population. However, the picture of galaxy morphology at higher redshift is less clear. Some studies (Papovich et al. (2005), Cameron et al. (2011), Dickinson (2000)) find that there are almost no Hubble type galaxies present at $z \sim 2$ and hence there must be large amounts of evolution occurring to transform the irregular galaxies seen in the high redshift Universe into their more settled counterparts that we see today. Other studies (Driver et al. (1998), Conselice et al. (2005), Szomoru et al. (2011), Conselice et al. (2011a), and Buitrago et al. (2013)) find that while the majority of $z \sim 2$ galaxies are peculiar, normal Hubble-type galaxies that we find in the local Universe do in fact exist at $z \sim 2$. Massive star-forming galaxies at $z=1-3$ have been found in previous studies (Steidel et al. (1999), Adelberger et al. (2004), and Daddi et al. (2004)) to be dominated by thick disk systems that are rotating and possess giant clumps (Elmegreen & Elmegreen (2006) Genzel et al. (2008), Stark et al. (2008), Law et al. (2009), Förster Schreiber et al. (2011), Wuyts et al. (2012), Guo et al. (2012), and Guo et al. (in prep.)). These systems were thought to be ‘chains’ edge-on and ‘clump clusters’ face-on Elmegreen et al. (2007) and many

were spectroscopically confirmed to be rotating disks (Genzel et al. (2006) and Förster Schreiber et al. (2009)). There is a lack of consensus in the literature over the state of galaxies in the $z \sim 2$ Universe.

Until recently, morphological studies at redshifts above 1 were based either on observed optical filters or low spatial resolution near-infrared (NIR) observations. High spatial resolution optical surveys performed using instruments such as WFPC2 and ACS on the Hubble Space Telescope (HST) have allowed morphological studies of nearby galaxies but are limited because beyond a redshift of 1, these optical instruments are measuring rest-frame wavelengths shorter than 4000 \AA and are thus probing ultraviolet (UV) light which is sensitive to star-forming regions and does not accurately trace the underlying old stellar population distribution. To properly compare the morphologies of galaxies beyond a redshift of 1 to local galaxy samples, it is necessary to use NIR filters to observe the rest-frame optical light distribution which more reliably trace the older stellar populations and give a better representation of the underlying stellar mass distribution of the galaxies. Previous NIR photometric surveys used either ground based wide-field cameras with poor spatial resolution (limiting the reliability of morphology measurements) or used the high spatial resolution but small field of view ground based adaptive optics cameras or NICMOS (Kriek et al. (2009) and Conselice et al. (2011b)) on HST (limiting the size of the galaxy sample studied). The installation of the near infrared Wide Field Camera 3 (WFC3) on HST in 2009 allowed high spatial resolution rest-frame optical light observations of a large sample of redshift >1 galaxies. This work uses observations in GOODS-South taken with WFC3 on HST as part of the Cosmic

Assembly Near-infrared Deep Extragalactic Legacy Survey (CANDELS)(Grogin et al. (2011) and Koekemoer et al. (2011)). These near infrared observations allows the study of the morphology and global galaxy properties of the $z>1$ universe in a way that is comparable (similar rest wavelengths) to the observations that have been made in the local universe. Several CANDELS studies exploring structure and morphology of $z>1$ galaxies have been produced (Barro et al. (2013), Wang et al. (2012), Bruce et al. (2012)). They have focused on describing the population of massive $z>1$ galaxies using Sérsic profile, visual classifications, stellar mass, and radii. In addition, several papers from the CANDELS team are published that use a subsample of the visual classifications described in this work to study particular subpopulations including AGN (Kocevski et al., 2012), bulge evolution (Bruce et al., 2012), and ultraluminous infrared galaxies (Kartaltepe et al., 2012).

Theoretical studies have focused on this $z\sim 2$ epoch to probe galaxy evolution and try to match their simulations to the new high-resolution rest-frame optical images. The zoom-in cosmological simulations of Agertz et al. (2009) and Ceverino et al. (2010) employed AMR hydrodynamics and confirmed the theoretical model of giant clumps in high redshift galaxies forming in situ in the disk by gravitational instability. These clumps were seen to migrate towards the center of the galaxy and build up the central bulge of the galaxy. The continuous streaming of cold gas onto the disk from the cosmic web keeps the disk density high enough for gravitational instabilities to form new clumps (Dekel et al. (2009) and Ocvirk et al. (2008)). These cosmological simulations are compared to observations to probe clump properties and galaxy evolution but previous

works have all used raw simulations to compare with the comparably fuzzy and low resolution high redshift observations. To do a fair comparison between the observations and simulations, one must degrade the high resolution simulations to the image quality of the observations and then ‘observe’ the simulations in the same way we observe and process the real galaxies. This study will be the first work to ‘observe’ these state-of-the-art simulations in a comparable way to the ACS and WFC3 CANDELS observations in GOODS-South. We will use visual morphologies and global galaxy qualities (stellar mass, color, radii, star formation rates, etc) to compare the star-forming galaxies in the observations with simulations.

This chapter is structured into seven sections and an appendix. Section 2 describes the Hydro-ART simulations, the processing of these simulations, and summarizes HST GOODS-South observations used to compare with the simulations. Section 3 discusses the morphological classification system, sample selection and limitations of the simulations. In Section 4, we discuss the basic characteristics of the observations and simulations. In Section 5, we compare the visual classifications to the Sérsic indices for galaxy morphology. Section 6 focuses on the clumpy nature of $z \sim 2$ galaxies. Finally, in Section 7, we summarize and discuss the key findings and implications of this study. Additional diagrams are provided in the appendix to highlight the structural evolution of individual simulations over redshift.

2.2 Data

2.2.1 Hydro ART Simulations

This study uses zoom-in hydro cosmological simulations with peak AMR (adaptive mesh refinement) resolution of 35-70 parsecs for 38 galaxies simulated starting at very high redshifts and allowed to evolve to redshifts below $z \sim 1.5$. These simulations use the ART code (Adaptive Refinement Tree) to track the evolution of a gravitating N-body system as well as the Eulerian gas dynamics using AMR. (ART is described in depth in Kravtsov et al. (1997) and Ceverino & Klypin (2009)) Additionally, the Hydro-ART simulations include subgrid physics to describe many of the processes important for galaxy formation. The subgrid physics includes: gas cooling by atomic hydrogen and helium, metals and molecular hydrogen, photoionization heating by the UV background with partial self-shielding, star formation, stellar mass loss, metal enrichment of the ISM, and feedback from stellar winds and supernovae, implemented as local injection of thermal energy. Applying a redshift dependent uniform radiation field (as described in Haardt & Madau (1996)) across the simulations, except for in high gas density regions where a severely reduced UV background is used ($5.9 \times 10^{26} \text{ ergs}^{-1} \text{ cm}^{-2} \text{ Hz}^{-1}$), allows the simulations to mimic self shielding in dense gas and allows the simulations to cool in dense regions to temperatures around 300K. The simulations use a stochastic star-formation model that roughly follows the observed Kennicutt-Schmidt law (Kennicutt (1998) and Schmidt (1959)) of 5% star-formation efficiency per free-fall time. Star-formation is set to occur in gas dense ($>1 \text{ cm}^{-3}$), cool regions ($<10^4 \text{ K}$) with the

vast majority of stars formed in the coolest regions $T=300-1000\text{K}$. The simulations include a thermal stellar feedback model in which energy from stellar winds and supernova explosions is emitted at a constant rate for 40 Myrs following star-formation in a region. No additional feedback (including radiation pressure) or artificial prescriptions are implemented to reduce or truncate star-formation. These simulations are described in more detail in Ceverino et al. (2010), Ceverino & Klypin (2009), and Ceverino et al. (2012).

The Hydro-ART simulations used in this study are selected by running lower resolution dissipationless N-body dark-matter simulations in large comoving cosmological boxes. The ΛCDM standard model cosmology with WMAP5 values ($h=0.7$, $\Omega_m=0.27$, $\Omega_\Lambda=0.73$, $\Omega_b=0.045$, and $\sigma_8=0.82$) for cosmological parameters was used in these dark matter halo simulations. From these lower resolution dark matter simulations, distinct haloes were identified through density peaks in dark matter. A subsample of these haloes were selected to be re-simulated at full resolution by selecting for a given virial mass at $z=1$ and to not be undergoing a major merger at $z=1$. This study uses four families of simulations - VELAs, VLs, MWGs, and SFGs. The MW, SFG, and VL families of simulations have halo masses between $10^{10}-10^{13} M_\odot$ while the VELA simulation has slightly reduced star formation efficiency and have halo masses ranging from $10^{11}-10^{12} M_\odot$. The requirement on haloes to not be undergoing a major merger at $z=1$ introduces a bias on our selection by removing haloes in dense environments. This bias is seen to remove $\sim 10\%$ of the haloes from the full halo sample at $z\sim 1$ which tend to be in dense environments and only introduces minor effects on the higher red-

shift sample. Selected haloes were rerun using the same initial cosmological conditions with the addition of gas and resolved on an adaptive mesh with higher resolution on a zoom-in Lagrangian volume encompassing twice the virial radius of the halo at $z \sim 1$ (roughly a sphere with a comoving radius $\sim 1\text{Mpc}$) which was embedded in a comoving cosmological box of length 20, 40, or 80Mpc/h. The simulations were all run to $z \sim 1$ or lower using the full Hydro-ART and subgrid physics to a spatial resolution of 35-70pc in the dense regions. This resolution enables cold disks and clumps to form and be resolved. Complete simulation data was saved at scale factor intervals (a) of ~ 0.01 . This work focuses on the simulations from $z=1.4-2.6$ and compares the global properties and clump properties to the CANDELS GOODS-South observations at this same redshift range.

2.2.2 Simulation Processing

2.2.2.1 Sunrise

To determine the distribution of light for each galaxy in various wavebands and to account for the absorption, scattering, and reemission effects of gas and dust within a galaxy, we use the SUNRISE Monte-Carlo radiative transfer code (Jonsson (2006), Jonsson et al. (2010)). SUNRISE calculates the appearance of each simulated galaxy across many wavebands (from submillimeter to far-ultraviolet wavelengths) which can then be convolved with filter curves to determine the galaxy's appearance in that filter. SUNRISE traces the emitted radiation from the simulation's individual stellar particles with their light contribution determined by their mass, age, and metallicity. The light is

ray-traced through the gas and dust (which is assumed to trace the density of metals in the galactic gas) taking into account the effects of scattering, absorption, and reemission by the dust. The emission from the dust is determined from each point in the simulation by scaling to the radiation intensity heating the dust particles and iterating until the dust absorption and emission is brought to equilibrium. Various dust models were tested that changed the scaling factor of the dust particles to the metal gas and also the distribution of dust grain sizes and properties within the dust particles. A wide range of dust models were tested internally during this study but the differences between the models were found to be very minor (differing on the few percent level of flux) over the wavebands of interest (near-infrared to optical). Given the robustness of the simulated galaxy flux on the dust models, we adopted a Milky Way dust model for this study. The dust models were robust in the infrared wavebands of interest but had large effects on the optical and infrared colors for the galaxies. These dust model experiments are discussed at length by Chris Moody in his PhD dissertation (Moody 2013). The results from SUNRISE are spatially resolved 2-dimensional images of the simulated galaxies at various filters for a variety of chosen viewing angles. For this study, we choose to calculate the SUNRISE images of each of the 38 simulations at each saved simulation time step from redshift 1.4 to 2.6 at six different viewing angles - 1 edge-on and 1 face-on (as determined by the angular momentum of the gas in the simulation), and 4 camera angles chosen at random (random for each galaxy at each time step with no correlation between the simulations) to ensure an unbiased sample of observations.

2.2.2.2 CANDELization Process

A major objective of this work is to compare observed morphologies of the galaxies created in the latest Hydro-ART simulations to observed galaxies from the CANDELS GOODS-South field. In order to fairly compare the simulated galaxies with observed galaxies from the CANDELS survey, we ‘downgrade’ the simulations so that they have similar observed image properties to the CANDELS observations in the full GOODS-South (wide+deep+ers) field. This process of modifying the simulations such that they resemble the image quality of observed galaxies is called ‘CANDELization’. The main steps in CANDELizing a simulated image are converting the flux units from SUNRISE to counts scaled to the redshift of the simulation, repixelating the simulation to match the coarse pixel scale of the detector, applying the point spread function (PSF) from the observations to the image, and adding background noise to the image from the observations to resemble the noise level in the observations.

SUNRISE (as described in the previous section) is used to process the particles in each simulation and create images of the simulations at multiple viewing angles after including the absorption, scattering, and reemission effects of dust. SUNRISE produces images at the resolution of the simulation for any given rest-frame or observed-frame filter by adjusting the produced SED to the appropriate wavelengths for a given redshift and convolving with a chosen filter. When producing observed frame images, SUNRISE does not adjust the flux or the size of the simulation - it only adjusts to the corresponding part of the SED to match with the observed filter at the given redshift. In order to

match our simulation ‘observations’ with those measured by the CANDELS team, we scale these images to the appropriate count values and pixel size. Assuming a standard cosmology (Hubble Constant $H_0=71$, Matter Density $\Omega_m=0.27$, Cosmological Constant $\Lambda_0=0.73$, and a flat curvature $k=0$) we rebin the flux (while preserving the surface brightness) from the simulations into pixels corresponding to the pixel size of the final drizzled images in CANDELS (30 mas for ACS images and 60 mas for WFC3 images). Using the zero-point values for each filter from the CANDELS observations and the median exposure time for the full GOODS-South two epoch depth (wide+deep+ers), we rescale the internal SUNRISE flux units ($\text{W/m}^2/\text{stradian}$) into counts comparable to the CANDELS GOODS-South observations. A point spread function (PSF) is convolved with the rebinned simulation images to recreate the effect of observing the simulations through the ACS and WFC3 cameras. Internal tests have shown that ‘hybrid’ PSFs do the best job at reproducing individual stellar profiles. These ‘hybrid’ PSFs use simulated PSFs generated from TinyTim at small radii and use empirical PSFs measured by stacking stars in the GOODS-South field at large radii. Generating PSFs using just stacked GOODS-South field stars or just TinyTim model PSFs does not accurately recreate observed stars in the CANDELS observations. In particular, the TinyTim PSF for WFC3 data appears to underestimate the light by $\sim 3\%$ at large radii. Using TinyTim model PSFs at small radii and empirical PSFs at large radii creates a PSF that does a reasonable job at recreating the observed light profiles. These ‘hybrid’ PSFs are used not only to convolve our simulations to recreate the effects of seeing but are also used when performing GALFIT analysis. Lastly, background noise

was added to the images to mimic the properties of the observed galaxy images. To estimate this background, random cutouts of blank sky are pulled from the CANDELS observations in each filter. The median value of these blank regions and the distribution of the background values are measured and then recreated on the simulated images by randomly adding values to the simulations with the same median value and random gaussian distribution. The resulting pixel scale and spatial resolution, exposure times, signal to noise, and background noise of the observed-frame images for the simulations are now comparable to those obtained by ACS and WFC3 in the CANDELS GOODS-South fields. These ‘CANDELized’ SUNRISED simulated images are the images used in this work.

2.2.3 CANDELS Observations

To test the simulations’s ability to create populations of galaxies found in the observable Universe, we compare these ‘CANDELized’ Hydro-ART galaxies to galaxies observed in the GOODS-South field (The Great Observatories Origins Deep Survey (GOODS) (Giavalisco et al., 2004)) by the CANDELS survey (Grogin et al. (2011) and Koekemoer et al. (2011)). The CANDELS survey is a Hubble Space Telescope (HST) Multi-Cycle Treasury Program (PIs: S. Faber and H.Ferguson, PID: GO-12060) that provides Wide Field Camera 3 (WFC3) and parallel Advanced Camera for Surveys (ACS) imaging in five legacy fields (GOODS-S, GOODS-N, COSMOS, UDS, and EGS). The three year, 902 orbit survey covered a total area of ~ 800 arcmin² over the five fields. For this paper, we will focus only on the GOODS-South region. The GOODS-

South portion of CANDELS has a two-tiered approach to partially cover the field of the original GOODS-South survey. A 7' x 10' 'deep' area consists of 13 orbits per WFC3 tile divided over the F105W (Y), F125W (J), and F160W (H) filters. A 4' x 10' 'wide' area consists of 2-3 orbits per WFC3 tile divided over the F125W and F160W filters. The 5σ point source magnitude limit in the F160W filter is ~ 28 AB in the 'deep' region and is ~ 27 AB in the 'wide' region. All of the infrared WFC3 exposures were accompanied by parallel visible light observations with ACS that were offset to lie in other parts of the WFC3 region so as to create an ACS region that nearly completely overlaps with the CANDELS WFC3 region. Please see Koekemoer et al. (2011) and Grogin et al. (2011) for further details on the GOODS-South observations.

WFC3 data from two previously completed surveys conducted in GOODS-South was combined with the CANDELS WFC3 observations. The Ultra Deep Field (UDF) is located within the CANDELS 'deep' region and was observed for ~ 28 orbits in F160W and ~ 15 orbits in both F105Y and F125W over a single WFC3 pointing (see Bouwens et al. (2010) for further details). The Early Release Science program (ERS) is located just north of the CANDELS GOODS-South region and was observed for ~ 2 orbits in F098M, F125W, and F160W each over a 4' x 9' area (see Windhorst et al. (2011) for further details). The WFC3 observations from these three surveys (CANDELS, ERS, and UDF) were combined to cover a large portion of the original GOODS-South survey field at varying filter depths. For this study we used the deepest available combined WFC3 observations. By drizzling individual WFC3 exposures together using the Multidrizzle pipeline and techniques described in Koekemoer et al. (2011), final

mosaics of the observations and accompanying weight maps were created at a resampled pixel scale of 60 mas (0.06"). These WFC3 mosaics were combined with mosaics of very deep ACS observations taken in 2004 (Giavalisco et al., 2004) in the F435W (B), F606W(V), F775W (i), and F850LP (z) filters. These ACS bands were similarly drizzled together into mosaics of 30 mas (0.03") pixel scale with a 5σ point source magnitude limit of ~ 28.2 in the F850LP filter. These ACS and WFC3 mosaics were the dataset used to compare to our simulations in this study.

2.2.4 Data Processing

As described in Guo et al. (2013) and in the previous chapter, a modified SEXTRACTOR v2.5 (Bertin & Arnouts, 1996) was used on the WFC3 CANDELS mosaics to detect objects in F160W. In order to detect large, bright objects as well as small, dim objects, the SEXTRACTOR routine is run with both ‘hot’ and ‘cold’ mode parameters (as implemented by the GALAPAGOS routine - Barden et al. (2012)) and then the two catalogs are combined into a single detection catalog of 34920 objects in the full depth CANDELS GOODS-South field (including the ERS and UDF). SEXTRACTOR was similarly run on the CANDELized Hydro-ART simulation images. In addition to identifying the number of objects in the F160W mosaic, a segmentation map assigning pixels in the mosaic to specific objects as well as a catalog of basic object parameters (magnitude, radii, axis ratio, position angle) are also created by SEXTRACTOR. This segmentation map and basic structure property catalog are later used in both visual classifications (see following section) and as starting points for GALFIT parametric fits.

Full descriptions of running SEXTRACTOR and generating these catalogs can be found in Guo et al. (2013) and Galametz et al. (2013).

For the GOODS-South observations, we used public archival data from ground and spaced-based surveys to gather reliable multiwavelength photometry from the ultraviolet (UV) to the mid-infrared (mid-IR) for each of the 34930 objects identified in the F160W mosaic (see Guo et al. (2013) for complete details and descriptions). In order to perform our photometry and SED fitting for observations, we combined the HST ACS and WFC3 observations from the GOODS-South (Giavalisco et al., 2004) and CANDELS (Grogin et al. (2011) and Koekemoer et al. (2011)) surveys with U-band data from the CTIO Blanco telescope, Visible Multi-Object Spectrograph (VIMOS) U-band data from the Very Large Telescope (VLT), Infrared Spectrometer and Array Camera (ISAAC) Ks-band data from the VLT, High Acuity Wide Field K-band Imager (HAWK-I) K-band data from the VLT, and 3.5, 4.5, 5.8, and 8.0 μm data from Spitzer.

Photometry from the different bands were obtained by rebinning and PSF matching the high resolution images to match the spatial resolution ($\sim 0.17''$) of F160W H-band before running dual-mode SEXTRACTOR to obtain matching photometry across the bands. This method can not be used reliably to measure consistent photometry from the ground based or Spitzer observations because their spatial resolutions differ strongly (often by a factor of 10 or more) from the F160W observations. To account for the possible blending of sources in the lower resolution data, TFIT (Laidler et al., 2006) is used to measure accurate photometry in these wavebands. TFIT is fully described in Laidler's paper and in the previous chapter. In this way, we are able to obtain reliable

photometry from the U-band to the NIR for the bright, faint, and crowded sources found in the F160W source catalog of GOODS-South. Fluxes and images in various observed wavebands are generated by SUNRISE for the Hydro-ART simulations and thus TFIT and psf matching is not necessary. SUNRISE is also able to produce rest-frame magnitudes for the simulations and the masses, redshifts, and star formation rates are already known. For the GOODS-South observations, we use the EAZY routine (Brammer et al., 2008) to determine the photometric redshifts of the 34930 F160W detected objects by fitting combinations of seven different galaxy templates to the objects’s SEDs created by combining the TFIT magnitudes from over a dozen wavebands covering the UV to the mid-IR. As discussed in more detail in the previous chapter as well as in Brammer et al. (2008) and Whitaker et al. (2011), EAZY’s photometric redshifts match well with known GOODS-South spectroscopic redshifts (mostly from the FIREWORKS catalog Wuyts et al. (2008)). For $z < 1$, our photometric redshifts have a normalized median absolute deviation (NMAD) (defined as $1.48 \times \text{median}(|\Delta z|/(1+z_{spec}))$) of 2.8% and an outlier fraction ($|\Delta z|/(1+z_{spec}) > 0.15$) of 5.5%. For higher redshift galaxies ($z > 1.5$), these values become 2.3% and 4.0% respectively (Guo et al., 2013). The final redshift sample for the F160W sources includes the spectroscopic redshifts with the best fit photometric redshifts from EAZY. The FAST routine (Kriek et al., 2009) was used to estimate the rest-frame colors, stellar masses and star formation rates (SFR) of the GOODS-South observations. EAZY used a grid of Bruzual & Charlot (2003) models, a Chabrier (2003) initial mass function (IMF), and a range of star formation histories, galaxy ages, and extinction parameters. The total SFR for each galaxy was estimated

using rest-frame UV luminosities and correcting for extinction (A_v) (Bell et al. (2005) and Kennicutt (1998)). Taking the extinction derived from SED fits (Wuyts et al., 2011b) and using the slope of the Calzetti extinction law (Calzetti et al., 2000), total SFRs are determined using $\text{SFR}_{total} = \text{SFR}_{2800} * 10^{20.4 * 1.8 A_v}$ where A_v and SFR_{2800} come from FAST and the 1.8 factor comes from the slope of the Calzetti extinction law to convert A_v into the UV. More information on the techniques used to implement EAZY and FAST can be found in Wuyts et al. (2011a), Dahlen et al. (2013), and Guo et al. (2013).

GALFIT (Peng et al., 2002) was used to fit a single component Sérsic fit to the 2-Dimensional galaxy light profiles of each Hydro-ART simulation and each GOODS-South object identified in the F160W SEXTRACTOR catalog (van der Wel et al., 2012). GALAPAGOS (Barden et al., 2012) was used as a wrapping routine to run GALFIT. GALAPAGOS estimates the sky value for the mosaic, runs SEXTRACTOR, makes cutouts of the observations and noise images for the GALFIT fits. GALAPAGOS uses the magnitudes, radii, axis ratios, and positions estimated by SEXTRACTOR as starting values for the GALFIT fits to reduce processing time and help ensure that GALFIT finds a global χ^2 minimum when fitting Sérsic profiles. These best-fit Sérsic profiles provide an estimated F160W magnitude (H_{F160W}), a global Sérsic index (n) describing the light profile shape, an effective radius (R_{eff}), and an axis ratio ($\frac{b}{a}$) (as well as their estimated errors) for each galaxy. The radii presented in this study are the semi-major axis containing half the F160W light in the ellipse of the best fit single-Sérsic model. The Sérsic index is the exponent in the Sérsic profile (Sersic, 1968) describing

how the intensity of light of a galaxy changes as a function of distance from the center. Lower Sérsic values indicate a flatter light profile in the center with a quicker drop off at larger radii. A Sérsic value of 0.5 describes a Gaussian profile. A Sérsic value of 1 is an exponential disk and is a good description of spiral, bulgeless disk galaxies in the local Universe. A Sérsic value of 4 describes the de Vaucouleurs profile and has been used historically in literature as a description of traditional elliptical galaxies in the local Universe. For more details on how GALFIT and GALAPAGOS were run on the GOODS-South galaxies, see van der Wel et al. (2012) and for details on how GALAPAGOS was run on the CANDELized Hydro-ART simulations, see Kollipara et al. (in prep).

2.3 Morphology Classifications

To classify galaxies in the simulations and CANDELS survey, a visual morphology classification system was developed called the ‘Morphology Working Group Unified System’ (MWGUnified). This system was developed for the CANDELS observations and while applied to galaxies at all redshifts, was developed specifically with $z \sim 2$ galaxies in mind. The MWGUnified system ensures that the often clumpy and asymmetric nature as well as the high fraction of interactions and mergers of $z \sim 2$ galaxies is properly recorded in the visual inspections. This visual classification system was applied to all of our Hydro-ART $z=1.4-2.6$ simulations and all of the observed GOODS-South galaxies with a $H_{F160W} \leq 24.5$. This magnitude limit for the observations was adopted from the

van der Wel et al. (2012) study that found this magnitude to be the limit for the robustness of galaxy size and profile fits by GALFIT for CANDELS HST WFC3 observations. Each simulated and observed galaxy was classified by at least three classifiers (average was five classifiers per galaxy). By comparing and combining the various classifications, we are able to create a final catalog of visual classifications for all $z \sim 2$ simulations and observations.

The visual classifications of each galaxy were based primarily on cutouts from the F160W 2-orbit mosaic that covers the full CANDELS GOODS-South area including the ERS, and UDF regions. Postage stamps were made in F606W (V-Band), F850L (z-Band) from archival ACS data (Giavalisco et al., 2004) and in F125W (J-Band) and F160W (H-band) from the CANDELS WFC3 observations. The visual classifications were based primarily on the H-Band cutouts with the other bands being used for supplemental information and to classify clumpy structure. The cutout sizes were scaled to each object using the semi-major axis (r_{sma}), the ellipticity (ε), and the position angle (Θ_{PA}) estimated by the SEXTRACTOR routine (as described in Peng et al. (2002)) with a minimum box size set to three arcseconds ($3''$).

$$\text{POSTAGE STAMP SIZE} \begin{cases} = 2.5r_{sma} * (|\sin(\Theta_{PA})| + (1 - \varepsilon) * |\cos(\Theta_{PA})|) \\ \geq 3'' \end{cases}$$

Using the V, z, J, and H postage stamps along with an image of the object's segmentation map (determined by SEXTRACTOR), each object was visually classified in terms of basic morphology, interactions, structural and image quality flags, and clumpiness/patchiness. Examples of all the visual morphology classes are pro-

vided in the Appendix. The basic morphology section allows classifiers to classify an object's global morphological shape in F160W as a spheroid, disk, irregular/peculiar, compact/unresolved, or unclassifiable or some combination thereof. Visually classified spheroids are defined as objects that are generally round and appear to have a smooth, centrally concentrated light profile. Disks are objects with clear disk structures or profiles that may or may not contain spiral arms and central bulges. Irregular objects are those that are not regular nor easily classified by one of the other core morphology classes. This class includes objects severely affected by mergers and interactions. Compact objects are objects that are either a clear point source (such as a star with Airy rings) or an object that is unresolved in F160W. Unclassifiable objects are problematic objects that can not be classified by any of the other morphological classes such as unreal objects caused by image artifacts and bad pixels or an object on the edge of the mosaic or an object with extremely low surface brightness. Classifiers base their classifications on the dominant object in F160W within the segmentation map and may select as many global morphology classifications as are applicable.

The interaction morphology class allows classifiers to identify objects that are interacting with neighboring objects, undergoing a merger, or have nearby objects without any visible sign of interaction. Classifiers select the degree of interaction (or lack of interaction) based on the F160W cutout stamps. Classifiers were to select one of the following: merger, interaction within the primary object's segmentation map, interaction beyond the primary object's segmentation map, non-interacting companion, or none. Mergers are defined as objects that are single objects (including sources with double

nuclei) that appear to have undergone a merger by evidence of tidal features/structures such as tails, loops or highly-irregular outer isophotes (note: all mergers are irregular but not all irregular galaxies are mergers). An interacting galaxy is defined as objects that appear to be tidally interacting with a companion galaxy. Interactions have clear signatures of tidal interaction; e.g., tidal arms, bridges, dual asymmetries, off-center isophotes, or otherwise disturbed morphology. If the 2 interacting objects are located within the same segmentation map then ‘interaction within the primary object’s segmentation map’ is selected. If the two interacting objects have been identified as separate objects in the segmentation map then ‘interaction beyond the primary object’s segmentation map’ is selected. A non-interacting companion is defined as objects that have a close companion (in projection), yet no evidence of tidal interaction or disturbed morphology is apparent. The companion galaxy may be within or beyond the primary galaxy’s segmentation map. If each neighboring galaxy resides in its own segmentation map, the companion segmentation map must be separated from the primary galaxy’s segmentation map by less than the diameter of whichever galaxy’s segmentation map is larger.

Image and quality flags allow the classifier to further comment on the structure and features of the objects as well as flag any potential problems/issues with the images. Quality flags are used to identify cases where the classifier believes their classification to be uncertain/unreliable. These cases include examples of a poorly deblended (both over and under deblended) objects by SEXTRACTOR in the segmentation map, image quality problems where nearby bright objects, an image edge, or other image defects are

inhibiting a reliable classification, and cases where the classifier is uncertain of his/her classification yet no image quality problem exists. K-Correct Flags are for cases where the difference in morphological structure between the F160W cutout and bluer bands is so severe that a classifier would select a different classification for that band. These flags are used to identify objects where galaxies do not appear in certain bands or appear but are drastically different from the F160W image. Structural flags are used to identify common object properties as well as to provide more details about the general morphology classification. The structure flags include tidal arms, double nuclei (within a single stellar envelope), asymmetric light distribution in F160W, spiral arm/ring, bar, point source contamination, edge-on disk, face-on disk, tadpole (object with at least a 2:1 axis ratio with a bright core at one end of an elongated structure), chain (elongated object with at least a 3:1 axis ratio and multiple bright clumps embedded in a considerable background envelope with no signs of a tidal interaction), disk-dominated (an object in which multiple morphology classifications were selected and the disk classification is the dominant class in F160W), and bulge-dominated (an object in which multiple morphology classifications were selected and the spheroid classification is the dominant class in F160W).

The clumpiness matrix is a method developed to allow classifiers to characterize the observed presence of clear clumps and/or patchy light distributions in the objects. The clumpiness classification is based largely on the bluer bands (F606W and F850L). Clumps are defined as clear self-contained, centrally concentrated knots of light while patches are defined as spotty, uneven light distributions within the profile. Patchiness

can be viewed as obscured/faded clumps. This difference between clumps and patchiness is used to help the classifier but there is no distinction made between clumps and patches when determining an objects degree of clumpiness. The classifier selects the degree of clumpiness (none, a couple clumps, many clumps) as well as the degree of patchiness (none, some, a lot) and is able to select multiple classes if unsure. The values are then averaged together to produce a single clumpiness/patchiness value for that classifier for each object.

The classifications from the over fifty classifiers were combined to create a single ‘metric’ visual morphology catalog which is publicly available. For all of the combined classifications provided in the ‘metric’ catalog, three different combined values were given based on the completeness/reliability of the individual classifiers. The ‘reliable’ values use only galaxy classifications in which the galaxy was fully classified (defined as having both a standard morphology classifications and clumpy/patchy classification) and the catalog/classifier is considered reliable ($\geq 85\%$ of galaxies in the catalog by that classifier were fully classified). These galaxy classifications can reliably be used for all parameters and flags. It was determined that if the classifier classifies both the morphology and the clumpiness/patchiness then he/she has gone through all four sections of the MWGUnified system and has thus provided a complete classification. The ‘all fully’ values use all galaxy classifications that are fully classified (defined as having both a standard morphology classifications and clumpy/patchy classification) including those fully classified in catalogs in which the classifier is not considered reliable ($< 85\%$ of the galaxies in the catalog were fully classified). With some care, these galaxy classifica-

tions may be used for all parameters and flags though they may contain some unreliable classifications. The ‘all’ values use all galaxy classifications - including incomplete classifications in which clumpy/patchiness, interaction, and flags were not classified. These galaxy classifications have only been classified using standard morphology classifications (disk, spheroid, irregular, compact, and unclassifiable) and should not be considered reliable for other measurements. The ‘metric’ catalog provides all three sets of values for all of the classifications but for this paper only the ‘all fully’ values are used. Mean values as well as the sigma of the distribution of the values between classifiers of the various morphology classes, interaction classes, flags, and clumpiness/patchiness were determined for each galaxy for all three classes of galaxy classification reliability. The complete ‘metric’ catalog of the MWGUNified visual classification system is released with this publication.

In addition to providing the combined mean values for the MWGUNified visual classification system, the catalog also includes several unique quantities derived from the combined classifications. A new measurement, Spheroidicity (\mathcal{S}), is designed to measure the gradient of object shapes from a pure traditional spheroid to a traditional disk. Bulge dominated and disk dominated flags are used in conjunction with spheroid and disk morphology classifications to assign Spheroidicity values for each classifier which are then combined with other classifiers to determine an object’s mean Spheroidicity. Below is a description for determining Spheroidicity:

$$\text{SPHEROIDICITY}(\mathcal{S}) = \begin{cases} 1.00 \text{ (Spheroid Only)} \\ 0.75 \text{ (Spheroid and Disk [Bulge Dominated])} \\ 0.50 \text{ (Spheroid and Disk [No Domination Flag])} \\ 0.25 \text{ (Spheroid and Disk [Disk Dominated])} \\ 0.00 \text{ (Disk selected only)} \end{cases}$$

In addition to Spheroidicity, several other metrics were derived for the ‘metric’ catalog. Irregularity(ι) quantifies how likely a galaxy was seen to be irregular and has the following values: an object classified as only irregular has $\iota = 1.0$, an object classified as irregular in addition to another global morphology class has $\iota = 0.5$, an object not classified as irregular has $\iota = 0.0$. Interaction Class (\mathcal{I}) measures the degree of interaction an object is experiencing. Mergers have $\mathcal{I}=1.0$, interactions within a common segmentation map have $\mathcal{I}=0.75$, interactions between objects with independent segmentation maps have $\mathcal{I}=0.5$, objects with nearby non-interacting companions have $\mathcal{I}=0.25$, and objects classified as ‘None’ in the interaction section of the MWGunified system have $\mathcal{I}=0.0$. A combined interaction flag was also created to combine the two interaction classes (interactions between 2 objects within a common segmentation map and interactions between objects in two separate segmentation maps). Lastly, a single Clumpiness (\mathcal{C}) quantity was included in the ‘metric’ catalog to combine the clumpiness/patchiness values selected by the classifiers. The clumpiness/patchiness matrix selections made by each classifier were assigned values and averaged together before being combined with the other classifiers to determine a single Clumpiness value for each galaxy. A Clumpiness value of 0 refers to an object with no clumps or areas of patchiness while a Clumpiness value of 1 refers to an object with multiple clumps and

Table 2.1: Clumpiness Matrix (\mathcal{C})

	No Major Clumps	1-2 Major Clumps	3+ Major Clumps
No Patchiness	0.00	0.25	0.50
Low/Moderate levels of Patchiness	0.25	0.50	0.75
High Levels of Patchiness	0.50	0.75	1.0

a high degree of patchiness. As discussed earlier in this section, Clumpiness is based in large part on the bluer images (F606W and F850L).

2.3.1 Sample Selection

Of the 34,930 independent objects identified by SEXTRACTOR in the F160W GOODS-South CANDELS mosaic (CANDELS ‘wide’ + CANDELS ‘deep’ + ERS + UDF), there are 7628 galaxies with $H_{F160W} \leq 24.5$ and were visually classified. Of these 7628 visually classified galaxies, 6095 had F160W fits from GALFIT that were deemed reliable (flag=0), and had reliable rest colors, star formation rates, photometric redshifts, and stellar masses (as calculated by EAZY and FAST - see previous chapter). The galaxy sample has been shown (Wuyts et al. (2011a) and Newman et al. (2012)) to be $> 90\%$ complete at $z=1.4-3.0$ at stellar masses $> 10^{10}M_{\odot}$. Figure 2.1 plots the full $z\sim 2$ sample as a function of F160W magnitude and the derived stellar mass versus color. Investigating the galaxies that were visually classified ($H_{160W} < 24.5AB$) we find that our high redshift sample does not start becoming significantly incomplete until stellar masses below $10^{9.4}$. This figure emboldens us to lower our completeness limit from 10^{10} to $10^{9.4}$. This stellar mass cut of $10^{9.4}$ brings our total sample to 2727 galaxies with enough classifiers to be considered reliable. Focusing this study on the $z\sim 2$ ($z=1.4-2.6$) Universe reduces this number to 1131 galaxies. For reasons that will be discussed in the next

section, the Hydro-ART simulations are only able to make star-forming galaxies. The simulations are unable to effectively quench star formation and can not make quiescent spheroids. In order to compare the simulations to a similar population, we exclude the quiescent galaxies from the GOODS-South observations. To make this division, we use a U-V vs V-J color-color cut. This UVJ cut has been used in previous works (Labbé et al. (2006), Wuyts et al. (2007), Williams et al. (2009), Patel et al. (2011), and Patel et al. (2012)) to separate between a quiescent population in the upper region and an extended sequence of star-forming galaxies from the blue systems to the dusty reddened systems located below the quiescent sample. Following Patel et al. (2013), we isolate our quiescent population using the UVJ selection criteria determined by Williams et al. (2009) for galaxies $1.0 \leq z < 2.0$ ($(U-V) > 0.88(V-J) + 0.49$, with $U-V \geq 1.3$ and $V-J \leq 1.6$). Making this UVJ cut, we are left with a $z \sim 2$ sample of 891 star-forming galaxies. One final conservative cut is made to ensure the reliability of classifications and colors. This ‘clean’ sample removes all galaxies that have questionable photometry/classifications as well as objects thought to be undergoing major interactions or mergers. The ‘clean’ sample is roughly half the size (644 visually classified) of the full $z \sim 2$ population (1131 visually classified) and enables us to ensure that observed trends are not the result of bad photometry or interactions. Performing the ‘clean’ cut on the star-forming sample reduces the total number of $z \sim 2$ galaxies from 891 to 547 galaxies. These 547 $z \sim 2$ star-forming galaxies are the final sample used in this study. This is the result of conservative cuts to ensure that the observed EAZY colors, photometric redshifts, stellar masses, rest colors, star formation rates, GALFIT parametric fits, visual classifications, and mass

and redshift ranges are reliable and complete.

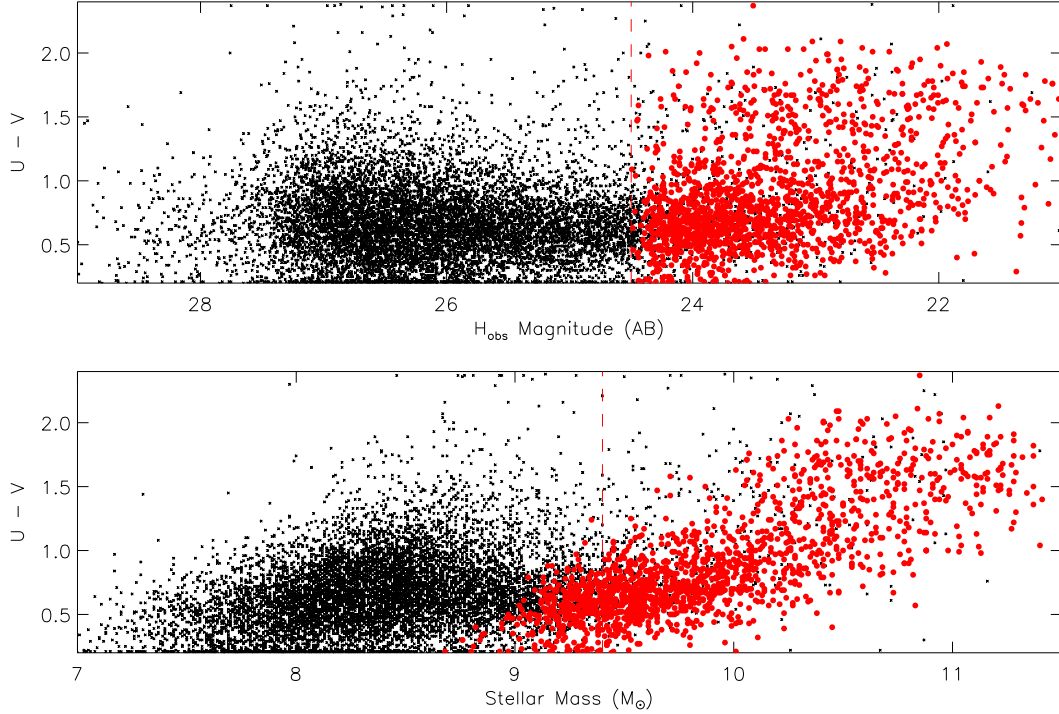


Figure 2.1: Sample Selection. The black points represent the 11706 objects identified in the GOODS-South region using SEXTRACTOR that were fit with EAZY to have photometric redshifts between $z=1.4$ and $z=2.6$. The red points represent the 1695 galaxies in this redshift range that had an observed F160W magnitude ≤ 24.5 AB and were successfully visually classified. As can be seen from the bottom plot, there does not seem to be a significant population of red galaxies between $10^{9.4}$ and $10^{10.0}$. Thus the adopted F160W magnitude cut of 24.5 AB gives a fairly complete visually classified sample down to a stellar mass of $\sim 10^{9.4}$. We use this $M_{\text{stellar}}=10^{9.4}$ as our lower mass limit.

The 38 Hydro-ART simulations were ‘CANDELized’ and classified using the MWGunified system for 6 different viewing angles (1 face-on, 1 edge-on, and 4 random) for each available time step between $z=1.4$ - 2.6 . This gave a total sample of 2046 simulated $z\sim 2$ galaxies of which 1982 were considered to have reliable visual and photo-

metric classifications. The majority of our comparisons to GOODS-South observations will only use the random camera angles so as to avoid the bias of over representing face-on and edge-on systems. This random camera angle population has 1364 galaxies of which 1325 have reliable visual classifications.

2.3.2 Hydro-ART Simulation Caveats

The Hydro-ART simulations have known issues that limit their ability to be a truly representative sample of $z \sim 2$ galaxies. These caveats/issues are discussed in more detail in Ceverino et al. (2012) but a brief overview of their effects will be provided here. The MW, SFG, and VL families (Generation 1) of simulations have halo masses between 10^{10} - $10^{13} M_{\odot}$ and were all run without radiation pressure and had a high star formation efficiency. This resulted in an over production of stars at early times by upwards of a factor of 10 (when compared to abundance-matching estimates). The VELA simulations (Generation 2) also have no radiation pressure included and have moderate star formation efficiency. These simulations have halo masses ranging from 10^{11} - $10^{12} M_{\odot}$. The result of this early over production of stars is that the stellar mass for the simulations is too high for their given halos. None of the simulations include quenching mechanisms such as AGN able to shut down star formation. This means the simulations are unable to produce quenched systems. Therefore, we will only compare our Hydro-ART simulations to star-forming galaxies observed in GOODS-South. Our simulations may not be a representative sample of $z \sim 2$ galaxies but they are still useful to probe galaxy formation among massive star-forming galaxies. To partially correct

the stellar masses of the Hydro-ART simulations we scale the $\frac{M_{stellar}}{M_{halo}}$ for each family (MWG, SFG, VL, and VELA) of simulations onto the Behroozi et al. (2013) relation for the $z \sim 2$ universe. Figure 2.2 shows the $\frac{M_{stellar}}{M_{halo}}$ of our Hydro-ART simulations before and after this forced scaling onto the Behroozi curve. To move the simulations inline with the Behroozi curve, the stellar masses needed to be reduced by a factor of 3-10. See Behroozi et al. (2013) for more details on how this stellar mass to halo mass relationship was determined using abundance matching methods. This scaled stellar mass is the mass used throughout this work for all Hydro-ART simulations.

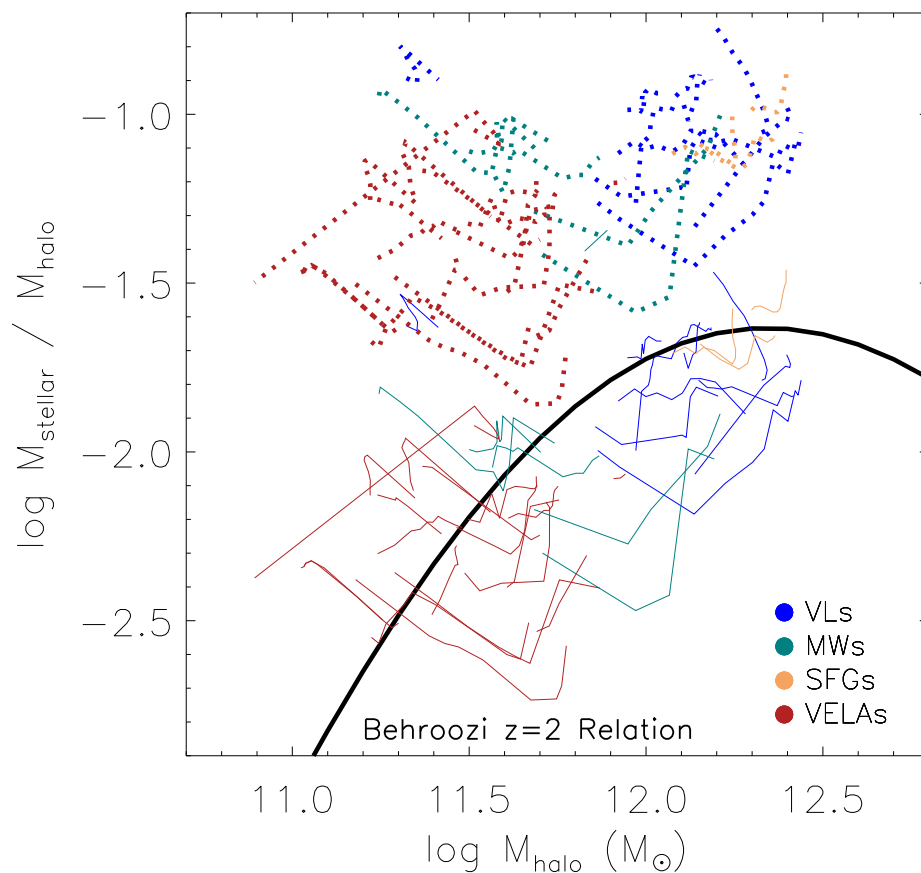


Figure 2.2: $M_{stellar}$ to M_{halo} fraction for each of the Hydro-ART Simulations. The dotted lines are the individual galaxies in each family of simulations (VL, MW, SFG, VELA) at each epoch from $z=1.6-2.6$. The solid black curve is the stellar mass to halo relation at $z\sim 2$ found using abundance matching methods by Behroozi et al. (2013). The Hydro simulations are clearly over producing stars leading to stellar masses factors of 3-10 times the Behroozi relation. To better match the Behroozi relation, each family of simulations are scaled together to the Behroozi curve. This is shown by the solid colored lines. These scaled stellar masses are adopted throughout this work.

2.4 Global Parameters

Figures 2.3 to 2.8 show the global properties of the GOODS-South galaxies and the Hydro-ART simulations in 5-part plots involving U-V and V-J colors, specific star formation rates (sSFR), effective radii, stellar mass, Sérsic index, and visual classification. Figure 2.3 and 2.4 show where the full ‘clean’ $z\sim 2$ GOODS-South galaxies fall colored by visual spheroidicity classification and Sérsic index, respectively. Figures 2.5 and 2.6 show the same ‘clean’ GOODS-South population but remove the quiescent population using UVJ cuts. Figures 2.7 and 2.8 show where the Hydro-ART simulations lie in these diagrams colored by visual classification and Sérsic index, respectively. To probe galaxy shape, we primarily used our visual classification system. We divided our sample into three types. Disk-like objects had total spheroidicity values from all reliable classifiers in the ‘all fully’ catalog of 0.3 and below. Spheroid-like objects had total spheroidicity values of 0.7 and above and the region between disk-like and spheroid-like with $\mathcal{S}=0.3-0.7$ were called transitional/intermediate objects. To supplement this visual classification system, we used Sérsic indices as well. We divided our galaxies into five classes by Sérsic: Sub-Disk (gaussian-like profiles) have $n\leq 0.8$, Disks have $0.8\leq n<1.5$, Transitional objects have $1.5\leq n<2.5$, Spheroidal galaxies have $2.5\leq n<5.0$, and Super-Spheroidal galaxies have $n\geq 5.0$. These five figures (Color-Mass, Color-Color, sSFR-Mass, R_{eff} -Mass, and R_{eff} -sSFR) have been shown in the previous chapter and earlier works to be very powerful in separating and identifying different galaxy populations.

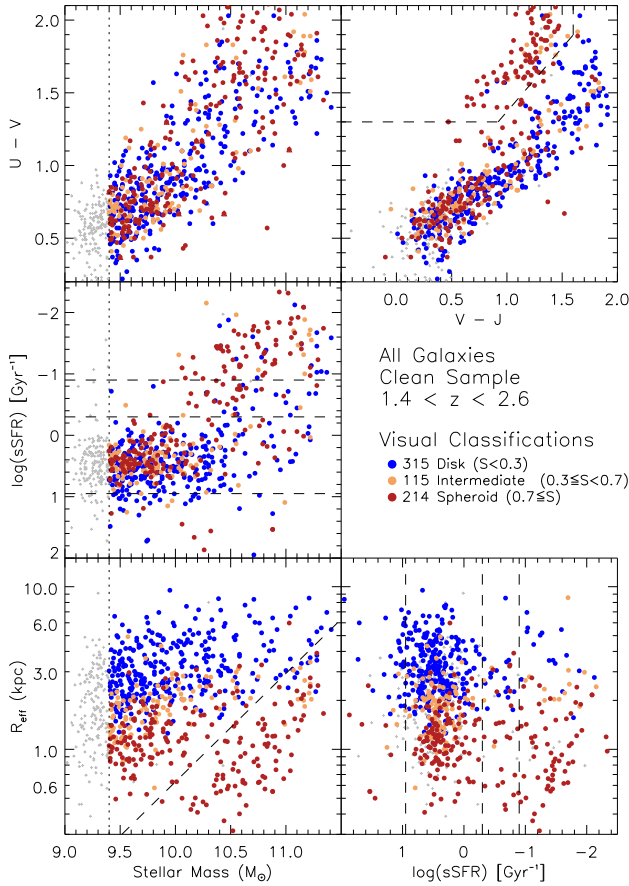


Figure 2.3: Global Properties of Full ‘clean’ $z \sim 2$ GOODS-South Sample by Visual Classifications. This is the full ‘clean’ reliable sample removing irregular, interacting, and otherwise untrustworthy classifications to ensure results are not skewed. Grey points are below the mass threshold of $9.4 M_{\odot}$. Three different methods could be used to separate out the quiescent GOODS-South galaxies. We chose to use Williams et al. (2009) to separate the quiescent population from the dusty star-forming galaxies in the UVJ color-color plot. Alternatively, we could use the sSFR divisions between star-forming ($\log \text{sSFR} > 0.3$) (with highest 10% of star formers > 1), transitional ($-0.9 > \log \text{sSFR} \geq -0.3$), and quiescent ($\log \text{sSFR} < -0.9$). Additionally, quiescent galaxies are separated from the star-forming sample in $R_{\text{eff}}-M_{\text{stellar}}$ space by adopting a dividing line from Barro et al. (2013) of $\log M_{\text{stellar}}/R_{\text{eff}}^{1.5} = 10.3 M_{\odot} \text{kpc}^{-1.5}$ - making a quiescent ‘red triangle’ in the lower right of the diagram. All three methods are efficient at removing quiescent populations and select a similar population (see previous chapter for more details). The visual classifications highlight an additional spheroidal population in addition to the quiescent spheroids. There is also an apparent radius bias towards identifying all small galaxies as spheroidal.

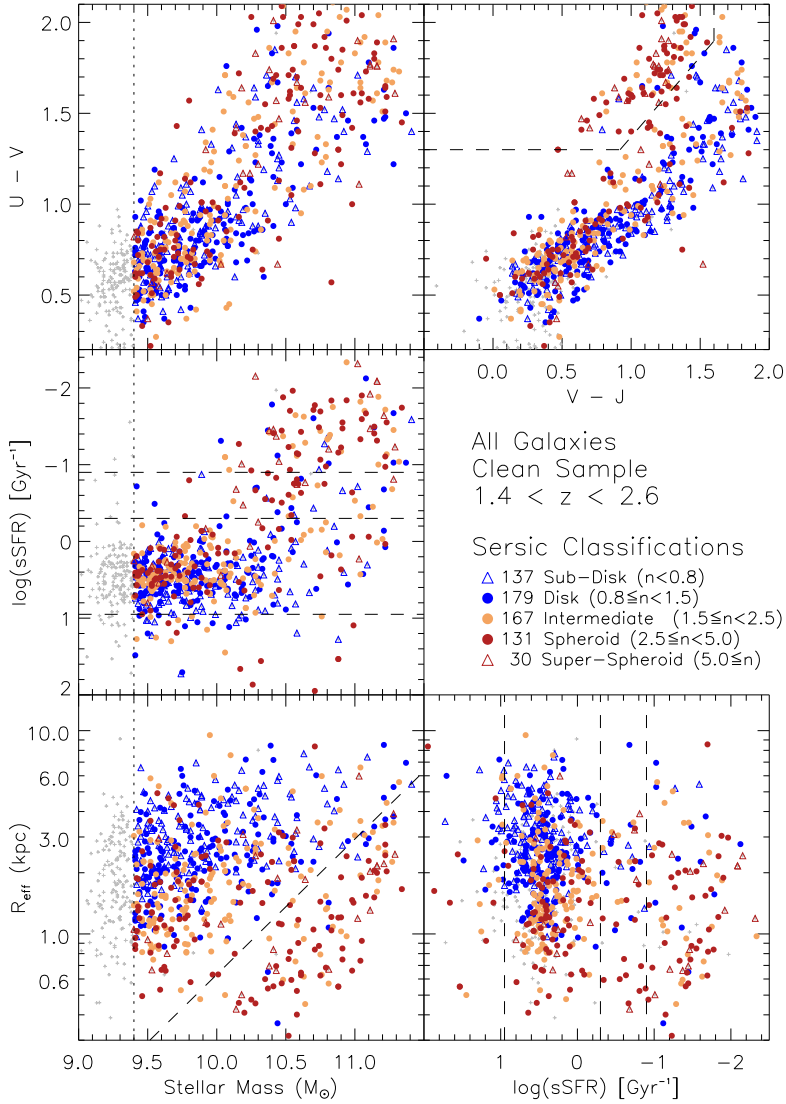


Figure 2.4: Global Properties of Full ‘clean’ $z \sim 2$ GOODS-South Sample by Sérsic Indices. See Figure 2.3 for plot details. The colors correspond to the Sérsic index of each GOODS-South galaxy. Like Figure 2.3, the divisions adopted in the UVJ, sSFR, and $M_{\text{stellar}}-R_{\text{eff}}$ diagrams to isolate quiescent populations nicely divide our $z \sim 2$ galaxies into morphologically different regions as well. Many galaxies that were visually identified as spheroidal are classified as intermediate in Sérsic. The visual classification bias for spheroids at low radii is not present for Sérsic.

Figure 2.3 and 2.4 show where the full ‘clean’ $z\sim 2$ GOODS-South galaxies fall colored by visual spheroidicity classification and Sérsic index, respectively. These figures illustrate the same general $z\sim 2$ galaxy trends that were studied in depth in the previous chapter. I will summarize briefly some key features of these figures before continuing to compare to the Hydro-Art simulations. In both visual classifications and Sérsic index, there is a bimodal spheroid population of galaxies between the red, quiescent, low sSFR traditional spheroidal galaxies and a population of spheroids that have blue color, high sSFR values and occupy the same color-color space as star-forming galaxies. Thus, there exists a population of spheroids (both in terms of Sérsic and spheroidicity) that are in the quiescent region of the UVJ and the quiescent region of the sSFR plots. In addition, there is also a large population of spheroids concentrated at the lower left of the UVJ color-color diagram (grouped with the star-forming primarily disk objects), and the lower mass ($<10^{10}$) and star-forming region of the sSFR diagrams. These compact star-forming ‘blue nuggets’ are the dominant form of spheroidal galaxies accounting for nearly 2/3 of all spheroids at $z\sim 2$ in our sample. This population is inline with Wuyts et al. (2011a) in which they discussed a population of compact, high Sérsic index, galaxies with enhanced star formation rates at $z\sim 2$. Note that this population for us is independent of whether we use visual classification or Sérsic fits to identify the spheroids. There is a possible R_{eff} bias in our visual classifications with almost all compact objects ($R_{eff} < 1$ kpc) being classified as spheroidal. This result is expected since compact objects are all defined to be at or below the resolution limit (0.17”) of F160W. This radii bias could account for a misclassification of star-forming,

low mass, small radii disks as spheroids and thus artificially create a blue spheroid population. This blue spheroid population, however, is also seen when using Sérsic indices to identify spheroids. Unlike the visual classifications, GALFIT is able to fit objects below the resolution limit of the F160W mosaics assuming the psf is well known (van der Wel et al., 2012). Internal tests show that the Sérsic and radii measured from GALFIT differ when the psf is blurred but the results do not change significantly enough under realistic psfs to affect the observed trends. We acknowledge the limitation of the MWGunified system for unresolved systems and use Sérsic as a check for all compact objects with high spheroidicity. In addition to compact objects being visually classified as spheroidal, the visual classification system has a radii dependence across all morphological classes. The mass-radii plot in Figure 2.3 illustrates a progression observed at all masses from being spheroid dominated at small radii to intermediate dominated at larger radii to being disk dominated at the largest radii. This clear radii dependence in our visual classifications is not observed in Figure 2.4 where Sérsic is used. Though systems with smaller R_{eff} do tend to have Sérsic values that are intermediate or spheroidal, the classes are mixed across the various radii and no clear transitions are present like in the visual classification case. This radii bias is clearly a limitation for accurately classifying all galaxies at any radii using a visual classification method but is particularly apparent for unresolved systems.

As shown in other studies (Patel et al., 2012) the UVJ diagram separates galaxies into a star-forming main sequence and a quiescent region. The V-J color separates between red galaxies in U-V colors that are red due to quiescence and those that are

reddened by the effects of dust. Our figures show that $z \sim 2$ galaxy morphology also divide between these regions. The spheroidicity metric places a nearly uniform sample of spheroidal galaxies in the quiescent region of the UVJ diagram (above the dotted lines). The lower left portion of the star-forming continuum in the UVJ diagram contains large numbers of disks, intermediate, and spheroids (blue nuggets). The upper right portion of the UVJ diagram has been shown (Brammer et al., 2011) to consist of star-forming galaxies that are being reddened by dust. We find that this ‘dusty’ region of the UVJ diagram contains galaxies mostly visually classified as disks with 10-20% classified as intermediate with the spheroidal population along the border with the quiescent region. Similarly, in Sérsic index, this dusty region is made up mostly of objects with disky and intermediate Sérsic indices. The population of UVJ quiescent galaxies matches well with the sSFR identified quiescent population as well as with the ‘red triangle’ of galaxies in the R_{eff} - $M_{stellar}$ diagram. The previous chapter discusses these quiescent populations in more detail. The UVJ diagram does an excellent job at $z \sim 2$ separating between red dusty star-forming disky systems and the quiescent spheroidal systems. This diagram was used to remove these quiescent systems from the GOODS-South population so we only compare star-forming GOODS-South galaxies with the Hydro-ART simulations. This UVJ cut to our GOODS-South sample to include only star-forming galaxies is shown in Figure 2.5 and 2.6 and is referred to as our star-forming ‘clean’ sample.

The R_{eff} vs $M_{stellar}$ diagram cleanly separates our quiescent sample as well. Recent studies (Wuyts et al. (2011a), Barro et al. (2013), and Williams et al. (2010)) have shown that separate size-mass relations are followed by star-forming and quiescent

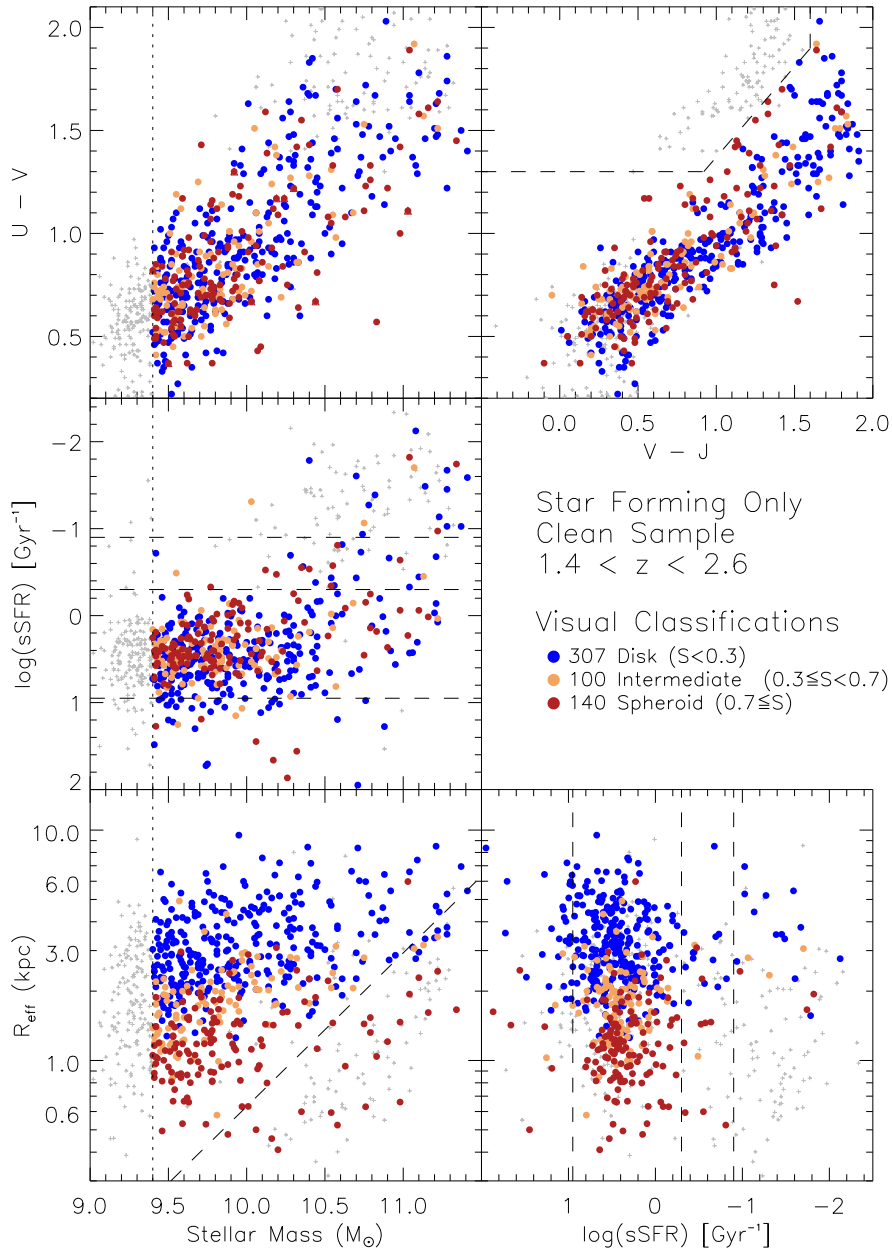


Figure 2.5: Global Properties of Full ‘clean’ $z \sim 2$ Star-Forming Only GOODS-South Sample by Visual Classification. See Figure 2.3 for details. The quiescent galaxies were isolated using UVJ color-color cuts following Williams et al. (2009) and are shown in grey. The colors show the visual classification for each galaxy.

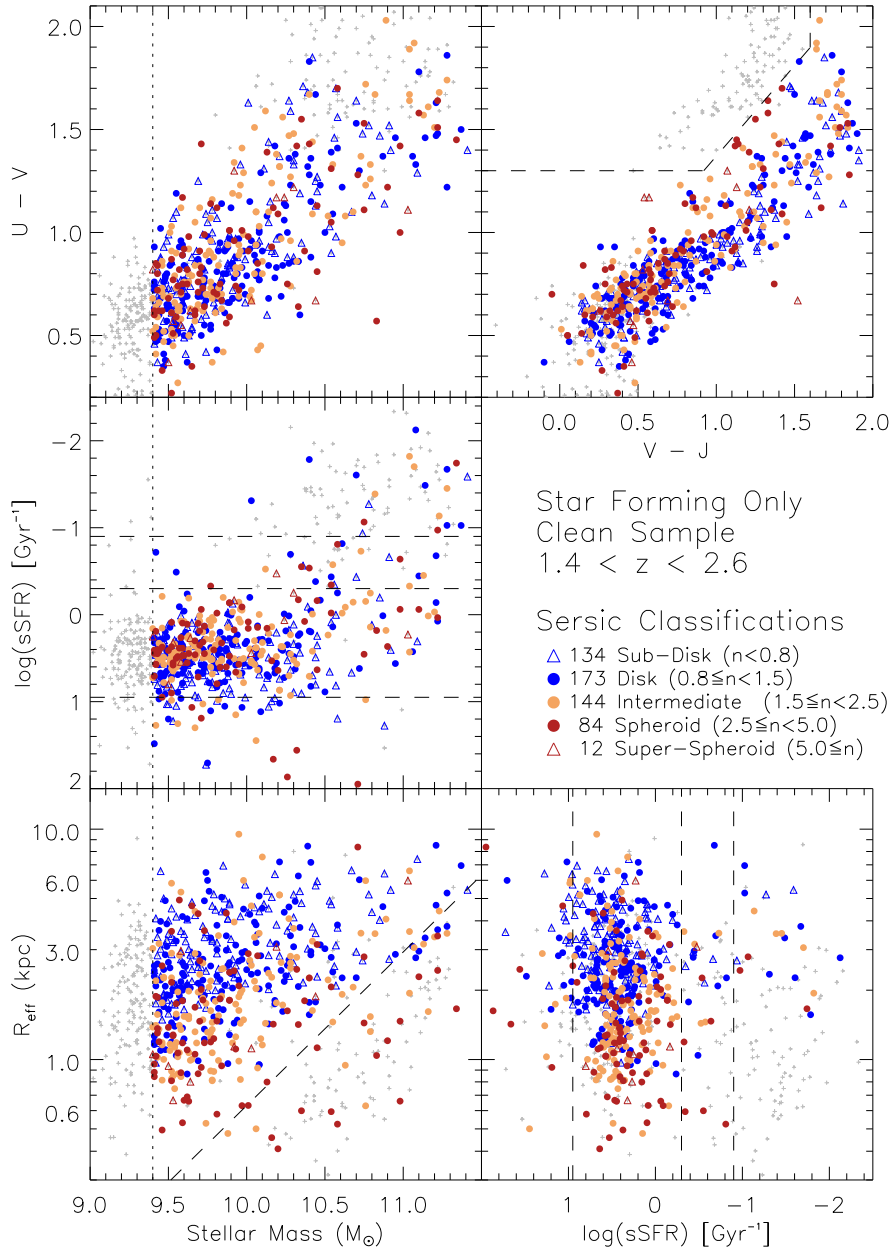


Figure 2.6: Global Properties of Full ‘clean’ $z \sim 2$ Star-Forming Only GOODS-South Sample by Sérsic Index. See Figure 2.5 for details. The colors represent the various populations identified using Sérsic index.

galaxies at the local and $z \sim 2$ Universe. Our results are inline with these findings and a clear separation exists between the star-forming sequence at lower masses and larger radii and the quiescent galaxies in the lower right at higher masses and smaller radii. The gap between the star-forming and quiescent populations in size-mass is fairly wide at $z \sim 2$ and thus the exact slope and zero point of this division is not shown to change the findings. We adopt a dividing line from Barro et al. (2013) of $\log M_{\text{stellar}}/R_{\text{eff}}^{1.5} = 10.3 \text{ M}_{\odot} \text{ kpc}^{-1.5}$ which is inline with previous dividing criteria found using $M_{\text{stellar}}/R_{\text{eff}}$ and $M_{\text{stellar}}/R_{\text{eff}}^2$ (Franx et al. (2008) and Newman et al. (2012)).

These general $z \sim 2$ trends in GOODS-South observations are explained in more detail in the previous chapter. Figures 2.7 and 2.8 show where the Hydro-ART $z \sim 2$ simulations fall in these plots. As discussed in the previous section, the stellar masses for these simulations are not reliable. The masses being used are those corrected to the Behroozi et al. (2013) curve (see previous section) but because the simulations are forming an unrealistically large fraction of the baryons into stars, the simulations themselves are not entirely realistic. Questionable mass values affect not only the stellar mass plots but also the sSFR values. Though the absolute positions may not be reliable, it is reassuring to note that our simulations do not seem to have sSFR resembling quenched GOODS-South galaxies nor are they in the quenched ‘red triangle’ region in the size-mass plot. The simulated galaxy population is very tight in the UVJ color-color diagram and the slope of this population is too steep compared to the observed star-forming sequence in GOODS-South. The Hydro-ART simulations have a variety of halo sizes and histories but they occupy a very narrow space in the UVJ diagram. Compared

to the observed GOODS-South galaxies, the U-V color is too high for given V-J and there are no simulations with the redder V-J colors expected for dusty star-forming galaxies. All of these simulations are blue star-forming galaxies so they are expected to have blue colors in both U-V and V-J. These blue galaxies have similar underlying spectra to each other but dust will redden their appearance and cause them to move to the upper right in the UVJ diagram following the Calzetti dust law (Calzetti et al., 2000). SUNRISE takes dust into account when generating magnitudes and images but it was unable to recreate the slope of the star-forming sequence observed in GOODS-South in the UVJ plots in Figures 2.3 and 2.4. This issue with the dust (so called ‘grey dust’ excessively absorbing red wavelengths) was probed in great detail by Chris Moody in his PhD dissertation (Moody 2013).

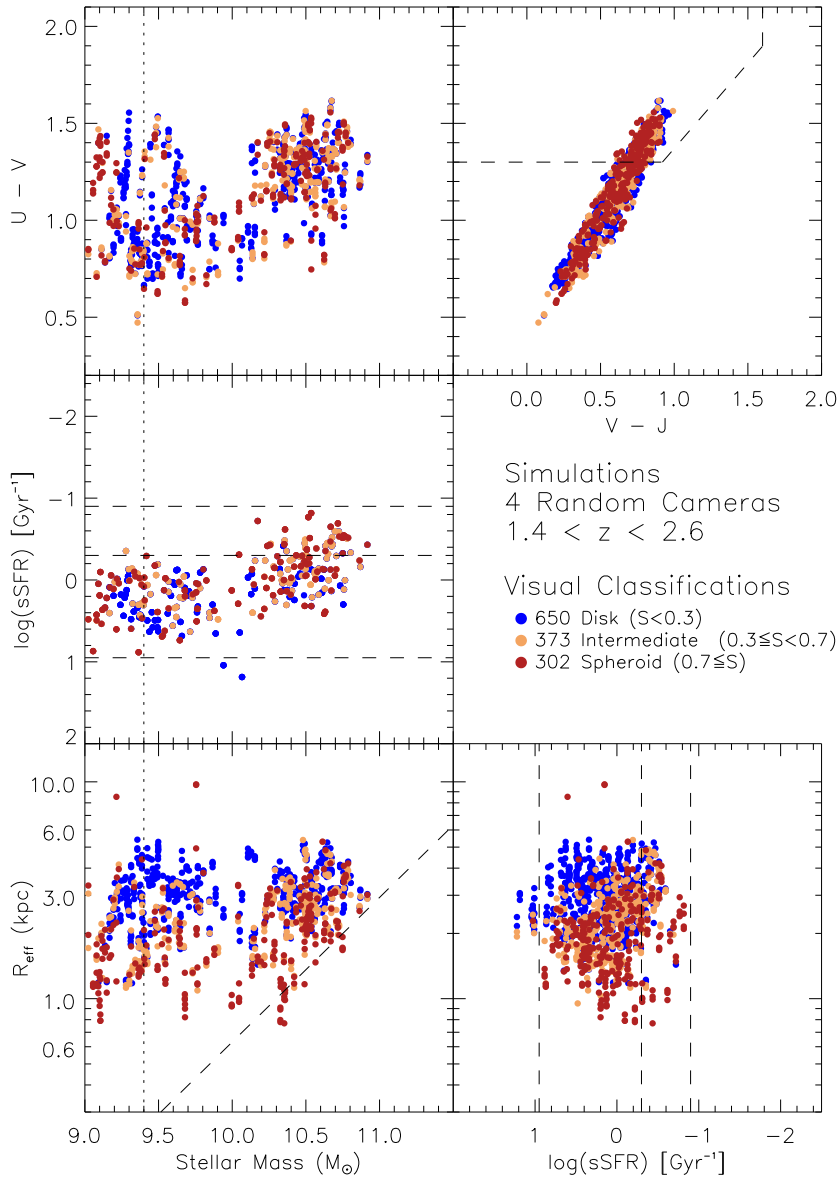


Figure 2.7: Global Properties of the Hydro-ART $z \sim 2$ Simulations by Visual Classification. See Figure 2.3 for details. The simulations do not recreate the UVJ color-color star-forming sequence found in Figure 2.3 - the simulations are too red in U-V at a given V-J which results in the reddening angle to be too steep. Also apparent is the narrow radii range of galaxies produced by the simulations when compared to the GOODS-South observations. The point colors represent the various visual classifications.

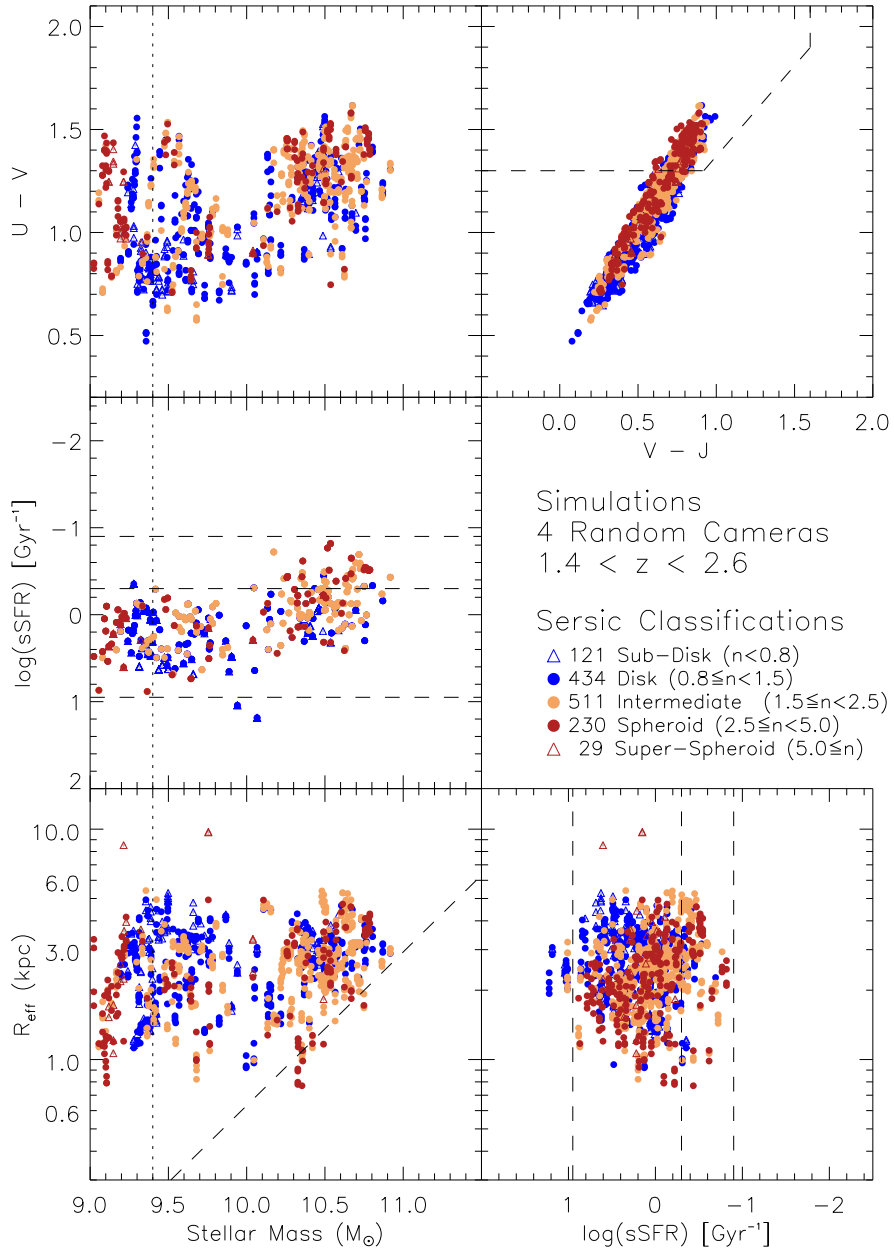


Figure 2.8: Global Properties of the Hydro-ART $z \sim 2$ Simulations by Sérsic Index. See Figure 2.7 for details. The colors depict the galaxy populations identified by Sérsic indices.

2.5 Visual Classifications and Sérsic

Single component Sérsic profiles have been used to separate between elliptical/spheroidal galaxies and disk structures. A Sérsic index (n) of 4 corresponds to a de Vaucouleurs profile and has been shown in the local Universe to correspond well with elliptical structures. A Sérsic index of 1 is an exponential profile and corresponds well with spiral disk galaxies in the local Universe. In this way, the Sérsic index can be used to identify galaxies with higher Sérsic values as more elliptical-like and galaxies with lower Sérsic values as more disk-like.

Figures 2.9 and 2.10 plot Sérsic vs R_{eff} colored according to the galaxies's visual classifications. Figure 2.9 plots the GOODS-South 'clean' star-forming sample and Figure 2.10 displays the 4 random camera angles for the Hydro-ART simulations. In both figures, there is a correlation between Sérsic and visual classifications. Galaxies with higher Sérsic indices tend to be classified as spheroidal with very few disk systems being identified above a Sérsic index of 2. The majority of disk systems have Sérsic values below $n=1.5$. This division between disk and spheroidal systems is more pronounced in the GOODS-South galaxies.

The measured R_{eff} distribution of the Hydro-ART simulations is significantly more narrow than in the GOODS-South observations. Very few simulations have $R_{eff} < 1.0$ kpc or > 4.0 kpc. Despite this narrow R_{eff} distribution, a visual classification dependence on R_{eff} is apparent for the simulations. The majority of objects in both the simulations and GOODS-South observations are usually classified as spheroidal

below a R_{eff} of 2 kpc. This effect could be the result of resolution bias on visual classifications. The spatial resolution limit of the F160W observations is $0.17''$ which is ~ 1.5 kpc at $z=2$. Below this size, the visual classifications are unreliable and there is a strong bias toward spheroidal classifications. This could produce an artificial visually identified compact spheroidal population as compact disks are misclassified as spheroids. As mentioned in the previous section, GALFIT Sérsic fits do not suffer from this bias at low radii.

In addition to compact objects being visually classified as spheroidal, the visual classification system has a radius dependence on all morphological classes. Both Figures 2.9 and 2.10 illustrate a progression from being spheroid dominated at small radii to intermediate dominated at larger radii to disk dominated at the largest radii. This clear radii dependence in our visual classifications is not mirrored as strongly in the Sérsic index. Though systems with smaller R_{eff} do tend to have Sérsic values that are intermediate or spheroidal, the classes are mixed across the various radii and no clear transitions are present like in the visual classification case. This radii bias is clearly a limitation for accurately classifying all galaxies at any radii using a visual classification method but is particularly apparent for unresolved systems.

The distribution of galaxy classes for simulations is more skewed towards transitional objects compared to the GOODS-South galaxies. For the GOODS-South $z\sim 2$ ‘clean’ star-forming galaxies, 55% are disk, 18% are intermediate, and 26% are spheroidal. The Hydro-ART $z\sim 2$ simulations are 49% disk, 28% intermediate, and 23% spheroidal. The simulations have a larger intermediate population of galaxies than the

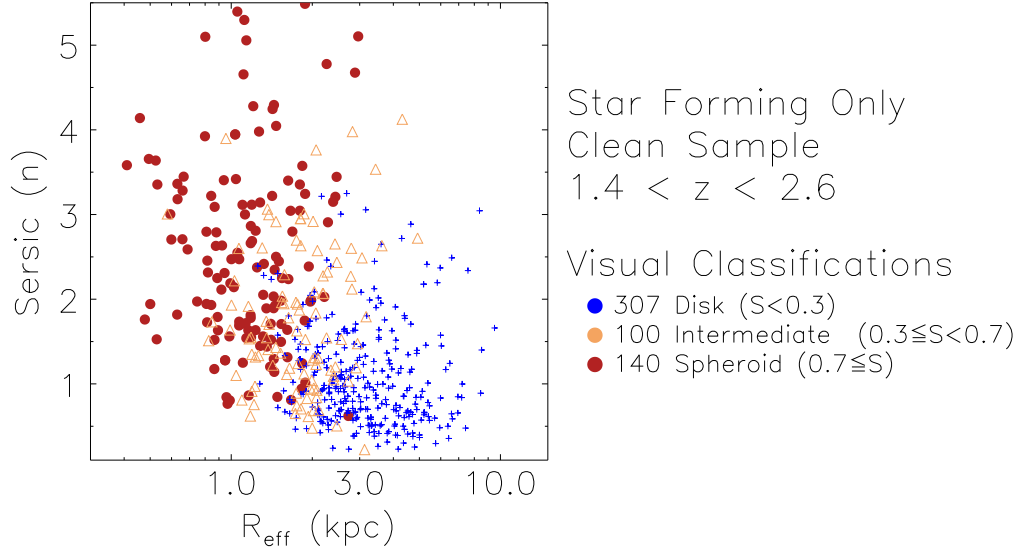


Figure 2.9: Sérsic - R_{eff} of Various Visual Classifications for the ‘clean’ Star-Forming GOODS-South Galaxies. A general radius trend exists for $z \sim 2$ star-forming galaxies going from spheroid dominated systems with small radii to intermediate dominated at larger radii to disk dominated with the largest radii. Sérsic and visual classification correspond well with the majority of disks having $n \leq 1.5$ and spheroids having larger Sérsic values. Systems with small radii are biased to be visually classified as spheroids.

observations. We can see this population of galaxies in Figure 2.10 as the concentration at $n=1.5-2.0$ and moderate $R_{eff}=1.5-3.0$ kpc. This concentration is not apparent in Figure 2.9 and does not seem to exist in the GOODS-South $z \sim 2$ galaxies.

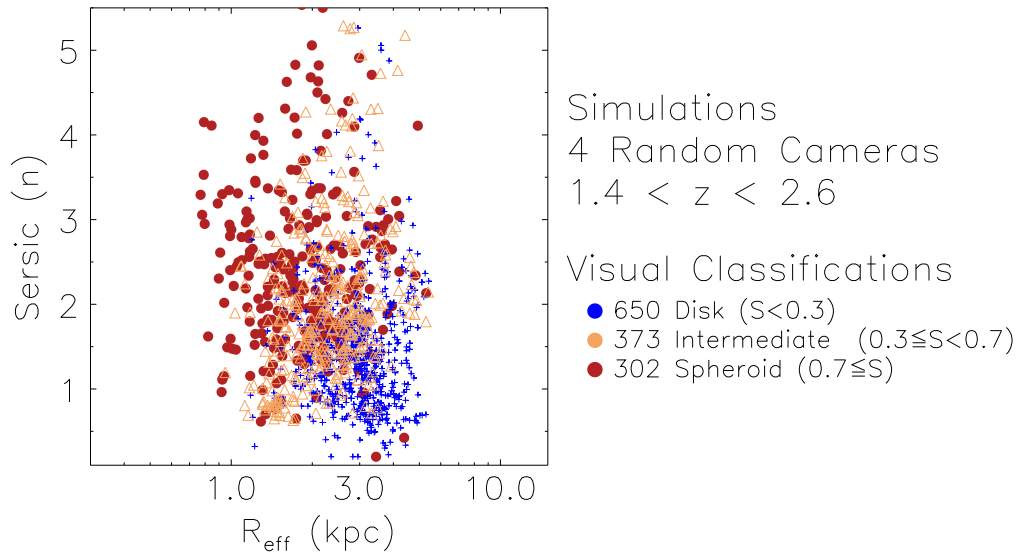


Figure 2.10: Sérsic - R_{eff} of Various Visual Classifications for the Hydro-ART Simulations. The radii measured for Hydro-Art galaxies are all intermediate between 1 and 3 kpc. The diversity of size observed in GOODS-South is not reproduced by the simulations. General trends between Sérsic and visual classifications exist as shown in Figure 2.9 but simulations exhibit an additional large intermediate class of galaxies at moderate radii and Sérsic that is not observed in the GOODS-South observations.

2.6 Clumpiness

The visual classification system we designed put emphasis on being able to characterize the clumpy nature of $z\sim 2$ galaxies. Mandelker et al. (2013) and Moody et al. (in prep) demonstrated that these Hydro-ART simulations do possess clumpy star-forming regions formed in situ in the disks by gravitational instabilities. Once we CANDELize the simulations and visually observe them, we want to test whether these clumps will still be visible. The clumpy-patchy classification matrix used was collapsed into a single clumpiness value (\mathcal{C}) as described in Section 3.3. Clumpy visual classifications was based largely on the bluer bands (F606W and F850L) which correspond to rest-frame UV light at $z\sim 2$. These clumpy UV bright regions are tracing star formation activity in contrast to H160W tracing the older stellar mass distribution. Using this clumpy measurement of the bluer light, we are able to identify galaxies undergoing strong regional star formation. Internal tests and visual confirmation of a subsample of the GOODS-South catalog showed that $\mathcal{C} > 0.2$ acted as a good lower limit to identify clumpy galaxies but not include spurious galaxies misidentified by individual classifiers. Galaxies possessing clumps or patchy structure had $\mathcal{C} > 0.2$ while smooth galaxies with no apparent clumpy regions had $\mathcal{C} < 0.2$. Guo et al. (in prep) describes an automated clump finder that is found to be in good agreement with our visual classifications at identifying clumpy structure (see his paper for details on how the two methods compare). Similarly, to identify subclasses of clumpy galaxies (namely chain and tadpole systems), the individual flags for these systems were used with minimum cutoffs set to

0.1. The lower minimum value for these subclasses was found to be necessary due to the classifiers tendencies to not reliably check morphology flags.

Figures 2.11 and 2.12 display the GOODS-South ‘clean’ star-forming $z\sim 2$ sample and the Hydro-ART $z\sim 2$ simulations. The plots separate the visually identified clumpy galaxies from the smooth structures. The first thing that jumps out is that the simulations overproduce clumpy systems compared to the GOODS-South observations by almost a factor of two. Figure 2.11 shows that 30% of $z\sim 2$ ‘clean’ star-forming galaxies in GOODS-South are visually identified as being clumpy while figure 2.12 shows that 56% of the Hydro-ART simulations are similarly called clumpy. In addition, the plots highlight again that the CANDELized simulations have a narrow R_{eff} range compared to the GOODS-South galaxies. For both the GOODS-South galaxies and simulations, the clumpy structures are found at higher R_{eff} and lower Sérsic. Clumpy star-forming regions tend to be in systems that are larger and more disk-like. Very few galaxies are clumpy below $R_{eff}=2$ kpc and the majority of star-forming galaxies are clumpy above $R_{eff}=3$ kpc. Please note that the Sérsic value and R_{eff} are determined using GALFIT fits on the F160W band light while the clumpiness of a galaxy is determined using the bluer wavebands. Thus this observed relation is not a result of the decentralized star-forming clumpy regions adding light to larger radii which would both increase R_{eff} and drop the Sérsic index.

It is hard to see any axis ratio dependence for clumpiness in these figures but looking at Table 2.2 we can probe the effects of viewing angle on visual clumpy classification. Table 2.2 shows that while clumpy systems can be visually observed at

	Face-on Camera (325)	Edge-on Camera (332)	4 Random Cameras (1325)	All Cameras (1982)
$n < 0.8$	23 (7.1%)	65 (19.6%)	121 (9.1%)	209 (10.5%)
$0.8 \leq n < 1.5$	86 (26.5%)	158 (47.6%)	434 (32.8%)	678 (34.2%)
$1.5 \leq n < 2.5$	126 (38.8%)	65 (19.6%)	511 (38.6%)	702 (35.4%)
$2.5 \leq n < 5.0$	83 (25.5%)	42 (12.7%)	230 (17.4%)	355 (17.9%)
$5.0 \leq n$	7 (2.2%)	2 (0.6%)	29 (2.2%)	38 (1.9%)
VisClass-D	151 (46.5%)	218 (65.7%)	650 (49.1%)	1019 (51.4%)
VisClass-I	85 (26.2%)	69 (20.8%)	373 (28.2%)	527 (26.6%)
VisClass-S	89 (27.4%)	45 (13.6%)	302 (22.8%)	436 (22.0%)
Clumpy	206 (63.4%)	168 (50.6%)	747 (56.4%)	1121 (56.6%)
Tadpole	0 (0.0%)	19 (5.7%)	45 (3.4%)	64 (3.2%)
Chain	1 (0.3%)	40 (12.0%)	39 (2.9%)	80 (4.0%)
Asymmetric	120 (36.9%)	163 (49.1%)	557 (42.0%)	840 (42.4%)
Merg/Int	44 (13.5%)	65 (19.6%)	211 (15.9%)	320 (16.1%)
Irregular	18 (5.5%)	31 (9.3%)	79 (6.0%)	128 (6.5%)

Table 2.2: Simulation Classification Dependence on Viewing Angle

all viewing angles (56% over all random angles), there is a $\sim 13\%$ increase in clumpy classifications for face-on (63%) over edge-on (50%) viewing angles. This increase in identifying systems as clumpy in face-on orientations suggests that some of the clumps are masked or blocked by dust or other structures when viewed edge-on. 56% of these simulations viewed over random viewing angles are found to be clumpy which is in good agreement with the 50-60% found in Mandelker et al. (2013) which used the clumpiness of gas to identify clumpy galaxies in these same Hydro-ART simulations. It is worth pointing out from Table 2.2 that chains and tadpole systems are never found in face-on galaxies and are predominantly detected in edge-on systems. This points to chains and tadpole systems being edge-on disks and not oblong structures in the simulations. On a

side note, these simulations tend to under produce chain and tadpole systems compared to the GOODS-South observations. For the Hydro-ART simulations, 3.4% are identified as tadpoles and 3% as chains in the random camera angles while in the GOODS-South observations, 7% are identified as tadpoles and 5% as chains in the lower mass systems ($M_{stellar}=9.4-11$). In the simulations, chains make up 5% of the total clumpy population while in the GOODS-South observations chains are 10% of the clumpy population.

Figures 2.13 to 2.18 show these GOODS-South (2.13 - 2.15) and Hydro-ART (2.16 - 2.18) populations broken up into mass bins. For the GOODS-South ‘clean’ star-forming $z\sim 2$ population, the higher mass galaxies tend to have larger effective radii as expected. The narrowness of the measured effective radii for the Hydro-ART simulations prevents us from confirming this with the simulations. The mass ranges for the bins are not the same between the GOODS-South observations and the Hydro-ART simulations. As discussed in 3.4, the stellar masses of the Hydro-ART simulations are not reliable. The masses we are using are adjusted to match the Behroozi et al. (2013) stellar mass-halo mass ratio but even so are questionable on a galaxy by galaxy basis. For this reason, direct comparisons between the mass bins of the simulations and those of the GOODS-South observations are not performed. Instead, we focus on general trends with relative stellar masses. For the GOODS-South observations, 27% of galaxies in the low mass, 39% of galaxies in the middle mass range, and 19% of galaxies in the high mass range are clumpy (note the sample space in this high mass bin is only 27 galaxies). Thus clumpiness in star-forming galaxies in GOODS-South is seen to peak at intermediate stellar masses ($M_{stellar}=10.0 - 11.0$). This is in agreement with Guo et

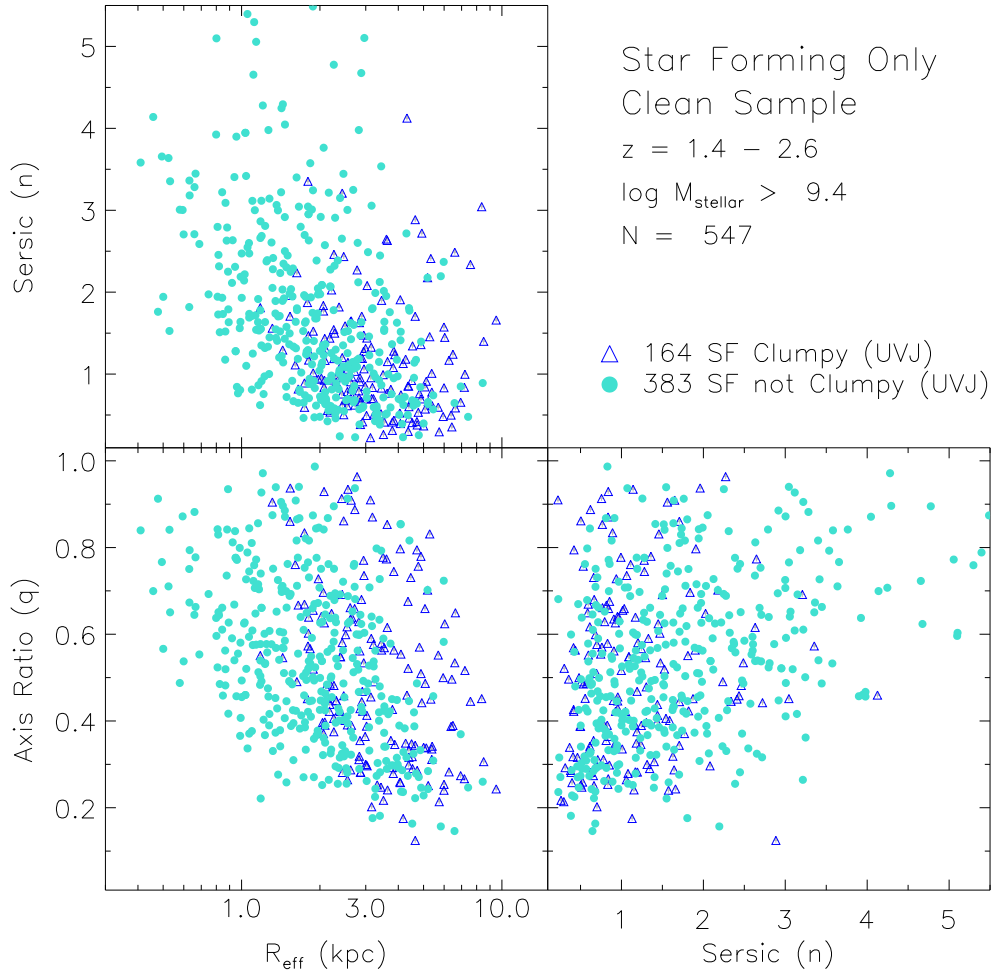


Figure 2.11: Clumpy Star-Forming GOODS-South Galaxies. 30% of $z \sim 2$ star-forming galaxies are clumpy. These clumpy systems tend to have larger R_{eff} and lower Sérsic indices.

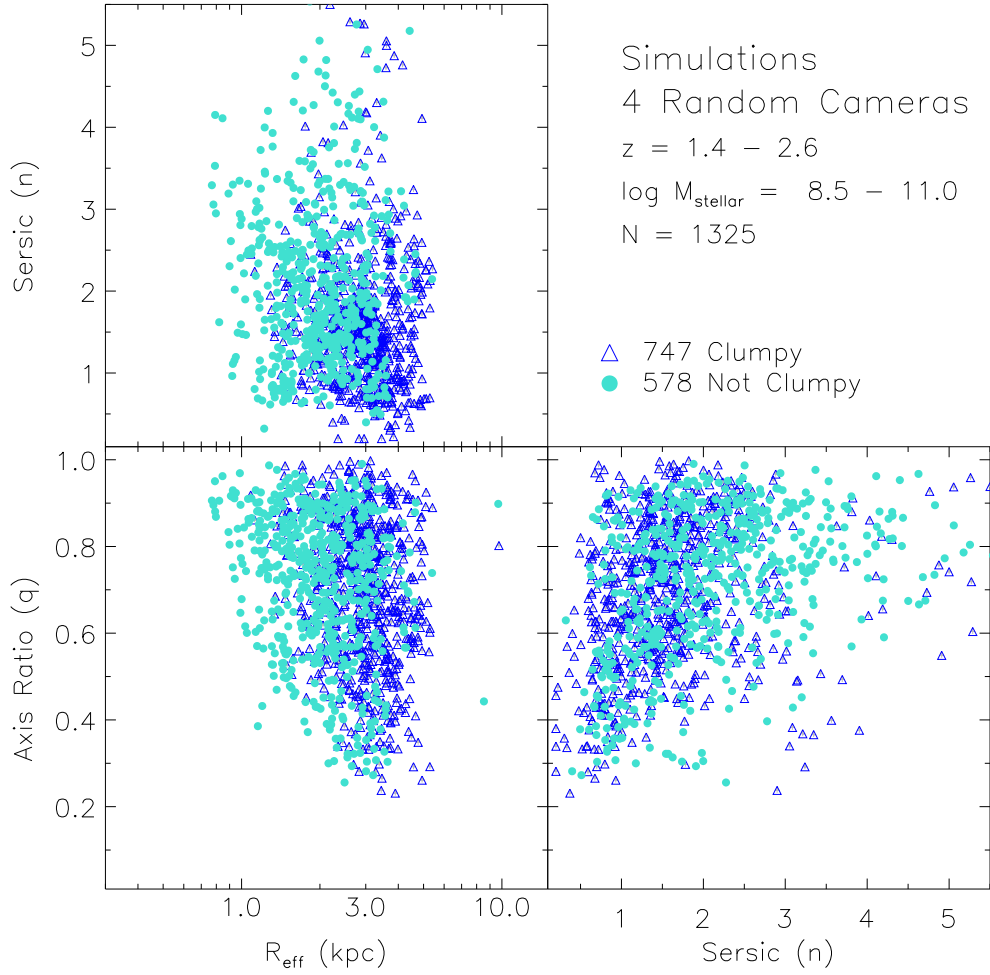


Figure 2.12: Clumpy Hydro-ART Simulations. 56% of the full Hydro-ART sample are clumpy (nearly twice the fraction seen in GOODS-South observations). As was true for the GOODS-South galaxies, the clumpy simulation galaxies are systems with larger R_{eff} and lower Sérsic indices.

al. (in prep) that found clump fractions peaked at $M_{stellar}=10.3 - 10.5$ for $z\sim 2$. For the Hydro-ART simulations, 42% of galaxies in the low mass, 60% of galaxies in the middle mass range, and 67% of galaxies in the high mass range are clumpy. Instead of a peak at intermediate masses, we see an increase in clumpiness fraction at higher stellar masses.

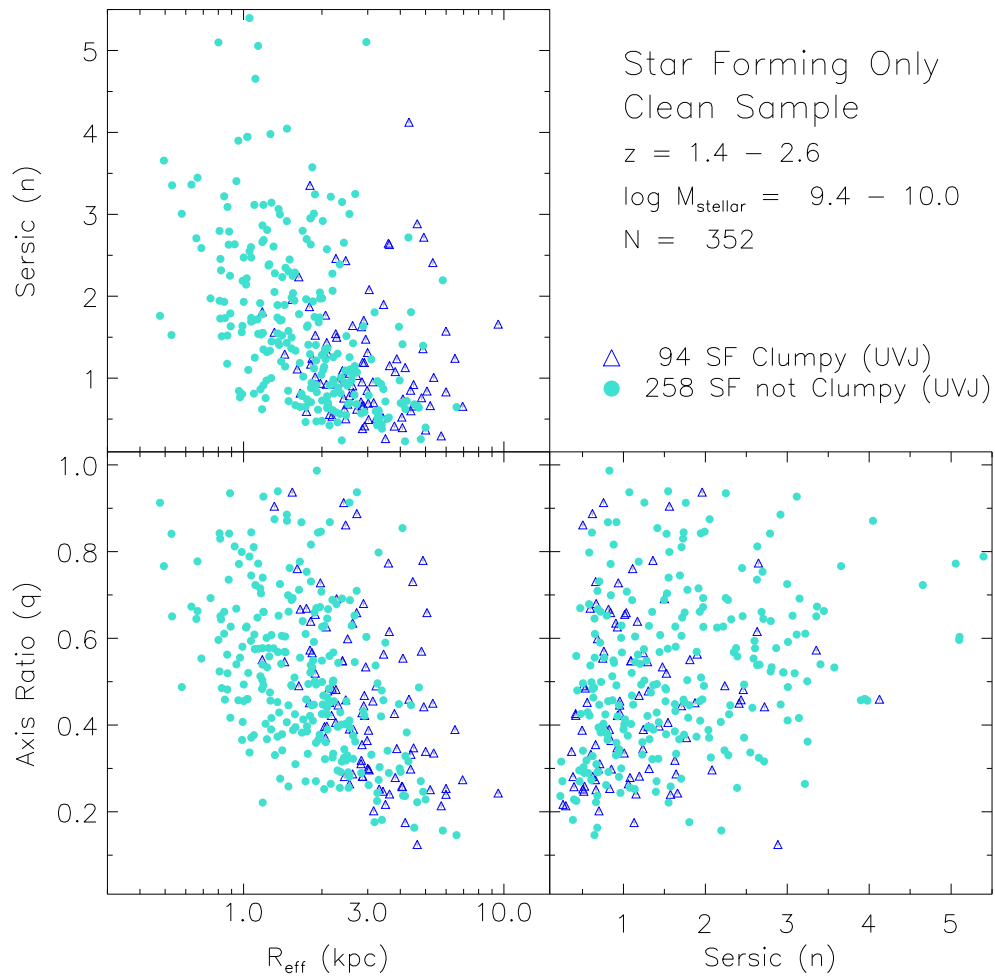


Figure 2.13: Clumpy Star-Forming GOODS-South Low Mass Galaxies. 27% of GOODS-South star-forming $z \sim 2$ galaxies with $\log M_{\text{stellar}} = 9.4 - 10.0$ are clumpy.

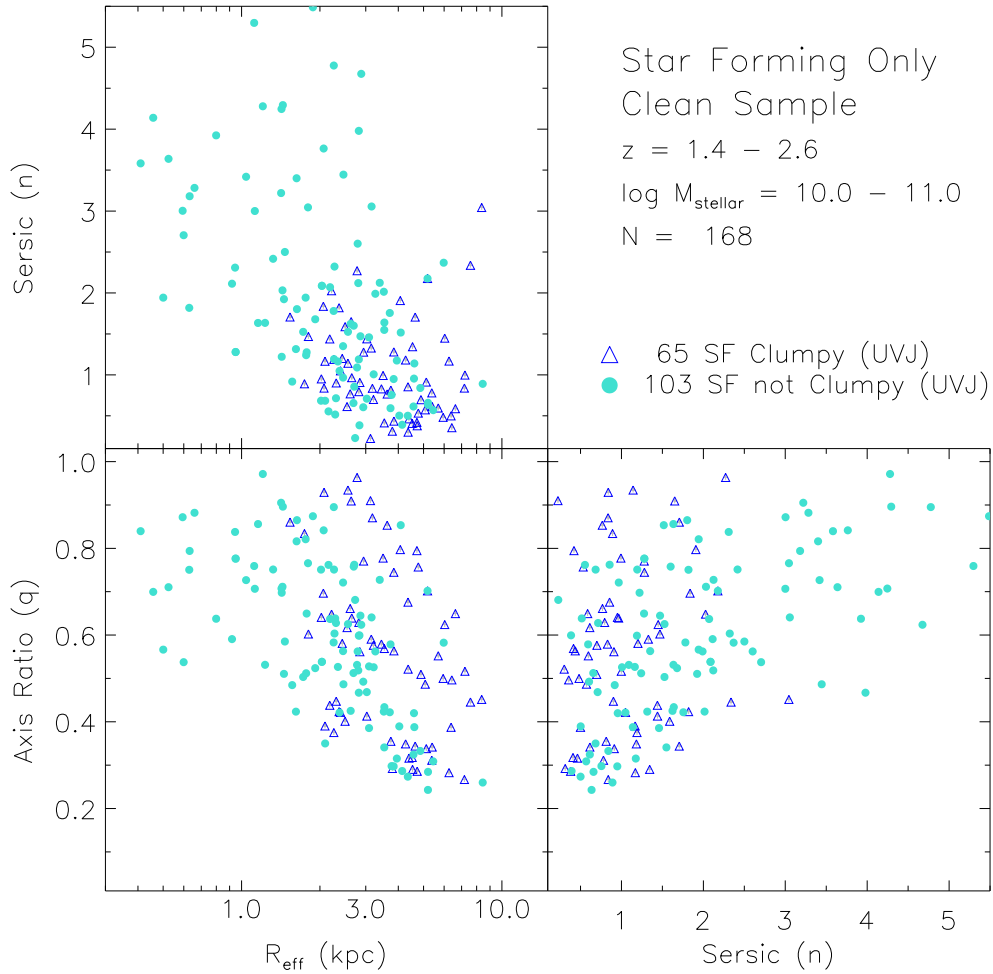


Figure 2.14: Clumpy Star-Forming GOODS-South Moderate Mass Galaxies. 39% of GOODS-South star-forming $z \sim 2$ galaxies with $\log M_{\text{stellar}} = 10.0 - 11.0$ are clumpy. This is the highest clump fract among the mass bins. Clumpiness in star-forming galaxies in GOODS-South is seen to peak at intermediate stellar masses ($M_{\text{stellar}} = 10.0 - 11.0$). This is in agreement with Guo et al. (in prep) that found clump fractions peaked at $M_{\text{stellar}} = 10.3 - 10.5$ for $z \sim 2$.

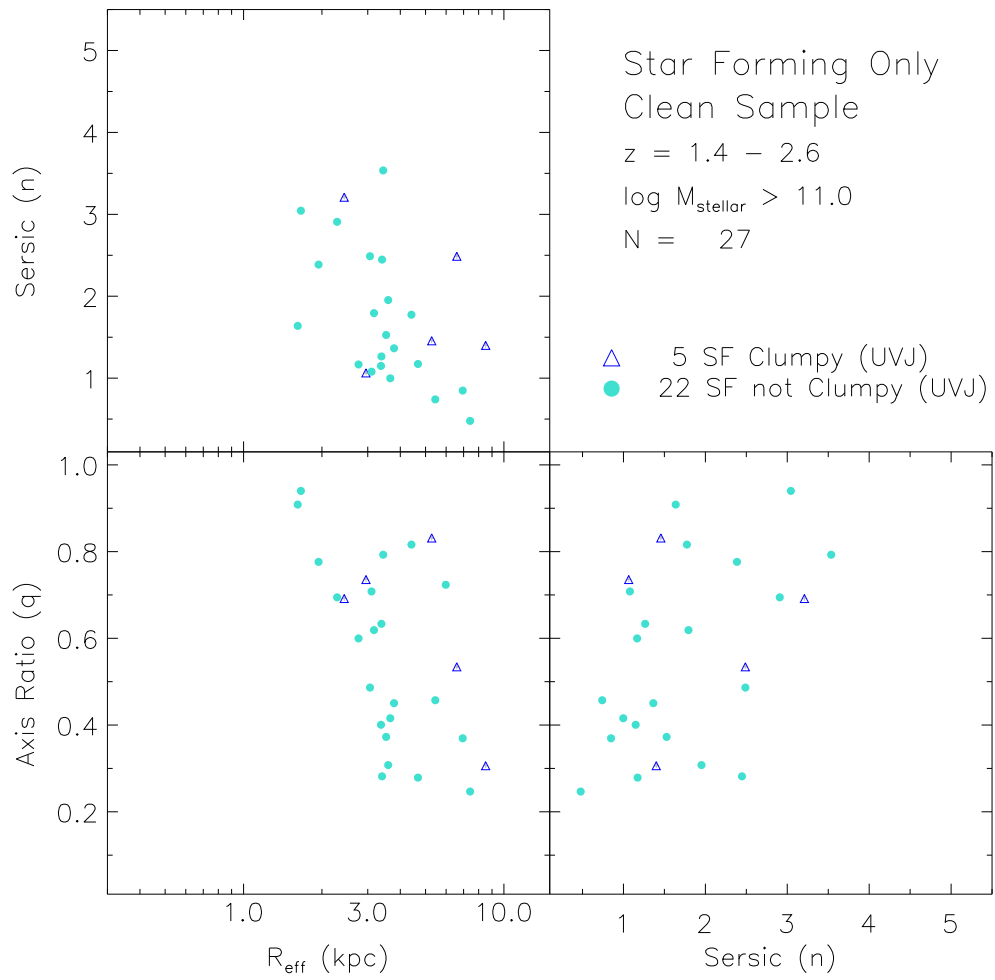


Figure 2.15: Clumpy Star-Forming GOODS-South High Mass Galaxies. 19% of GOODS-South star-forming $z \sim 2$ galaxies with $\log M_{\text{stellar}} > 11.0$ are clumpy.

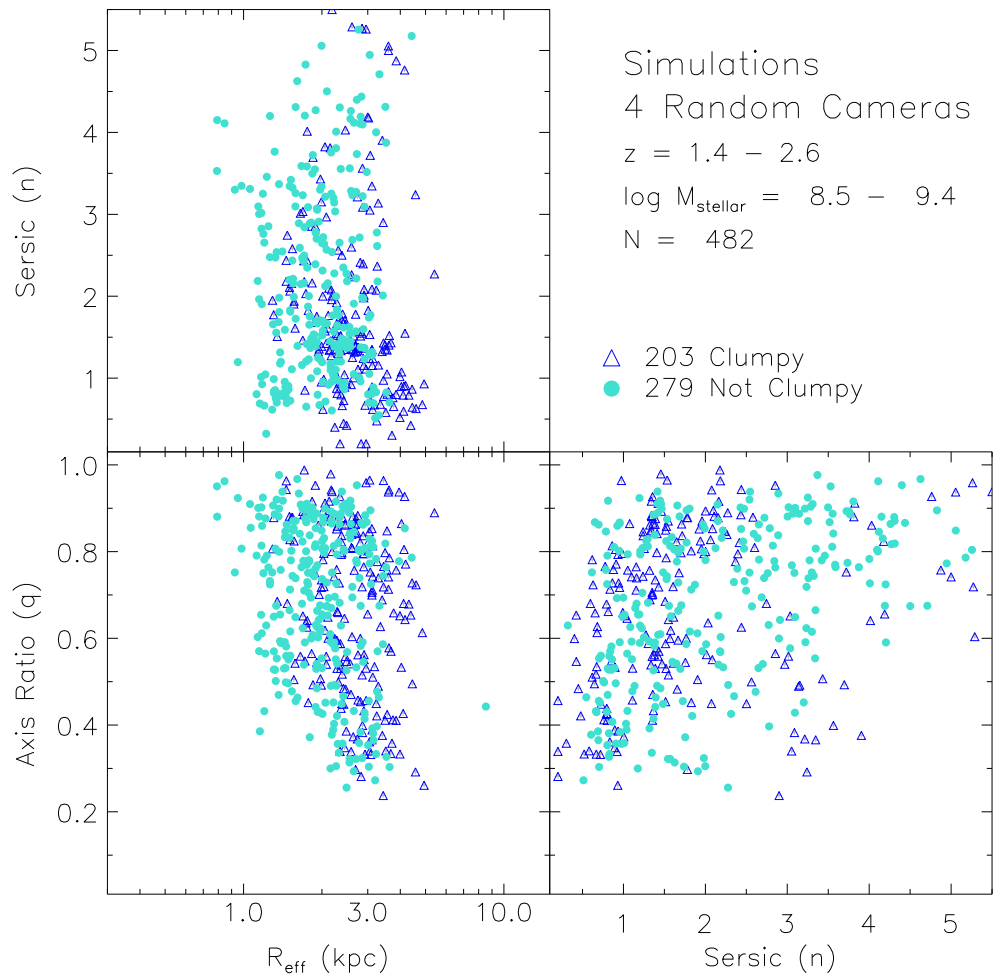


Figure 2.16: Clumpy Hydro-ART Low Mass Simulations. 42% of Hydro-ART $z \sim 2$ galaxies with $\log M_{\text{stellar}} = 8.5 - 9.4$ are clumpy.

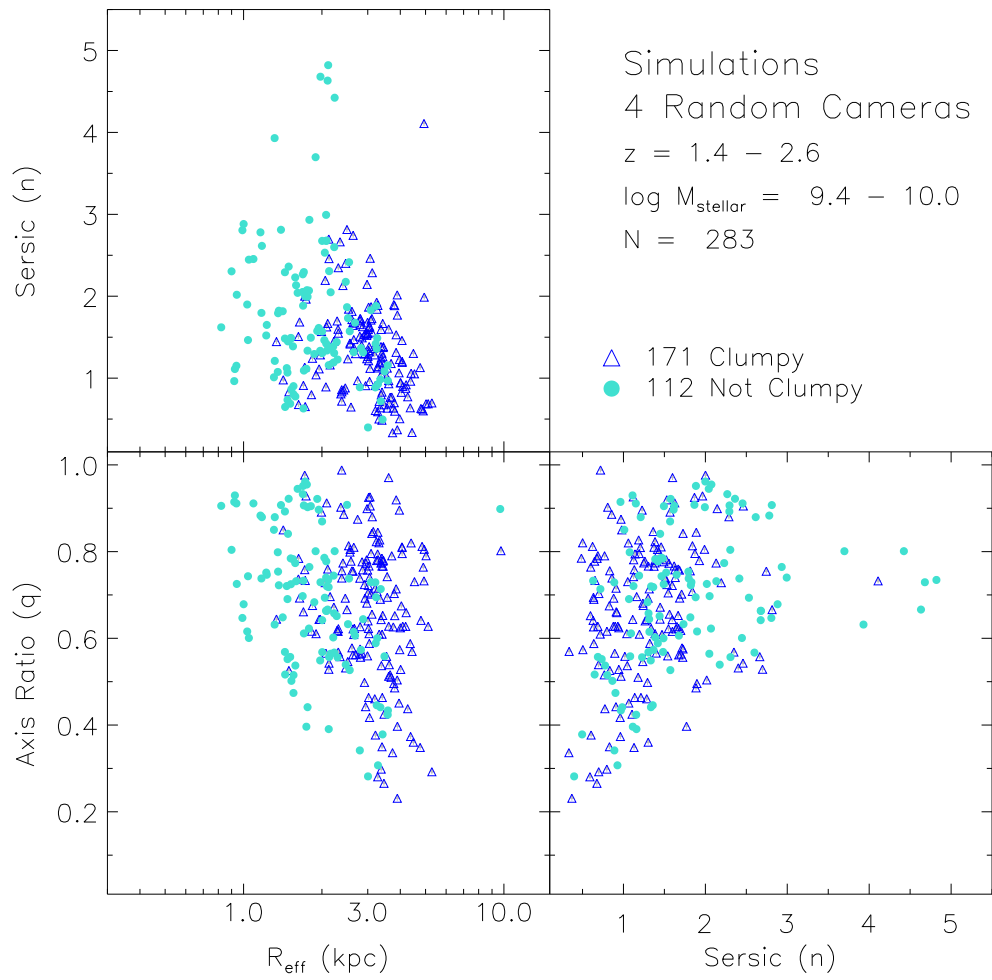


Figure 2.17: Clumpy Hydro-ART Intermediate Mass Simulations. 60% of Hydro-ART $z \sim 2$ galaxies with $\log M_{\text{stellar}} = 9.4 - 10.0$ are clumpy.

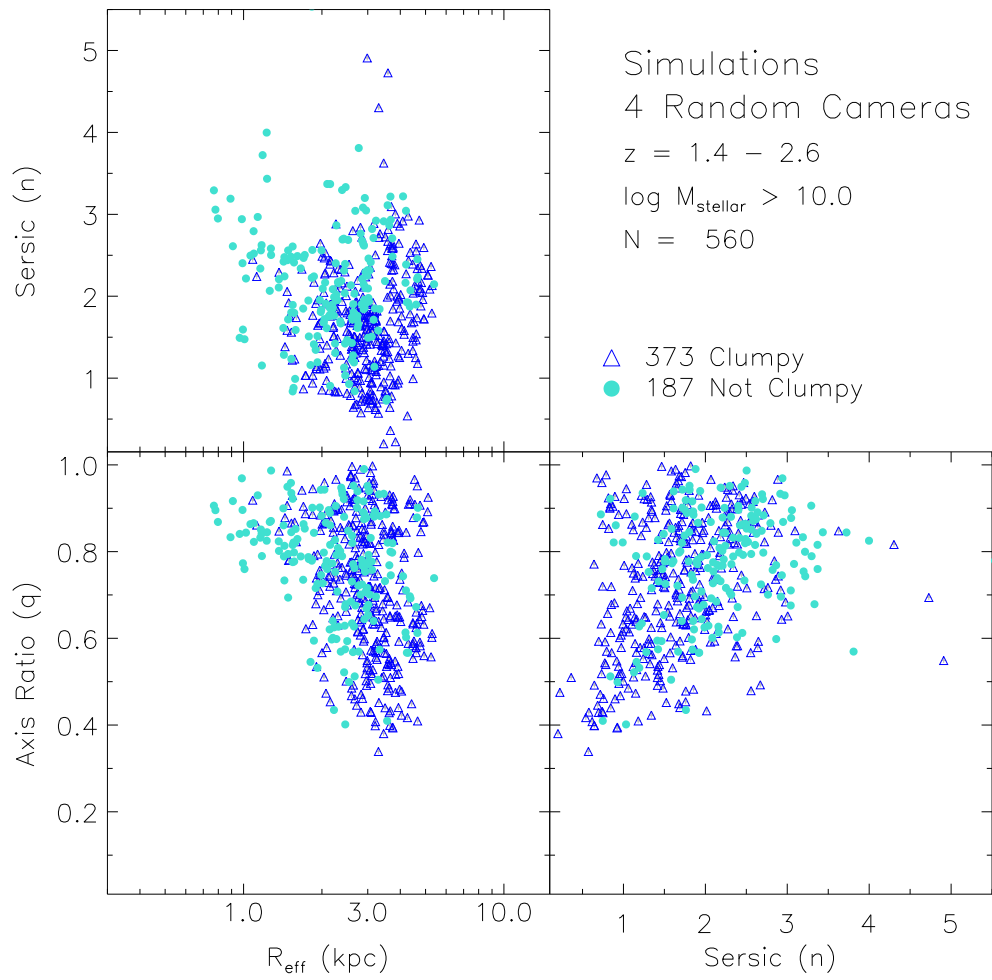


Figure 2.18: Clumpy Hydro-ART High Mass Simulations. 67% of Hydro-ART $z \sim 2$ galaxies with $\log M_{\text{stellar}} > 10.0$ are clumpy.

2.7 Conclusions

We are the first study to ‘observe’ Hydro-ART simulations in a way completely comparable to the HST images obtained by CANDELS. This allows us to probe how our simulations compare to the $z\sim 2$ observations directly. We develop a comprehensive visual classification system to classify the morphologies of thousands of observed CANDELS GOODS-South galaxies as well as to classify thousands of CANDELized simulations that have been processed to have the same background, psf, and pixel resolution as the WFC3 HST CANDELS observations. The simulations used in this study are not a representative sample of all $z\sim 2$ galaxies. The halos simulated are evenly spaced in $\log M_{halo}$, unlike galaxies. The lack of quenching and radiation pressure in these simulations causes stars to be formed too quickly and efficiently at early times. This leads to stellar masses that are a factor of 3-10 times the $M_{stellar}/M_{halo}$ ratios found using abundance matching methods for a given halo mass. In addition, the simulations are unable to form quenched systems. Despite these limitations, the simulations produce a small sample of star-forming galaxies that can be CANDELized and ‘observed’ to directly compare with star-forming GOODS-South observations. This study has produced several key results:

- Dust modeling in SUNRISE is unable to recreate the observed slope of the star-forming sequence of galaxies in UVJ color-color space.
- The effective radii measured from CANDELized Hydro-ART simulations is narrow (almost all simulations have $1 \text{ kpc} \leq R_{eff} \leq 3 \text{ kpc}$) and intermediate in its distribu-

tion, lacking both the large and small radius systems observed in GOODS-South.

- GALFIT Sérsic indices and our visual classification system correspond well with each other at $z \sim 2$ with systems identified as disks tending to have lower Sérsic indices and systems identified as spheroids have higher Sérsic indices.
- The visual classification system is unable to distinguish between disks and spheroids below the spatial resolution of the image ($0.17''$). All compact objects are identified visually as spheroids. GALFIT (with a well known psf) is able to fit diverse Sérsic models to these compact systems and is not biased towards spheroids at small radii.
- GOODS-South observations and simulations both show the general trend of spheroids dominating at small radii and disky structures dominating at larger radii.
- Clumps remain visible in Hydro-ART simulations after the CANDELization process smears the light with a psf, drops the spatial resolution to match HST WFC3 pixel scales, and adds background noise comparable to HST CANDELS observations.
- Simulations are nearly twice as likely to be clumpy compared to observed $z \sim 2$ galaxies in GOODS-South.
- For both GOODS-South observations and Hydro-ART simulations, clumps are predominantly found in large radii systems.

- Clumpiness in the GOODS-South observations peak in galaxies with intermediate stellar mass ($10^{10.5}M_{\odot}$).
- Chains and tadpoles are found in simulations viewed edge-on - supporting the view that they might be clumpy edge-on disks as well as oblong structures.
- Chains and tadpoles are underproduced in the simulations by almost a factor of 2 compared to observed $z\sim 2$ galaxies in GOODS-South.

The in-depth visual classification system was successful at identifying clumpy galaxies and providing general morphologies that agreed well with measured Sérsic indices. The visual classifications, however, were not reliable for poorly resolved galaxies causing us to rely entirely on Sérsic indices for compact objects. The reliability of Sérsic and the improving automated clump finding routines may limit the usefulness of performing the human-resource intensive process of visually classifying a large population of galaxies in future surveys.

The next generation of Hydro-ART models incorporates radiation pressure and does not suffer as strongly from an over production of stars at early times. It will be valuable to perform a similar analysis on these simulations to see how the radiation pressure affects the global structure and visual classifications of galaxies as well as the formation and visibility of clumps. The radiation pressure may be enough to dampen smaller star forming clumps and thus help alleviate the factor of two over population of clumps observed in current simulations without radiation pressure. Despite the limitations of the current simulations, we were able to study a restricted sample of

star-forming galaxy simulations and compare their mock ‘observed’ morphologies with the latest HST WFC3 observations. While many opportunities for improving the models remain, the current Hydro-ART simulations already produce galaxies that share many observed properties with the GOODS-South galaxies and thus add weight to the adopted galaxy formation pathway.

Appendix A

MWGunified Visual Classification

System Examples

Provided below are example images of the morphological classes and flags used in the MWGunified visual classification system. The visual classifications were based primarily on HST WFC3 images using F160W. The example images below are all cutouts in F160W taken from the CANDELS GOODS-South field. Details on the visual classification system can be found in the text.

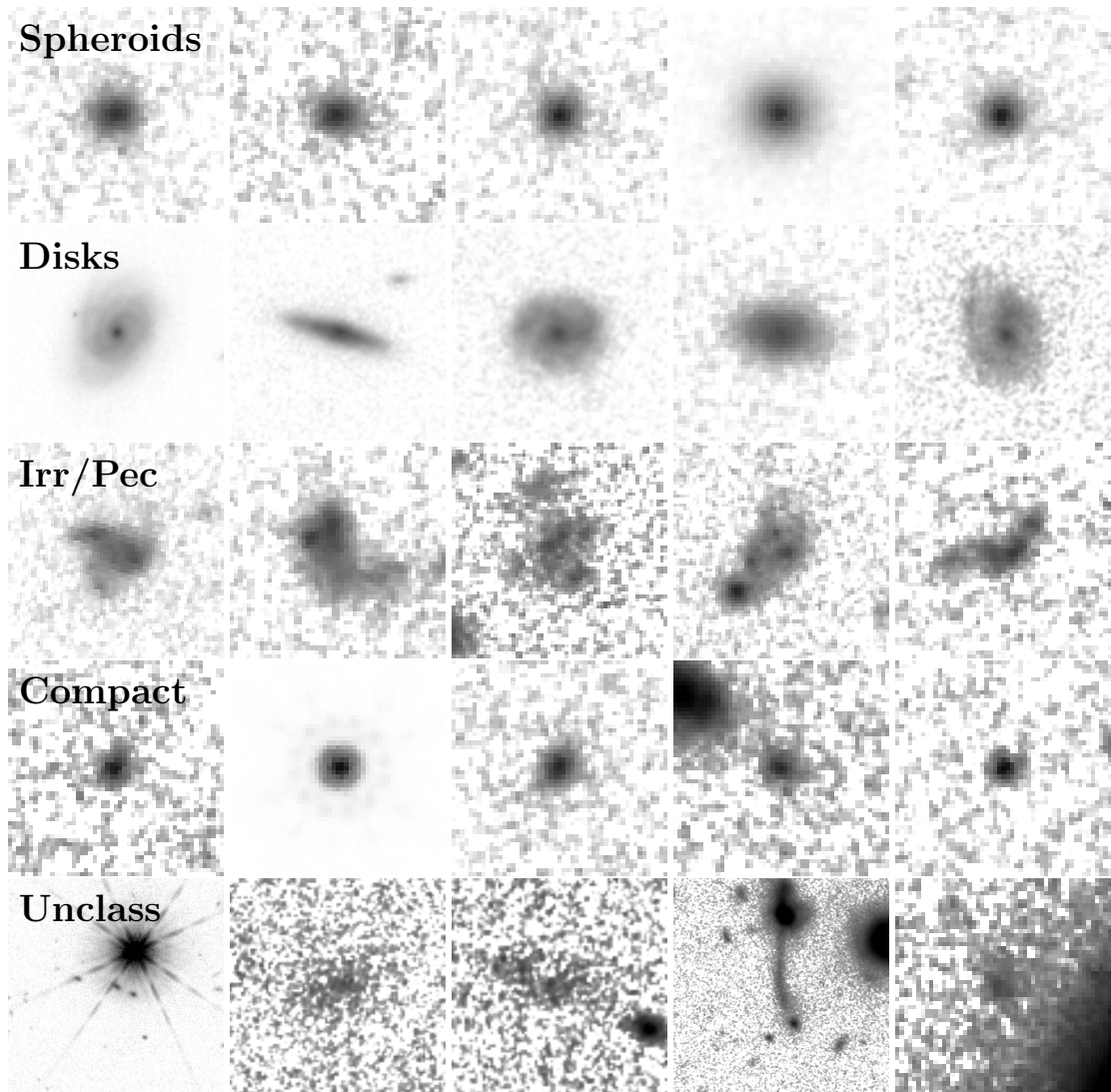


Figure A.1: Examples of the global morphological classes used in the MWGunified Visual Classification System. All images are the F160W cutouts used to classify the galaxies. The size of each cutout is scaled to the galaxy size as described in the text.

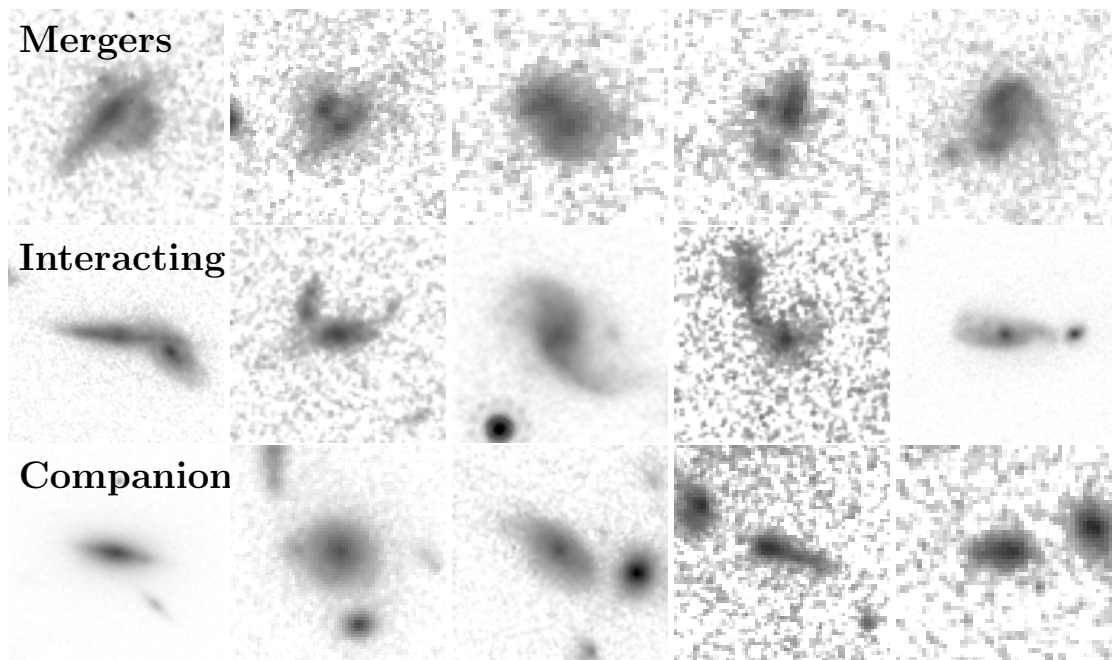


Figure A.2: Examples of the interaction classes used in the MWGunified Visual Classification System. All images are the F160W cutouts used to classify the galaxies. The size of each cutout is scaled to the galaxy size as described in the text. Both the "Interaction between two objects within a single segmentation map" and the "Interaction between two objects in separate segmentation maps" are shown as a single "Interaction" class.

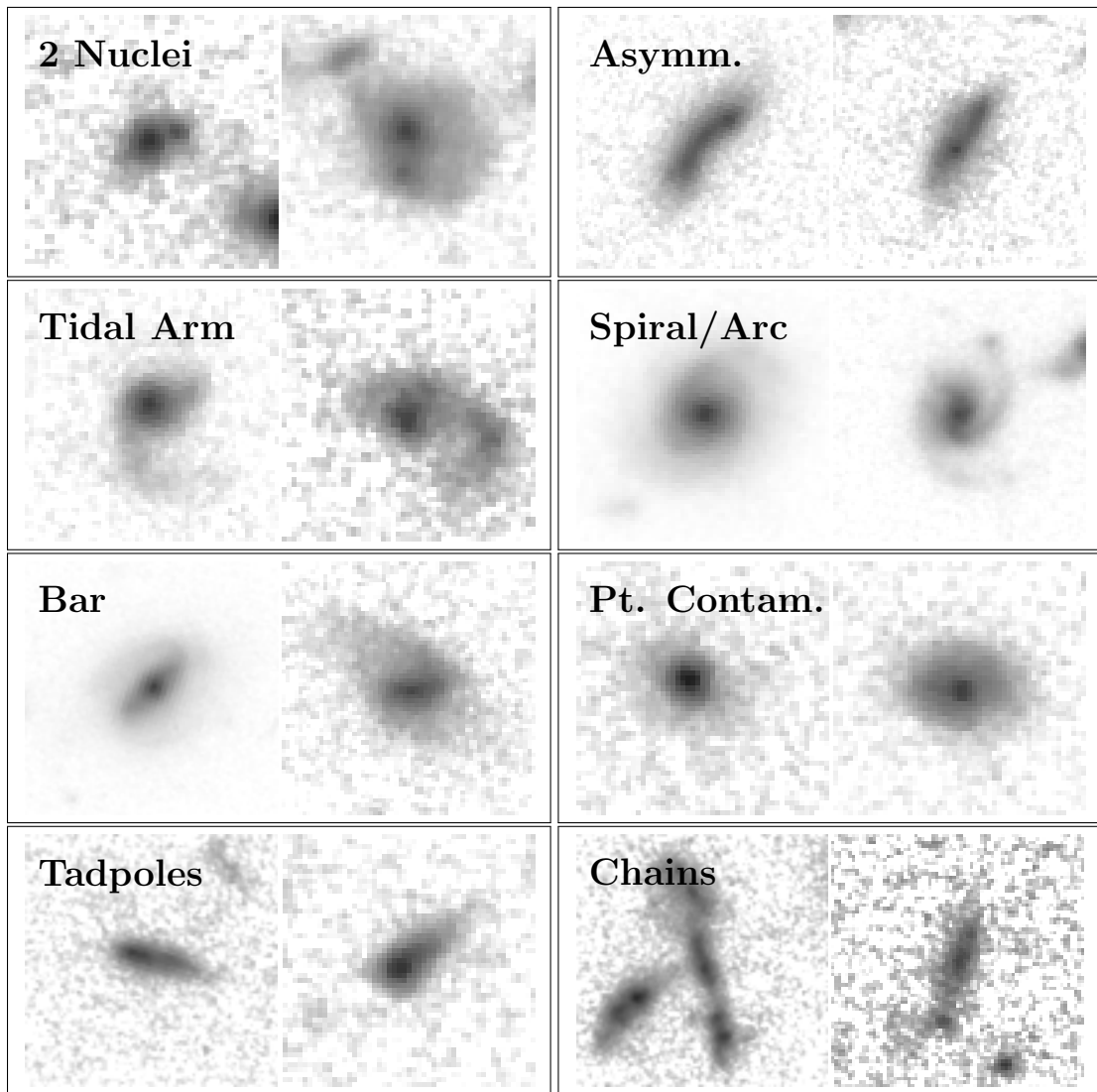


Figure A.3: Examples of the Structural Flags (Part 1) used in the MWGunified Visual Classification System. All images are the F160W cutouts used to classify the galaxies. The size of each cutout is scaled to the galaxy size as described in the text.

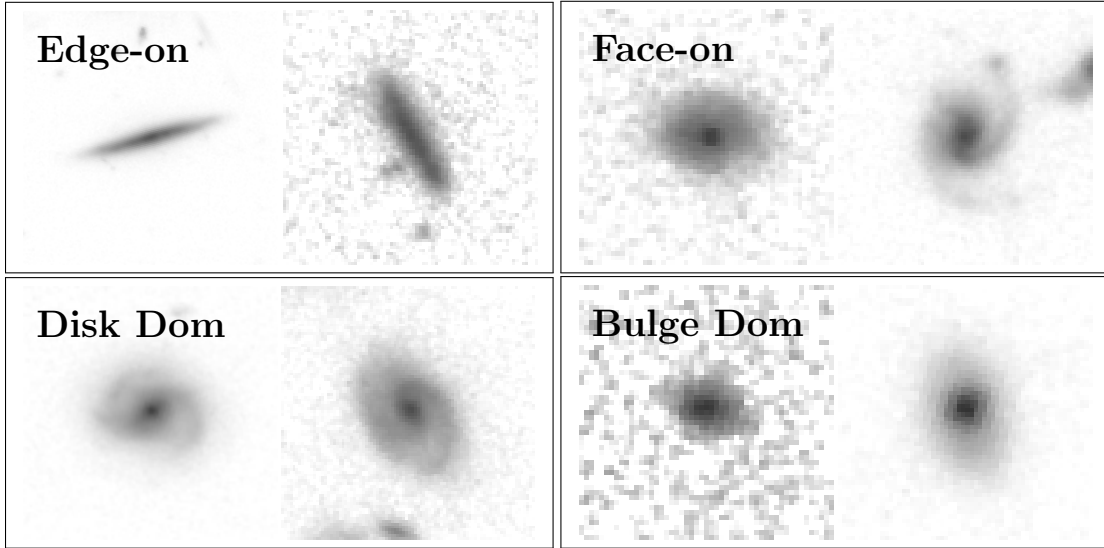


Figure A.4: Examples of the Structural Flags (Part 2) used in the MWGunified Visual Classification System. All images are the F160W cutouts used to classify the galaxies. The size of each cutout is scaled to the galaxy size as described in the text.

		Major Clumpiness								
Blue Patchiness				<input type="checkbox"/> No Major Clumps No Patchiness			<input type="checkbox"/> 1-2 Major Clumps No Patchiness			<input type="checkbox"/> 3+ Major Clumps No Patchiness
				<input type="checkbox"/> No Major Clumps Some Patchiness			<input type="checkbox"/> 1-2 Major Clumps Some Patchiness			<input type="checkbox"/> 3+ Major Clumps Some Patchiness
				<input type="checkbox"/> No Major Clumps Lots of Patchiness			<input type="checkbox"/> 1-2 Major Clumps Lots of Patchiness			<input type="checkbox"/> 3+ Major Clumps Lots of Patchiness

Figure A.5: Clumpiness-Patchiness Classification Matrix

The Clumpiness-Patchiness Classification Matrix used in the MWGunified Visual Classification System to classify the clumpiness of a galaxy. For each clumpiness classification example, the image on the left is F606W from ACS and the image on the right is F160W from WFC3. In MWGunified, the bluer ACS bands were used primarily to classify the clumpiness of an object. The size of each cutout is scaled to the galaxy size as described in the text.

Appendix B

GOODS-South Galaxy Fractions

Evolution Tables - ‘Bin Fraction’

Provided below are the supplementary tables to the ones provided in Chapter 1. Both the tables in Chapter 1 and the ones provided below give the number of galaxies with a certain morphological classification in a given mass, redshift, and sSFR or radius bin. The difference between the tables in Chapter 1 and the tables below are the fractions and percent values provided in each bin. The tables in Chapter 1 give the fraction of the objects in these mass, redshift, and sSFR or radius bins compared to the total number of galaxies of this class at that redshift. These tables show how a given visual classification class is distributed at a given redshift. The tables in the Appendix are called ‘bin fraction’. These ‘bin fraction’ tables give the percentage of a given morphology class as a fraction of total number of galaxies in the same redshift, mass, and sSFR/radii bin (the number of galaxies in a bin for a certain morphology

class divided by the number of galaxies in that bin at all morphologies). These tables demonstrate how galaxies of a certain mass, redshift, and sSFR or radii are distributed among the different morphology classes. The colors in the tables correspond to different percentages and are provided only to guide the eye.

Table B.1: Disk Galaxy Evolution Fractions with Redshift in Mass and sSFR Bins - ‘Bin Fraction’

	sSFR											
	Quiescent sSFR < 0.9			Transitional -0.9 ≤ sSFR < 0.3			Star Forming -0.3 ≤ sSFR < 0.95			High Star Forming 0.95 ≤ sSFR		
	$M_{stellar}$ 9.4-10.0	$M_{stellar}$ 10-11	$M_{stellar}$ >11	$M_{stellar}$ 9.4-10.0	$M_{stellar}$ 10-11	$M_{stellar}$ >11	$M_{stellar}$ 9.4-10.0	$M_{stellar}$ 10-11	$M_{stellar}$ >11	$M_{stellar}$ 9.4-10.0	$M_{stellar}$ 10-11	$M_{stellar}$ >11
2.6 ≤ z < 3.0 (140)	0 (-NaN%)	0 (0.0%)	4 (80.0%)	0 (-NaN%)	3 (60.0%)	1 (33.3%)	68 (56.2%)	52 (70.3%)	0 (-NaN%)	5 (33.3%)	7 (70.0%)	0 (-NaN%)
2.2 ≤ z < 2.6 (151)	2 (100.0%)	1 (7.7%)	4 (57.1%)	1 (100.0%)	2 (20.0%)	3 (100.0%)	83 (58.5%)	44 (62.0%)	3 (50.0%)	6 (75.0%)	1 (25.0%)	1 (100.0%)
1.8 ≤ z < 2.2 (191)	0 (0.0%)	4 (30.8%)	6 (50.0%)	0 (0.0%)	4 (44.4%)	4 (100.0%)	82 (50.6%)	69 (69.7%)	4 (66.7%)	9 (75.0%)	9 (69.2%)	0 (-NaN%)
1.4 ≤ z < 1.8 (312)	0 (-NaN%)	6 (14.3%)	2 (9.5%)	5 (55.6%)	9 (31.0%)	5 (62.5%)	175 (62.9%)	73 (77.7%)	1 (100.0%)	21 (70.0%)	15 (78.9%)	0 (-NaN%)
1.0 ≤ z < 1.4 (374)	2 (14.3%)	12 (15.2%)	10 (41.7%)	7 (46.7%)	22 (47.8%)	8 (66.7%)	205 (68.8%)	73 (69.5%)	1 (100.0%)	28 (90.3%)	6 (54.5%)	0 (-NaN%)
0.5 ≤ z < 1.0 (404)	7 (22.6%)	13 (10.2%)	3 (10.3%)	10 (41.7%)	33 (55.9%)	5 (100.0%)	215 (75.2%)	84 (78.5%)	5 (83.3%)	20 (55.6%)	9 (75.0%)	0 (-NaN%)
Total: 1572	11	36	29	23	73	26	828	395	14	89	47	1

Table B.2: Disk Galaxy Fractions Evolution with Redshift in Mass and R_{eff} Bins - ‘Bin Fraction’

	R_{eff} (F160W)											
	Compact $R_{eff} < 1\text{kpc}$			Moderate $1\text{kpc} \leq R_{eff} < 3\text{kpc}$			Extended $3\text{kpc} \leq R_{eff}$					
	$M_{stellar}$ 9.4-10.0	$M_{stellar}$ 10-11	$M_{stellar}$ >11	$M_{stellar}$ 9.4-10.0	$M_{stellar}$ 10-11	$M_{stellar}$ >11	$M_{stellar}$ 9.4-10.0	$M_{stellar}$ 10-11	$M_{stellar}$ >11	$M_{stellar}$ 9.4-10.0	$M_{stellar}$ 10-11	$M_{stellar}$ >11
2.6 ≤ z < 3.0 (140)	0 (0.0%)	0 (0.0%)	0 (0.0%)	47 (48.5%)	29 (64.4%)	2 (50.0%)	26 (83.9%)	33 (86.8%)	3 (100.0%)	0	0	0
2.2 ≤ z < 2.6 (151)	0 (0.0%)	0 (0.0%)	0 (0.0%)	63 (59.4%)	18 (47.4%)	4 (50.0%)	29 (85.3%)	30 (85.7%)	7 (87.5%)	0	0	0
1.8 ≤ z < 2.2 (191)	0 (0.0%)	0 (0.0%)	0 (0.0%)	53 (42.4%)	18 (36.0%)	2 (28.6%)	38 (95.0%)	68 (91.9%)	12 (85.7%)	0	0	0
1.4 ≤ z < 1.8 (312)	0 (0.0%)	0 (0.0%)	0 (-NaN%)	87 (50.0%)	27 (33.8%)	1 (5.3%)	114 (91.9%)	76 (93.8%)	7 (63.6%)	0	0	0
1.0 ≤ z < 1.4 (374)	0 (0.0%)	0 (0.0%)	0 (-NaN%)	83 (48.0%)	25 (22.3%)	2 (20.0%)	159 (94.6%)	88 (81.5%)	17 (63.0%)	0	0	0
0.5 ≤ z < 1.0 (404)	0 (0.0%)	1 (5.0%)	0 (-NaN%)	94 (49.5%)	31 (20.7%)	1 (16.7%)	158 (95.2%)	107 (78.7%)	12 (35.3%)	0	0	0
Total: 1572	0	1	0	427	148	12	524	402	58	0	0	0

Table B.3: Intermediate Galaxy Fractions Evolution with Redshift in Mass and sSFR Bins - ‘Bin Fraction’

	sSFR											
	Quiescent sSFR < -0.9			Transitional -0.9 ≤ sSFR < -0.3			Star Forming -0.3 ≤ sSFR < 0.95			High Star Forming 0.95 ≤ sSFR		
	$M_{stellar}$ 9.4-10.0	$M_{stellar}$ 10-11	$M_{stellar}$ >11	$M_{stellar}$ 9.4-10.0	$M_{stellar}$ 10-11	$M_{stellar}$ >11	$M_{stellar}$ 9.4-10.0	$M_{stellar}$ 10-11	$M_{stellar}$ >11	$M_{stellar}$ 9.4-10.0	$M_{stellar}$ 10-11	$M_{stellar}$ >11
2.6 ≤ z < 3.0 (49)	0 (-NaN%)	0 (0.0%)	0 (0.0%)	0 (-NaN%)	0 (0.0%)	1 (33.3%)	32 (26.4%)	10 (13.5%)	0 (-NaN%)	5 (33.3%)	1 (10.0%)	0 (-NaN%)
2.2 ≤ z < 2.6 (38)	0 (0.0%)	0 (0.0%)	0 (0.0%)	0 (0.0%)	20 (20.0%)	0 (0.0%)	25 (17.6%)	10 (14.1%)	0 (0.0%)	1 (12.5%)	0 (0.0%)	0 (0.0%)
1.8 ≤ z < 2.2 (71)	0 (0.0%)	2 (15.4%)	4 (33.3%)	0 (0.0%)	1 (11.1%)	0 (0.0%)	42 (25.9%)	16 (16.2%)	1 (16.7%)	3 (25.0%)	2 (15.4%)	0 (-NaN%)
1.4 ≤ z < 1.8 (85)	0 (-NaN%)	5 (11.9%)	5 (23.8%)	2 (22.2%)	4 (13.8%)	1 (12.5%)	49 (17.6%)	13 (13.8%)	0 (0.0%)	5 (16.7%)	1 (5.3%)	0 (-NaN%)
1.0 ≤ z < 1.4 (113)	2 (14.3%)	19 (24.1%)	7 (29.2%)	5 (33.3%)	7 (15.2%)	4 (33.3%)	47 (15.8%)	19 (18.1%)	0 (0.0%)	0 (0.0%)	3 (27.3%)	0 (-NaN%)
0.5 ≤ z < 1.0 (137)	5 (16.1%)	35 (27.3%)	11 (37.9%)	8 (33.3%)	13 (22.0%)	0 (0.0%)	41 (14.3%)	16 (15.0%)	0 (0.0%)	6 (16.7%)	2 (16.7%)	0 (-NaN%)
Total: 493	7	61	27	15	27	6	236	84	1	20	9	0

 Table B.4: Intermediate Galaxy Fractions Evolution with Redshift in Mass and R_{eff} Bins - ‘Bin Fraction’

	R_{eff} (F160W)											
	Compact $R_{eff} < 1\text{kpc}$			Moderate $1\text{kpc} \leq R_{eff} < 3\text{kpc}$			Extended $3\text{kpc} \leq R_{eff}$					
	$M_{stellar}$ 9.4-10.0	$M_{stellar}$ 10-11	$M_{stellar}$ >11	$M_{stellar}$ 9.4-10.0	$M_{stellar}$ 10-11	$M_{stellar}$ >11	$M_{stellar}$ 9.4-10.0	$M_{stellar}$ 10-11	$M_{stellar}$ >11	$M_{stellar}$ 9.4-10.0	$M_{stellar}$ 10-11	$M_{stellar}$ >11
2.6 ≤ z < 3.0 (49)	0 (0.0%)	0 (0.0%)	0 (0.0%)	34 (35.1%)	8 (17.8%)	1 (25.0%)	3 (9.7%)	3 (7.9%)	0 (0.0%)	0 (0.0%)	0 (0.0%)	0 (0.0%)
2.2 ≤ z < 2.6 (38)	1 (7.7%)	0 (0.0%)	0 (0.0%)	21 (19.8%)	8 (21.1%)	0 (0.0%)	4 (11.8%)	4 (11.4%)	0 (0.0%)	0 (0.0%)	0 (0.0%)	0 (0.0%)
1.8 ≤ z < 2.2 (71)	2 (18.2%)	0 (0.0%)	0 (0.0%)	42 (33.6%)	17 (34.0%)	4 (57.1%)	1 (2.5%)	4 (11.2%)	1 (7.1%)	1 (5.4%)	1 (27.3%)	0 (0.0%)
1.4 ≤ z < 1.8 (85)	2 (10.5%)	0 (0.0%)	0 (-NaN%)	47 (27.0%)	22 (27.5%)	3 (15.8%)	7 (5.6%)	1 (1.2%)	3 (27.3%)	0 (0.0%)	0 (0.0%)	0 (0.0%)
1.0 ≤ z < 1.4 (113)	1 (5.9%)	2 (9.5%)	0 (-NaN%)	45 (26.0%)	31 (27.7%)	3 (30.0%)	8 (4.8%)	15 (13.9%)	8 (29.6%)	0 (0.0%)	0 (0.0%)	0 (0.0%)
0.5 ≤ z < 1.0 (137)	0 (0.0%)	0 (0.0%)	0 (-NaN%)	53 (27.9%)	49 (32.7%)	2 (33.3%)	7 (4.2%)	17 (12.5%)	9 (26.5%)	0 (0.0%)	0 (0.0%)	0 (0.0%)
Total: 493	6	2	0	242	135	13	30	44	21	0	0	0

Table B.5: Spheroid Galaxy Fractions Evolution with Redshift in Mass and sSFR Bins - ‘Bin Fraction’

	sSFR											
	Quiescent sSFR < -0.9			Transitional -0.9 ≤ sSFR < -0.3			Star Forming -0.3 ≤ sSFR < 0.95			High Star Forming 0.95 ≤ sSFR		
	$M_{stellar}$ 9.4-10.0	$M_{stellar}$ 10-11	$M_{stellar}$ >11	$M_{stellar}$ 9.4-10.0	$M_{stellar}$ 10-11	$M_{stellar}$ >11	$M_{stellar}$ 9.4-10.0	$M_{stellar}$ 10-11	$M_{stellar}$ >11	$M_{stellar}$ 9.4-10.0	$M_{stellar}$ 10-11	$M_{stellar}$ >11
2.6 ≤ z < 3.0 (48)	0 (-NaN%)	4 (100.0%)	1 (20.0%)	0 (-NaN%)	2 (40.0%)	1 (33.3%)	21 (17.4%)	12 (16.2%)	0 (-NaN%)	5 (33.3%)	2 (20.0%)	0 (-NaN%)
2.2 ≤ z < 2.6 (79)	0 (0.0%)	12 (92.3%)	3 (42.9%)	0 (0.0%)	6 (60.0%)	0 (0.0%)	34 (23.9%)	17 (23.9%)	3 (50.0%)	1 (12.5%)	3 (75.0%)	0 (0.0%)
1.8 ≤ z < 2.2 (70)	1 (100.0%)	7 (53.8%)	2 (16.7%)	1 (100.0%)	4 (44.4%)	0 (0.0%)	38 (23.5%)	14 (14.1%)	1 (16.7%)	0 (0.0%)	2 (15.4%)	0 (-NaN%)
1.4 ≤ z < 1.8 (134)	0 (-NaN%)	31 (73.8%)	14 (66.7%)	2 (22.2%)	16 (55.2%)	2 (25.0%)	54 (19.4%)	8 (8.5%)	0 (0.0%)	4 (13.3%)	3 (15.8%)	0 (-NaN%)
1.0 ≤ z < 1.4 (149)	10 (71.4%)	48 (60.8%)	7 (29.2%)	3 (20.0%)	17 (37.0%)	0 (0.0%)	46 (15.4%)	13 (12.4%)	0 (0.0%)	3 (9.7%)	2 (18.2%)	0 (-NaN%)
0.5 ≤ z < 1.0 (182)	19 (61.3%)	80 (62.5%)	15 (51.7%)	6 (25.0%)	13 (22.0%)	0 (0.0%)	30 (10.5%)	7 (6.5%)	1 (16.7%)	10 (27.8%)	1 (8.3%)	0 (-NaN%)
Total: 662	30	182	42	12	58	3	223	71	5	23	13	0

 Table B.6: Spheroid Galaxy Fractions Evolution with Redshift in Mass and R_{eff} Bins - ‘Bin Fraction’

	R_{eff} (F160W)											
	Compact $R_{eff} < 1\text{kpc}$				Moderate $1\text{kpc} \leq R_{eff} < 3\text{kpc}$				Extended $3\text{kpc} \leq R_{eff}$			
	$M_{stellar}$ 9.4-10.0	$M_{stellar}$ 10-11	$M_{stellar}$ >11	$M_{stellar}$ >11	$M_{stellar}$ 9.4-10.0	$M_{stellar}$ 10-11	$M_{stellar}$ >11	$M_{stellar}$ >11	$M_{stellar}$ 9.4-10.0	$M_{stellar}$ 10-11	$M_{stellar}$ >11	$M_{stellar}$ >11
2.6 ≤ z < 3.0 (48)	8 (100.0%)	10 (100.0%)	1 (100.0%)	16 (16.5%)	8 (17.8%)	1 (25.0%)	2 (6.5%)	2 (5.3%)	0 (0.0%)	0 (0.0%)	0 (0.0%)	0 (0.0%)
2.2 ≤ z < 2.6 (79)	12 (92.3%)	25 (100.0%)	1 (100.0%)	22 (20.8%)	12 (31.6%)	4 (50.0%)	1 (2.9%)	1 (2.9%)	1 (12.5%)	1 (7.1%)	1 (9.1%)	1 (12.5%)
1.8 ≤ z < 2.2 (70)	9 (81.8%)	10 (100.0%)	1 (100.0%)	30 (24.0%)	15 (30.0%)	1 (14.3%)	1 (2.5%)	2 (2.7%)	1 (7.1%)	1 (9.1%)	1 (12.5%)	1 (12.5%)
1.4 ≤ z < 1.8 (134)	17 (89.5%)	23 (100.0%)	0 (-NaN%)	40 (23.0%)	31 (38.8%)	15 (78.9%)	3 (2.4%)	4 (4.9%)	1 (9.1%)	1 (9.1%)	1 (12.5%)	1 (12.5%)
1.0 ≤ z < 1.4 (149)	16 (94.1%)	19 (90.5%)	0 (-NaN%)	45 (26.0%)	56 (50.0%)	5 (50.0%)	1 (0.6%)	5 (4.6%)	2 (7.4%)	2 (16.7%)	2 (15.4%)	2 (15.4%)
0.5 ≤ z < 1.0 (182)	21 (100.0%)	19 (95.0%)	0 (-NaN%)	43 (22.6%)	70 (46.7%)	3 (50.0%)	1 (0.6%)	12 (8.8%)	13 (38.2%)	13 (38.2%)	13 (38.2%)	13 (38.2%)
Total: 662	83	106	3	196	192	29	9	26	18	18	18	18

Table B.7: Clumpy Galaxy Fractions Evolution with Redshift in Mass and sSFR Bins - ‘Bin Fraction’

	Quiescent sSFR < -0.9				Transitional -0.9 ≤ sSFR < -0.3				Star Forming -0.3 ≤ sSFR < 0.95				High Star Forming 0.95 ≤ sSFR			
	M_{stellar} 9.4-10.0	M_{stellar} 10-11	M_{stellar} >11	M_{stellar} >11	M_{stellar} 9.4-10.0	M_{stellar} 10-11	M_{stellar} >11	M_{stellar} >11	M_{stellar} 9.4-10.0	M_{stellar} 10-11	M_{stellar} >11	M_{stellar} >11	M_{stellar} 9.4-10.0	M_{stellar} 10-11	M_{stellar} >11	
2.6 ≤ z < 3.0 (126)	0 (-NaN%)	0 (0.0%)	0 (0.0%)	1 (33.3%)	2 (40.0%)	2 (33.3%)	0	62 (51.2%)	49 (66.2%)	0	8 (53.3%)	4 (40.0%)	0			
2.2 ≤ z < 2.6 (115)	0 (0.0%)	1 (7.7%)	0 (0.0%)	2 (66.7%)	2 (20.0%)	2 (66.7%)	2	59 (41.5%)	40 (56.3%)	2	7 (87.5%)	0 (0.0%)	0			
1.8 ≤ z < 2.2 (139)	0 (0.0%)	1 (7.7%)	2 (16.7%)	3 (75.0%)	1 (11.1%)	3 (75.0%)	3	58 (35.8%)	58 (58.6%)	1	10 (83.3%)	5 (38.5%)	0			
1.4 ≤ z < 1.8 (233)	0 (-NaN%)	1 (2.4%)	2 (9.5%)	4 (50.0%)	2 (6.9%)	4 (50.0%)	4	136 (48.9%)	62 (66.0%)	1	13 (43.3%)	10 (52.6%)	0			
1.0 ≤ z < 1.4 (325)	0 (0.0%)	6 (7.6%)	8 (33.3%)	11 (91.7%)	19 (41.3%)	11 (91.7%)	11	168 (56.4%)	85 (81.0%)	0	20 (64.5%)	6 (54.5%)	0			
0.5 ≤ z < 1.0 (340)	3 (9.7%)	10 (7.8%)	5 (17.2%)	3 (60.0%)	18 (30.5%)	3 (60.0%)	3	177 (61.9%)	84 (78.5%)	5	24 (66.7%)	9 (75.0%)	0			
Total: 1278	3	19	17	24	44	24	24	660	378	9	82	34	0			

Table B.8: Clumpy Galaxy Fractions Evolution with Redshift in Mass and R_{eff} Bins - ‘Bin Fraction’

	Compact $R_{\text{eff}} < 1\text{kpc}$			Moderate $1\text{kpc} \leq R_{\text{eff}} < 3\text{kpc}$			Extended $3\text{kpc} \leq R_{\text{eff}}$		
	M_{stellar} 9.4-10.0	M_{stellar} 10-11	M_{stellar} >11	M_{stellar} 9.4-10.0	M_{stellar} 10-11	M_{stellar} >11	M_{stellar} 9.4-10.0	M_{stellar} 10-11	M_{stellar} >11
2.6 ≤ z < 3.0 (126)	0 (0.0%)	0 (0.0%)	0 (0.0%)	44 (45.4%)	24 (53.3%)	0 (0.0%)	26 (83.9%)	31 (81.6%)	1 (33.3%)
2.2 ≤ z < 2.6 (115)	0 (0.0%)	0 (0.0%)	0 (0.0%)	38 (35.8%)	16 (42.1%)	1 (12.5%)	30 (88.2%)	27 (77.1%)	3 (37.5%)
1.8 ≤ z < 2.2 (139)	0 (0.0%)	0 (0.0%)	0 (0.0%)	36 (28.8%)	13 (26.0%)	2 (28.6%)	32 (80.0%)	52 (70.3%)	4 (28.6%)
1.4 ≤ z < 1.8 (233)	0 (0.0%)	0 (0.0%)	0 (-NaN%)	57 (32.8%)	22 (27.5%)	2 (10.5%)	94 (75.8%)	53 (65.4%)	5 (45.5%)
1.0 ≤ z < 1.4 (325)	0 (0.0%)	0 (0.0%)	0 (-NaN%)	61 (35.3%)	33 (29.5%)	0 (0.0%)	129 (76.8%)	83 (76.9%)	19 (70.4%)
0.5 ≤ z < 1.0 (340)	1 (4.8%)	0 (0.0%)	0 (-NaN%)	66 (34.7%)	28 (18.7%)	0 (0.0%)	139 (83.7%)	93 (68.4%)	13 (38.2%)
Total: 1278	1	0	0	302	136	5	450	339	45

Table B.9: Chain Galaxy Fractions Evolution with Redshift in Mass and sSFR Bins - ‘Bin Fraction’

	sSFR											
	Quiescent sSFR < -0.9			Transitional -0.9 ≤ sSFR < -0.3			Star Forming -0.3 ≤ sSFR < 0.95			High Star Forming 0.95 ≤ sSFR		
	M_{stellar} 9.4-10.0	M_{stellar} 10-11	M_{stellar} >11	M_{stellar} 9.4-10.0	M_{stellar} 10-11	M_{stellar} >11	M_{stellar} 9.4-10.0	M_{stellar} 10-11	M_{stellar} >11	M_{stellar} 9.4-10.0	M_{stellar} 10-11	M_{stellar} >11
2.6 ≤ z < 3.0 (16)	0 (0.0%)	0 (0.0%)	0 (0.0%)	0 (-NaN%)	0 (0.0%)	1 (33.3%)	9 (7.4%)	5 (6.8%)	0 (-NaN%)	1 (6.7%)	0 (0.0%)	0 (-NaN%)
2.2 ≤ z < 2.6 (11)	0 (0.0%)	0 (0.0%)	0 (0.0%)	0 (0.0%)	0 (0.0%)	0 (0.0%)	7 (4.9%)	3 (4.2%)	0 (0.0%)	1 (12.5%)	0 (0.0%)	0 (0.0%)
1.8 ≤ z < 2.2 (13)	0 (0.0%)	0 (0.0%)	0 (0.0%)	0 (0.0%)	0 (0.0%)	0 (0.0%)	11 (6.8%)	2 (2.0%)	0 (0.0%)	0 (0.0%)	0 (0.0%)	0 (-NaN%)
1.4 ≤ z < 1.8 (24)	0 (0.0%)	0 (0.0%)	0 (0.0%)	0 (0.0%)	0 (0.0%)	1 (12.5%)	16 (5.8%)	4 (4.3%)	0 (0.0%)	2 (6.7%)	1 (5.3%)	0 (-NaN%)
1.0 ≤ z < 1.4 (18)	0 (0.0%)	0 (0.0%)	0 (0.0%)	0 (0.0%)	0 (0.0%)	0 (0.0%)	15 (5.0%)	0 (0.0%)	0 (0.0%)	3 (9.7%)	0 (0.0%)	0 (-NaN%)
0.5 ≤ z < 1.0 (18)	0 (0.0%)	0 (0.0%)	0 (0.0%)	0 (0.0%)	0 (0.0%)	0 (0.0%)	12 (4.2%)	3 (2.8%)	0 (0.0%)	3 (8.3%)	0 (0.0%)	0 (-NaN%)
Total: 100	0	0	0	0	0	2	70	17	0	10	1	0

Table B.10: Chain Galaxy Fractions Evolution with Redshift in Mass and R_{eff} Bins - ‘Bin Fraction’

	R_{eff} (F160W)											
	Compact $R_{\text{eff}} < 1\text{kpc}$			Moderate $1\text{kpc} \leq R_{\text{eff}} < 3\text{kpc}$			Extended $3\text{kpc} \leq R_{\text{eff}}$					
	M_{stellar} 9.4-10.0	M_{stellar} 10-11	M_{stellar} >11	M_{stellar} 9.4-10.0	M_{stellar} 10-11	M_{stellar} >11	M_{stellar} 9.4-10.0	M_{stellar} 10-11	M_{stellar} >11	M_{stellar} 9.4-10.0	M_{stellar} 10-11	M_{stellar} >11
2.6 ≤ z < 3.0 (16)	0 (0.0%)	0 (0.0%)	0 (0.0%)	3 (3.1%)	0 (0.0%)	0 (0.0%)	7 (22.6%)	5 (13.2%)	1 (33.3%)	0	0	0
2.2 ≤ z < 2.6 (11)	0 (0.0%)	0 (0.0%)	0 (0.0%)	4 (3.8%)	0 (0.0%)	0 (0.0%)	4 (11.8%)	3 (8.6%)	0 (0.0%)	0	0	0
1.8 ≤ z < 2.2 (13)	0 (0.0%)	0 (0.0%)	0 (0.0%)	1 (0.8%)	0 (0.0%)	0 (0.0%)	10 (25.0%)	2 (2.7%)	0 (0.0%)	0	0	0
1.4 ≤ z < 1.8 (24)	0 (0.0%)	0 (0.0%)	0 (-NaN%)	6 (3.4%)	0 (0.0%)	0 (0.0%)	12 (9.7%)	5 (6.2%)	1 (9.1%)	0	0	0
1.0 ≤ z < 1.4 (18)	0 (0.0%)	0 (0.0%)	0 (-NaN%)	4 (2.3%)	0 (0.0%)	0 (0.0%)	14 (8.3%)	0 (0.0%)	0 (0.0%)	0	0	0
0.5 ≤ z < 1.0 (18)	0 (0.0%)	0 (0.0%)	0 (-NaN%)	7 (3.7%)	0 (0.0%)	0 (0.0%)	8 (4.8%)	3 (2.2%)	0 (0.0%)	0	0	0
Total: 100	0	0	0	25	0	0	55	18	2	0	0	0

Table B.11: Tadpole Galaxy Fractions Evolution with Redshift in Mass and sSFR Bins - ‘Bin Fraction’

	sSFR											
	Quiescent sSFR < -0.9			Transitional -0.9 ≤ sSFR < -0.3			Star Forming -0.3 ≤ sSFR < 0.95			High Star Forming 0.95 ≤ sSFR		
	M_{stellar} 9.4-10.0	M_{stellar} 10-11	M_{stellar} >11	M_{stellar} 9.4-10.0	M_{stellar} 10-11	M_{stellar} >11	M_{stellar} 9.4-10.0	M_{stellar} 10-11	M_{stellar} >11	M_{stellar} 9.4-10.0	M_{stellar} 10-11	M_{stellar} >11
2.6 ≤ z < 3.0 (27)	0 (0.0%)	0 (0.0%)	0 (0.0%)	0 (0.0%)	0 (0.0%)	0 (0.0%)	16 (13.2%)	7 (9.5%)	0 (-NaN%)	3 (20.0%)	1 (10.0%)	0 (-NaN%)
2.2 ≤ z < 2.6 (21)	0 (0.0%)	0 (0.0%)	0 (0.0%)	1 (100.0%)	0 (0.0%)	0 (0.0%)	14 (9.9%)	4 (5.6%)	1 (16.7%)	1 (12.5%)	0 (0.0%)	0 (0.0%)
1.8 ≤ z < 2.2 (22)	1 (100.0%)	0 (0.0%)	0 (0.0%)	1 (100.0%)	0 (0.0%)	1 (25.0%)	9 (5.6%)	7 (7.1%)	1 (16.7%)	2 (16.7%)	0 (0.0%)	0 (-NaN%)
1.4 ≤ z < 1.8 (39)	0 (0.0%)	0 (0.0%)	0 (0.0%)	0 (0.0%)	2 (6.9%)	0 (0.0%)	27 (9.7%)	6 (6.4%)	0 (0.0%)	3 (10.0%)	1 (5.3%)	0 (-NaN%)
1.0 ≤ z < 1.4 (38)	0 (0.0%)	0 (0.0%)	0 (0.0%)	0 (0.0%)	2 (4.3%)	0 (0.0%)	26 (8.7%)	4 (3.8%)	0 (0.0%)	4 (12.9%)	2 (18.2%)	0 (-NaN%)
0.5 ≤ z < 1.0 (22)	1 (3.2%)	0 (0.0%)	0 (0.0%)	1 (4.2%)	2 (3.4%)	0 (0.0%)	12 (4.2%)	3 (2.8%)	0 (0.0%)	3 (8.3%)	0 (0.0%)	0 (-NaN%)
Total: 169	2	0	0	3	6	1	104	31	2	16	4	0

 Table B.12: Tadpole Galaxy Fractions Evolution with Redshift in Mass and R_{eff} Bins - ‘Bin Fraction’

	R_{eff} (F160W)											
	Compact $R_{\text{eff}} < 1\text{kpc}$			Moderate $1\text{kpc} \leq R_{\text{eff}} < 3\text{kpc}$			Extended $3\text{kpc} \leq R_{\text{eff}}$					
	M_{stellar} 9.4-10.0	M_{stellar} 10-11	M_{stellar} >11	M_{stellar} 9.4-10.0	M_{stellar} 10-11	M_{stellar} >11	M_{stellar} 9.4-10.0	M_{stellar} 10-11	M_{stellar} >11	M_{stellar} 9.4-10.0	M_{stellar} 10-11	M_{stellar} >11
2.6 ≤ z < 3.0 (27)	1 (12.5%)	0 (0.0%)	0 (0.0%)	9 (9.3%)	4 (8.9%)	0 (0.0%)	9 (29.0%)	4 (10.5%)	0 (0.0%)	3 (8.8%)	1 (12.5%)	0 (0.0%)
2.2 ≤ z < 2.6 (21)	0 (0.0%)	0 (0.0%)	0 (0.0%)	13 (12.3%)	1 (2.6%)	0 (0.0%)	3 (8.8%)	3 (8.6%)	1 (12.5%)	4 (10.0%)	2 (14.3%)	0 (0.0%)
1.8 ≤ z < 2.2 (22)	0 (0.0%)	0 (0.0%)	0 (0.0%)	9 (7.2%)	2 (4.0%)	0 (0.0%)	4 (10.0%)	5 (6.8%)	2 (6.2%)	5 (12.9%)	0 (0.0%)	0 (0.0%)
1.4 ≤ z < 1.8 (39)	0 (0.0%)	0 (0.0%)	0 (-NaN%)	18 (10.3%)	4 (5.0%)	0 (0.0%)	12 (9.7%)	5 (6.2%)	0 (0.0%)	17 (10.1%)	4 (3.7%)	0 (0.0%)
1.0 ≤ z < 1.4 (38)	0 (0.0%)	0 (0.0%)	0 (-NaN%)	13 (7.5%)	4 (3.6%)	0 (0.0%)	7 (10.1%)	4 (3.7%)	0 (0.0%)	4 (2.9%)	0 (0.0%)	0 (0.0%)
0.5 ≤ z < 1.0 (22)	0 (0.0%)	0 (0.0%)	0 (-NaN%)	10 (5.3%)	1 (0.7%)	0 (0.0%)	7 (4.2%)	4 (2.9%)	0 (0.0%)	4 (2.9%)	0 (0.0%)	0 (0.0%)
Total: 169	1	0	0	72	16	0	52	25	3	16	4	0

Table B.13: Asymmetric Galaxy Fractions Evolution with Redshift in Mass and sSFR Bins - ‘Bin Fraction’

	sSFR											
	Quiescent sSFR < 0.9			Transitional -0.9 ≤ sSFR < -0.3			Star Forming -0.3 ≤ sSFR < 0.95			High Star Forming 0.95 ≤ sSFR		
	$M_{stellar}$ 9.4-10.0	$M_{stellar}$ 10-11	$M_{stellar}$ >11	$M_{stellar}$ 9.4-10.0	$M_{stellar}$ 10-11	$M_{stellar}$ >11	$M_{stellar}$ 9.4-10.0	$M_{stellar}$ 10-11	$M_{stellar}$ >11	$M_{stellar}$ 9.4-10.0	$M_{stellar}$ 10-11	$M_{stellar}$ >11
2.6 ≤ z < 3.0 (149)	0 (-NaN%)	0 (0.0%)	4 (80.0%)	0 (-NaN%)	2 (40.0%)	1 (33.3%)	70 (57.9%)	53 (71.6%)	0 (-NaN%)	12 (80.0%)	7 (70.0%)	0 (-NaN%)
2.2 ≤ z < 2.6 (144)	2 (100.0%)	0 (0.0%)	2 (28.6%)	2 (200.0%)	2 (20.0%)	0 (0.0%)	77 (54.2%)	46 (64.8%)	2 (33.3%)	10 (125.0%)	1 (25.0%)	0 (0.0%)
1.8 ≤ z < 2.2 (173)	1 (100.0%)	5 (38.5%)	1 (8.3%)	1 (100.0%)	3 (33.3%)	3 (75.0%)	84 (51.9%)	56 (56.6%)	3 (50.0%)	8 (66.7%)	8 (61.5%)	0 (-NaN%)
1.4 ≤ z < 1.8 (235)	0 (-NaN%)	3 (7.1%)	1 (4.8%)	4 (44.4%)	7 (24.1%)	4 (50.0%)	138 (49.6%)	49 (52.1%)	1 (100.0%)	16 (53.3%)	12 (63.2%)	0 (-NaN%)
1.0 ≤ z < 1.4 (255)	0 (0.0%)	6 (7.6%)	4 (16.7%)	2 (13.3%)	5 (10.9%)	3 (25.0%)	154 (51.7%)	54 (51.4%)	0 (0.0%)	21 (67.7%)	6 (54.5%)	0 (-NaN%)
0.5 ≤ z < 1.0 (199)	2 (6.5%)	4 (3.1%)	4 (13.8%)	4 (16.7%)	9 (15.3%)	1 (20.0%)	109 (38.1%)	44 (41.1%)	1 (16.7%)	16 (44.4%)	5 (41.7%)	0 (-NaN%)
Total: 1155	5	18	16	13	28	12	632	302	7	83	39	0

 Table B.14: Asymmetric Galaxy Fractions Evolution with Redshift in Mass and R_{eff} Bins - ‘Bin Fraction’

	R_{eff} (F160W)											
	Compact $R_{eff} < 1\text{kpc}$			Moderate $1\text{kpc} \leq R_{eff} < 3\text{kpc}$			Extended $3\text{kpc} \leq R_{eff}$					
	$M_{stellar}$ 9.4-10.0	$M_{stellar}$ 10-11	$M_{stellar}$ >11	$M_{stellar}$ 9.4-10.0	$M_{stellar}$ 10-11	$M_{stellar}$ >11	$M_{stellar}$ 9.4-10.0	$M_{stellar}$ 10-11	$M_{stellar}$ >11			
2.6 ≤ z < 3.0 (149)	2 (25.0%)	0 (0.0%)	0 (0.0%)	57 (58.8%)	28 (62.2%)	2 (50.0%)	23 (74.2%)	34 (89.5%)	3 (100.0%)			
2.2 ≤ z < 2.6 (144)	2 (15.4%)	0 (0.0%)	0 (0.0%)	58 (54.7%)	23 (60.5%)	2 (25.0%)	31 (91.2%)	26 (74.3%)	2 (25.0%)			
1.8 ≤ z < 2.2 (173)	0 (0.0%)	1 (10.0%)	0 (0.0%)	64 (51.2%)	17 (34.0%)	1 (14.3%)	30 (75.0%)	54 (73.0%)	6 (42.9%)			
1.4 ≤ z < 1.8 (235)	1 (5.3%)	0 (0.0%)	0 (-NaN%)	72 (41.4%)	19 (23.8%)	0 (0.0%)	85 (68.5%)	52 (64.2%)	6 (54.5%)			
1.0 ≤ z < 1.4 (255)	0 (0.0%)	1 (4.8%)	0 (-NaN%)	69 (39.9%)	16 (14.3%)	1 (10.0%)	108 (64.3%)	54 (50.9%)	6 (22.2%)			
0.5 ≤ z < 1.0 (199)	0 (0.0%)	0 (0.0%)	0 (-NaN%)	45 (23.7%)	11 (7.3%)	0 (0.0%)	86 (51.8%)	51 (37.5%)	6 (17.6%)			
Total: 1155	5	2	0	365	114	6	363	271	29			

Table B.15: Merger Galaxy Fractions Evolution with Redshift in Mass and sSFR Bins - ‘Bin Fraction’

	sSFR											
	Quiescent sSFR < -0.9			Transitional -0.9 ≤ sSFR < -0.3			Star Forming -0.3 ≤ sSFR < 0.95			High Star Forming 0.95 ≤ sSFR		
	$M_{stellar}$ 9.4-10.0	$M_{stellar}$ 10-11	$M_{stellar}$ >11	$M_{stellar}$ 9.4-10.0	$M_{stellar}$ 10-11	$M_{stellar}$ >11	$M_{stellar}$ 9.4-10.0	$M_{stellar}$ 10-11	$M_{stellar}$ >11	$M_{stellar}$ 9.4-10.0	$M_{stellar}$ 10-11	$M_{stellar}$ >11
2.6 ≤ z < 3.0 (55)	0 (-NaN%)	0 (0.0%)	0 (0.0%)	0 (-NaN%)	2 (40.0%)	1 (33.3%)	22 (18.2%)	22 (29.7%)	0 (-NaN%)	5 (33.3%)	3 (30.0%)	0 (-NaN%)
2.2 ≤ z < 2.6 (64)	2 (100.0%)	0 (0.0%)	0 (0.0%)	1 (100.0%)	0 (0.0%)	0 (0.0%)	35 (24.6%)	17 (23.9%)	2 (33.3%)	7 (87.5%)	0 (0.0%)	0 (0.0%)
1.8 ≤ z < 2.2 (66)	0 (0.0%)	3 (23.1%)	0 (0.0%)	0 (0.0%)	0 (0.0%)	2 (50.0%)	31 (19.1%)	23 (23.2%)	0 (0.0%)	6 (50.0%)	1 (7.7%)	0 (-NaN%)
1.4 ≤ z < 1.8 (100)	0 (-NaN%)	5 (11.9%)	3 (14.3%)	3 (33.3%)	5 (17.2%)	0 (0.0%)	56 (20.1%)	20 (21.3%)	0 (0.0%)	3 (10.0%)	5 (26.3%)	0 (-NaN%)
1.0 ≤ z < 1.4 (123)	1 (7.1%)	3 (3.8%)	0 (0.0%)	0 (0.0%)	6 (13.0%)	2 (16.7%)	71 (23.8%)	26 (24.8%)	0 (0.0%)	11 (35.5%)	3 (27.3%)	0 (-NaN%)
0.5 ≤ z < 1.0 (110)	3 (9.7%)	2 (1.6%)	5 (17.2%)	2 (8.3%)	9 (15.3%)	1 (20.0%)	52 (18.2%)	22 (20.6%)	2 (33.3%)	6 (16.7%)	6 (50.0%)	0 (-NaN%)
Total: 518	6	13	8	6	22	6	267	130	4	38	18	0

Table B.16: Merger Galaxy Fractions Evolution with Redshift in Mass and R_{eff} Bins - ‘Bin Fraction’

	R_{eff} (F160W)											
	Compact $R_{eff} < 1kpc$			Moderate $1kpc \leq R_{eff} < 3kpc$			Extended $3kpc \leq R_{eff}$					
	$M_{stellar}$ 9.4-10.0	$M_{stellar}$ 10-11	$M_{stellar}$ >11	$M_{stellar}$ 9.4-10.0	$M_{stellar}$ 10-11	$M_{stellar}$ >11	$M_{stellar}$ 9.4-10.0	$M_{stellar}$ 10-11	$M_{stellar}$ >11	$M_{stellar}$ 9.4-10.0	$M_{stellar}$ 10-11	$M_{stellar}$ >11
2.6 ≤ z < 3.0 (55)	0 (0.0%)	0 (0.0%)	0 (0.0%)	18 (18.6%)	11 (24.4%)	1 (25.0%)	9 (29.0%)	16 (42.1%)	0 (0.0%)	0	0	0
2.2 ≤ z < 2.6 (64)	0 (0.0%)	0 (0.0%)	0 (0.0%)	29 (27.4%)	7 (18.4%)	0 (0.0%)	16 (47.1%)	10 (28.6%)	2 (25.0%)	0	0	0
1.8 ≤ z < 2.2 (66)	1 (9.1%)	0 (0.0%)	0 (0.0%)	19 (15.2%)	6 (12.0%)	1 (14.3%)	17 (42.5%)	21 (28.4%)	1 (7.1%)	0	0	0
1.4 ≤ z < 1.8 (100)	1 (5.3%)	1 (4.3%)	0 (-NaN%)	23 (13.2%)	12 (15.0%)	3 (15.8%)	38 (30.6%)	22 (27.2%)	0 (0.0%)	0	0	0
1.0 ≤ z < 1.4 (123)	0 (0.0%)	1 (4.8%)	0 (-NaN%)	30 (17.3%)	14 (12.5%)	0 (0.0%)	53 (31.5%)	23 (21.3%)	2 (7.4%)	0	0	0
0.5 ≤ z < 1.0 (110)	0 (0.0%)	0 (0.0%)	0 (-NaN%)	23 (12.1%)	8 (5.3%)	0 (0.0%)	40 (24.1%)	31 (22.8%)	8 (23.5%)	0	0	0
Total: 518	2	2	0	142	58	5	173	123	13	0	0	0

Appendix C

Morphology Evolution of Individual $z \sim 2$ Hydro-ART Simulations

The included figures show the measured Sérsic index (n), effective radius (R_{eff}), and axis ratio (q) at each available $z \sim 2$ time step for our 38 Hydro-ART simulations. These morphological properties were calculated on the CANDELized images of the $z \sim 2$ simulations as described in Chapter 2. The simulation name and available redshift range are shown on each subplot. To show the effect of viewing angle on the measured quantities, the values from both the edge-on (triangular points) and face-on (circular points) cameras are displayed. The face-on and edge-on quantities at the same epoch are connected with a solid line and a dashed line is used to connect the face-on quantities from high redshift to low redshift. The size of the points depends on the simulation's stellar mass at a given epoch with larger points corresponding to larger masses. Finally, the color of the points depends on the measured specific star formation

rate (sSFR) of the simulation at that epoch. Galaxies with high sSFR are shown in purple, galaxies with moderate sSFR are shown in blue, and galaxies with low sSFR are shown in green. The wide variety of morphological evolution seen in the simulations is surprising. Some simulations seem very stable and their morphologies do not change significantly over time. Other simulations undergo large swings in their morphologies from one epoch to another. The behavior of a simulation depends on the halo size and specific history of that simulation.

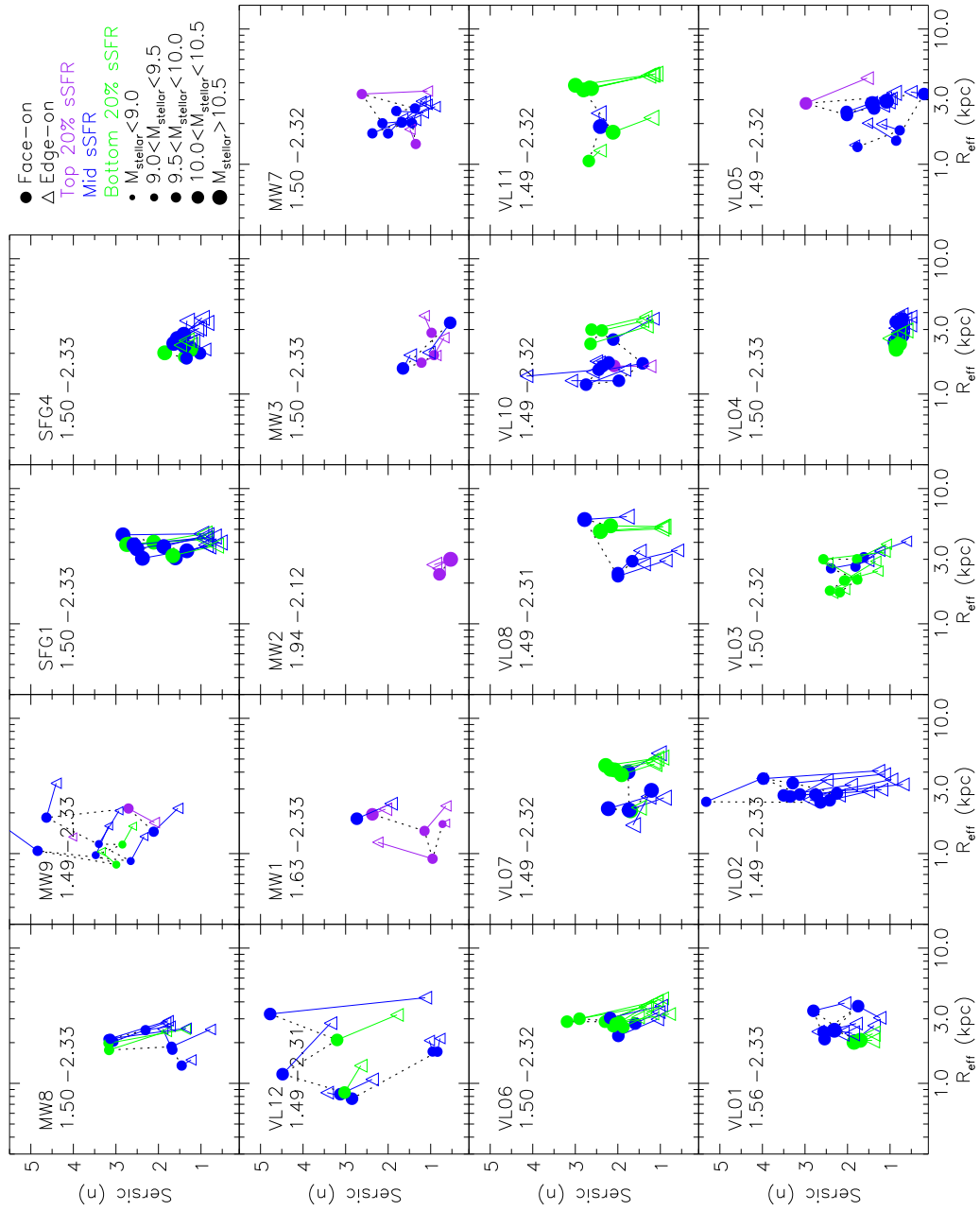


Figure C.1: Sérsic - R_{eff} Evolution of $z \sim 2$ Hydro-ART Simulations: 1

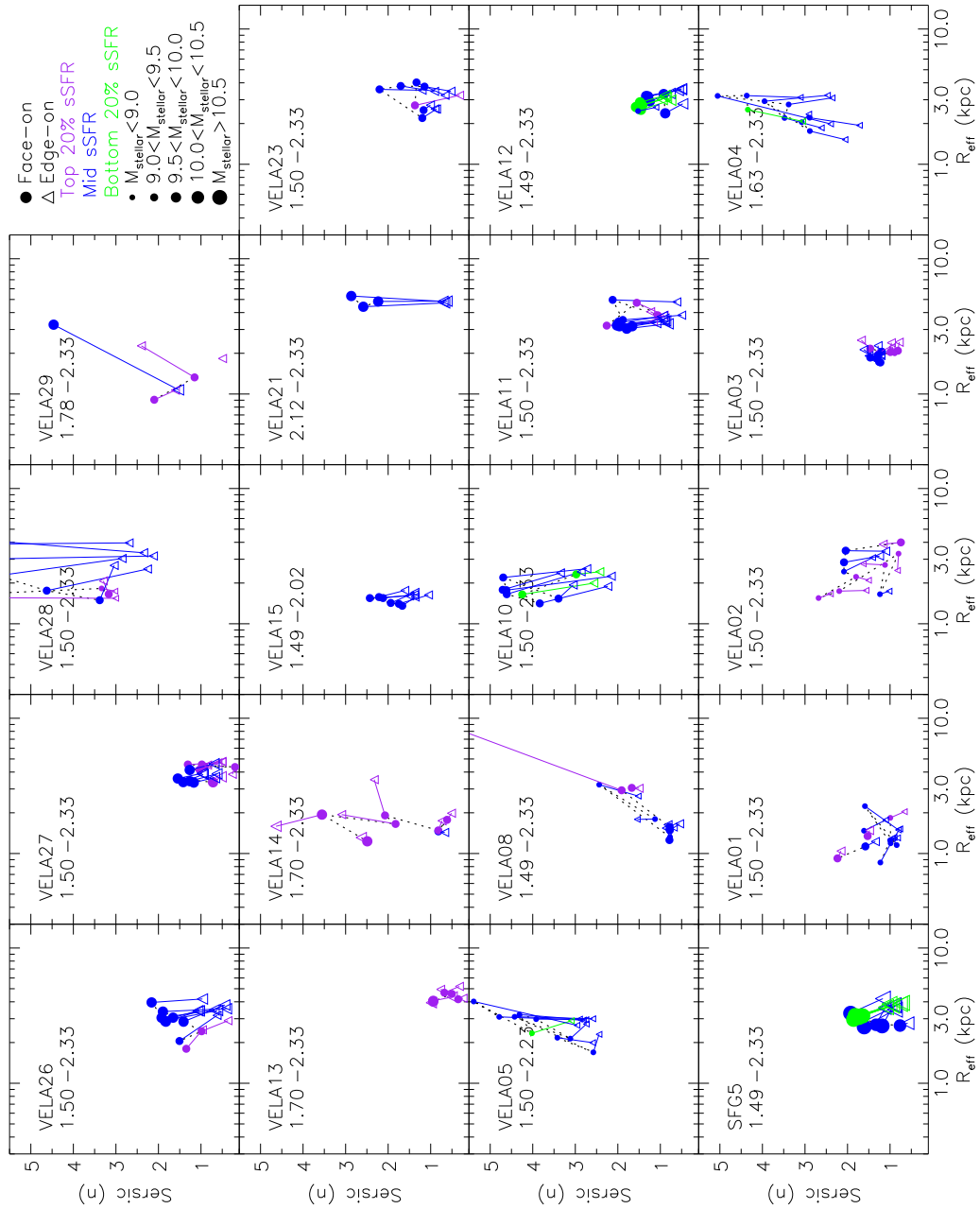


Figure C.2: Sérsic - R_{eff} Evolution of $z \sim 2$ Hydro-ART Simulations: 2

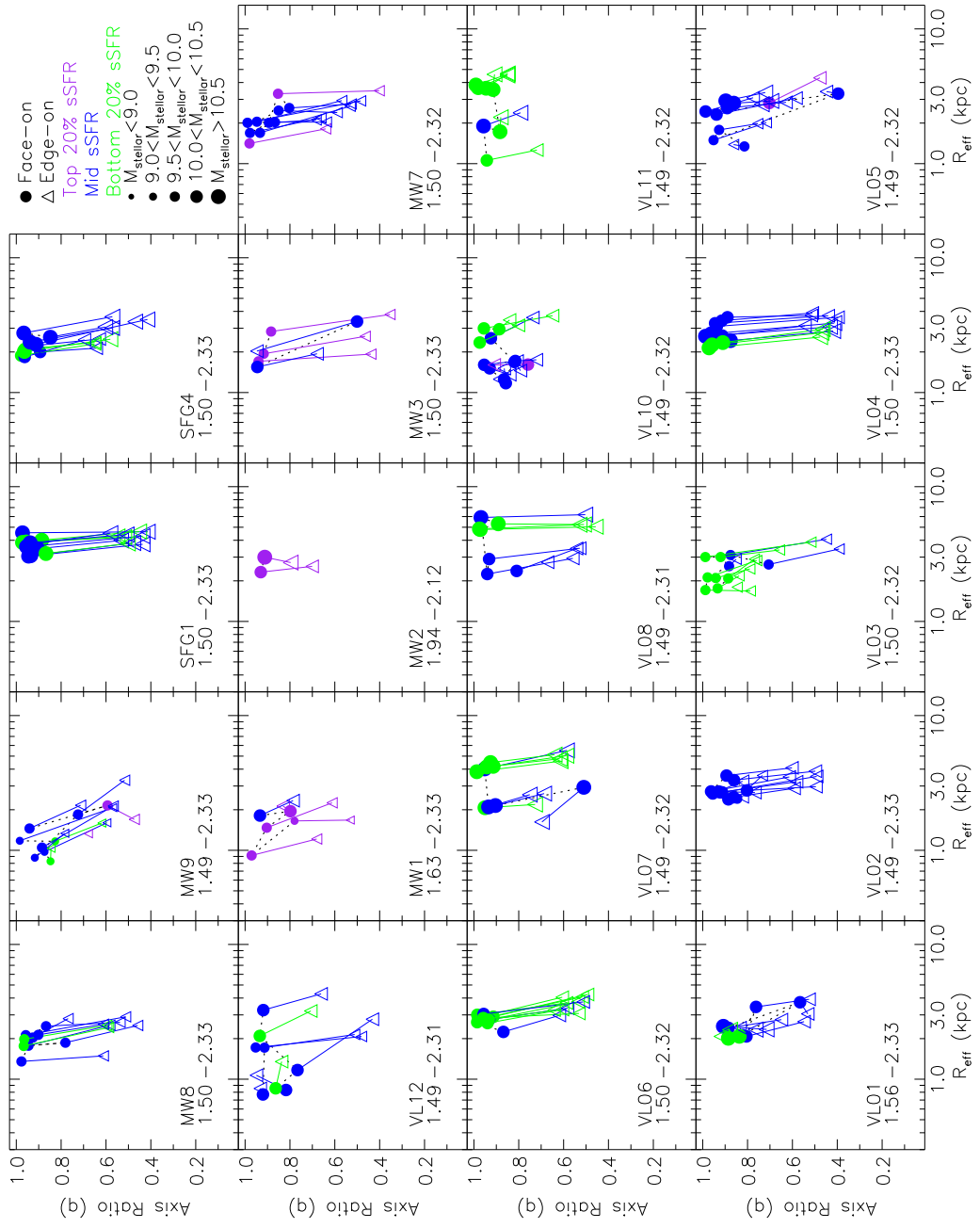


Figure C.3: Axis Ratio - R_{eff} Evolution of $z \sim 2$ Hydro-ART Simulations: 1

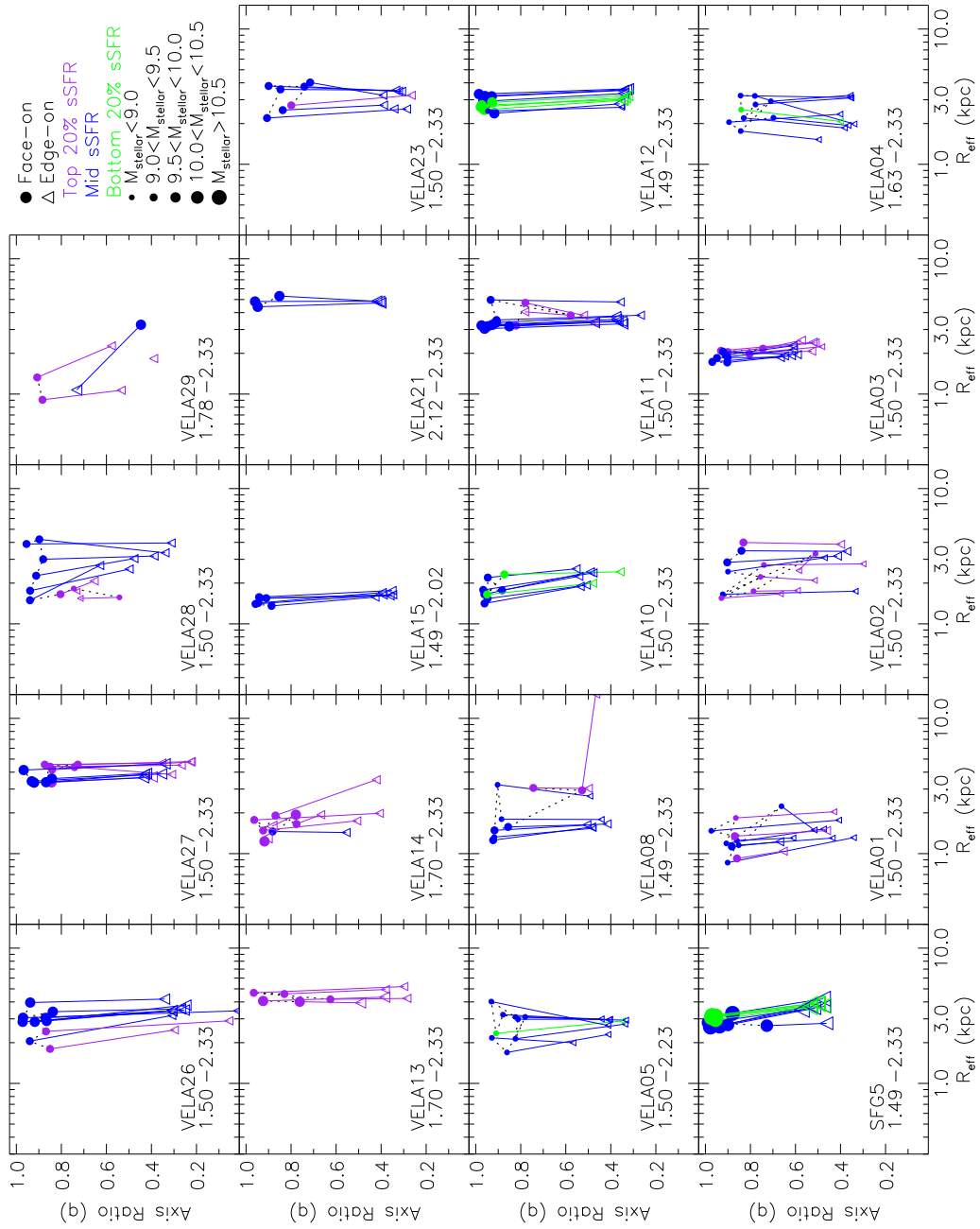


Figure C.4: Axis Ratio - R_{eff} Evolution of $z \sim 2$ Hydro-ART Simulations: 2

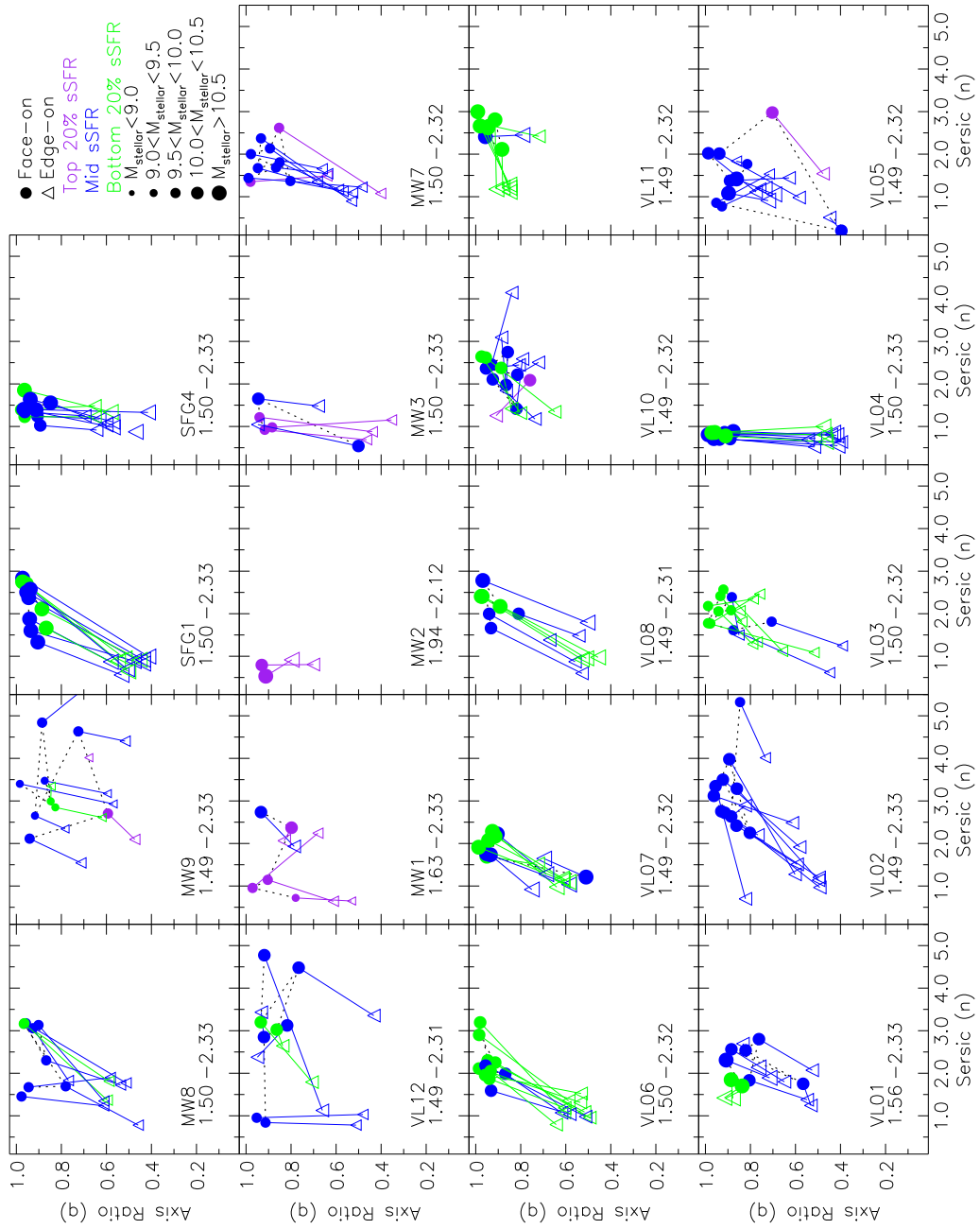


Figure C.5: Axis Ratio - Sérsic Evolution of $z \sim 2$ Hydro-ART Simulations: 1

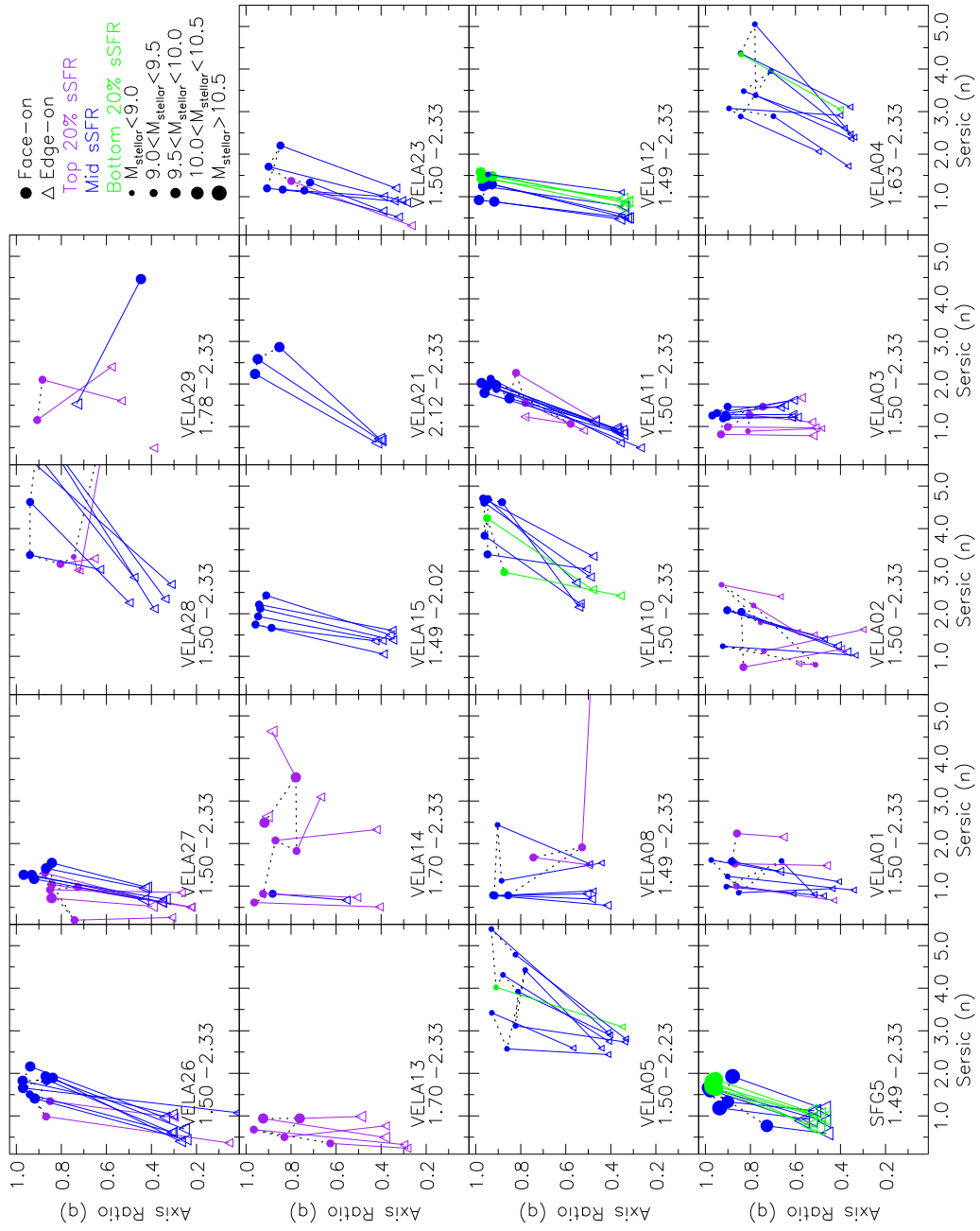


Figure C.6: Axis Ratio - Sérsic Evolution of $z \sim 2$ Hydro-ART Simulations: 2

Bibliography

- Abraham, R. G., Tanvir, N. R., Santiago, B. X., et al. 1996, MNRAS, 279, L47, L47
- Adelberger, K. L., Steidel, C. C., Shapley, A. E., et al. 2004, ApJ, 607, 226, 226
- Agertz, O., Teyssier, R., & Moore, B. 2009, MNRAS, 397, L64, L64
- Baldry, I. K., Glazebrook, K., Brinkmann, J., et al. 2004, ApJ, 600, 681, 681
- Bamford, S. P., Nichol, R. C., Baldry, I. K., et al. 2009, MNRAS, 393, 1324, 1324
- Barden, M., Häußler, B., Peng, C. Y., McIntosh, D. H., & Guo, Y. 2012, MNRAS, 422, 449, 449
- Barro, G., Faber, S. M., Pérez-González, P. G., et al. 2013, ApJ, 765, 104, 104
- Behroozi, P. S., Wechsler, R. H., & Conroy, C. 2013, ApJ, 770, 57, 57
- Bell, E. F., Zheng, X. Z., Papovich, C., et al. 2007, ApJ, 663, 834, 834
- Bell, E. F., McIntosh, D. H., Barden, M., et al. 2004, ApJ, 600, L11, L11
- Bell, E. F., Papovich, C., Wolf, C., et al. 2005, ApJ, 625, 23, 23

Bell, E. F., van der Wel, A., Papovich, C., et al. 2012, *ApJ*, 753, 167, 167

Bertin, E., & Arnouts, S. 1996, *A&AS*, 117, 393, 393

Bouwens, R. J., Illingworth, G. D., Oesch, P. A., et al. 2010, *ApJ*, 709, L133, L133

Brammer, G. B., van Dokkum, P. G., & Coppi, P. 2008, *ApJ*, 686, 1503, 1503

Brammer, G. B., Whitaker, K. E., van Dokkum, P. G., et al. 2011, *ApJ*, 739, 24, 24

Brinchmann, J., Abraham, R., Schade, D., et al. 1998, *ApJ*, 499, 112, 112

Bruce, V. A., Dunlop, J. S., Cirasuolo, M., et al. 2012, *MNRAS*, 427, 1666, 1666

Bruzual, G., & Charlot, S. 2003, *MNRAS*, 344, 1000, 1000

Buitrago, F., Trujillo, I., Conselice, C. J., & Häußler, B. 2013, *MNRAS*, 428, 1460, 1460

Bundy, K., Ellis, R. S., Conselice, C. J., et al. 2006, *ApJ*, 651, 120, 120

Bundy, K., Scarlata, C., Carollo, C. M., et al. 2010, *ApJ*, 719, 1969, 1969

Calzetti, D., Armus, L., Bohlin, R. C., et al. 2000, *ApJ*, 533, 682, 682

Cameron, E., Carollo, C. M., Oesch, P. A., et al. 2011, *ApJ*, 743, 146, 146

Ceverino, D., Dekel, A., & Bournaud, F. 2010, *MNRAS*, 404, 2151, 2151

Ceverino, D., Dekel, A., Mandelker, N., et al. 2012, *MNRAS*, 420, 3490, 3490

Ceverino, D., & Klypin, A. 2009, *ApJ*, 695, 292, 292

Chabrier, G. 2003, *PASP*, 115, 763, 763

- Chang, Y.-Y., van der Wel, A., Rix, H.-W., et al. 2013, *ApJ*, 773, 149, 149
- Conselice, C. J. 2003, *ApJS*, 147, 1, 1
- . 2006, *ApJ*, 638, 686, 686
- Conselice, C. J., Blackburne, J. A., & Papovich, C. 2005, *ApJ*, 620, 564, 564
- Conselice, C. J., Bluck, A. F. L., Ravindranath, S., et al. 2011a, *MNRAS*, 417, 2770, 2770
- Conselice, C. J., Rajgor, S., & Myers, R. 2008, *MNRAS*, 386, 909, 909
- Conselice, C. J., Bluck, A. F. L., Buitrago, F., et al. 2011b, *MNRAS*, 413, 80, 80
- Cowie, L. L., Hu, E. M., & Songaila, A. 1995, *AJ*, 110, 1576, 1576
- Daddi, E., Cimatti, A., Renzini, A., et al. 2004, *ApJ*, 600, L127, L127
- Daddi, E., Renzini, A., Pirzkal, N., et al. 2005, *ApJ*, 626, 680, 680
- Dahlen, T., Mobasher, B., Faber, S. M., et al. 2013, *ApJ*, 775, 93, 93
- Dekel, A., Sari, R., & Ceverino, D. 2009, *ApJ*, 703, 785, 785
- Dekel, A., Zolotov, A., Tweed, D., et al. 2013, *ArXiv e-prints*, arXiv:1303.3009
- Dickinson, M. 2000, in *Royal Society of London Philosophical Transactions Series A*, Vol. 358, Astronomy, physics and chemistry of H^+_3 , 2001
- Driver, S. P., Fernandez-Soto, A., Couch, W. J., et al. 1998, *ApJ*, 496, L93, L93

Driver, S. P., Allen, P. D., Graham, A. W., et al. 2006, MNRAS, 368, 414, 414

Drory, N., & Fisher, D. B. 2007, ApJ, 664, 640, 640

Elmegreen, B. G., & Elmegreen, D. M. 2006, ApJ, 650, 644, 644

Elmegreen, D. M., Elmegreen, B. G., Ravindranath, S., & Coe, D. A. 2007, ApJ, 658,
763, 763

Elmegreen, D. M., Elmegreen, B. G., Rubin, D. S., & Schaffer, M. A. 2005, ApJ, 631,
85, 85

Förster Schreiber, N. M., Shapley, A. E., Erb, D. K., et al. 2011, ApJ, 731, 65, 65

Förster Schreiber, N. M., Genzel, R., Bouché, N., et al. 2009, ApJ, 706, 1364, 1364

Franx, M., van Dokkum, P. G., Schreiber, N. M. F., et al. 2008, ApJ, 688, 770, 770

Galametz, A., Grazian, A., Fontana, A., et al. 2013, ApJS, 206, 10, 10

Genzel, R., Tacconi, L. J., Eisenhauer, F., et al. 2006, Nature, 442, 786, 786

Genzel, R., Burkert, A., Bouché, N., et al. 2008, ApJ, 687, 59, 59

Giavalisco, M., Ferguson, H. C., Koekemoer, A. M., et al. 2004, ApJ, 600, L93, L93

Grogin, N. A., Kocevski, D. D., Faber, S. M., et al. 2011, ApJS, 197, 35, 35

Guo, Y., Giavalisco, M., Ferguson, H. C., Cassata, P., & Koekemoer, A. M. 2012, ApJ,
757, 120, 120

Guo, Y., Ferguson, H. C., Giavalisco, M., et al. 2013, ApJS, 207, 24, 24

- Haardt, F., & Madau, P. 1996, *ApJ*, 461, 20, 20
- Hubble, E. P. 1926, *ApJ*, 64, 321, 321
- Ilbert, O., Lauger, S., Tresse, L., et al. 2006, *A&A*, 453, 809, 809
- Jonsson, P. 2006, *MNRAS*, 372, 2, 2
- Jonsson, P., Groves, B. A., & Cox, T. J. 2010, *MNRAS*, 403, 17, 17
- Kartaltepe, J. S., Dickinson, M., Alexander, D. M., et al. 2012, *ApJ*, 757, 23, 23
- Kauffmann, G., Heckman, T. M., White, S. D. M., et al. 2003, *MNRAS*, 341, 54, 54
- Kennicutt, Jr., R. C. 1998, *ARA&A*, 36, 189, 189
- Kocevski, D. D., Faber, S. M., Mozena, M., et al. 2012, *ApJ*, 744, 148, 148
- Koekemoer, A. M., Faber, S. M., Ferguson, H. C., et al. 2011, *ApJS*, 197, 36, 36
- Kravtsov, A. V., Klypin, A. A., & Khokhlov, A. M. 1997, *ApJS*, 111, 73, 73
- Kriek, M., van Dokkum, P. G., Franx, M., Illingworth, G. D., & Magee, D. K. 2009,
ApJ, 705, L71, L71
- Kriek, M., van Dokkum, P. G., Franx, M., et al. 2006, *ApJ*, 649, L71, L71
- Labbé, I., Bouwens, R., Illingworth, G. D., & Franx, M. 2006, *ApJ*, 649, L67, L67
- Laidler, V. G., Grogin, N., Clubb, K., et al. 2006, in *Astronomical Society of the Pacific
Conference Series*, Vol. 351, *Astronomical Data Analysis Software and Systems XV*,
ed. C. Gabriel, C. Arviset, D. Ponz, & S. Enrique, 228

- Law, D. R., Steidel, C. C., Erb, D. K., et al. 2009, *ApJ*, 697, 2057, 2057
- Law, D. R., Steidel, C. C., Shapley, A. E., et al. 2012, *ApJ*, 745, 85, 85
- Lee, B., Giavalisco, M., Williams, C. C., et al. 2013, *ApJ*, 774, 47, 47
- Mandelker, N., Dekel, A., Ceverino, D., et al. 2013, *ArXiv e-prints*, arXiv:1311.0013
- Masters, K. L., Mosleh, M., Romer, A. K., et al. 2010, *MNRAS*, 405, 783, 783
- McGrath, E. J., Stockton, A., Canalizo, G., Iye, M., & Maihara, T. 2008, *ApJ*, 682, 303, 303
- Mortlock, A., Conselice, C. J., Hartley, W. G., et al. 2013, *MNRAS*, 433, 1185, 1185
- Nair, P. B., & Abraham, R. G. 2010, *ApJS*, 186, 427, 427
- Newman, A. B., Ellis, R. S., Bundy, K., & Treu, T. 2012, *ApJ*, 746, 162, 162
- Newman, J. A. 2008, *ApJ*, 684, 88, 88
- Ocvirk, P., Pichon, C., & Teyssier, R. 2008, *MNRAS*, 390, 1326, 1326
- Oesch, P. A., Carollo, C. M., Feldmann, R., et al. 2010, *ApJ*, 714, L47, L47
- Padilla, N. D., & Strauss, M. A. 2008, *MNRAS*, 388, 1321, 1321
- Papovich, C., Dickinson, M., Giavalisco, M., Conselice, C. J., & Ferguson, H. C. 2005, *ApJ*, 631, 101, 101
- Patel, S. G., Holden, B. P., Kelson, D. D., et al. 2012, *ApJ*, 748, L27, L27

- Patel, S. G., Kelson, D. D., Holden, B. P., Franx, M., & Illingworth, G. D. 2011, *ApJ*, 735, 53, 53
- Patel, S. G., van Dokkum, P. G., Franx, M., et al. 2013, *ApJ*, 766, 15, 15
- Peng, C. Y., Ho, L. C., Impey, C. D., & Rix, H.-W. 2002, *AJ*, 124, 266, 266
- Sandage, A. 1986, *A&A*, 161, 89, 89
- Scarlata, C., Carollo, C. M., Lilly, S., et al. 2007, *ApJS*, 172, 406, 406
- Schmidt, M. 1959, *ApJ*, 129, 243, 243
- Sersic, J. L. 1968,
- Stark, D. P., Swinbank, A. M., Ellis, R. S., et al. 2008, *Nature*, 455, 775, 775
- Steidel, C. C., Adelberger, K. L., Giavalisco, M., Dickinson, M., & Pettini, M. 1999, *ApJ*, 519, 1, 1
- Stockton, A., Canalizo, G., & Maihara, T. 2004, *ApJ*, 605, 37, 37
- Strateva, I., Ivezić, Ž., Knapp, G. R., et al. 2001, *AJ*, 122, 1861, 1861
- Straughn, A. N., Cohen, S. H., Ryan, R. E., et al. 2006, *ApJ*, 639, 724, 724
- Szomoru, D., Franx, M., Bouwens, R. J., et al. 2011, *ApJ*, 735, L22, L22
- Szomoru, D., Franx, M., & van Dokkum, P. G. 2012, *ApJ*, 749, 121, 121
- Trujillo, I., Förster Schreiber, N. M., Rudnick, G., et al. 2006, *ApJ*, 650, 18, 18

van den Bergh, S. 2002, *PASP*, 114, 797, 797

van den Bergh, S., Abraham, R. G., Ellis, R. S., et al. 1996, *AJ*, 112, 359, 359

van den Bergh, S., Cohen, J. G., Hogg, D. W., & Blandford, R. 2000, *AJ*, 120, 2190, 2190

van der Wel, A., Rix, H.-W., Wuyts, S., et al. 2011, *ApJ*, 730, 38, 38

van der Wel, A., Bell, E. F., Häussler, B., et al. 2012, *ApJS*, 203, 24, 24

van Dokkum, P. G., Franx, M., Kriek, M., et al. 2008, *ApJ*, 677, L5, L5

Wang, T., Huang, J.-S., Faber, S. M., et al. 2012, *ApJ*, 752, 134, 134

Whitaker, K. E., Labbé, I., van Dokkum, P. G., et al. 2011, *ApJ*, 735, 86, 86

Williams, R. J., Quadri, R. F., Franx, M., van Dokkum, P., & Labbé, I. 2009, *ApJ*, 691, 1879, 1879

Williams, R. J., Quadri, R. F., Franx, M., et al. 2010, *ApJ*, 713, 738, 738

Windhorst, R. A., Cohen, S. H., Hathi, N. P., et al. 2011, *ApJS*, 193, 27, 27

Wuyts, S., Labbé, I., Schreiber, N. M. F., et al. 2008, *ApJ*, 682, 985, 985

Wuyts, S., Labbé, I., Franx, M., et al. 2007, *ApJ*, 655, 51, 51

Wuyts, S., Förster Schreiber, N. M., van der Wel, A., et al. 2011a, *ApJ*, 742, 96, 96

Wuyts, S., Förster Schreiber, N. M., Lutz, D., et al. 2011b, *ApJ*, 738, 106, 106

Wuyts, S., Förster Schreiber, N. M., Genzel, R., et al. 2012, *ApJ*, 753, 114, 114